AFRL-SR-AR-TR-10-0197

REPORT DOCUMENTATION PAGE

Public reporting burden for this collection of information is estimated to average 1 hour per response, including the time for reviewing instru.
dete needed, and completing and reviewing this collection of information. Send comments regarding this burden estimate or any other asp
this burden to Department of Defense, Washington Headquarters Services, Directorate for Information Operations and Reports (0704-0188
4302. Respondents should be aware that notwithstanding any other provision of law, no person shall be subject to any penalty for failing to comply with a collection of information if it does not display a currently
valid OMB control number. **PLEASE DO NOT RETURN YOUR FORM TO THE ABOVE ADDRESS.**

1. REPORT DATE *(DD-MM-YYYY)*	2. REPORT TYPE	3. DATES COVERED *(From - To)*
05/21/2010	Submitted manuscript	05/01/2007 to 02/28/2010

4. TITLE AND SUBTITLE: LARGE EDDY SIMULATIONS OF SUPERCRITICAL MIXING LAYERS FOR AIR FORCE APPLICATIONS	5a. CONTRACT NUMBER
	5b. GRANT NUMBER
	FA9550-07-1-0348
	5c. PROGRAM ELEMENT NUMBER

6. AUTHOR(S)	5d. PROJECT NUMBER
Josette Bellan	
	5e. TASK NUMBER
	5f. WORK UNIT NUMBER

7. PERFORMING ORGANIZATION NAME(S) AND ADDRESS(ES)	8. PERFORMING ORGANIZATION REPORT NUMBER
California Institute of Technology 1200 E. California Blvd. Pasadena, CA 91125	

9. SPONSORING / MONITORING AGENCY NAME(S) AND ADDRESS(ES)	10. SPONSOR/MONITOR'S ACRONYM(S)
AFOSR/NA RSA 875 North Randolph Street Suite 325, Room 3112 Arlington VA 22203-1768	
	11. SPONSOR/MONITOR'S REPORT NUMBER(S)

12. DISTRIBUTION / AVAILABILITY STATEMENT

Approved for public release; distribution is unlimited.

13. SUPPLEMENTARY NOTES

14. ABSTRACT A general study has been undertaken to develop subgrid-scale (SGS) models for conducting Large Eddy Simulation (LES) of supercritical turbulent flows. In a first step, we have shown that due to strong dynamic/ thermodynamic coupling in these flows, there is a necessity of additional SGS models for LES compared to atmospheric-flow LES where only SGS-flux models are used. Two important such terms were identified, which we call "corrections". The first correction term was in the momentum equation for the pressure-gradient term. We proposed two models for the pressure-correction term, both based on a Taylor expansion and showed that with this correction, the LES were considerably more accurate when compared to a template based on Direct numerical Simulation (DNS). The second term needing correction was the heat flux in the energy equation. We have developed a heat-flux-correction model based on the Approximate Deconvolution Method. The results showed that with the heat-flux-correction model, LES results are substantially improved when compared to typical LES using only SGS-flux models. The new model improves the heat flux prediction up to an irreducible error. We have also shown that mean flow variables, first o... fluctuations and second-order correlations, all benefit from inclusion of this new model.

20100617305

15. SUBJECT TERMS
Supercritical fluid mixing; compressible mixing

16. SECURITY CLASSIFICATION OF:			17. LIMITATION OF ABSTRACT	18. NUMBER OF PAGES	19a. NAME OF RESPONSIBLE PERSON
a. REPORT	b. ABSTRACT	c. THIS PAGE	UL	[8]	Mitat birkan
Unclassified	Unclassified	Unclassified			19b. TELEPHONE NUMBER *(include area code)* (703) 696-7234

Standard Form 298 (Rev. 8-98)
Prescribed by ANSI Std. Z39.18

LARGE EDDY SIMULATIONS OF SUPERCRITICAL MIXING LAYERS FOR AIR FORCE APPLICATIONS
Grant Number: FA9550-07-1-0348

Final report

Josette Bellan
Mechanical Engineering Department
California Institute of Technology
Pasadena, CA 91125

to

Abstract

This report describes a study performed under AFOSR sponsorship, addressing the investigation of mixing and fluid disintegration under supercritical turbulent flow conditions. Because the study has been very fruitful and produced a very large amount of information, including major publications in refereed journals, this final report is in the form of an Executive Summary succinctly describing the results, with particular emphasis on the connection among the publications or manuscripts which have not yet reached the print. The publications/manuscripts are individually listed as Appendices, and attached to this report.

TABLE OF CONTENTS

EXECUTIVE SUMMARY

The highlights of the results from publications and papers submitted, as shown in Appendices 1-4, as well as several conference papers (not included) are here summarized.

The objective of this study was to obtain a fundamental understanding of fuel disintegration and mixing at supercritical pressure conditions (relative to the fuel). At supercritical pressures, fluids depart from the ubiquitous perfect gas and mixture ideality situations prevailing at atmospheric pressure; the atmospheric-pressure condition has overwhelmingly been studied so far. Because according to the binary species combinations, a spectrum of quantitative departures from perfect gas and mixture ideality is obtained, the present study proposed to leverage against a program focused on one species combination so as to more completely address the different regimes, understand the interconnections between them, and more fully understand how to model gas turbines, liquid rockets, and ramjets.

The goal of the present investigation was to propose Subgrid Scale (SGS) models for performing Large Eddy Simulations of fluid disintegration and mixing under supercritical pressure conditions. In our previous work, we had performed Direct Numerical Simulations (DNS) of such flows and identified specific flow characteristics not encountered under atmospheric-pressure conditions. The DNS portrayed a three-dimensional (3D) mixing layer the lower stream of which is initially composed of pure heptane and the upper stream of which is initially composed of pure nitrogen; these were denoted as HN runs. The free-stream pressure was 60 atm, the upper free-stream temperature was 1000K and that of the lower stream was 600K. Other binary-species pairs that were simulated were oxygen/hydrogen (OH runs) and oxygen/helium (OHe), both at 100 atm and for several free-stream temperatures of each of the streams. A database DNS of eight simulations was thus created. The peculiar behavior occurred independently of the binary-species pairs or other conditions of the calculations. This peculiarity was the existence of regions of high density-gradients magnitude (HDGM). These exist both in the pre-transitional (Miller et al. (2001)) and transitional (Okong'o and Bellan (2002; Okong'o et al. (2002)) settings. At the transitional state, the HDGM regions resemble convoluted threads, such as observed by Chehroudi and Talley (1999), Oschwald and Schik (1999), and Segal and Polikhov (2008) at fully turbulent Reynolds numbers. The magnitude of the density gradient in the DNS at the transitional state was of same order as, or even inferior to, that detected experimentally. Visualizations of the time sequence leading to transition showed that the HDGM regions form due to two coupled processes: the convolution/distortion of the original density boundary, and the mixing of the species. Because the HDGM regions impede the formation of small scales, they are the sites of the highest irreversible entropy production (Okong'o and Bellan (2002; Okong'o et al. (2002)); the irreversible entropy production is the dissipation, and it is the quantity that SGS models must reproduce. That is, the maximum dissipation regions are located in the HDGM regions. The existence of HDGM regions and their relationship to dissipation is independent of the binary system of species. Moreover, since a budget of the dissipation at the transitional state showed that its largest contribution is from the species mass flux -- i.e. what is called "the scalar dissipation"-- (Okong'o and Bellan (2002; Okong'o et al. (2002)), the indication is that SGS modeling targeted at duplicating the viscous effects, as it is typical under subcritical conditions, is likely to be inappropriate under supercritical conditions.

1

A previously conducted *a priori* study (Selle et al. 2007) encompassing all DNS runs confirmed the indications obtained from analysis of the database. In the *a priori* study, the DNS equations were first filtered and the terms in the equations were ranked based on their importance measured by the domain r.m.s. It turns out that whereas the usual SGS-flux terms were indeed important, other terms which are usually neglected in the LES equations were here even more important than the SGS-flux terms. These were: (1) a term appearing in the momentum equation that is the difference between the gradient of the filtered pressure and the gradient of the pressure computed from the filtered flow field; this term was prominent for HN runs and moderately important for the OHe run, but not for OH runs, and (2) a term appearing in the energy conservation equation that is the difference between the divergence of the filtered heat flux and the divergence of the heat flux computed from the filtered flow field; this term was prominent for OH runs, moderately important for the OHe runs but not for HN runs. The importance of both of these terms is directly traced, through the gradients, to the HDGM regions; the fact that these regions are a feature of fully turbulent flows immediately implies that modeling these terms will be of paramount importance for LES. Thus, in that paper we proposed models and performed *a priori* tests not only for the SGS-flux terms but also for these additional two terms. The model for the pressure-gradient difference term was based on a Taylor expansion of the pressure, on computing the derivatives of this expansion using the real-gas equation of state and on assuming that the filter is a projection which nulled the first-order term of the Taylor expansion and allowed the model of the second-order term utilizing models for the variances that were the same as for the SGS fluxes. The model proved very successful for a LES grid which is 64 times volumetrically larger than the DNS grid, but deteriorated for a grid that was 512 times volumetrically larger than the DNS grid; this deterioration is understandable given that Taylor expansions are only valid in a small neighborhood of the reference location. Modeling of the new term in the energy equation proved considerably more difficult (compared to that in the momentum equation) as it is the sum of three terms, each being a gradient of one of the thermodynamic variables multiplied by a coefficient that is function of the thermodynamic variables. Whereas the coefficients could be very well modeled using Taylor expansion concepts, the entire term was poorly rendered due to a lack of model for the filtered gradients. The two issues of the desirability of having an even more accurate model for the momentum equation terms that could possibly be valid for coarser LES grids, and that an appropriate model for the term in the energy equation remained to be addressed in *a posteriori* studies.

In a first *a posteriori* study (Appendix 1) conducted for HN runs, the issue of the momentum equation term was addressed. An additional model for this term was proposed based on the first-order Taylor expansion term, but without adding the second-order Taylor expansion term which could not be easily modeled without the assumption of the filter being a projection, which nulled the first-order term. LES conducted with only SGS-flux models, and with SGS-flux models and this additional modeled term were compared with the filtered-and-coarsened DNS, which is the template that must be achieved. Several conclusions were drawn: (1) A LES using a model for the additional term in the momentum equation is considerably closer to the template compared to a LES only using SGS-flux terms. (2) The model based on the first-order Taylor expansion term was more successful than that based on the second-order expansion term, which is understandable since the former is a better approximation than the latter. These conclusions were obtained with constant-coefficient SGS-flux models. Since among SGS-flux models the Scale-Similarity constant-coefficient model was most successful in those tests, dynamic-coefficient

2

modeling was also pursued because they rely on the same concepts as scale-similarity models. Not only were these dynamic-coefficient LES performed with single SGS-flux models, but we also combined SGS-flux models into 'mixed' models to complement the best aspects of each model. The dynamic models were also successful when used in conjunction with the model for the new term in the momentum equation, although each of the dynamic models was best at reproducing certain aspects of the flow field. We considered good predictions of the pressure as being crucial since without them the velocity field would be incorrect, and also predictions of the HDGM regions since they are instrumental to the flow development and mixing. Studies of the LES grid spacing impact and the choice of the initial conditions were also carried out.

In a second *a posteriori* study (Appendix 3) conducted for the OH DNS run having the largest initial Reynolds number and the OHe run, the issue of the model for the new term in the energy equation was addressed. The *a priori* investigation was re-visited and it was realized that one must focus on the reconstruction of the filtered gradients in the heat flux from the gradients computed using the filtered flow field. Based on this realization, seven models for the new energy equation term were proposed. In all models, we used the approximate deconvolution model (ADM) to capture the filtered temperature gradient, filtered mass fraction gradient and filtered pressure gradient variation. It turns out that ADM is very successful at recovering the new term in the energy equation, and one of these seven models was chosen to pursue the LES study, based on its accuracy and computational efficiency. The LES computations show that there is a definite advantage in including the new term for recovering the heat flux in the system; it is well known that recovery of the heat flux is of outmost importance for liquid rocket propulsion, as documented by Tucker et al. 2008. Our results show that by using ADM we recover the heat flux up to an irreducible error; the remaining error is simply due to the fact that the flow field reconstruction is performed on the coarser (i.e. LES) grid compared to the DNS one. Of note, LES conducted with no SGS-flux models but including a heat-flux-correction model shows substantial improvements over the LES conducted without SGS-flux models and no heat-flux-correction model meaning that this new SGS contribution introduces substantial physical information into the simulation. With SGS-flux and heat-flux-correction models, the LES yields a good approximation of the filtered DNS flow field for both OH and OHe runs. This success with two different species systems having different equations of state and transport properties illustrates the power of the concept and proposed models.

The success obtained with SGS models additional to the typical SGS-flux ones are transformational for the LES field of study in that never before have LES been shown to need other than SGS-flux models, and LES have never been conducted with other models additional to those for the SGS fluxes. Moreover, this success bodes well for conducting LES with coarse grids, such as needed for large geometries typical of liquid rocket engines.

Two additional supporting studies complete this investigation. In the first study (Appendix 2), we showed that by an appropriate non-dimensionalization of the dissipation (not to be confused with the turbulent energy dissipation), it appears that in all fully turbulent flows the scalar dissipation is the most important contributor to the dissipation. The dissipation has contributions from three modes associated with viscous stresses, temperature-gradient and species-mass-gradient effects. Non-dimensionalization of the dissipation and its contributions revealed the essential mechanisms governing each of the modes and their relative contributions

to the total dissipation. The viscous, temperature-gradient and species-mass-gradient dissipation contributions scale as $O(Re^{-1})$, $O(Re^{-1}Pr^{-1}Ma^{-2})$ and $O(Ma^{-2})$, respectively; where Re is the Reynolds number, Pr is the Prandtl number and Ma is the Mach number. As a result of this scaling, for Reynolds number values in the fully turbulent flow regime, the species-mass-gradient mode is predicted to dominate the other modes. Even for the transitional Reynolds number values of the examined database, assessment of the DNS-scale domain-averaged dissipation confirmed previous findings that out of the three modes of dissipation, the species-mass dissipation is the main contributor to the total dissipation. The results revealed that, remarkably, the percentage of species-mass by total dissipation is nearly invariant across species systems and initial conditions. This dominance of the species-mass dissipation is due to the HDGM regions populating the flow. The domain average being the result of both the local values and the extent of the HDGM regions, the expectations were that the response to filtering will vary with these flow characteristics. All filtering was performed in the dissipation range of the Kolmogorov spectrum, at filter sizes from four to sixteen times the DNS grid spacing. The small-scale (subgrid-scale, SGS) dissipation was found by subtracting the filtered-field dissipation from the DNS-field dissipation. In contrast to the DNS dissipation, the SGS dissipation is not necessarily positive; negative values indicate backscatter. Backscatter was shown to be spatially widespread in all modes of dissipation and in the total dissipation (25% to 60% of the domain). The maximum magnitude of the negative subgrid-scale dissipation was as much as 17% of the maximum positive subgrid-scale dissipation, indicating that not only is backscatter spatially wide spread in these flows, but it is considerable in magnitude and thus cannot be ignored for the purpose of LES modeling. With increased filter size, there is only a modest decrease in the spatial extent of backscatter. The implication is that even at large LES grid spacings, the issue of backscatter and related SGS-flux modeling decisions are unavoidable. As a fraction of the total dissipation, the small-scale dissipation is between 10% and 30% of the total dissipation for a filter size that is four times the DNS grid spacing, with all OH cases bunched at 10% and the HN cases spanning 24%-30%. A scale similarity was found in that the domain-average proportion of each small-scale dissipation mode with respect to the total small-scale dissipation is very similar to equivalent results at the DNS scale. With increasing filter size, the proportion of the small-scale dissipation in the dissipation increases substantially, although not quite proportionally. When the filter size increases by four fold, 52% for all OH runs and 70% for HN runs of the dissipation is contained in the subgrid-scale portion with virtually no dependence on the initial conditions of the DNS. The indications from the dissipation analysis are that modeling efforts in LES of thermodynamically supercritical flows should be focused primarily on mass-flux effects, with temperature and viscous effects being secondary although by no means negligible; this confirmed the preliminary findings from our previous studies.

In a second supporting study (Appendix 4), we conducted an investigation into the correct form of the LES equations for multicomponent atmospheric-pressure flows. The common trend with the supercritical study is the necessity, expressed by the *a priori* study, of including in the LES equations additional SGS terms than the usual SGS fluxes. As the number of species increases in a system, the structure of the flow becomes finer grained and therefore the modeling difficulty increases. We have here shown, both for single-phase and two-phase flow with phase change, that these additional terms can dominate SGS modeling requirements.

Thus, it is clear that the activity performed under this study has far-reaching implications and proposes solutions for the practicality of LES in real applications.

REFERENCES

Chehroudi, B., Talley, D. and Coy, E., Initial growth rate and visual characteristics of a round jet into a sub- to supercritical environment of relevance to rocket, gas turbine, and Diesel engines", AIAA 99-0206, presented at the 37th Aerospace Sciences Meeting, Reno, NV, 1999

Miller, R. S., Harstad, K. and Bellan, J., Direct Numerical Simulations of Supercritical Fluid Mixing Layers Applied to Heptane – Nitrogen, *J. Fluid Mech.*, 436, 1-39, 2001

Okong'o, N. and Bellan, J., Direct numerical simulation of a transitional supercritical binary mixing layer: heptane and nitrogen, *J. Fluid Mech.*, 464, 1-34, 2002.

Okong'o, N., Harstad, K. and Bellan, J., Direct Numerical Simulations of O_2/H_2 temporal mixing layers under supercritical conditions, *AIAA J.*, 40(5), 914-926, 2002

Oschwald, M. and Schik, A., Supercritical nitrogen free jet investigated by spontaneous Raman scattering, *Exp. Fluids*, 27, 497—506, 1999.

Segal, C. and Polikhov, S., Subcritical to supercritical mixing, *Phys. Fluids*, 20, 052101-7, 2008.

Selle, L. C., Okong'o, N. A., Bellan, J. and Harstad, K. G., Modeling of subgrid scale phenomena in supercritical transitional mixing layers: an *a priori* study, *J. Fluid Mech.*, 593, 57-91, 2007

Tucker, P. K., Menon, S., Merkle, C. L., Oefelein, J. C. and Yang, V., Validation of high-fidelity CFD simulations for rocket injector design. AIAA 2008-5226, presented at the 44th Joint Propulsion Conference, Hartford, CT., 2008

Appendix 1

A *posteriori* study using a DNS database describing fluid disintegration and binary-species mixing under supercritical pressure: heptane and nitrogen

EZGI S. TASKINOGLU[1] AND JOSETTE BELLAN[1,2]†

[1]California Institute of Technology, Pasadena, CA 91125, USA

[2]Jet Propulsion Laboratory, California Institute of Technology, Pasadena, CA 91109, USA

A large eddy simulation (LES) *a posteriori* study is conducted for a temporal mixing layer which initially contains different species in the lower and upper streams and in which the initial pressure is larger than the critical pressure of either species. A vorticity perturbation, initially imposed, promotes roll-up and a double pairing of four initial spanwise vortices to reach a transitional state. The LES equations consist of the differential conservation equations coupled with a real-gas equation of state, and the equations utilize transport properties depending on the thermodynamic variables. Unlike all LES models to date, the differential equations contain, additional to the subgrid-scale (SGS) fluxes, a new SGS term denoted a 'pressure correction' (p correction) in the momentum equation. This additional term results from filtering the Navier–Stokes equations and represents the gradient of the difference between the filtered p and p computed from the filtered flow field. A previous *a priori* analysis, using a direct numerical simulation (DNS) database for the same configuration, found this term to be of leading order in the momentum equation, a fact traced to the existence of regions of high density-gradient magnitude that populated the entire flow; in that study, the appropriateness of several SGS-flux models was assessed, and a model for the p-correction term was proposed.

In the present study, the constant-coefficient SGS-flux models of the *a priori* investigation are tested *a posteriori* in LES devoid of, or including, the SGS p-correction term. A new p-correction model, different from that of the *a priori* study, is used, and the results of the two p-correction models are compared. The results reveal that the former is less computationally intensive and more accurate than the latter in reproducing global and structural features of the flow. The constant-coefficient SGS-flux models encompass the Smagorinsky (SMC) model, in conjunction with the Yoshizawa (YO) model for the trace, the gradient (GRC) model and the scale similarity (SSC) models, all exercised with the *a priori* study constant-coefficient values calibrated at the transitional state. Further, dynamic SGS-flux model LESs are performed with the p correction included in all cases. The dynamic models are the Smagorinsky (SMD) model, in conjunction with the YO model, the gradient (GRD) model and 'mixed' models using SMD in combination with GRC or SSC utilized with their theoretical coefficient values. The LES comparison is performed with the filtered-and-coarsened DNS (FC-DNS) which represents an ideal LES solution. The constant-coefficient models including the p correction (SMCP, GRCP and SSCP)

† Email address for correspondence: josette.bellan@jpl.nasa.gov

are substantially superior to those devoid of it; the SSCP model produces the best agreement with the FC-DNS template. For duplicating the local flow structure, the predictive superiority of the dynamic mixed models is demonstrated over the SMD model; however, even better predictions in capturing vortical features are obtained with the GRD model. The GRD predictions improve when LES is initiated at a time past the initial range in which the p-correction term rivals in magnitude the leading-order term in the momentum equation. Finally, the ability of the LES to predict the FC-DNS irreversible entropy production is assessed. It is shown that the SSCP model is the best at recovering the domain-averaged irreversible entropy production. The sensitivity of the predictions to the initial conditions and grid size is also investigated.

1. Introduction

Counterflow motion of different species and species mixing at pressures initially higher than the critical pressure p_c of either fluid has peculiarities not encountered in atmospheric-pressure mixing. Specifically, transcritical-condition experimental observations using jets of various chemical species have identified structures termed 'fingers', or 'comb-like', extending from one of the streams; these structures have an increasingly gaseous appearance with increasing pressure p (Mayer *et al.* 1996, 1998; Chehroudi, Talley & Coy 1999; Oschwald & Schik 1999; Oschwald *et al.* 1999; Segal & Polikhov 2008). All these experiments were performed in the Reynolds number Re regime $O(10^4)$ to $O(10^5)$. No three-dimensional simulations currently exist that can recover the distinctive features of these $p \geqslant p_c$ flows in this Re number regime. This is because of the following reasons: (i) Reynolds-averaged Navier–Stokes simulations are completely inadequate for reproducing the time-dependent strong inhomogeneities observed in these flows. (ii) Direct numerical simulation (DNS) is not routinely feasible for such large Reynolds numbers because of its high computational expense. (iii) Large eddy simulation (LES) is a promising methodology for supercritical-p flows, but so far it has been utilized for $p \geqslant p_c$ flows with models developed for incompressible or atmospheric-p compressible situations (Oefelein & Yang 1998; Zong *et al.* 2004; Oefelein 2005) in which the flow peculiarities discussed above do not exist. Extending current LES models to $p \geqslant p_c$ flows is a necessity if one wishes to simulate gas turbine, diesel or liquid rocket engines in which mixing of species – a precursor to ignition and combustion – occurs at $p \geqslant p_c$ (for mixtures, p_c and the critical temperature T_c depend on the composition (Hirshfelder, Curtis & Bird 1964; Prausnitz, Lichtenthaler & de Azevedo 1986)).

Although DNS is not suitable for practical applications at fully turbulent Re values, it may provide information leading to a thorough understanding of the flow at transitional Re values, thus enabling LES model development. Such DNSs were performed for a temporal mixing layer by Miller, Harstad & Bellan (2001) and Okong'o & Bellan (2002*b*, 2003) using real-gas equations of state (EOSs) for non-ideal mixtures in conjunction with realistic transport properties and thermal diffusion (Soret and Dufour) effects. The results showed that one of the most prominent aspects of $p \geqslant p_c$ flows is the existence of regions of high density-gradient magnitude (HDGM), akin to those seen in the experiments. These HDGM regions were found in both pre-transitional (Miller *et al.* 2001) and transitional (Okong'o & Bellan 2002*b*; Okong'o, Harstad & Bellan 2002) temporal mixing layers and were shown to arise from the combined effect of the distortion of the initial density boundary and of

mixing (Okong'o & Bellan 2002b, 2004b). It is this filamentary morphology that we call fluid disintegration. Scrutiny of the HDGM composition showed that the HDGM fluid is a mixture of the heavy and light fluids; this situation is very different from that under atmospheric p, where the equivalent of the HDGM regions contains exclusively the heavy fluid, as during atomization.

Further, in an *a priori* analysis of the DNS database (Selle *et al.* 2007), it was found that the utilization of a real-gas EOS (Harstad & Bellan 2000; Okong'o & Bellan 2002b) results in the strictly atmospheric-p LES equations being no longer valid, as new significant terms arise from the filtering of the conservation equations. These terms are directly associated with the HDGM regions observed in both simulations and experiments, meaning that the validity of the novel terms extends to Re values higher than those of the transitional databases. The new terms originated from subgrid-scale (SGS) effects and thus required modelling, being conceptually but not mathematically similar to the well-known SGS fluxes. We call these new SGS models 'corrections' because they stemmed from the usual 'LES assumptions' – that the difference between a filtered quantity and the same quantity computed from the filtered flow field is negligible with respect to other terms in the equation – not being satisfied. Two such terms were identified – for the p gradient and the divergence of the heat flux. The p correction was shown to be necessary for the heptane–nitrogen (HN, C_7H_{16}–N_2) system which exhibited strong departures from perfect gas and species ideality, whereas the heat-flux correction term for this species system was negligible. The required heat-flux correction was substantial for the oxygen–hydrogen (OH, O_2–H_2) system, but the p-correction term was negligible; for this species system, the departures from perfect gas and mixture non-ideality are negligible. That a correction is necessary even for small departures from perfect gas and mixture ideality can be understood given the strong nonlinearity of the real-gas EOS, meaning that even slight real-gas or non-ideal mixture behaviour may impart considerable departures from the atmospheric-p LES equations; this is the nature of nonlinearity. For the oxygen–helium (OHe, O_2–He) system, which has modest departures from perfect gas and small departures from mixture non-ideality, the situation was intermediate between the HN and OH systems. Both p-correction and heat-flux correction models were based on Taylor expansion concepts (Selle *et al.* 2007). In the *a priori* analysis, SGS-flux models were also evaluated for the typical SGS fluxes (stresses, heat and species mass). The SGS-flux models evaluated were the Smagorinsky (SM) model (Smagorinksy 1963, 1993), the scale-similarity (SS) model (Bardina, Ferziger & Reynolds 1980) and the gradient (GR) model (Clark, Ferziger & Reynolds 1979). It was concluded that the SM model is inadequate to represent the SGS fluxes, whereas both the SS and the GR model captured the functional form of the SGS fluxes. The poor performance of the SM model was observed despite it being used in conjunction with the well-performing Yoshizawa (YO; Yoshizawa 1986) model for the SGS-stress trace.

Whereas the *a priori* analysis is only concerned with the behaviour of the small turbulent scales, what ultimately matters in LES is the ability of the model to reproduce the interaction among all scales. This interaction is here investigated in an *a posteriori* study in which the *a priori* developed models, as well as other models, are tested in LES, and the results are compared with the DNS database for the HN system (the OH system is relegated to a future study). However, an unprocessed DNS database is not the proper template for comparison with LES. The proper template is the filtered-and-coarsened (FC) DNS: filtered to remove the small scales that are not computed in LES and coarsened to reduce the number of nodes from DNS to those of LES. Thus, the FC-DNS field can be considered as a sample of the DNS

field and a generally ideal, unachievable, LES template. Following the presentation in §2 of the LES governing equations, the databases are summarized in §3. The LES initial and boundary conditions are presented in §4, and the numerical methodology is described in §5. In §6, we first address the effectiveness of a p-correction model by comparing two sets of LES that are identical in all respects, except that one set excludes and the other includes the p correction. The p-correction model is in the same spirit but different from that tested *a priori* (Selle *et al.* 2007), and thus its utilization can be considered as a general assessment of the p-correction concept. Having established the necessity of the p correction, the attention is turned to dynamic-coefficient SGS-flux models combined with a p-correction model; we first examine there the influence of the type of p-correction model, after which we compare dynamic-coefficient LESs that use the same p-correction model. Completing the physical picture, the replication in LES of the irreversible entropy production, which is the dissipation (not to be confused with the turbulent kinetic energy, or TKE, dissipation), is addressed. Considerations on initial conditions (ICs) are made in Appendix A, and an inquiry on grid size is presented in Appendix B. All above evaluations are performed using one realization of the DNS database. To assess the general validity of the results, further evaluations are performed for other realizations in the HN database, and for brevity, only some of the pertinent results are presented in Appendix C. Conclusions and a short discussion of future studies are offered in §7.

2. LES governing equations

The LES equations were derived by Selle *et al.* (2007) from the conservation equations by spatial filtering. The filtering operation is defined as

$$\overline{\psi}(x) = \int_V \psi(y) G(x - y) \, dy, \tag{2.1}$$

where G is the filter function and V is the filtering volume; G has the property that for a spatially invariant function, the filtered function is identical to the unfiltered one. For compressible flows, Favre filtering is used, defined as $\tilde{\psi} = \overline{\rho \psi}/\bar{\rho}$, where ρ is the density. The variance of two quantities φ and θ is defined as $\vartheta(\overline{\varphi}, \overline{\theta}) = \overline{\varphi \theta} - \overline{\varphi} \, \overline{\theta}$ or $\vartheta(\widetilde{\varphi}, \widetilde{\theta}) = \widetilde{\varphi \theta} - \widetilde{\varphi}\widetilde{\theta}$, depending on the filtering. The governing equations are written for the conservative variables $\phi = \{\rho, \rho u_i, \rho e_t, \rho Y_\alpha\}$ rather than the primitive variables $\psi(\phi) = \{u_i, p, X_\alpha, T\}$, where u_i is the velocity component in the x_i-direction spatial coordinate, e_t is the total energy, T is the temperature, and Y_α and X_α are the mass fraction and mole fraction of species α.

2.1. *LES differential equations*

The LES differential equations, obtained under the assumption that filtering and differentiation commute (the top-hat filter is used here for which the operations commute except near boundaries), are for the HN mixture (Selle *et al.* 2007):

$$\frac{\partial \bar{\rho}}{\partial t} + \frac{\partial \bar{\rho} \tilde{u}_j}{\partial x_j} = 0, \tag{2.2}$$

$$\frac{\partial \bar{\rho} \tilde{u}_i}{\partial t} + \frac{\partial \bar{\rho} \tilde{u}_i \tilde{u}_j}{\partial x_j} = -\frac{\partial p\left(\overline{\phi}\right)}{\partial x_i} + \frac{\partial \sigma_{ij}\left(\overline{\phi}\right)}{\partial x_j} - \frac{\partial}{\partial x_j}\left(\bar{\rho} \tau_{ij}\right) - \frac{\partial}{\partial x_i}\left[\overline{p(\phi)} - p\left(\overline{\phi}\right)\right]. \tag{2.3}$$

$$\frac{\partial \bar{\rho} \tilde{e}_t}{\partial t} + \frac{\partial \bar{\rho} \tilde{e}_t \tilde{u}_j}{\partial x_j} = -\frac{\partial p\left(\overline{\phi}\right) \tilde{u}_j}{\partial x_j} - \frac{\partial q_{IKj}\left(\overline{\phi}\right)}{\partial x_j} + \frac{\partial \sigma_{ij}\left(\overline{\phi}\right) \tilde{u}_i}{\partial x_j} - \frac{\partial}{\partial x_j}\left(\bar{\rho}\zeta_j\right) - \frac{\partial \left(\bar{\rho}\tau_{ij}\widetilde{u}_i\right)}{\partial x_j},$$

(2.4)

$$\frac{\partial \bar{\rho} \tilde{Y}_\alpha}{\partial t} + \frac{\partial \bar{\rho} \tilde{Y}_\alpha \tilde{u}_j}{\partial x_j} = -\frac{\partial j_{\alpha j}\left(\overline{\phi}\right)}{\partial x_j} - \frac{\partial}{\partial x_j}(\bar{\rho}\eta_{\alpha j}),$$

(2.5)

where the SGS fluxes are

$$\tau_{ij} = \vartheta(\widetilde{u}_i, \widetilde{u}_j), \quad \zeta_j = \vartheta(\tilde{h}, \tilde{u}_j), \quad \eta_{\alpha j} = \vartheta(\widetilde{Y}_\alpha, \widetilde{u}_j) \text{ with } \sum_{\alpha=1}^{N} \eta_{\alpha j} = 0,$$

(2.6)

and the additional SGS term modelled *a priori* by Selle *et al.* (2007) is $\nabla[\overline{p(\phi)} - p(\overline{\phi})]$. In (2.2)–(2.5), t is the time; σ is the viscous stress tensor; q_{IK} is the Irwing–Kirkwood (denoted by the subscript IK) heat flux (Sarman & Evans 1992); $e = e_t - e_K$ is the internal energy; $e_K = u_i u_i / 2$ is the kinetic energy; N is the number of species; and j_α is the species-mass flux of species α. Furthermore,

$$\sum_{\alpha=1}^{N} Y_\alpha = 1, \quad \sum_{\alpha=1}^{N} j_{\alpha j} = 0.$$

(2.7)

Here, the Einstein summation is used for roman indices (i, j, k) but not for Greek indices (α, β). The thermodynamic variables are functions of the LES flow field $\overline{\phi}$:

$$e = e\left(\overline{\phi}\right), \quad p = p\left(\overline{\phi}\right), \quad Y = Y\left(\overline{\phi}\right), \quad T = T\left(\overline{\phi}\right), \quad h = h\left(\overline{\phi}\right),$$

(2.8)

where p, T and the enthalpy $h = e + p/\rho$ are computed from the EOS. Likewise, the fluxes are functions of $\overline{\phi}$:

$$\sigma_{ij} = \sigma_{ij}\left(\overline{\phi}\right), \quad j_{\alpha j} = j_{\alpha j}\left(\overline{\phi}\right), \quad q_{IKj} = q_{IKj}\left(\overline{\phi}\right).$$

(2.9)

For a Newtonian fluid,

$$\sigma_{ij} = \mu\left(\frac{\partial u_i}{\partial x_j} + \frac{\partial u_j}{\partial x_i} - \frac{2}{3}\frac{\partial u_k}{\partial x_k}\delta_{ij}\right), \quad S_{ij} = \frac{1}{2}\left(\frac{\partial u_i}{\partial x_j} + \frac{\partial u_j}{\partial x_i}\right),$$

(2.10)

where μ is the viscosity and S_{ij} is the rate-of-strain tensor.

The species-mass and heat fluxes originate in the fluctuation–dissipation theory (see Keizer 1987), which is consistent with non-equilibrium thermodynamics, converges to kinetic theory in the low-p limit and relates fluxes and forces from first principles. For a binary-species system (light species 1, heavy species 2), the species-mass and heat fluxes, including the Soret and Dufour effects (Harstad & Bellan 2000), are

$$j_2(\overline{\psi}) = B_Y(\overline{\psi})\nabla Y_2\left(\overline{\phi}\right) + B_T(\overline{\psi})\nabla T\left(\overline{\phi}\right) + B_P(\overline{\psi})\nabla p\left(\overline{\phi}\right),$$

(2.11)

$$q_{IK}(\overline{\psi}) = C_Y(\overline{\psi})\nabla Y_2\left(\overline{\phi}\right) + C_T(\overline{\psi})\nabla T\left(\overline{\phi}\right) + C_P(\overline{\psi})\nabla p\left(\overline{\phi}\right),$$

(2.12)

where $\overline{\psi} \equiv \psi(\overline{\phi})$ and functionally

$$B_Y \equiv -\rho D\alpha_D, \qquad\qquad C_Y \equiv -\rho D\alpha_D\alpha_{IK}R_u T\frac{m}{m_1 m_2},$$

(2.13)

$$B_T \equiv -\alpha_{BK}Y_1 Y_2\frac{\rho D}{T}, \qquad\qquad C_T \equiv -\lambda - \rho D\alpha_{IK}\alpha_{BK}R_u\frac{m}{m_1 m_2}Y_1 Y_2,$$

(2.14)

$$B_P \equiv -\rho D\frac{Y_1 Y_2}{R_u T}\frac{m_2 m_1}{m}\Lambda, \qquad C_P \equiv -\rho D\alpha_{IK}\Lambda Y_1 Y_2.$$

(2.15)

Species	m (g mol^{-1})	T_c (K)	p_c(MPa)
N_2	28.013	126.3	3.399
C_7H_{16}	100.205	540.2	2.74

TABLE 1. Pure species properties.

In (2.13)–(2.15),

$$\alpha_{BK} = \alpha_{IK} - \alpha_h, \quad \alpha_h = \frac{1}{R_u T} \frac{m_2 m_1}{m} \Theta, \tag{2.16}$$

$$\Lambda \equiv \left(\frac{1}{m_2} \frac{\partial v}{\partial X_2} - \frac{1}{m_1} \frac{\partial v}{\partial X_1} \right), \quad \Theta \equiv \left(\frac{1}{m_2} \frac{\partial (mh)}{\partial X_2} - \frac{1}{m_1} \frac{\partial (mh)}{\partial X_1} \right), \tag{2.17}$$

$$\alpha_D \equiv 1 + X_\alpha \frac{\partial \ln \gamma_\alpha}{\partial X_\beta}, \tag{2.18}$$

where λ is the thermal conductivity with $\lim_{p \to 0} \lambda = \lambda_{KT}$ as discussed in Harstad & Bellan (2000); the subscript KT denotes the kinetic theory; R_u is the universal gas constant; m is the mixture molar mass; and v is the molar volume with $v = m/\rho$. For species α, m_α is the molar mass, $X_\alpha = mY_\alpha/m_\alpha$ and γ_α is the fugacity. Furthermore, α_{IK} is the IK form of the thermal diffusion factor; α_{BK} is the Bearman–Kirkwood (denoted by the subscript BK) form of the thermal diffusion factor; D is the binary diffusion coefficient; and α_D is the mass diffusion factor.

The models for the unclosed terms in (2.2)–(2.5), namely τ_{ij}, ζ_j, $\eta_{\alpha j}$ and $\nabla [\overline{p(\phi)} - p(\overline{\phi})]$, for the HN mixture are described in §2.4.1.

2.2. Equation of state

The pressure is calculated from the well-known Peng–Robinson (PR) EOS, given T and the PR molar volume (v_{PR}), as

$$p = \frac{R_u T}{(v_{PR} - b_m)} - \frac{a_m}{\left(v_{PR}^2 + 2b_m v_{PR} - b_m^2 \right)}, \tag{2.19}$$

where a_m and b_m are functions of T and X_α, the mathematical forms of which are given in detail in Miller et al. (2001) and Okong'o et al. (2002). At high p, the v_{PR} value may differ significantly from that of v (Prausnitz et al. 1986), but this difference is negligible for the HN system (Harstad, Miller & Bellan 1997). All thermodynamic quantities, including α_D, h, $C_p = (\partial h/\partial T)_{p.x}$ and the speed of sound (a_s), are calculated from the EOS using standard thermodynamic relations (Miller et al. 2001; Okong'o & Bellan 2002b; Okong'o et al. 2002). The implementation of the EOS to calculate p and T from ρ, e and Y_α uses an energy fit (Okong'o & Bellan 2002b) for the HN mixture. The pure species properties are listed in table 1.

2.3. Transport coefficients

The viscosity, the Schmidt number ($Sc = \mu/(\rho \alpha_D D)$) and the Prandtl number ($Pr = \mu C_p/(m\lambda)$) were calculated from high-pressure single-species transport properties using mixing rules, as in Harstad & Bellan (1998). The calculated values were correlated, as summarized in table 2, and these correlations are then used to compute the transport properties μ, D and λ. The relationship between α_{BK} and α_{IK} stated in (2.16) means that either one can be specified, and the other can then be calculated.

Transport property	Model
$\mu = \mu_R(T/T_R)^n$	$n = 0.7$
$Sc \equiv \mu/(\rho\alpha_D D)$	$1.5 - Y_h$
$Pr \equiv \mu C_p/(m\lambda)$	$0.5Sc/\exp(-1.5Y_h)$
α_{IK}	0.1

TABLE 2. Transport properties for binary mixtures; $T_R = (T_1 + T_2)/2$, T in Kelvin; α_{IK} is from Harstad & Bellan (2000). The functional fits are valid over the T range of 500–1100 K and the p range of 40–80 atm.

2.4. *SGS models*

2.4.1. *SGS-flux models*

Three categories of models are here employed for SGS fluxes (τ_{ij}, $\eta_{\alpha j}$, ζ_j), namely constant-coefficient models, dynamic models and dynamic mixed models.

The constant-coefficient SGS models considered are the Smagorinsky (SMC; Smagorinksy 1963, 1993), the gradient (GRC; Clark *et al.* 1979) and the scale-similarity models (SSC; Bardina *et al.* 1980).

The SMC model is based on the gradient-diffusion (eddy-viscosity) concept. As such it does not lend itself to computing variances in general. The SGS fluxes in (2.6) are

$$\vartheta_{SM}(\widetilde{\psi}_m, \tilde{u}_j) = -C_{SM}\bar{\Delta}^2 S\left(\bar{\phi}\right)\frac{1}{2}\frac{\partial\widetilde{\psi}_m}{\partial x_j}, \qquad \psi_m \neq u_j, \tag{2.20}$$

with τ_{ij} modelled in trace-free form as

$$\tau_{ij} - \frac{1}{3}\tau_{kk}\delta_{ij} = -C_{SM}\bar{\Delta}^2 S\left(\bar{\phi}\right)\left[S_{ij}\left(\bar{\phi}\right) - \frac{1}{3}S_{kk}\left(\bar{\phi}\right)\delta_{ij}\right], \tag{2.21}$$

where $S^2(\phi) = S_{ij}(\phi)S_{ij}(\phi)$. The YO (Yoshizawa 1986) model for τ_{kk} is

$$\tau_{kk} = C_{YO}\bar{\Delta}^2 S^2\left(\bar{\phi}\right). \tag{2.22}$$

The GRC model, derived from a Taylor series expansion (Okong'o & Bellan 2004*a*), is

$$\vartheta_{GR}(\widetilde{\psi}_m, \widetilde{\psi}_n) = C_{GR}\bar{\Delta}^2\frac{\partial\tilde{\psi}_m}{\partial x_k}\frac{\partial\tilde{\psi}_n}{\partial x_k}. \tag{2.23}$$

(Note that $\vartheta(\tilde{u}_1, \tilde{u}_1) = \tau_{11}$, $\vartheta(\tilde{u}_2, \tilde{u}_2) = \tau_{22}$, $\vartheta(\tilde{u}_3, \tilde{u}_3) = \tau_{33}$.) Theoretically, C_{GR} is proportional to the moments of inertia of the filtering volume; for a cubic top-hat filter $C_{GR} = 1/12$ (Okong'o & Bellan 2004*a*).

The SSC model, which postulates similarity between the SGS and the small resolved scale, is (Bardina *et al.* 1980)

$$\vartheta_{SS}(\widetilde{\psi}_m, \widetilde{\psi}_n) = C_{SS}\left(\widehat{\widetilde{\psi}_m\widetilde{\psi}_n} - \widehat{\widetilde{\psi}}_m\widehat{\widetilde{\psi}}_n\right), \tag{2.24}$$

where the overhat ($\widehat{}$) denotes (unweighted) filtering at the test-filter level $\hat{\Delta}$. The test-filter width considered is $\hat{\Delta}/\bar{\Delta} = 2$, as is generally recommended. While scale similarity would imply that $C_{SS} = 1$, the actual value is filter-width dependent (Clark *et al.* 1979; Liu, Meneveau & Katz 1994; Pruett, Sochacki & Adams 2001; Okong'o & Bellan 2004*a*).

For transient flows with strong inhomogeneities, constant-coefficient models may not be accurate enough. An increase in accuracy may be expected from a solution in which the coefficients are computed using the LES solution through dynamic modelling. The premise of dynamic modelling is that a scale similarity exists, and thus the SGS behaviour may be deduced from that of the small resolved scales. A test filter is introduced, $\hat{\Delta}$, such that $\hat{\Delta} > \bar{\Delta}$, and through the action of double filtering, $\widehat{\bar{\Delta}}$, a field with scales larger than the resolved field is generated. Here $\widehat{\bar{\Delta}}$ is the effective filter width, not actually used for filtering, that corresponds to filtering at $\bar{\Delta}$ followed by filtering at $\hat{\Delta}$ and the value of which depends on the filter type. For the top-hat filter used here for both the grid and the test filter, $\widehat{\bar{\Delta}}$ is optimally approximated by $\widehat{\bar{\Delta}}^2 = \bar{\Delta}^2 + \hat{\Delta}^2$ (Vreman, Geurts & Kuerten 1997). The essence of dynamic modelling is to relate the grid-level SGS flux and the test-level SGS flux to the test-level resolved flux. For any quantity φ, such as $\tilde{h}$, $\widetilde{Y}_\alpha$ or $\tilde{u}_i$, the grid-level and test-level SGS fluxes associated with the velocity $\tilde{u}_j$ are denoted as $\vartheta_j(\varphi)$ and $\mathcal{T}_j(\varphi)$, respectively, and are defined as

$$\vartheta_j(\varphi) = \widetilde{\varphi u_j} - \tilde{\varphi}\tilde{u}_j, \tag{2.25}$$

$$\mathcal{T}_j(\varphi) = \vartheta_j(\widehat{\varphi}) = \widehat{\widetilde{\varphi u_j}} - \hat{\tilde{\varphi}}\hat{\tilde{u}}_j, \tag{2.26}$$

where $\vartheta_j(u_i) = \tau_{ij}$, $\vartheta_j(Y_V) = \eta_j$ and $\vartheta_j(h) = \zeta_j$. The test-level resolved flux L_j is computed through the Germano identity (Germano et al. 1991). For compressible flows, L_j takes the form (Moin et al. 1991)

$$L_j(\varphi) \equiv \hat{\bar{\rho}}\mathcal{T}_j - \widehat{\bar{\rho}\vartheta_j} = \widehat{\bar{\rho}\tilde{\varphi}\tilde{u}_j} - \frac{\widehat{\bar{\rho}\tilde{\varphi}}\,\widehat{\bar{\rho}\tilde{u}}_j}{\hat{\bar{\rho}}}, \tag{2.27}$$

where $\hat{\tilde{\psi}} = \widehat{\bar{\rho}\tilde{\psi}}/\hat{\bar{\rho}}$. In the above equation, $\vartheta_j(\varphi)$ can be modelled using the generic model coefficient $C(\varphi)$ as

$$\vartheta_j(\varphi) = C(\varphi)\mu_j(\varphi, \bar{\Delta}), \tag{2.28}$$

where $\mu_j(\varphi, \bar{\Delta})$ is associated with the filter width $\bar{\Delta}$ and the velocity $\tilde{u}_j$. In a similar fashion, $\mathcal{T}_j$ can be modelled as $\mu_j(\widehat{\varphi}, \widehat{\bar{\Delta}})$, associated with $\widehat{\bar{\Delta}}$ and the velocity $\hat{\tilde{u}}_j$. If $C(\varphi)$ is assumed to be constant within the test filter, then the left-hand side of (2.27) can be calculated in terms of $C(\varphi)$ as

$$L_j(\varphi) = C(\varphi)M_j(\varphi) = C(\varphi)(\hat{\bar{\rho}}\mu_j(\widehat{\varphi}) - \widehat{\bar{\rho}\mu_j(\varphi)}). \tag{2.29}$$

Here, the SGS-flux model, μ_j, can be chosen to be any of the mathematical forms given in (2.20)–(2.24), excluding the model coefficient.

Despite the observation in the *a priori* study (Selle et al. 2007) that the SSC and GRC models have much better correlations with the SGS fluxes than does the SMC model, we still investigate the predictive abilities of the SM model not only in its constant-coefficient or dynamic form but also as the underlying model for 'mixed' models (Speziale et al. 1988; Zang, Street & Koseff 1993; Vreman, Geurts & Kuerten 1996b). Typically, in mixed models, the SM model is used with the addition of similarity-based models. The popular belief is that while the SM model provides the necessary dissipation to keep the simulation numerically stable, the similarity-based models contribute the structural details lacking in the SM model. However, this is not the reason that mixed models are used here, as explained in §6.2, because our computations have no numerical stability issues.

In the present dynamic mixed-model calculations, the SM model is used in combination with either the gradient model (MGRD) or the scale-similarity model (MSSD). The dynamic mixed model follows the approach of Vreman *et al.* (1997): the coefficient of the SM model is dynamically calculated, and those of the similarity-based models are kept constant at their theoretical value.

For dynamic mixed models, (2.29) becomes

$$L_j(\varphi) = H_j(\varphi) + C(\varphi) M_j(\varphi), \tag{2.30}$$

with $H_j(\varphi) = (\hat{\bar{\rho}} \vartheta_j(\widehat{\varphi}) - \widehat{\overline{\rho \vartheta_j(\varphi)}})$, and ϑ_j is computed using the theoretical values $C_{GR} = 1/12$ and $C_{SS} = 1$ for the GR and SS models, respectively (Okong'o & Bellan 2004a). Following Lilly (1992), we use a least squares method to minimize the error in computing the coefficient from an overdetermined equation set, which yields the coefficients

$$C_H(\varphi) = \frac{\langle (L_j(\varphi) - H_j(\varphi)) M_j(\varphi) \rangle}{\langle M_j(\varphi) M_j(\varphi) \rangle} \quad \text{or} \quad C_D(\varphi) = \frac{\langle\langle (L_j(\varphi) - H_j(\varphi)) M_j(\varphi) \rangle\rangle}{\langle\langle M_j(\varphi) M_j(\varphi) \rangle\rangle}, \tag{2.31}$$

where, for the present mixing-layer configuration, $\langle \rangle$ denotes averaging over homogeneous (x_1, x_3) planes, while $\langle\langle \rangle\rangle$ denotes averaging over the entire domain. For the SM model, the summation over repeated indices in (2.31) is over three quantities for the SGS-stress diagonal terms and over three quantities for the SGS-stress off-diagonal terms. Unlike for the SM model, the summation for the GR model is over six quantities for the SGS-stress terms. For all dynamic models, both ζ_j and η_j are found by summation over the three components. (The use of dimensional variables in the present formulation necessitates the separate computation of the coefficient for each type of SGS flux.) The simulations are performed with a multi-coefficient formulation, where there is a different coefficient for each type of flux according to

$$C\left(\tau_{ij}\right) = C_\tau, \quad C\left(\zeta_j\right) = C_\zeta, \quad C\left(\eta_j\right) = C_\eta. \tag{2.32}$$

For the SM-based models, there are two different coefficients associated with the anisotropic and the isotropic part of the stress tensor as

$$C\left(\tau_{ij,i=j}\right) = C_{\tau d}, \ C\left(\tau_{ij,i\neq j}\right) = C_{\tau x}. \tag{2.33}$$

The dynamic coefficient values replacing those of the constant coefficients are computed as follows:

(a) For the dynamic SM (SMD) model, μ_j is computed from (2.20)–(2.22), and $H_j = 0$.

(b) For the dynamic mixed GR (MGRD) model, μ_j is computed from (2.20)–(2.22), and ϑ_j in H_j is computed from (2.23) using $C_{GR} = 1/12$.

(c) For the dynamic mixed SS (MSSD) model, μ_j is computed from (2.20)–(2.22), and ϑ_j in H_j is computed from (2.24) using $C_{SS} = 1$.

(d) For the dynamic GR (GRD) model, μ_j is computed from (2.23), and $H_j = 0$.

2.4.2. *Pressure correction*

To model $\nabla[\overline{p(\phi)} - p(\overline{\phi})]$, Selle *et al.* (2007) have expanded the EOS (2.19) in a Taylor series around the reference state $\overline{\phi}$, obtaining

$$\overline{p(\phi)} = \overline{p\left(\overline{\phi}\right)} + \overline{\left.\frac{\partial p}{\partial \phi_m}\right|_{\phi=\overline{\phi}} \left(\phi_m - \overline{\phi_m}\right)} + \overline{\frac{1}{2} \left.\frac{\partial^2 p}{\partial \phi_m \partial \phi_n}\right|_{\phi=\overline{\phi}} \left(\phi_m - \overline{\phi_m}\right)\left(\phi_n - \overline{\phi_n}\right)} + \text{h.o.t.} \tag{2.34}$$

The developed model was under the verified assumption that $(\phi - \overline{\phi})$ is small (at $\overline{\Delta} = 4\Delta x_{DNS}$ and $\overline{\Delta} = 8\Delta x_{DNS}$) and under the non-rigorous assumptions that

$$\overline{p(\overline{\phi})} = p(\overline{\phi}), \tag{2.35}$$

that $(\partial p/\partial \phi_m)_{\phi=\overline{\phi}}$ and $(\partial^2 p/(\partial \phi_m \partial \phi_n))_{\phi=\overline{\phi}}$ can be removed from the filtering operation and that the filter is a projection which implies that $(\overline{\overline{\phi_m}} - \overline{\overline{\phi_m}}) = 0$, all of which led to

$$\overline{p(\phi)} = p(\overline{\phi}) + \delta, \quad \delta = \frac{1}{2} \left.\frac{\partial^2 p}{\partial \phi_m \partial \phi_n}\right|_{\phi=\overline{\phi}} (\overline{\phi_m \phi_n} - \overline{\phi_m}\ \overline{\phi_n}) = \frac{1}{2} \left.\frac{\partial^2 p}{\partial \phi_m \partial \phi_n}\right|_{\phi=\overline{\phi}} \vartheta(\overline{\phi_m}, \overline{\phi_n}),$$
$$\tag{2.36}$$

where m and n index the components of vectors ϕ and ψ and δ is the second-order approximation in the LES assumption for the pressure. Extensive and tedious mathematics permitted the computation of $(\partial^2 p/(\partial \phi_m \partial \phi_n))_{\phi=\overline{\phi}}$ from the knowledge of $(\partial^2 p/(\partial \psi'_m \partial \psi'_n))_{\psi'=\overline{\psi'}}$, where $\psi'(\phi) = \{u_i, v, X_\alpha, T\}$, through the PR EOS. The quantities $\vartheta(\overline{\phi_m}, \overline{\phi_n})$ in (2.36) are not inherent SGS models, as they do not appear directly as a result of equation filtering but rather as the result of the chosen p-correction model. Consistent with other variance models, $\vartheta(\overline{\phi_m}, \overline{\phi_n})$ were modelled using one of the SGS-flux models described in §2.4.1. The results showed excellent success at a filter size $\overline{\Delta} = 4\Delta x_{DNS}$, where the DNS grid spacing was uniform with $\Delta x_1 \simeq \Delta x_2 \simeq \Delta x_3$ and $\Delta x_{DNS} = \max\{\Delta x_i\}$; however, a model deterioration was evident at $\overline{\Delta} = 8\Delta x_{DNS}$. Because the assumption that '$(\phi - \overline{\phi})$ is small' is justified even at $\overline{\Delta} = 8\Delta x_{DNS}$, this deterioration is attributed to two consequences of the assumption that the filter is a projection: (i) the nulling of the first-order term in the Taylor expansion and (ii) the approximation of the differences in the second-order term using SGS-flux models for the variances.

The present approach for modelling $[\overline{p(\phi)} - p(\overline{\phi})]$ is different from that developed by Selle *et al.* (2007) because the wish is to improve the chances of success at higher filter size than $\overline{\Delta} = 4\Delta x_{DNS}$. Indeed, for LES to be computationally beneficial with respect to DNS, the minimum $\Delta x_{LES} = 2\Delta x_{DNS}$ (a factor of eight increase in the computational volume). Since it has been recommended that a minimum $\overline{\Delta} = 2\Delta x_{LES} = 4\Delta x_{DNS}$ should be chosen in order to ensure that the SGS term is larger than numerical errors (Ghosal 1996; Chow & Moin 2003), this implies that $\overline{\Delta} = 4\Delta x_{DNS}$ is the minimum acceptable filter value. Realistically, it is more desirable to have $\Delta x_{LES} = 4\Delta x_{DNS}$, which would mean an increase by a factor of 64 in the computational volume for LES compared with DNS, implying that a more realistic value of the filter size is $\overline{\Delta} = 2\Delta x_{LES} = 8\Delta x_{DNS}$, the value for which the model of Selle *et al.* (2007) for the second-order Taylor expansion term showed deteriorating results. This situation motivated the development of a new p-correction model.

Thus, we no longer assume here that the filter is a projection, although we still assume that $(\partial p/\partial \phi_m)_{\phi=\overline{\phi}}$ can be removed from the filtering operation, being a constant in the filtering volume, as it is evaluated at its centre node. Thus, the model is now

$$\overline{p(\phi)} = \overline{p(\overline{\phi})} + \left.\frac{\partial p}{\partial \phi_m}\right|_{\phi=\overline{\phi}} \left(\overline{\phi_m} - \overline{\overline{\phi_m}}\right). \tag{2.37}$$

The quantity $\overline{\phi_m}$ is the LES solution and $\overline{\overline{\phi_m}}$ is computed by filtering the LES solution. The idea behind using the first-order Taylor series term is that it inherently is a more accurate approximation of $[\overline{p(\phi)} - p(\overline{\phi})]$ than the second-order term only. Thus, we now rely uniquely on the first-order term of the Taylor expansion, as the second-order

term is not easily modelled without the assumption of the filter being a projection, which nulls the first-order term. Results using the first-order p correction (FOC) for the LES described in §6 are compared in §6.2.1 with results using the second-order p correction (SOC) at same ICs. Otherwise, when a p-correction model is used, all LESs in §6 employ the FOC $[\overline{p(\phi)} - p(\overline{\phi})]$ model.

The model of (2.37) was implemented in (2.3) by computing

$$\nabla(p(\overline{\phi})) + \nabla(\overline{p(\phi)} - p(\overline{\phi})) = \nabla(\overline{p(\phi)}) = \nabla\left[\overline{p(\overline{\phi})} + \left.\frac{\partial p}{\partial \phi_m}\right|_{\phi=\overline{\phi}}\left(\overline{\phi_m} - \overline{\overline{\phi_m}}\right)\right], \quad (2.38)$$

where $p(\overline{\phi})$ is the p value computed in LES.

3. Description of the DNS database

The DNS database consists of supercritical temporal mixing-layer simulations of a two species ($N = 2$) HN (heptane, subscript h; nitrogen, subscript n) mixture. Because the DNSs described in Okong'o & Bellan (2002b) and analysed *a priori* by Selle *et al.* (2007) were performed on a previous computer platform which has now been superseded by a faster supercomputer, the same DNS code used by Okong'o & Bellan (2002b) was used to re-create the database on the current supercomputer to enable CPU-time comparisons with the LES. The newly obtained DNS results were carefully compared with the previous ones (Okong'o & Bellan 2002b) to ensure agreement within machine accuracy.

A detailed description of the DNS methodology has been given by Miller *et al.* (2001) and Okong'o & Bellan (2002b). The DNS differential equations combined with the EOS described in §2.2, using the transport coefficient models presented in §2.3, were numerically solved using a fourth-order explicit Runge–Kutta time integration and a sixth-order compact scheme with eighth-order filter for spatial derivatives (Kennedy & Carpenter 1994); the filtering (applied at interior points only) is required to maintain numerical stability for long-time integrations, but since it acts only on the shortest waves that can be resolved on the grid, it does not act as a turbulence model allowing under-resolved computations. The computations were parallelized using three-dimensional domain decomposition and message passing and an efficient parallel tridiagonal solver (Muller & Scheerer 1991).

The configuration is that of a temporally developing mixing layer, as depicted in figure 1, which shows the definition of the streamwise (x_1), cross-stream (x_2) and spanwise (x_3) coordinates. Species 1 and 2 initially reside in the upper and the lower stream, respectively. The layer is not symmetric in extent in the x_2 direction, to accommodate the larger layer growth in the lighter fluid side. The free-stream density (ρ_1 or ρ_2) is calculated for each pure species at its free-stream temperature (T_1 or T_2) and at the initial uniform pressure (p_0). The vorticity thickness is defined as $\delta_\omega(t) = \Delta U_0/(\partial\langle u_1\rangle/\partial x_2)_{max}$, where $\Delta U_0 = U_1 - U_2$ is the velocity difference across the layer; U_1 and U_2 were chosen with the intent of keeping the ultimate vortex stationary in the computational domain (Papamoschou & Roshko 1988; Miller *et al.* 2001); the specification of the convective Mach number (see table 3) $M_{c,0}$ determines ΔU_0. Given the initial streamwise velocity profile u_1 based on U_1 and U_2, $(\partial\langle u_1\rangle/\partial x_2)_{max}$ and hence $\delta_{\omega,0} \equiv \delta_\omega(0)$ are calculated. The initial momentum ratio $|\rho_2 U_2|/|\rho_1 U_1| \sim 5$ and the initial momentum flux ratio $(\rho_2 U_2^2)/(\rho_1 U_1^2) = 2.2$. The specified value of the initial flow Reynolds number $Re_0 = (1/2)(\rho_1 + \rho_2)\Delta U_0 \delta_{\omega,0}/\mu_R$, chosen so as to enable the resolution of all relevant length scales, is then used to calculate μ_R, which scales μ.

Run	Re_0	$\lambda_1/\delta_{\omega,0}$	$L_1 \times L_2 \times L_3$ (m³)	$N_1 \times N_2 \times N_3$	Δx $(10^{-4}$ m)	$Re_{m,tr}$	t_{tr}^*	CPU (h)
HN500	500	7.29	0.200×0.232×0.120	240×288×144	8.36	1250	155	371
HN600	600	7.29	0.200×0.232×0.120	288×336×176	6.97	1452	135	667
HN800	800	4.57	0.125×0.148×0.075	240×272×144	5.23	1258	100	356

TABLE 3. Listing of the DNS realizations and associated resolution; L_i is the size of the domain in the x_i direction, in metres. For all layers, $L_1=4\lambda_1$, $\delta_{\omega,0}=6.859\times10^{-3}$ m, $F_{2D}=0.1$ and $F_{3D}=0.05$. Moreover, $p_0 = 60$ atm, $T_1 = 1000$ K, $T_2 = 600$ K and $\rho_2/\rho_1 = 12.88$, with $M_{c,0}=0.40$. The subscript tr denotes the transitional time. The CPU time is an estimate, based on an aggregate over parallel processors on an SGI Altix 3000 system and represents the time used to reach the DNS transitional time.
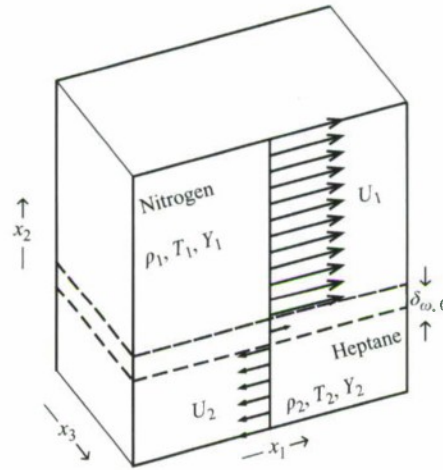
FIGURE 1. The C_7H_{16}–N_2 mixing-layer configuration.

The grid spacing is approximately inversely proportional to Re_0, suggested by the relationship $l/\eta_K \sim Re^{3/4}$ (Tennekes & Lumley 1989), where l is the integral scale and η_K is the Kolmogorov scale.

The simulations are started with error-function profiles for the mean streamwise velocity, mass fraction and temperature, upon which are imposed spanwise and streamwise vorticity perturbations (Moser & Rogers 1991, 1993) of strengths F_{2D} and F_{3D} respectively, whose streamwise (λ_1) and spanwise (λ_3) wavelengths are $\lambda_1=C\delta_{\omega,0}$ and $\lambda_3=0.6\lambda_1$, where $C=7.29$ is the most unstable wavelength for incompressible flow. For the simulations reported here, listed in table 3, another value of C obtained from stability analyses (Okong'o & Bellan 2003) was also used: $C = 4.57$ for the shortest (estimated) unstable wavelength. The grid is chosen for all simulations so as to accommodate four wavelengths in the streamwise and spanwise directions, and the evolution of the layer is meant to encompass roll-up and two pairings of the four initial spanwise vortices into an ultimate vortex.

The boundary conditions are periodic in the x_1 and x_3 directions and of outflow type for real gas in the x_2 direction, as derived by Okong'o & Bellan (2002a). The outflow-type conditions are essential to maintain numerical stability, since the initial perturbation causes large p waves that must be allowed out of the domain with minimal reflection.

The database used for the *a priori* analysis is summarized in table 3, including the transitional time $t^*_{tr} = t_{tr}\Delta U_0/\delta_{\omega,0}$ and the value of the momentum-thickness-based Reynolds number $Re_m = Re_0\delta_m/\delta_{\omega,0}$ at transition, where

$$\delta_m = \frac{\int_{x_{2,min}}^{x_{2,max}} \left[\langle\rho u_1\rangle_{x_{2,max}} - \langle\rho u_1\rangle\right]\left[\langle\rho u_1\rangle - \langle\rho u_1\rangle_{x_{2,min}}\right] \, \mathrm{d}x_2}{\left(\langle\rho u_1\rangle_{x_{2,max}} - \langle\rho u_1\rangle_{x_{2,min}}\right)^2}, \qquad (3.1)$$

with $x_{2,max} = L_2/2$, $x_{2,min} = -L_2/2$ (Okong'o & Bellan 2002*b*) and t_{tr} is the time at which the one-dimensional velocity-fluctuation-based energy spectra become smooth, except for the forcing frequency. The goal of the LES is to reproduce the features of the FC-DNS, with special attention to the HDGM regions which populate the entire mixing layer. Their significance has been discussed by Miller *et al.* (2001) and Bellan (2006): the effect of the HDGM regions is to redistribute turbulent energy from the normal direction to the tangential direction, as found in the experiments of Hannoun, Fernando & List (1988) at sharp density boundaries. Unless one can capture this local aspect of the flow, it is very unlikely that mixing and combustion could be faithfully simulated in gas turbine, diesel or liquid rocket engines. For thinner HDGM regions, the corresponding LES may require higher resolution relative to DNS (i.e. less grid coarsening, smaller $\bar{\Delta}/\Delta x_{DNS}$ and $\Delta x_{LES}/\Delta x_{DNS}$) than LES with thicker HDGM regions, since the appropriate Δx_{LES} depends on the gradients of the filtered flow field.

4. LES initial and boundary conditions

In *a posteriori* LES studies, the choice of the ICs is distinct from that for LES of practical flows in which comparison is performed with experimental data. In the present study in which LES will be compared with DNS results, it is natural to think that the simulations should start with the same ICs. However, a function well resolved on a DNS grid cannot be represented with the same accuracy on an LES grid, which is coarser. Additionally, filtering results in loss of information. Since the LES equations are obtained from the original conservation equations through filtering, it is also natural to assume that filtering the DNS ICs should be the first step (e.g. Vreman *et al.* 1997; Geurts & Frohlich 2002; Leboissetier, Okong'o & Bellan 2005), followed by grid coarsening to retain only those nodes that will be used in LES. This is indeed the approach typically followed, and it has been adopted here as well; this is what we call the FC-DNS. Another approach is to compute analytically prescribed ICs on the LES grid, followed by filtering. If so, there are two choices in filtering: one could filter using all DNS points (as in the FC-DNS) or only using the LES grid; we call the latter choice a coarsened-and-filtered (CF) DNS database. Although the same filter is used in both cases, application of the numerical filter over the coarse grid yields slightly different ICs than those over the fine grid; and this small difference affects the solution. It turns out that this CF-DNS choice of ICs yields LES results that are closer to the FC-DNS during the layer development (including transition) than the LES using the FC-DNS ICs is with respect to the FC-DNS during the entire layer evolution. The reason that both solutions are compared with the FC-DNS is that the LES template is the filtered DNS solution, which is unique irrespective of LES considerations (e.g. the LES ICs). The CF-DNS results are presented in Appendix A. An alternate way to conduct LES is to provide ICs at a $t^* > 0$ DNS time station rather than at $t^* = 0$ (e.g. Geurts & Frohlich 2002). The advantage of initiating

LES at a $t^* > 0$ DNS time station is that one may choose t^* to be past all large transients associated with the p evolution from the IC, a choice which dramatically improves the agreement between the LES and the FC-DNS. Two such examples are provided: one for constant-coefficient models in Appendix A (where some *a priori* tabulated results that identify the time station at which the p-correction term begins to no longer rival the leading-order term in the momentum equation are also shown) and another for dynamic models in §6.2. However, under typical circumstances, this $t^* > 0$ information is unknown, and for this reason, $t^* = 0$ of the DNS is generally chosen as the LES IC.

The boundary conditions are periodic in the x_1 and x_3 homogeneous directions and non-reflective in the x_2 direction similar to that of DNS. The non-reflective boundary conditions, which were developed on the equivalent Euler equations (Okong'o & Bellan 2002a), do not explicitly involve the p-correction term (when operative). In these boundary conditions, p is that computed in LES, which, according to the SGS model, may or may not contain the p correction.

5. LES numerical methodology

The numerical method is essentially the same as in DNS (see §3) so as to ensure that differences between LES and DNS are overwhelmingly due to the SGS models rather than the numerics. The LES grid must be fine enough to represent the mean initial profiles, and to resolve the large eddies, and coarse enough to necessitate SGS modelling and to show increase in computational efficiency. In this study, the choice is $\Delta x_{LES} = 4\Delta x_{DNS}$. This choice of grid resolution is justified by the energy spectra and by LES comparisons with the FC-DNS and with an LES devoid of SGS model, called the No Model case (see §6.1). It is noteworthy that although the mathematical form of the equations for the No Model case is identical to the unfiltered equations, the meaning of the dependent variables is different, since the No Model computed solution is that of the filtered equations; the meaning of the variables is important when one wishes to compare simulation results with experimental data. Thus, even for the No Model case, the scientific target is to reproduce the FC-DNS; because of the identical form of the equations, one may consider the No Model case to be an under-resolved DNS, depending on the viewpoint of interest, and then it should be compared with the coarsened DNS. To study the influence of the grid size, an LES study with a finer grid ($\Delta x_{LES} = 2\Delta x_{DNS}$) is performed with and without SGS model (Appendix B). The LES using an SGS model and performed on this finer grid is shown to basically be numerically equivalent to an under-resolved DNS, although here also the meaning of the dependent variables is not the same as in DNS. This equivalence indicates that an LES on a grid finer than $\Delta x_{LES} = 4\Delta x_{DNS}$ does not require SGS modelling.

The grid and test filters have a cubic top-hat mathematical form (for which the filtered value is simply the integrated value over the filter width), being the only one consistent with easy interpretation of results when using a finite-difference scheme. The spatial discretization is the same sixth-order accurate compact scheme used in the DNS, and time integration is performed using a fourth-order explicit Runge–Kutta scheme. The $\bar{\Delta}$ width is a compromise between retaining the maximum amount of information in the resolved scales and minimizing the discretization-error influences. In order to limit numerical errors, $\bar{\Delta}/\Delta x_{LES}$ must be chosen according to the accuracy of the space discretization scheme, irrespective of the grid resolution. For a sixth-order Padé scheme, this ratio must be $\bar{\Delta} \geqslant 2\Delta x_{LES}$ (Ghosal 1996; Chow & Moin 2003),

and the present choice is $\bar{\Delta} = 2\Delta x_{LES}$, meaning that the smallest resolved eddy is represented by at least two grid points.

Time stability is ensured by applying an explicit high-order filter to the conservative variables in each spatial direction. Since the role of this filter is to remove any unphysical high-wavenumber information from the solution before it contaminates the lower-wavenumber scales (Kennedy & Carpenter 1994), it is sometimes advisable to use filtering at every time step of the time integration. For the well-resolved DNS grid, the frequency of the high-order filtering is not expected to alter the solution. For LES devoid of an SGS model, since the LES grid resolution is only sufficient to resolve the large scales, it is expected that the selected filtering frequency affects the solution. Preliminary two-dimensional and three-dimensional numerical experiments with the No Model LES using various filter orders and filtering frequencies and decreasing grid resolution showed that when applying the filter more often, the results diverged from the filtered DNS. (The fact that the No Model solution is obtainable indicates that to a certain extent, this high-order filter may act like an implicit SGS model.) Thus, in LES we applied the filtering with the largest allowable time window, every two time steps (any larger period results in noise build-up in p and dilatation fields). Moreover, unlike in DNS, the filtering is performed over the entire domain including the points at and close to the non-periodic boundaries, and the order of the filter is increased to 12 in the interior with sixth-order boundary closures. Finally, the Courant–Friedrichs–Levy (CFL) number was adjusted to 0.85 from the unity DNS value, in order to apply filtering with a large time window.

The filtering frequency was investigated by exploring its dependence on the SGS model. When an SGS model is employed, the maximum allowable filtering frequency increases and is larger for some SGS models than for others. As the filtering frequency increases, the numerical dissipation associated with it decreases. Basically, the choice of the filtering frequency is a compromise between ensuring that the overwhelming amount of information is retained in the solution and allowing the computation to proceed for long enough times. For sake of consistency, the same filtering frequency was used in all LES runs.

6. Results

Throughout the presented results, we distinguish between the solution of the LES equations (2.2)–(2.5) and (2.19), which is the conservative variable vector ϕ_{LES}, with the equivalent primitive variable vector $\psi_{LES} \equiv \psi(\phi_{LES})$ and the ideal (but presumably unachievable) LES solution represented by $\bar{\phi}$ computed from the FC-DNS and the corresponding vector $\bar{\psi} = \psi(\bar{\phi})$. As stated in §1, ϕ_{LES} will be here compared to $\bar{\phi}$ at the LES grid nodes. We first inquire in §6.1 into the performance of constant-coefficient SGS-flux models and also evaluate the effect of the FOC model (2.37) by using HN600 as the baseline study. Then, we transcend in §6.2 the constant-coefficient LES conducted with a p correction by performing LES with dynamic-coefficient SGS-flux models combined with a p-correction model. At this juncture, we first assess the performance of the p-correction type model by comparing the SOC model (2.36) with the FOC model (2.37) and choose the best of these two models for all other LESs. Finally, the extent to which the FC-DNS irreversible entropy production is recovered in LES is addressed in §6.3. The stringent goal here is to obtain in LES both spatial and temporal equivalence with the FC-DNS. Clearly, if the interest is only in statistical equivalence (Pope 2004), then a larger set of models than the ones recommended for reaching our stringent requirements would be available to the user.

Run	SGS Model		CPU hours
	SGS-flux model	Pressure correction	
SMC	SMC; (2.20) and (2.22)	None	3
GRC	GRC; (2.23)	None	3
SSC	SSC; (2.24)	None	16
SMCP	SMC; (2.20) and (2.22)	Included; (2.37)	9
GRCP	GRC; (2.23)	Included; (2.37)	10
SSCP	SSC; (2.24)	Included; (2.37)	22
No Model	None	None	3
DNS	None	None	667

TABLE 4. The name convention and time requirements to reach $t^* = 135$ for the LES and DNS runs for HN600. For all LES cases, the grid is $72 \times 84 \times 44$. CPU hours are an estimate: aggregate over parallel processors on an SGI Altix 3000 system.

6.1. Constant-coefficient LES and effect of the pressure correction

The SMC, GRC and SSC models are here used in LES with the calibrated coefficient values for $\bar{\Delta}/\Delta x_{DNS} = 8$ obtained from the corresponding DNS at the transitional time (see Selle *et al.* 2007) $t^* = 135$ as follows:

$$C_{SM} = 0.0579 \text{ and } C_{YO} = 0.2471, \quad \text{SMC}, \tag{6.1}$$

$$C_{GR} = 0.1193, \quad \text{GRC}, \tag{6.2}$$

$$C_{SS} = 0.5770 \text{ for } \widehat{\Delta} = 2\bar{\Delta}, \quad \text{SSC}. \tag{6.3}$$

To investigate the effect of the p correction, LESs are conducted first without and then with the FOC model. Hence, there are six SGS-flux-including LES runs analysed. The results are compared with both the FC-DNS results and the No Model LES. The comparison with the latter is as important as with the former, since it provides insight into the necessity of an SGS model. The comparisons involve the timewise evolution of important global quantities, as well as the rendition of selected flow-variable spatial distribution at the DNS transitional time. Table 4 lists the name convention used for HN600 LES runs and compares the computational time requirements of LES cases and DNS to reach the time station of the DNS transitional state.

6.1.1. Evolution of the global quantities

Figure 2 displays the time evolution of $\delta_m/\delta_{\omega,0}$, the resolved kinetic energy $E_K = \langle\langle\rho(u_i u_i/2)\rangle\rangle$, the domain-averaged positive spanwise vorticity $\langle\langle\omega_3^+\rangle\rangle$ and the domain-averaged enstrophy $\langle\langle\omega_i\omega_i\rangle\rangle$ for LES runs along with the FC-DNS as the ideal LES and for the DNS run; $\delta_m/\delta_{\omega,0}$, presented in figure 2(a), shows the mixing-layer growth, which is essentially the same for the DNS and the FC-DNS. Several regions of varying slopes are identified. The first region is the roll-up period epitomizing laminar growth and lasting up to $t^* = 25$. What follows is a region culminating with the the first pairing at $t^* = 50$ and a further increase with a higher $\delta_m/\delta_{\omega,0}$ rate indicating a faster growth because of turbulent mixing. A second pairing eventually occurs, after which the layer transitions to turbulence and eventually the mixing-layer growth slows down. All LESs, except for SMC and SMCP, agree well with the FC-DNS before the first pairing; this is to be expected, considering that turbulence is relatively subdued before the first pairing. After the first pairing, GRC, SMC and SMCP LESs predict a much thinner layer than the template; the p correction does not seem here effective
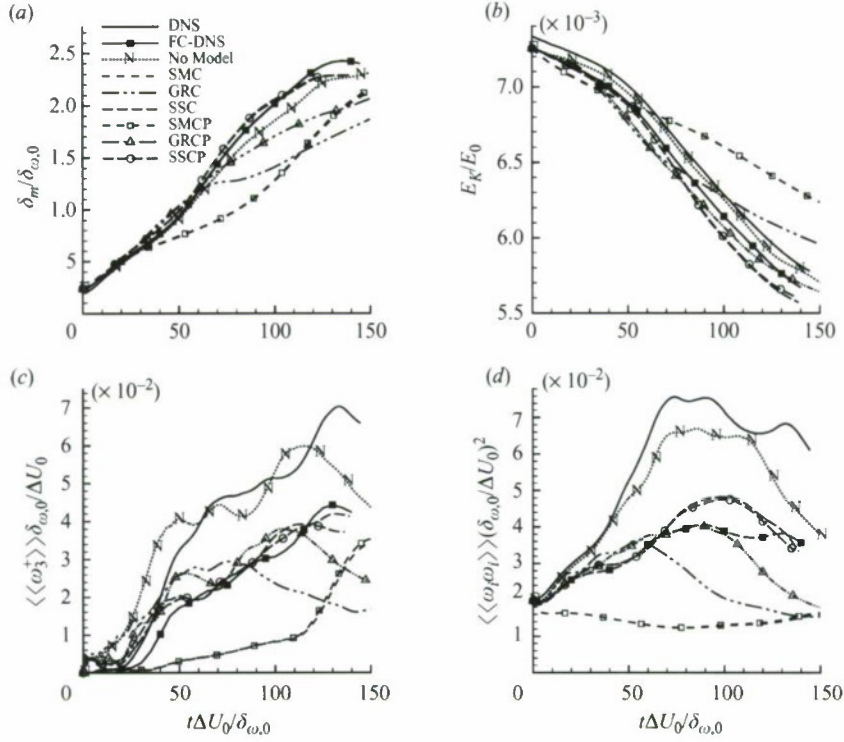
FIGURE 2. Time evolution of non-dimensional global quantities for HN600: (a) $\delta_m/\delta_{\omega,0}$, (b) E_K/E_0, (c) $\langle\langle\omega_3^+\rangle\rangle\delta_{\omega,0}/\Delta U_0$ and (d) $\langle\langle\omega_i\omega_i\rangle\rangle(\delta_{\omega,0}/\Delta U_0)^2$ for DNS, FC-DNS and LES listed in table 4; $E_0 = 452.076$ kJ is the initial total energy in the domain.

in mitigating the deficiencies of the SMC model. However, the *p*-correction model does delay the vortex breakdown in the GRC LES, and the GRCP is an improvement over the GRC, but even the GRCP model cannot fully recover from this discrepancy with the FC-DNS. Clearly, the SSC and SSCP LESs have the best agreement with the FC-DNS data. The comparison with the solution shows that none of the SMC, SMCP, GRC or GRCP models is an asset in the prediction of $\delta_m/\delta_{\omega,0}$; only SSC and SSCP overperform the No Model LES.

The time evolution of E_K/E_0 is displayed in figure 2(*b*). Filtering removes the SGS kinetic energy and results in a downshift for the FC-DNS compared with the DNS. However, the difference in kinetic energy between filtered and unfiltered DNS is small, being less than 3 %, with the maximum occurring at the DNS transition. The No Model case falls between the DNS and the FC-DNS and is considerably superior to either SMC or SMCP, both of which widely deviate from the FC-DNS template. The SMC model's characteristic dissipative nature overpredicts the energy decay at the early stages of the simulation and hinders turbulence development; thus, not having enough small scale structures, SMC underpredicts the energy decay after the first pairing. When supplemented with the *p* correction, the GRC model improves its performance, and after $t^* = 80$ it exhibits better agreement with the FC-DNS compared with the No Model case. Similar to the $\delta_m/\delta_{\omega,0}$ findings, both SSC and SSCP produce the best agreement with the FC-DNS, indicating that the amount of dissipation added with this model is adequate until $t^* = 80$. After $t^* = 80$, GRCP overperforms all other models.

Figure 2(*c*) illustrates $\langle\langle\omega_3^+\rangle\rangle\delta_{\omega,0}/\Delta U_0$, which, being initially null, measures the resolved small-scale activity; this activity experiences a sudden increase after roll-up. Filtering removes the smallest structures and thus considerably reduces $\langle\langle\omega_3^+\rangle\rangle\delta_{\omega,0}/\Delta U_0$ as clearly seen in figure 2(*c*). Understandably, the No Model simulation displays much larger values than the FC-DNS target solution, since the small structures are not subject to dissipative effects through SGS-flux models in that simulation, resulting in $\langle\langle\omega_3^+\rangle\rangle\delta_{\omega,0}/\Delta U_0$ being overpredicted. On the other hand, both SMC and SMCP underpredict $\langle\langle\omega_3^+\rangle\rangle\delta_{\omega,0}/\Delta U_0$ owing to their dissipative nature. The GRC model erroneously produces vorticity very early in the simulation, even before roll-up is finished, and eventually exhibits an earlier vorticity decay compared with the FC-DNS. To a certain extent, GRCP is an improvement of GRC, since the *p* correction delays the vorticity decay. The best agreement is obtained with SSC and SSCP, consistent with the $\delta_m/\delta_{\omega,0}$ and E_K findings.

Enstrophy is a measure of stretching and tilting effects, both of which instigate vorticity production. Plots of $\langle\langle\omega_i\omega_i\rangle\rangle(\delta_{\omega,0}/\Delta U_0)^2$ in figure 2(*d*) display results similar to $\langle\langle\omega_3^+\rangle\rangle\delta_{\omega,0}/\Delta U_0$. The best and worst overall agreements are obtained with the SSC or SSCP and the SMC or SMCP models, respectively, and the performance of GRC is considerably improved by the addition of the *p* correction included in GRCP.

Despite the fact that the No Model LES has better agreement with the DNS for these global measures than any of the other models, as already stated, from the LES viewpoint, the No Model target is the FC-DNS, not the DNS, and it is obvious that this simulation fails the most among all LESs in reaching the FC-DNS template. CPU times for all runs are listed in table 4 showing that all LESs have considerably reduced CPU times, boding well for LES utilization in practical applications. The No Model CPU time is similar to the smallest CPU time obtained with LES including only SGS-flux models. Finally, the SGS model embodied in the *p* correction either adds less than 40 % of CPU time (SSCP model versus SSC model) or increases the CPU time by factors of 2.7 (SMC versus SMCP) to 3.3 (GRC versus GRCP). However, even with the *p* correction, the CPU time is at a minimum a factor of 30 and at the maximum almost two orders of magnitude smaller than that for DNS, while the *p*-correction model improves the LES results considerably.

A global quantitative evaluation of the LES accuracy in predicting temporally mean values compared with the template FC-DNS can be obtained by defining, for any quantity of interest Ψ, relative errors

$$\varepsilon_{1,\psi} = \frac{\sum_{l=0}^{l=N} |\langle\langle\Psi_{LES}(t_l)\rangle\rangle - \langle\langle\Psi_{FCDNS}(t_l)\rangle\rangle|}{\sum_{l=0}^{l=N} |\langle\langle\Psi_{FCDNS}(t_l)\rangle\rangle|}, \tag{6.4}$$

$$\varepsilon_{2,\psi} = \frac{\int_0^{t_{ir}^*} ([\langle\langle\Psi_{LES}(t)\rangle\rangle - \langle\langle\Psi_{FCDNS}(t)\rangle\rangle]^2)\,dt}{\int_0^{t_{ir}^*} [\langle\langle\Psi_{FCDNS}(t)\rangle\rangle]^2\,dt} \tag{6.5}$$

computed according to the L1 and L2 norms (e.g. Meyer, Geurts & Baelmans 2003), where t_l represents the time at which the solution has been outputted. Both $\varepsilon_{1,\psi}$ and $\varepsilon_{2,\psi}$ can account for any deviations between each LES and the FC-DNS. Since $\delta_m/\delta_{\omega,0}$, E_K/E_0, $\langle\langle\omega_3^+\rangle\rangle\delta_{\omega,0}/\Delta U_0$ and $\langle\langle\omega_i\omega_i\rangle\rangle(\delta_{\omega,0}/\Delta U_0)^2$ are already domain-averaged quantities, they already represent $\langle\langle\Psi\rangle\rangle$. Listed in table 5 are ε_ψ values

Run	$\delta_m/\delta_{\omega,0}$		E_K/E_0		$\langle\langle\omega_3^+\rangle\rangle\delta_{\omega,0}/\Delta U_0$		$\langle\langle\omega_i\omega_i\rangle\rangle(\delta_{\omega,0}/\Delta U_0)^2$	
	$\varepsilon_{1,\psi}$	$\varepsilon_{2,\psi}$	$\varepsilon_{1,\psi}$	$\varepsilon_{2,\psi}$	$\varepsilon_{1,\psi}$	$\varepsilon_{2,\psi}$	$\varepsilon_{1,\psi}$	$\varepsilon_{2,\psi}$
SMC	304	345	30	40	775	760	573	612
SMCP	299	341	30	41	767	755	570	608
GRC	200	253	13	16	444	400	249	317
GRCP	110	136	10	12	281	259	49	69
SSC	35	34	9	13	163	164	102	144
SSCP	37	36	9	12	169	180	94	130
No Model	64	73	11	12	1015	889	521	586

TABLE 5. Computed errors (in $\times 10^{-3}$) for LES with respect to the FC-DNS for different constant-coefficient SGS models according to (6.4) and (6.5).

for all constant-coefficient models and the No Model LES. Among $\varepsilon_{1,\psi}$ and $\varepsilon_{2,\psi}$ for the four quantities, errors associated with E_K/E_0 decay are smallest, while those for $\langle\langle\omega_3^+\rangle\rangle\delta_{\omega,0}/\Delta U_0$ are the most prominent, followed by $\langle\langle\omega_i\omega_i\rangle\rangle(\delta_{\omega,0}/\Delta U_0)^2$. The fact that both norms predict similar relative ordering of model accuracy is encouraging in terms of evaluating the models' capability. For both $\varepsilon_{1,\psi}$ and $\varepsilon_{2,\psi}$ the minimum error in $\langle\langle\omega_3^+\rangle\rangle\delta_{\omega,0}/\Delta U_0$ is for the SSC and SSCP models (for the SSC model, the p correction does not seem beneficial for this quantity) followed by the GRCP model, whereas the largest error is for the No Model LES, followed by SMC and SMCP. For $\langle\langle\omega_i\omega_i\rangle\rangle(\delta_{\omega,0}/\Delta U_0)^2$, both $\varepsilon_{1,\psi}$ and $\varepsilon_{2,\psi}$ indicate that the minimum error is for GRCP (which is considerably smaller than for GRC), followed by SSCP, while the largest error is for SMC followed by SMCP. With the exception of $\langle\langle\omega_3^+\rangle\rangle\delta_{\omega,0}/\Delta U_0$, for all other global quantities, $\varepsilon_{1,\psi}$ and $\varepsilon_{2,\psi}$ are larger for SMC and SMCP than for the No Model case, casting great doubts about the SMC and SMCP predictive capabilities for these temporally mean values. The p-correction model seems most effective for the GR model for which it reduces errors for $\langle\langle\omega_3^+\rangle\rangle\delta_{\omega,0}/\Delta U_0$ by approximately 40 % and by as much as approximately a factor of five for $\langle\langle\omega_i\omega_i\rangle\rangle(\delta_{\omega,0}/\Delta U_0)^2$.

6.1.2. *Flow visualizations*

To better understand the impact of the SGS models in reproducing the FC-DNS we turn to flow visualizations at $t^* = 135$. Although many dependent variables could be plotted, we focus here for obvious reasons on the vortical aspect of the flow, on $|\nabla\rho|$ because it directly influences the turbulence distribution in the flow field (Hannoun *et al.* 1988), on p because of its strong nonlinear relationship to other thermodynamic variables through the EOS and because a deficient p field implies inaccuracies in the velocity field through the momentum equation and on Y_h because its distribution is a manifestation of mixing.

Figure 3 illustrates $\omega_3\delta_{\omega,0}/\Delta U_0$ for all LESs. The No Model simulation displays more small-scale structures than can possibly be resolved on such a coarse grid, and the vortex strength is comparable to the FC-DNS data. The SMC and SMCP simulations show that the size of the large-scale vortex is well captured, but the vortex completely lacks small-scale structure. The GRC simulation has the thinnest layer among all LESs and also the weakest vorticity. The p correction, included in GRCP, restores some of the physics, as it enlarges the layer thickness and strengthens the vorticity intensity. The SSC simulation, especially after the p-correction addition embedded in SSCP, has the best agreement with the FC-DNS, although it predicts
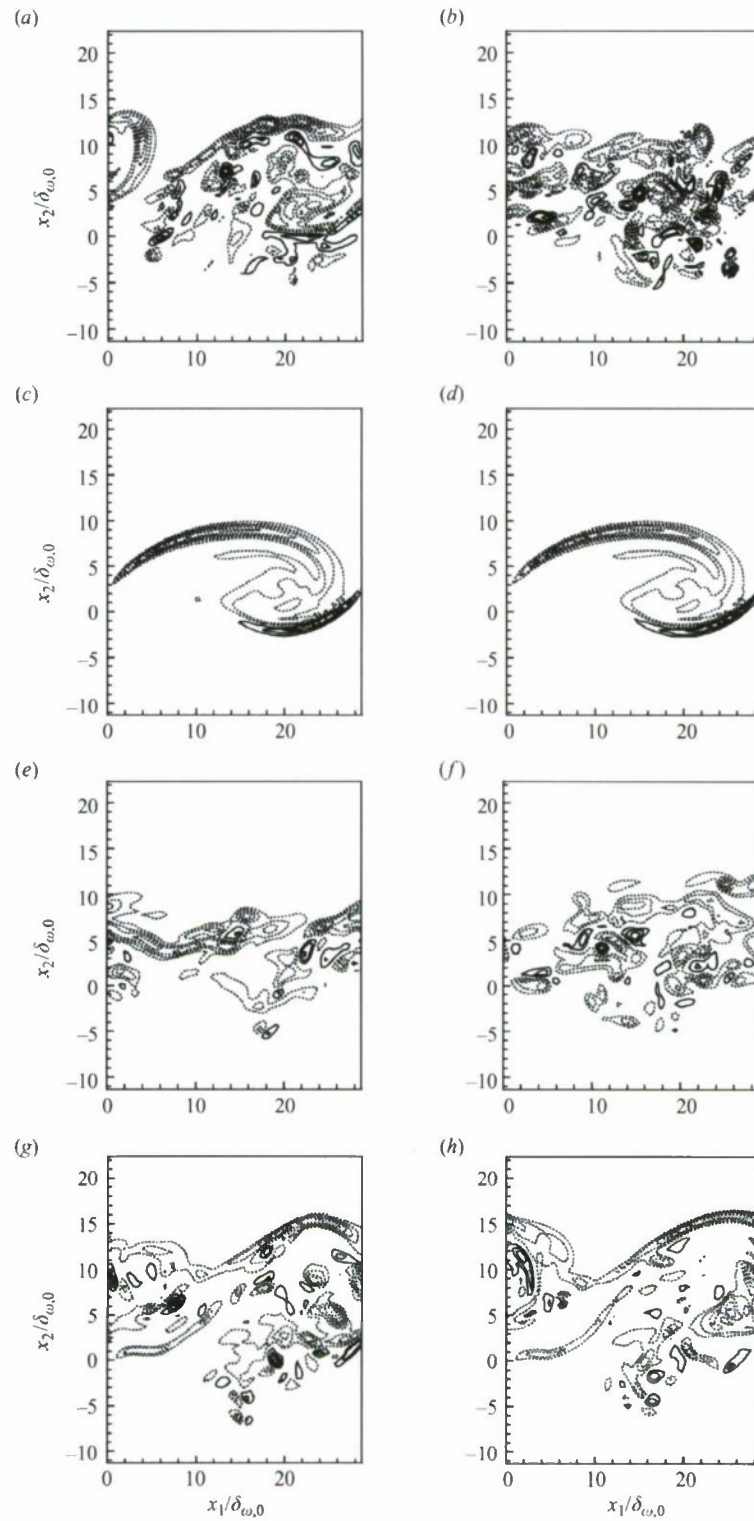
FIGURE 3. Spanwise vorticity $\omega_3 \delta_{\omega,0}/\Delta U_0$ for HN600 at t^*_{tr} of the DNS ($t^* = 135$) in the between-the-braid plane ($x_3/L_3 = 0.06$): (a) FC-DNS; (b) No Model; (c) SMC; (d) SMCP; (e) GRC; (f) GRCP; (g) SSC; (h) SSCP. The solid lines denote positive values, and the dotted lines represent negative values. There are 12 contour levels ranging between -0.7 and 0.5.
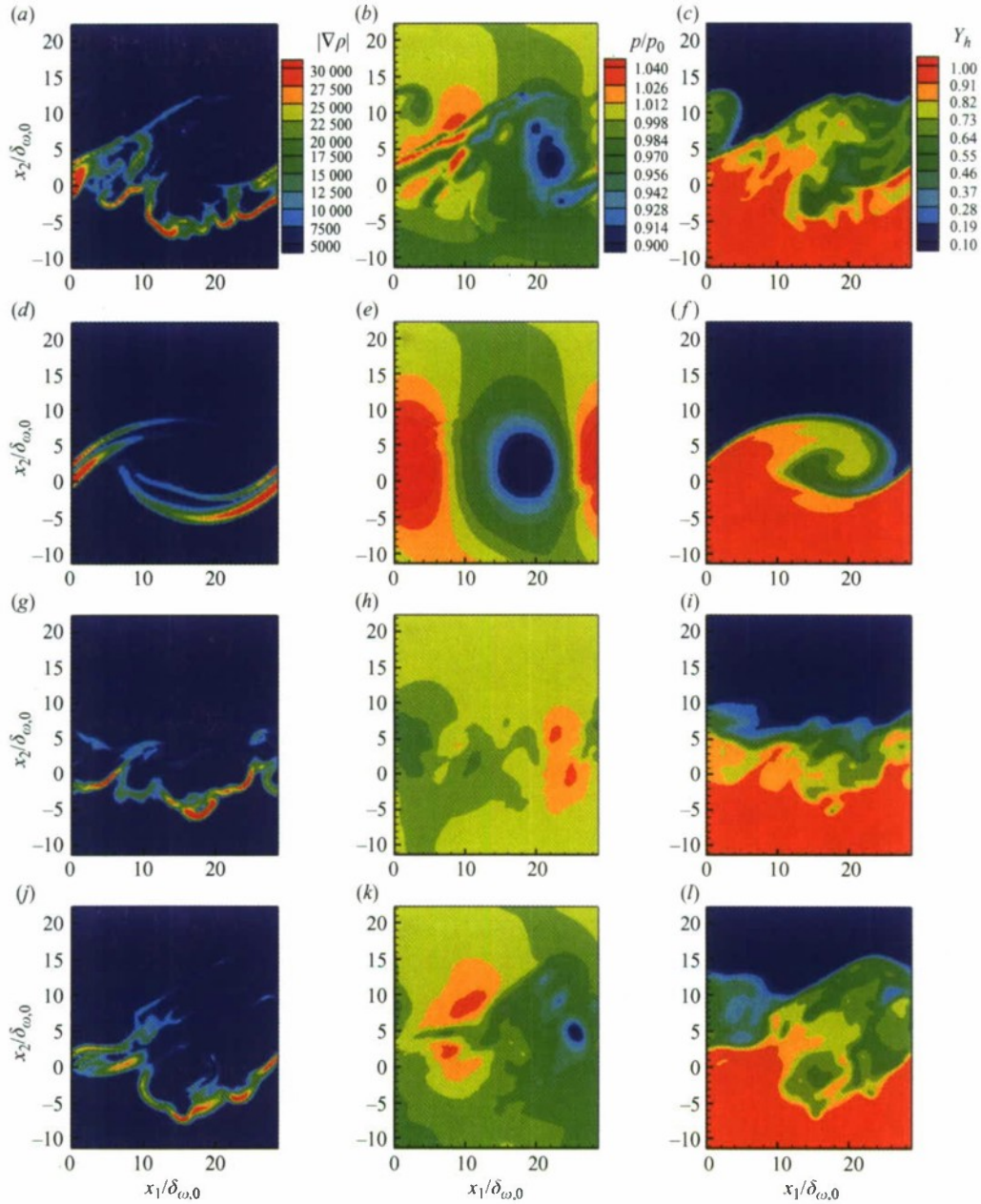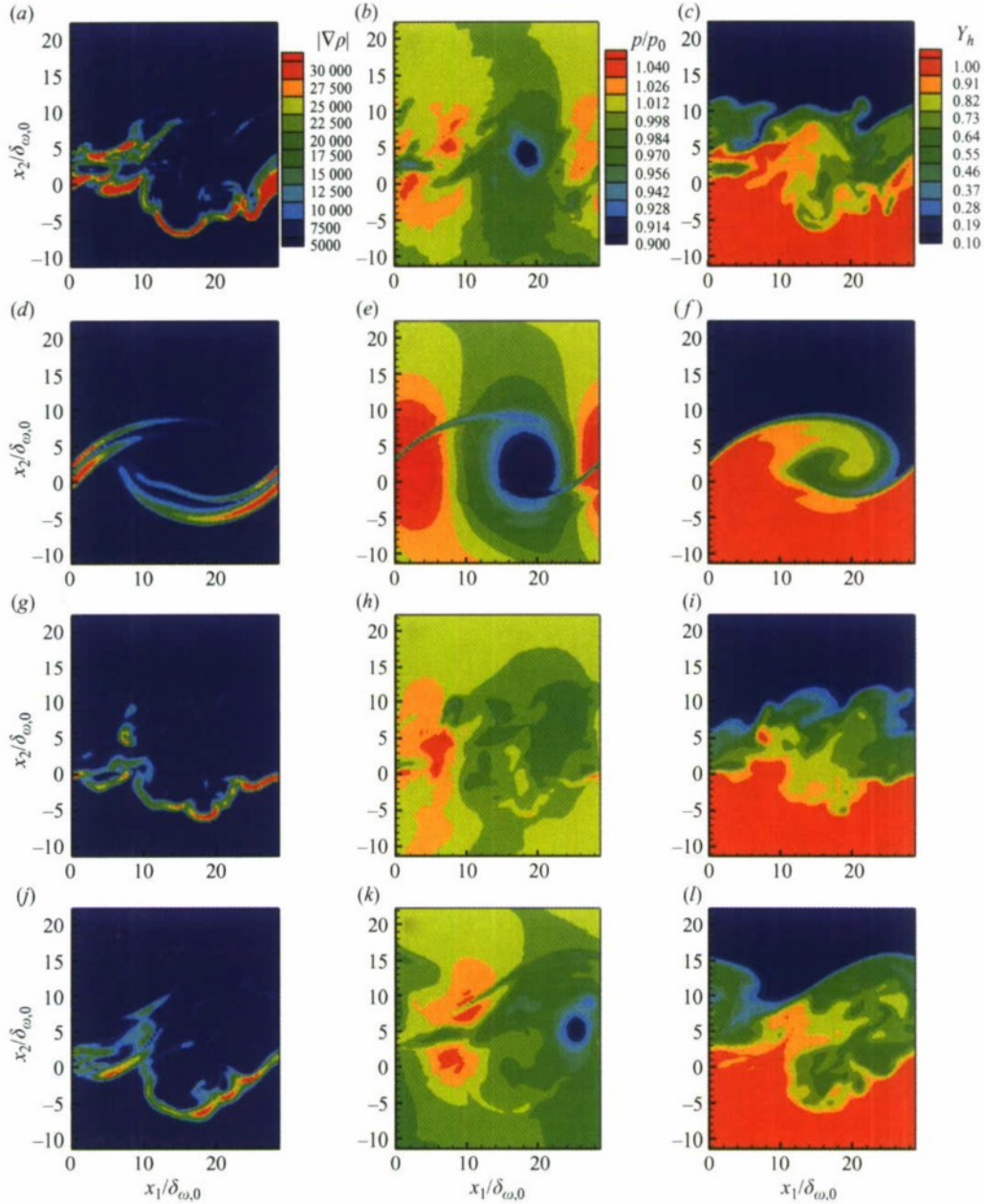
FIGURE 4. Comparison of $|\nabla\rho|$ in kg m^{-4} (first column), p/p_0 (second column) and Y_h (third column) for HN600 at t^*_{tr} of the DNS ($t^* = 135$) in the between-the-braid plane ($x_3/L_3 = 0.06$) for (a, b, c) FC-DNS, (d, e, f) SMC, (g, h, i) GRC and (j, k, l) SSC (SMC, GRC and SSC are devoid of the p correction).

an excessively large vortex size, a decreased structure and diminished vortical strength.

Figures 4 and 5 depict the $|\nabla\rho|$, p/p_0 and Y_h contour plots from the FC-DNS (figures $4a$–$4c$) and all LESs at $t^* = 135$. The SMC model predicts well the large-scale behaviour but entirely lacks small structures, as indicated by smooth features seen in the contours of all $|\nabla\rho|$, p/p_0 and Y_h (figures $4d$–$4f$). Lacking the resolved small-scale

FIGURE 5. Comparison of $|\nabla\rho|$ in kg m^{-4} (first column), p/p_0 (second column) and Y_h (third column) for HN600 at t_{tr}^* of the DNS ($t^* = 135$) in the between-the-braid plane ($x_3/L_3 = 0.06$) for (a, b, c) No Model, (d, e, f) SMCP, (g, h, i) GRCP and (j, k, l) SSCP (SMCP, GRCP and SSCP include the p correction).

structure, it is not surprising that SMC captures to a certain extent the p/p_0 field, since it is precisely the presence of the small scales that necessitated the p correction. Because of the SM highly dissipative nature, the addition of the p correction (SMCP results in figures 5d–5f) does not significantly improve the predictive ability of SMC, although it does add some more realistic features to p/p_0. The GRC model exhibits considerably more small structures than SMC in both $|\nabla\rho|$ and Y_h contours (figures 4g
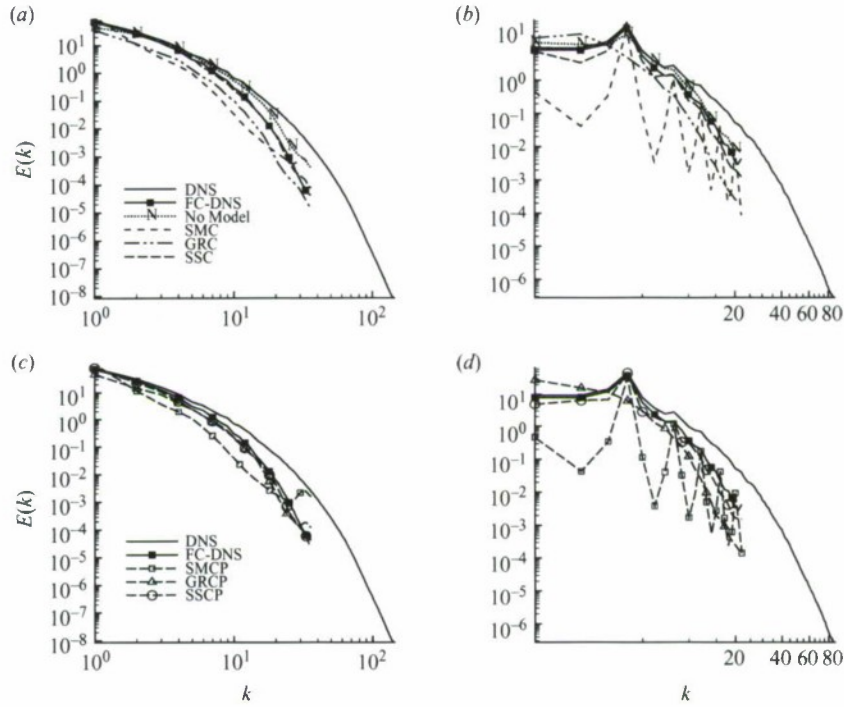
FIGURE 6. Energy spectra of u_1 for HN600 at $t^* = 135$: (a, b) without p correction and (c, d) with p correction; (a, c) streamwise and (b, d) spanwise. Energy in $m^2\ s^{-2}$.

and 4i), but its p/p_0 field (figure 4h) does not resemble at all that of the FC-DNS and in particular relatively misplaces the regions of low and high p/p_0. Adding the p correction improves considerably the solution (GRCP results in figures 5g–5i), in particular by having a correct relative placement of low- and high-p/p_0 regions, but deficiencies are still apparent. The second best results are obtained with the SSC model (figures 4j–4l), and the best solution is that of SSCP (figures 5j–5l) in that it captures substantial, although not all, the FC-DNS distinctive features of $|\nabla\rho|$, p/p_0 and Y_h but smoothes them out. Finally, the No Model simulation (figures 5a–5c) captures the $|\nabla\rho|$ location to a reasonable extent but overpredicts its magnitude and captures p/p_0 less well than it does $|\nabla\rho|$.

6.1.3. *One-dimensional spectra of the streamwise velocity*

Figure 6 displays the spanwise and streamwise energy spectra $E(k)$ of u_1 at $t^* = 135$. The plots show that the wavenumber range which must be resolved in LES is smaller than that of the DNS, as expected, since filtering removes the higher wavenumbers and reduces the energy content of the highest resolved wavenumber.

The streamwise spectra in figures 6(a) and 6(c) show that the No Model simulation has higher energy content than the FC-DNS throughout the spectrum because of excessive small-scale activity. The SMC model is the only one producing slightly higher energy content at the lowest wavenumbers and exhibiting lower energy for most of the spectrum, implying both inaccuracy at the large scales and lack of resolved small-scale activity. The GRC model deviates from the FC-DNS at all scales, with the exception of the smallest resolved scales. The SSC model reproduces reasonably well the streamwise spectral energy at the large scales. With the addition of the

p correction, there is an obvious improvement only for the GR model. The GRCP spectra agree well with those of FC-DNS, except for the largest resolved wavenumber at which they predict slightly more energy in small scales than the FC-DNS.

The striking feature of the spanwise spectra in figures 6(b) and 6(d) are the peaks exhibited by both SMC and SMCP, indicating that neither simulation has achieved transition at the DNS transitional time, in contrast to all other LESs. (The peak seen in the FC-DNS curve at $k = 4$ is attributed to spanwise forcing.) This information is consistent with the error analysis of §6.1.1. The large-scale energy in SMC and SMCP is considerably smaller than in the FC-DNS, which is attributed to the models' dissipative nature. In contrast, GRC and GRCP show excess large-scale energy (more in GRCP) compared with the FC-DNS, with the opposite for SSC and SSCP. These findings are consistent with the results of figure 2, identifying vortical activity earlier in GRC and GRCP than in the FC-DNS.

6.2. *Dynamic-model LES with pressure correction*

The constant-coefficient LES study revealed that at one extreme is the SMC model, which displays unrealistically smooth contours but in which the central low-p-magnitude region does appear, albeit devoid of the correct FC-DNS structure. At the other extreme is the GRC model, which predicts small-scale structures (although the spatial distributions are only modestly reproducing the FC-DNS) but in which the computed p field is unlike that of the FC-DNS and where particularly the relative placement of low- and high-p/p_0 regions is incorrect. The SSC model is more successful at duplicating both the small-scale structure and the p/p_0 field. Basically, with the exception of SSC, the other SGS-flux models can modestly predict either $|\nabla\rho|$ or the p field but not both. Accepting a poor rendition of $|\nabla\rho|$ is not an option, since the HDGM regions strongly affect turbulence distribution by damping perpendicular modes and transmitting energy in the tangential direction (Hannoun *et al.* 1988). Furthermore, unlike in perfect-gas flows, here the thermodynamic variables are related through a strongly nonlinear EOS, and thus a small deviation in one of them from the FC-DNS can induce considerable deviations in the others, meaning that a poor rendition of the p field is not acceptable either; additionally, small inaccuracies in the p field induce large inaccuracies in the velocity field. Addition of the p-correction model mostly improves the GR model among similarity-based models, which is attributed to the fact that the model is precisely based on computing gradients, a computation that the p correction is meant to improve. The SS model also benefits from the p correction which introduces features more closely resembling that of the FC-DNS. The SM model is so dissipative that the small-scale structure introduced by the p correction is of little effect. Because the SSC and SSCP models show the best promise, the indication is that dynamic SGS-flux models, which inherently rely on the scale-similarity assumption, may be able to perform better than the constant-coefficient models.

Since the beneficial effect of a p-correction model has been established in §6.1, all dynamic-coefficient LES include this additional SGS model. To evaluate the effectiveness of the FOC model versus the SOC model, LES are first conducted to this effect. The results identify FOC as being best, and thus the remaining LES are conducted with this model. The runs are listed in table 6, and all, with the exception of one, use $C_H(\varphi)$ of (2.31) with the multi-coefficient model of (2.32). These runs are performed with the SMD, the MGRD or the MSSD model of (2.30) or with the GRD model for which the computation is initialized either at $t^* = 0$ (GRDA-IC0) or at $t^* = 25$ (GRDA-IC25) to avoid the initial transients which produce problematic

	SGS Model		
Run	SGS-flux model	Pressure correction	CPU hours
SMD	SMD with $C_H(\varphi)$ of (2.31)	Included; (2.37)	19
MGRD-NPC	MGRD with $C_H(\varphi)$ of (2.31)	None	15
MGRD-FOC	MGRD with $C_H(\varphi)$ of (2.31)	Included; (2.37)	20
MGRD-SOC	MGRD with $C_H(\varphi)$ of (2.31)	Included; (2.36)	22
MSSD	MSSD with $C_H(\varphi)$ of (2.31)	Included; (2.37)	45
GRDA-IC0	GRD with $C_H(\varphi)$ of (2.31)	Included; (2.37)	22
GRDA-IC25	GRD with $C_H(\varphi)$ of (2.31)	Included; (2.37)	18
GRDV	GRD with $C_D(\varphi)$ of (2.31)	Included; (2.37)	20

TABLE 6. The name convention and time requirements to reach $t^* = 135$ for the LES runs using dynamic modelling for HN600. For all LES cases, the grid is $72 \times 84 \times 44$. CPU hours are an estimate: aggregate over parallel processors on an SGI Altix 3000 system.

SGS-flux coefficients, as discussed below. Therefore, not only are we comparing the performance of SGS models, but we are also assessing strategies on how they can best be used in conjunction with other aspects of the computation. The mixed models' motivation is not here the typical one in which the SM model is combined with either the GR or the SS model as a means to provide numerical stability to the computation; numerical stability is not a problem in the present LES, as shown by the ability to perform LES with the GRD model alone. Rather, the mixed models are here explored as a means of combining the attribute of the SM model to produce a good, although overstated, approximation of the p field with the feature of the GR or SS model to produce an understated p field but a good approximation of the $\nabla \rho$ field, which is lacking in the SM models. The idea is that a combination of SM and GR or SS may have the ultimate desirable characteristics of the FC-DNS; it is well known that transitional flows have substantial backscatter, and the $t^* = 135$ state may not be predictable without the backscatter capability of the GR or SS model. The only model in which $C_D(\varphi)$ (i.e. domain-averaged coefficients) of (2.31) was used is GRDV, and the motivation is, as for GRDA-IC25, the mitigation of some large SGS-flux coefficients produced in homogeneous planes during the initial p transients. In all dynamic models, $\hat{\Delta} = 2\bar{\Delta}$. The dynamic-coefficient models are evaluated in similar manner as the constant-coefficient models, that is to say by comparing them with the FC-DNS in terms of the global quantities, the important quantities $|\nabla \rho|$, p/p_0 and Y_h and the spectra.

Because the HN600 simulation is distinctive among the DNSs in table 3, in that it has the most prominent small-scale structure, it is instructive to inquire whether the performance of LES models examined so far extends to the FC-DNS obtained for other realizations. This topic is addressed in Appendix C.

6.2.1. *Assessment of the first-order versus the second-order p-correction model*

The SOC model for p is subject to the assumption of (2.35) and is described by (2.36) in which $(\partial^2 p/(\partial \phi_m \partial \phi_n))_{\phi=\bar{\phi}}$ is computed from the knowledge of $(\partial^2 p/(\partial \psi'_m \partial \psi'_n))_{\psi'=\overline{\psi'}}$ through the PR EOS as described by Selle *et al.* (2007) and where quantities $\vartheta(\overline{\phi_m}, \overline{\phi_n})$ are modelled using the GRD SGS-flux model described in §2.4.1. The model is implemented in the code by computing in the momentum equation

$$\nabla(p(\overline{\phi})) + \nabla(\overline{p(\phi)} - p(\overline{\phi})) = \nabla(\overline{p(\phi)}) = \nabla \left[\overline{p(\overline{\phi})} + \frac{1}{2} \left. \frac{\partial^2 p}{\partial \phi_m \partial \phi_n} \right|_{\phi=\overline{\phi}} \vartheta(\overline{\phi_m}, \overline{\phi_n}) \right]. \quad (6.6)$$
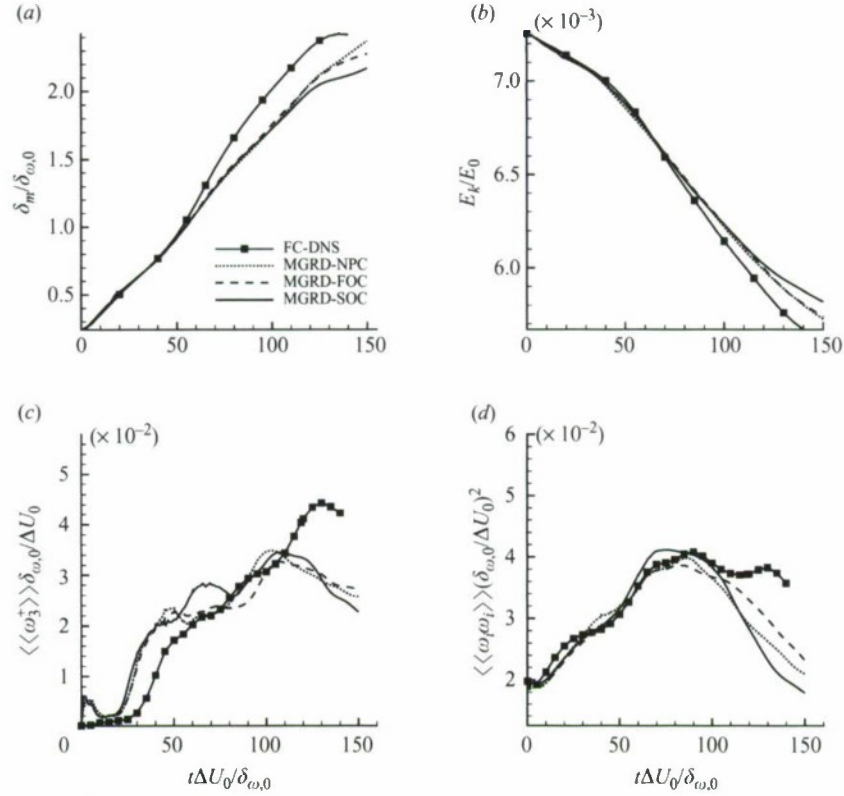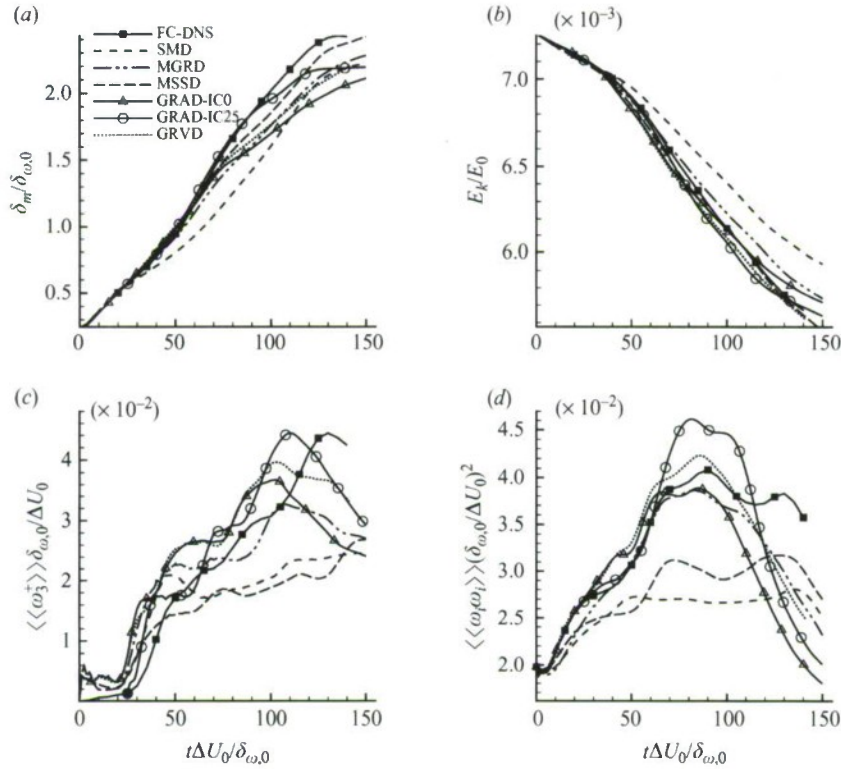
FIGURE 7. Time evolution of non-dimensional global quantities for HN600: (a) $\delta_m/\delta_{\omega,0}$, (b) E_K/E_0, (c) $\langle\langle\omega_3^+\rangle\rangle\delta_{\omega,0}/\Delta U_0$ and (d) $\langle\langle\omega_i\omega_i\rangle\rangle(\delta_{\omega,0}/\Delta U_0)^2$ for the no p correction (MGRD-NPC), first-order p correction (MGRD-FOC) and second-order p correction (MGRD-SOC); E_0 is the initial total energy in the domain.

The global-quantity results are presented in figure 7 for the LES conducted, as an example, with the MGRD model for the SGS fluxes and either with no p correction (NPC) or with FOC or SOC. The resolution is the same for all LESs, particularly $\bar{\Delta} = 8\Delta x_{DNS}$, which is the filter size at which Selle et al. (2007) found deterioration of the SOC model, as explained in §2.4.2. Results depicted in figure 7 show that compared with the FOC, the SOC model is slightly inferior in duplicating $\delta_m/\delta_{\omega,0}$ and E_K/E_0 of the FC-DNS, seems somewhat inferior in reproducing the vortical features of the flow embedded in $\langle\langle\omega_3^+\rangle\rangle\delta_{\omega,0}/\Delta U_0$ and is clearly inferior in reproducing $\langle\langle\omega_i\omega_i\rangle\rangle(\delta_{\omega,0}/\Delta U_0)^2$; more quantitative conclusions using $\varepsilon_{1,\psi}$ and $\varepsilon_{2,\psi}$ are presented in table 7 and discussed in conjunction with similar results for the other dynamic models in §6.2.2. Compared with the LES exercised with the MGRD model but NPC, both LESs with the p-correction model show better predictive capabilities. Flow visualizations presented in §6.2.3 reinforce these conclusions. Therefore, the FOC model will be used for all other LESs below.

6.2.2. Evolution of the global quantities

Figure 8 displays the time evolution of $\delta_m/\delta_{\omega,0}$, E_K/E_0, $\langle\langle\omega_3^+\rangle\rangle\delta_{\omega,0}/\Delta U_0$ and $\langle\langle\omega_i\omega_i\rangle\rangle(\delta_{\omega,0}/\Delta U_0)^2$ for the FC-DNS data and for all LESs performed with SGS-flux dynamic models and the FOC model for p. The SMD model performs considerably better compared with the SMC model presented in figure 2; $\delta_m/\delta_{\omega,0}$

Run	$\delta_m/\delta_{\omega,0}$		E_K/E_0		$\langle\langle\omega_3^+\rangle\rangle\delta_{\omega,0}/\Delta U_0$		$\langle\langle\omega_i\omega_i\rangle\rangle(\delta_{\omega,0}/\Delta U_0)^2$	
	$\varepsilon_{1,\psi}$	$\varepsilon_{2,\psi}$	$\varepsilon_{1,\psi}$	$\varepsilon_{2,\psi}$	$\varepsilon_{1,\psi}$	$\varepsilon_{2,\psi}$	$\varepsilon_{1,\psi}$	$\varepsilon_{2,\psi}$
SMD	179	201	18	24	344	330	227	263
MGRD-NPC	98	122	5	7	206	235	50	64
MGRD-FOC	91	112	6	8	211	225	41	48
MGRD-SOC	100	123	6	8	244	258	46	59
MSSD	53	64	4	5	363	365	175	198
GRDA-IC0	99	131	6	8	318	289	60	79
GRDA-IC25	42	59	6	8	183	202	96	142
GRDV	83	107	8	10	330	290	46	54

TABLE 7. Computed errors (in $\times 10^{-3}$) for LES with respect to the FC-DNS for different dynamic-coefficient SGS models according to (6.4) and (6.5).

FIGURE 8. Time evolution of non-dimensional global quantities for HN600 computed with dynamic SGS modelling: (a) $\delta_m/\delta_{\omega,0}$, (b) E_K/E_0, (c) $\langle\langle\omega_3^+\rangle\rangle\delta_{\omega,0}/\Delta U_0$ and (d) $\langle\langle\omega_i\omega_i\rangle\rangle(\delta_{\omega,0}/\Delta U_0)^2$ for FC-DNS and LES listed in table 5.

and E_K/E_0 evolutions are closer to that of the FC-DNS, and $\langle\langle\omega_3^+\rangle\rangle\delta_{\omega,0}/\Delta U_0$ and $\langle\langle\omega_i\omega_i\rangle\rangle(\delta_{\omega,0}/\Delta U_0)^2$, which were substantially underestimated in constant-coefficient runs, are here more realistic. When the SM model is used in conjunction with the GR or SS model, both $\delta_m/\delta_{\omega,0}$ growth and E_K/E_0 decay are better predicted, particularly at the earlier times, and better with MSSD than MGRD. The MGRD model predictions for both $\langle\langle\omega_3^+\rangle\rangle\delta_{\omega,0}/\Delta U_0$ and $\langle\langle\omega_i\omega_i\rangle\rangle(\delta_{\omega,0}/\Delta U_0)^2$ are much closer to the FC-DNS

than those of the SMD model. Compared with the MGRD results, those of the MSSD are considerably inferior for both $\langle\langle\omega_3^+\rangle\rangle\delta_{\omega,0}/\Delta U_0$ and $\langle\langle\omega_i\omega_i\rangle\rangle(\delta_{\omega,0}/\Delta U_0)^2$. Thus, among eddy-viscosity-based dynamic models, the best agreement with the FC-DNS in predicting vortical flow features is achieved by MGRD, while the CPU time is similar to the much worse SMD model (see table 6).

In implementing the dynamic modelling for the GR model it was observed that the dynamically computed coefficient values were too large to be physically acceptable at the very early stages of the simulations, where the flow is laminar and no significant contributions from the SGS fluxes are expected. Hence, a limiter was set, and all the coefficients were kept below a pre-specified value of 0.30. This value has a large margin over the theoretical value of $1/12$ for the GR model. Unlike for the SM model, there is no clear improvement on GR predictive abilities when dynamic modelling is applied. For all four global quantities examined, the results of GRDA-IC0 are worse than those of GRCP. Although the vortical features of the flow are better predicted with this model compared with the eddy-viscosity-based models, there is an unexpected sudden decrease in the $\delta_m/\delta_{\omega,0}$ prediction. Previous authors (e.g. Vreman *et al.* 1996*b*; Berselli, Iliescu & Layton 2006) have reported the GR model to be numerically unstable; however, other authors used it successfully for both single-phase and two-phase flow LESs of temporal mixing layers (e.g. Leboissetier *et al.* 2005). Because the GRC simulations of §6.1 showed that the GR model is very sensitive to the p correction, the conjecture is here that the poor performance of the GRDA-IC0 model may be due to the initial p-transients, which can be very substantial (Okong'o & Bellan 2002*b*). To avoid these p-transients, consistent with information discussed in Appendix A, the GRDA-IC25 simulation was conducted. This strategy led to considerably improved results as can be seen in figure 8. Another strategy for avoiding the full impact of the initial excessive value of dynamically computed coefficients in some of the homogeneous planes was to domain-average the computed coefficient (GRDV; earlier defined), leading similarly to results superior to GRDA-IC0, as portrayed in figure 8.

Figure 9 displays the evolution of the model coefficients in the $x_2 = 0$ plane. Figures 9(*a*)–9(*c*) are for the eddy-viscosity-based models with four coefficients, $C_{\tau d}$, $C_{\tau x}$, C_ζ, C_η. Figures 9(*d*)–9(*f*) are for GRD with three coefficients, C_τ, C_ζ, C_η. The YO coefficients of the SMD and MGRD models, $C_{\tau d}$, behave similarly: they are initially larger than 0.8, fall sharply to 0.20 by $t^* = 30$ and then increase to their maximum value of 0.30 around $t^* = 80$ (figures 9*a* and 9*b*). On the other hand, $C_{\tau d}$ of the MSSD model does not have unphysically large initial values (figure 9*c*). The values of the coefficients confirm that among SM-based models, the most dissipative model is the SMD model, having the largest coefficients, followed by the MSSD and the MGRD models. The indication is that the favourable predictions of MSSD are due to its effectiveness in eliminating the unphysical values of the YO coefficient that are observed at the beginning of the simulation. Although the SM-based models overcome these unrealistic high-coefficient values, the GR model is incapable of surmounting these initial difficulties. To illustrate the difficulty encountered in GRD models with large coefficients for $t^* < 25$ and the stabilization of their values with time, C_τ, C_ζ and C_η are shown in figure 9 in the $x_2 = 0$ plane, for GRDA-IC0, GRDA-IC25 and GRDV (figures 9*d*–9*f*), respectively. For GRDA-IC0, all three coefficients start from the pre-specified limiting value of 0.30 (not shown) and decline to approximately 0.10 within the roll-up period ($t^* = 25$). The maximum coefficient value is reached just after the first pairing and at transition for C_τ and C_η, and at transition for C_ζ. The maximum values for C_τ, C_ζ and C_η after the roll-up period are approximately 0.13,
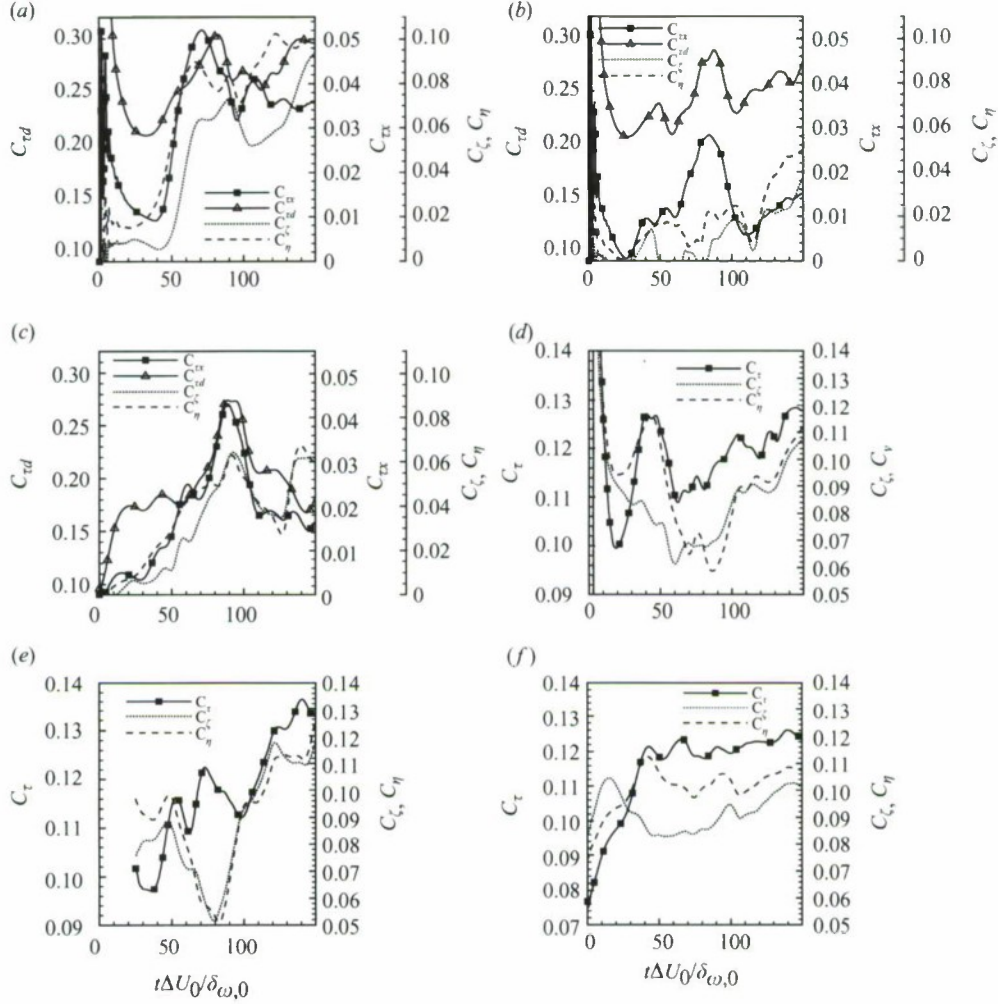
FIGURE 9. Evolution of the model coefficients of (a) SMD, (b) MGRD, (c) MSSD, (d) GRDA-IC0, (e) GRDA-IC25 and (f) GRDV for HN600 at $x_2 = 0$.

0.10 and 0.10, respectively (figure 9d). For both GRDA-IC25 and GRDV, the initially high-coefficient values were successfully avoided.

Results from an error analysis similar to that of §6.1.1 are listed in table 7. Compared with error values listed in table 5, the errors are here considerably reduced, even for SMD, which is the most inaccurate dynamic LES according to these evaluations. Similar to the findings for constant-coefficient LES, errors associated with E_K/E_0 decay are smallest in the group, and for dynamic LES they are negligible. Although errors for $\langle\langle\omega_3^+\rangle\rangle\delta_{\omega,0}/\Delta U_0$ remain the most prominent, by difference from constant-coefficient LES, they are followed in magnitude by errors in $\delta_m/\delta_{\omega,0}$. Of note is that the SSCP model errors in $\langle\langle\omega_3^+\rangle\rangle\delta_{\omega,0}/\Delta U_0$ are smaller than all dynamic-coefficient LES errors in this quantity. The worst models are the GRDV, MSSD and SMD models, not necessarily ranked in the same order according to $\varepsilon_{1,\psi}$ and $\varepsilon_{2,\psi}$. By starting the LES at $t^* = 25$, one improves the accuracy. Considering both $\varepsilon_{1,\psi}$ and $\varepsilon_{2,\psi}$, SSCP is also the best model in predicting $\delta_m/\delta_{\omega,0}$, while the worst predictions among dynamic-coefficient models are obtained with the SMD LES, which is also the

worst for reproducing $\langle\langle\omega_i\omega_i\rangle\rangle(\delta_{\omega,0}/\Delta U_0)^2$. The most favourable $\langle\langle\omega_i\omega_i\rangle\rangle(\delta_{\omega,0}/\Delta U_0)^2$ predictions are by the MGRD-FOC, while SMD produces the worst ones. Generally, all three MGRD models (MGRD-NPC, MGRD-FOC and MGRDS-SOC) have relatively similar errors when compared with the other models, indicating that the error is associated with the MGRD attributes rather than with the type of the p correction.

6.2.3. *Flow visualizations*

Figure 10 displays the $|\nabla\rho|$, p/p_0 and Y_h distributions at $t^* = 135$ obtained with each of the LESs using dynamic models, except GRDV; the GRDV model was omitted because it exhibits similar behaviour as, although somewhat less successful than, GRDA-IC25. The idea of combining the SM model with the GR or SS model to mitigate the overprediction of p/p_0 from the former model with the underprediction of the latter, and to incorporate the advantageous small-scale reproduction of the latter models, was successful to a certain extent in that MGRD of figures 10(d)–10(f) is a better representation of the FC-DNS of figures 4(a)–4(c) than either SMD of figures 10(a)–10(c) or GRD of figures 10(j)–10(l). Between mixed models, MGRD is better than MSSD, which is attributed to the more acute underprediction of p/p_0 in GRCP than in SSCP that balances the strong overprediction of p/p_0 in SMCP and to the higher production of small scales in GRCP than in SSCP. Nevertheless, because of their strong dissipative behaviour, all SM-based (i.e. eddy-viscosity) models produce flows which are too smooth compared with the FC-DNS. On the other hand, GRDA-IC25 (see figures 10m–10o) successfully captures these structures while also giving a reasonable approximation – only slightly inferior to that of MSSD – of the FC-DNS p/p_0, showing that success in LES is not only determined by the SGS models but also by the ICs.

When examining the flow visualizations of figure 11 for the NPC and SOC models and comparing them with figures 10(d)–10(f), the conclusion is that the SOC model is slightly inferior in replicating the detailed structure of the flow. Computationally, the utilization of the SOC model also comes at a small additional cost: 22 CPU hours compared to the 20 hours of the FOC model, that is to say a 10 % increase in CPU time. The flow visualizations are consistent with the global-quantity results in that LES with the same dynamic SGS-flux model but NPC model is inferior to LES with either of the p-correction approaches, lacking some of the low-pressure regions and introducing spurious large-pressure regions while at the same time not providing a significant CPU-time computational saving having required 15 CPU hours.

6.2.4. *One-dimensional spectra of the streamwise velocity*

The interest in achieving in LES both temporal and spatial duplication of DNS prompts an examination of the velocity-fluctuation-based energy spectra at $t^* = 135$, illustrated in figure 12. The streamwise spectra of figure 12(a) show that the MGRD model predicts a more energetic flow at the small scales, having higher energy content than that of FC-DNS at the highest wavenumber. The MSSD displays the opposite behaviour, and similar to MGRD it has at the largest scale a lower energy content than the FC-DNS. The SMD model predicts a reduced energy with respect to the FC-DNS for all wave-numbers, except for the largest scale. The spanwise spectra of figure 12(b) indicate that neither SMD nor MSSD LES has reached a transitional state, as clearly seen by the numerous peaks (other than that of the initial perturbation) over the entire range of scales. Moreover, these two models also substantially underestimate (for SMD, up to two orders of magnitude) the energy
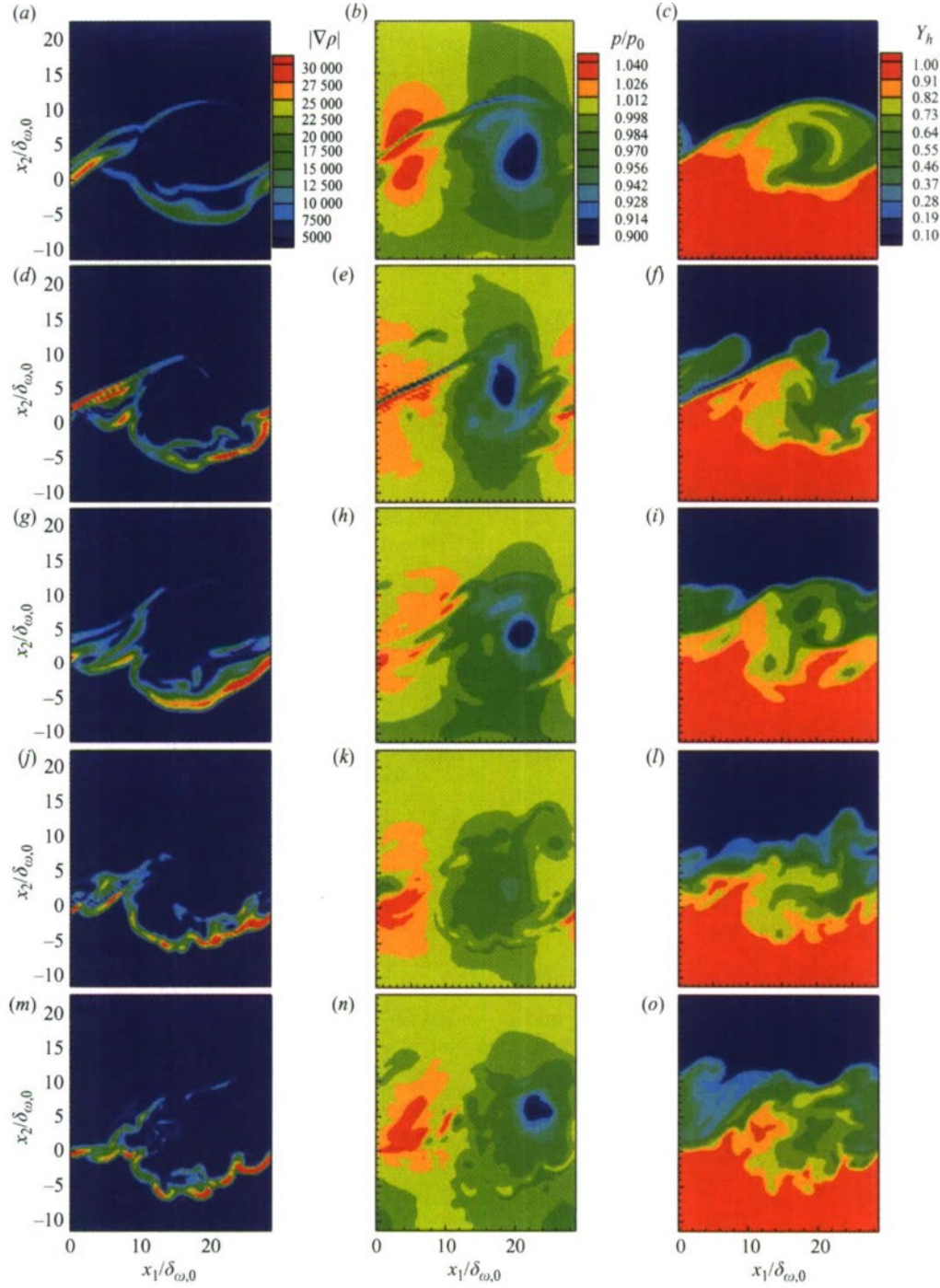
FIGURE 10. Comparison of $|\nabla \rho|$ in kg m^{-4} (first column), p/p_0 (second column) and Y_h (third column) for HN600 at t_{tr}^* of the DNS ($t^* = 135$) in the between-the-braid plane ($x_3/L_3 = 0.06$) for (a, b, c) SMD, (d, e, f) MGRD, (g, h, i) MSSD, (j, k, l) GRDA-IC0 and (m, n, o) GRDA-IC25. All models include the p correction.
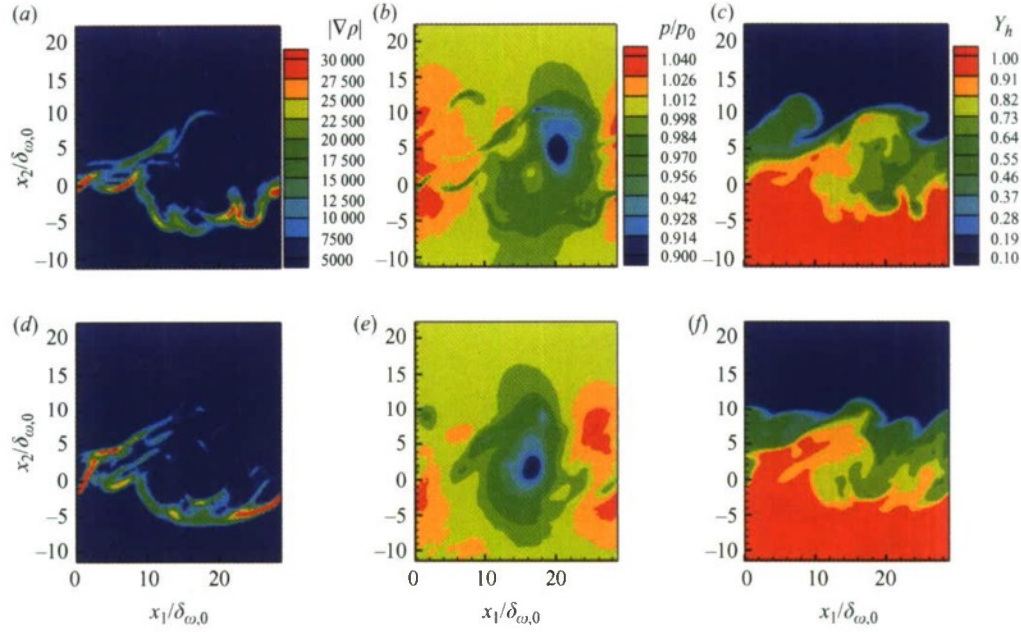
FIGURE 11. Flow visualizations comparing the MGRD using (a, b, c) the second-order p correction (MGRD-SOC) with MGRD using (d, e, f) no p correction (MGRD-NPC). Results are for $|\nabla \rho|$ in kg m^{-4} (first column), p/p_0 (second column) and Y_h (third column) for HN600 at t_{tr}^* of the DNS $(t^* = 135)$ in the between-the-braid plane $(x_3/L_3 = 0.06)$.

in the large scales. In contrast, the MGRD LES slightly overestimates the energy in the large scales and underestimates it in the small scales. Figure 12(c) indicates that for the largest scales of the spanwise spectra, GRDA-IC0 and GRDV are the most dissenting representations of the FC-DNS; however, the agreement at the smaller scales is very good. Similarly, the spanwise spectra of the dynamic gradient models (figure 12d) overestimate the energy content at both large and small scales.

6.3. Irreversible entropy production

The above results focused on primitive variables, which are the primary interest for flow predictions; however, we wish to highlight here the scientific information embedded in a higher-order quantity such as the irreversible entropy production which is essentially the dissipation (Hirshfelder et al. 1964); the dissipation is not to be confused with the TKE dissipation, as stated in § 1. Okong'o & Bellan (2000) have discussed in detail the irreversible entropy production concept and have shown that in the present situation the dissipation is the sum of three terms, each corresponding to a dissipation mode,

$$g_{tot} = g_{visc} + g_{temp} + g_{mass}, \qquad (6.7)$$

with

$$g_{visc} = \frac{\mu}{T} 2 \left(S_{ij} - \frac{1}{3} S_{kk} \delta_{ij} \right)^2, \quad g_{temp} = \frac{\lambda}{T^2} \frac{\partial T}{\partial x_i} \frac{\partial T}{\partial x_i}, \quad g_{mass} = \frac{1}{Y_1 Y_2 \rho D} \frac{R_u m}{m_1 m_2} j_{2i} j_{2i}, \qquad (6.8)$$

where g_{visc}, g_{temp} and g_{mass} represent contributions from the viscous, heat-flux and mass-flux modes, respectively. Different g_{tot} modes may be more prominent in various situations. For example, Okong'o & Bellan (2004a) have shown that in a compressible
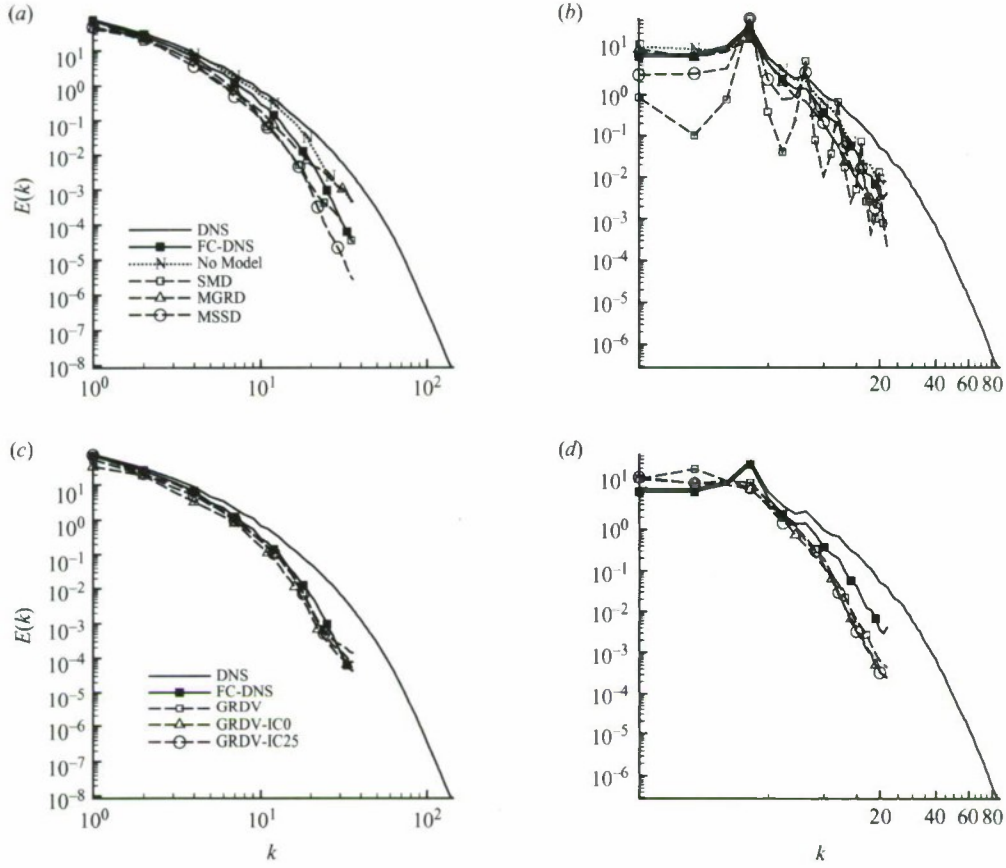
FIGURE 12. Energy spectra of u_1 for HN600 at $t^* = 135$ (a, b) with Smagorinsky-based dynamic models and (c, d) with similarity-based dynamic models; (a, c) streamwise and (b, d) spanwise. Energy in $m^2 s^{-2}$.

atmospheric-p transitional shear layer, g_{tot} is dominated by g_{visc}, with negligible g_{temp}. However, unlike for atmospheric-p turbulent flows, in situations in which $p > p_c$, g_{tot} is dominated by g_{mass} with moderate contribution from g_{temp} and negligible portion from g_{visc}; this situation prevailed for both HN layers (Okong'o & Bellan 2002b) and OH layers (Okong'o *et al.* 2002). The prominence of g_{mass} is a direct consequence of the HDGM regions, and since the HDGM regions are a feature of fully turbulent $p > p_c$ flows, the dominance of g_{mass} in g_{tot} is expected to remain at high Re values.

Because filtering of the entropy equation does not introduce additional source terms, the comparison for evaluating LES predictions is between $g_k(\overline{\phi})$, where k is $visc, temp$ or $mass$ computed with $\overline{\phi}$ being either the FC-DNS field or the LES field. Results are depicted in figure 13 as the time variation of the domain-averaged values of each mode for LES compared with the equivalent results from the FC-DNS, all normalized by the maximum DNS value found for each mode. Figures 13(a), 13(c) and 13(e) show the temporal variation observed in the eddy-viscosity-based dynamic models for viscous, heat-flux and mass-flux modes, respectively. The MGRD model, whether or not used in combination with a p correction, is clearly superior to the MSSD and SMD models in capturing the g_{visc} FC-DNS result (figure 13a). Until close to transition, this model overpredicts both g_{temp} and g_{mass}, but by $t^* = 100$ there is an underprediction for g_{temp}, while the values for g_{mass} are excellent; in comparison, both SMD and MSSD estimates are low with respect to the FC-DNS
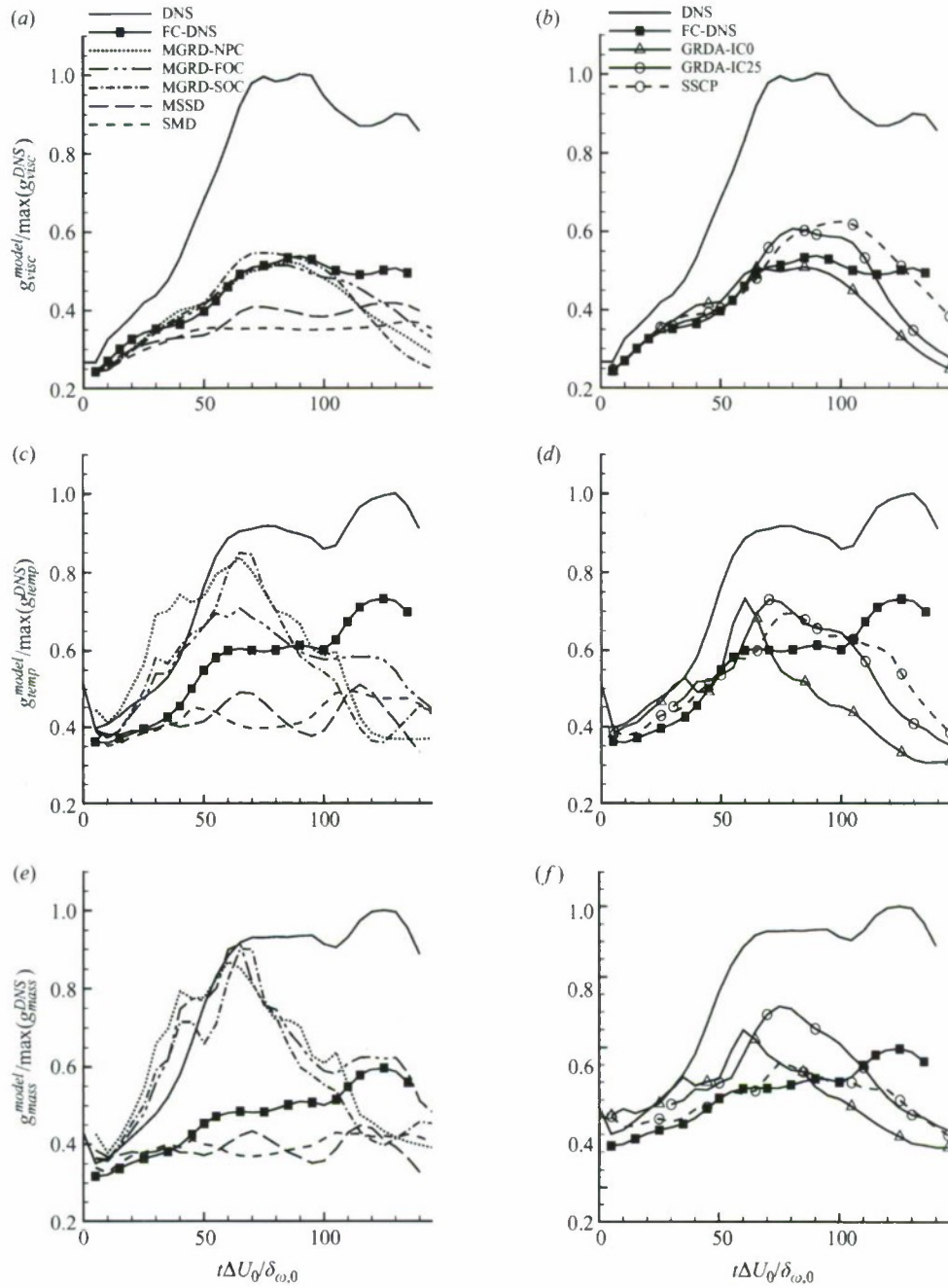
FIGURE 13. Time evolution of the domain-averaged irreversible entropy production for HN600 as computed from FC-DNS and (*a*, *c*, *e*) LES with eddy-viscosity-based dynamic models (SMD, MGRD, MSSD, MGRD-SOC, MGRD-NPC), (*b*, *d*, *f*) LES with dynamic GR model initiated from $t^* = 0$ (GRDA-IC0) and $t^* = 25$ (GRDA-IC25) with the SSCP model; (*a*, *b*) viscous mode, (*c*, *d*) heat-flux mode, (*e*, *f*) mass-flux mode, all normalized with the corresponding maximum DNS value.

data (figures 13c and 13e). Among different MGRD models, the best estimates are consistently obtained with MGRD-FOC. These results confirm those of §6.2.1 that the MGRD-SOC is not as successful as the MGRD-FOC and further show that MGRD-NPC is considerably inferior to an MGRD model with a p correction, definitely assigning the success of the MGRD-FOC to the Taylor series model for $\nabla[\overline{p(\phi)} - p(\bar{\phi})]$.

For the GRD and SSCP models, the time evolution of g_{visc}, g_{temp} and g_{mass} are illustrated in figures 13(b), 13(d)and 13(f), respectively. After $t^* = 70$, g_{visc} is overestimated for both the SSCP and GRDA-IC25 models, while it is underestimated with the GRDA-IC0 model. Although the SSCP and GRDA-IC25 models predict g_{visc} and g_{temp} equally well, the SSCP model gives a much better prediction for g_{mass}. Considering that for these type of flows g_{tot} is dominated by g_{mass}, the SSCP model is best overall.

7. Summary and conclusions

An *a posteriori* LES study has been conducted to identify the most promising SGS models for predicting fluid disintegration of two counterflow moving fluids and binary-fluid mixing at pressures initially higher than the critical pressure of either fluid. The LES governing equations consist of the filtered original equations for conservation of mass, momentum, species and total energy coupled with a real-gas EOS. These equations were previously solved using DNS. The transport properties were functions of the thermodynamic variables. Following a previous *a priori* investigation (Selle *et al.* 2007), the SGS terms in the differential equations consist of two types: (i) the typical SGS-flux terms and (ii) a pressure correction in the momentum equation accounting for the non-negligible difference between the filtered pressure and the pressure computed as a function of the filtered flow field. The second type of SGS term is the direct result of the strong EOS nonlinearity leading to the existence of HDGM regions in the flow having a complex small-scale structure.

The configuration was that of a three-dimensional mixing layer with initially heptane in the lower stream and nitrogen in the upper stream, and the DNS followed, for each realization, the evolution of the layer from an initial laminar state to a transitional state. The LESs were carried out with the same numerical discretization and time advancement numerical scheme as the DNSs. All LESs were conducted up to the same non-dimensional simulation time as the DNS, and the CPU time up to the DNS transitional state was considerably smaller than that of the DNS. Several types of LES models were assessed, all of which were compared with the FC-DNS: filtered to remove the small scales and coarsened to retain only the LES nodes. The FC-DNS represents an ideal, generally not achievable, LES. The three SGS-flux models assessed were the SM, the GR and the SS models. Two pressure-correction models were assessed. The first model relied on the first-order Taylor series expansion of the filtered pressure, and being the best quantitative approximation according to Taylor series concepts when using only one series term, it was used for all but one of the LESs. The second model was based on the second-order term of the Taylor expansion only, as the assumptions enabling utilization of the model based on this term had the consequence of nulling the first-order term; thus a combined first-order and second-order term model could not be used. The second-order term was modelled using variances which assumed one of the mathematical forms of the SGS-flux models. It turned out that the second-order term pressure correction was both more computationally intensive than the first-order one and a worse approximation of the FC-DNS. Thus the first-order Taylor expansion model was otherwise used.

Constant-coefficient SGS-flux models with coefficient values obtained at the transitional time in the *a priori* study were first evaluated in the LES, without or with the pressure correction model. Among models devoid of pressure correction, the SM model was overly dissipative, which resulted in lack of resolved small-scale structure; hence, it had a reasonable, although exaggerated, rendition of the pressure field. At the other extreme was the GR model which displayed small-scale structure, but the regions of low and high pressure were misplaced. The SS model was the most successful in that it combined small-scale structure and a reasonable, although understated, pressure field. The utilization of the pressure-correction model improved the morphology of the pressure field for the SM model, but the lack of resolved small-scale structure was still evident. The GR model benefitted most from the pressure correction in that the low- and high-pressure regions were now correctly placed, but the lowest pressure in the vortex core was still not reproduced. The most successful model was the one that combined the SS and pressure correction, as the morphology of the flow was closer to that of the FC-DNS than for the SS model with no pressure correction.

The good performance of the SS model motivated the evaluation of dynamic models, since they rely on the same underlying concept. Several dynamic models were assessed, including two mixed models utilizing the SM model in conjunction with either the GR or the SS model. Unlike in typical LES using mixed models, these combinations were not used to provide numerical stability to the computations (indeed, several LESs were successfully conducted using only the GR or the SS model) but to combine the good complementary predictions from each of the SM and GR or the SS model. The backscatter capability of the GR and SS models was also considered a potential asset in reproducing the FC-DNS transitional state. These mixed models were compared with the FC-DNS together with an SM-dynamic model and three GR-dynamic models. In one dynamic GR model LES, the computations were started at the time of the DNS IC. In another GR-dynamic model LES, the computation was initiated at a time past the DNS IC, so as to avoid the initial transients which made the pressure-correction term rival in magnitude the leading-order term in the momentum equation. Finally in the third dynamic GR model LES, the coefficients of the SGS-flux models were computed by domain averaging, whereas in all other LES with the GR or other SGS-flux models, it was computed by averaging in homogeneous planes. Among dynamic models, the SM-dynamic model was clearly the worst in all respects. The GR-dynamic model with the IC past the DNS transients was overall the best in terms both of the evolution of the global quantities and of flow visualizations at the transitional state of the DNS. Among all other models, the MGRD model was the best at duplicating the pressure but was not as adept as the GR-dynamic alone at reproducing the small-scale structure; the deficiency of the MGRD model was due to the presence of the SM model with its overly dissipative characteristics. An inquiry into the velocity-fluctuation-based spectra of dynamic models revealed that while MGRD reached transition at the DNS transitional time, neither SMD nor MSSD did so, and each furthermore underestimated the energy in the largest scales. The spectra examination showed that while all GR-dynamic model LESs reached transition at the DNS transitional time, they slightly overestimated the energy in the largest scales. Thus, the strategy of using mixed models to offset deficiencies from individual SGS models and instil small-scale duplication capabilities proved somewhat successful (tested also with DNS realizations other than those for which the models were developed); however, the lack of temporal equivalence

with the FC-DNS in achieving the transitional state makes some SM-based models problematic if both temporal and spatial equivalence with the FC-DNS are the goal, although the models may be considered acceptable for statistical equivalence. An alternate strategy to achieve LES/FC-DNS temporal and spatial equivalence was choosing an appropriate time for initiating the LES and avoiding the utilization of SM-based models. For practical applications, this would mean that measurements past initial transients should be used for initiating LES. Clearly, the LES dynamic models present many options for conducting simulations, and it is the privilege and responsibility of the user to choose the option which best suits the LES goal.

To further probe the capabilities of the LES models, an inquiry was made into the ability of the LES to reproduce the FC-DNS irreversible entropy production, which is the dissipation. Not only is this information of scientific interest, as the dissipation has special characteristics uniquely related to the flow (Okong'o & Bellan 2002*b*, 2004*a*), but this information also has practical applications in that numerical methods have been based on entropy conservation (Honein & Moin 2004). Examined here were the contribution from each of its three modes: viscous, heat flux and species mass flux. The mass-flux mode being known to dominate the dissipation for these high-pressure conditions (Okong'o & Bellan 2002*b*; Okong'o, Harstad & Bellan 2002), the constant-coefficient SS model in conjunction with the pressure correction proved best.

As a general observation, at the transitional-Reynolds-number values of this study the pressure correction improved the LES predictions, but an even more considerable improvement is expected at higher Reynolds numbers, since experimental observations (see examples in Selle *et al.* 2007) show that the gradients in the HDGM regions can have a value by an order of magnitude higher than those in the present DNS database.

This study addressed only one of the additional (to the SGS flux) SGS models found necessary to reproduce in LES the features of the supercritical-pressure FC-DNS. For the OH system an equivalent term, the divergence of the difference between the filtered heat flux and the heat flux computed from the filtered solution, was found of leading order in the energy equation. A future study will address the *a posteriori* modelling of that term. For other species combinations, e.g. OHe, both the pressure and heat flux correction terms are apparently necessary (Selle *et al.* 2007), and a future *a posteriori* study will examine their impact on the fidelity of the LES compared with the FC-DNS.

Finally, the general methodology introduced here of using (other than SGS-flux) SGS models to enable the LES computation of single-phase flows having strong localized gradients could be extended to other applications.

HN600 t^*	x_1 momentum				x_2 momentum				x_3 momentum			
	25	50	100	135	25	50	100	135	25	50	100	135
$\frac{\partial}{\partial x_j}(\bar{\rho}\tilde{u}_i\tilde{u}_j)$	5.87	11.69	19.37	20.81	2.72	7.70	13.87	14.61	1.17	4.60	10.03	13.08
$\frac{\partial}{\partial x_i}[p(\bar{\phi})]$	4.39	11.61	14.73	13.19	11.02	17.71	20.92	18.38	8.88	14.73	18.70	16.07
$\frac{\partial}{\partial x_i}[\Delta(\bar{p})]$	2.44	9.12	11.13	9.93	10.83	16.54	17.20	15.65	8.83	13.91	17.17	13.82

$\Delta(\bar{f}) \equiv \overline{f(\phi)} - f(\bar{\phi})$

TABLE 8. Activity (r.m.s.) of the three leading-order terms in the momentum equation at $t^*=25$, 50, 100, 135 from the HN600 DNS. The computation was made with $\bar{\Delta} = 8\Delta x_{DNS}$. Units are 10^6 N m^{-3}.

Appendix A. Influence of LES ICs for constant-coefficient SGS-flux models

The ICs are subject to choice in LES, and there is still no consensus on an optimal such set. Here we wish to explore two IC aspects, namely whether it is best to choose the FC-DNS or CF-DNS as the IC, as discussed in §4, and whether it is more appropriate to use as LES IC the FC-DNS at $t^* = 0$ or at a later DNS time station, as also discussed in §4. The latter inquiry can be understood by examining table 8 listing the magnitude (computed using the domain root mean square, or r.m.s., which is related to the L2 norm) of the leading first three terms in the momentum equation using the DNS database and $\overline{\Delta} = 8\Delta x_{DNS}$, corresponding to the filter width used in the present LES. The listed magnitude is at $t^* = 25$, 50, 100 and 135. Examination of the table shows that the LES assumption on ∇p, namely the term $\nabla[\overline{p(\phi)} - p(\overline{\phi})]$, which motivated the p-correction model, is one of the two leading-order terms in the x_2 and x_3 components of the momentum equation at $t^* = 25$, and only at $t^* = 50$ it seems to be very slightly smaller than (although of the same order of magnitude as) the leading, $\nabla[p(\overline{\phi})]$, term. It is thus legitimate to doubt whether an approximation, such as embedded in the p correction, would be able to recover at the early times the prominent features of a flow dominated by this $\nabla[\overline{p(\phi)} - p(\overline{\phi})]$ effect. The success obtained with constant-coefficient LES starting from $t^* = 0$, as shown in §6.1, is testimonial to the robustness and accuracy of the p-correction model, but here we show that those were conservative results and that a much better agreement with the FC-DNS at $t^* = 135$ can be obtained if the LES is initiated with the FC-DNS at $t^* = 50$. This choice of IC at a time later than the DNS $t^* = 0$ time station was also the approach of Geurts & Frohlich (2002) even though that flow did not display the strong non-uniformities manifested here in the HDGM regions.

Figure 14 compares the time evolution of global quantities obtained from the DNS and the LES using different ICs along with FC-DNS. All LES runs are performed with the GRCP model using the coefficient of (6.2) and reveal the following. The $\delta_m/\delta_{\omega,0}$ of the LES initiated from CF-DNS conditions (CFDNS-IC0) follows the FC-DNS up to $t^* = 60$ after which it departs from the template and has slightly better agreement with it at $t^* = 135$ compared with the LES run initiated from FC-DNS conditions (FCDNS-IC0). In comparison, $\delta_m/\delta_{\omega,0}$ of the LES started from $t^* = 50$ (FCDNS-IC50) agrees considerably better with the FC-DNS. Similarly, E_K/E_0 obtained with both CFDNS-IC0 and FCDNS-IC50 agrees better with the FC-DNS data up to $t^* = 120$ when compared with that obtained with FC-DNS-IC0. As for the vorticity activity, FCDNS-IC0 and CFDNS-IC0 perform similarly, and they are inferior to FCDNS-IC50.
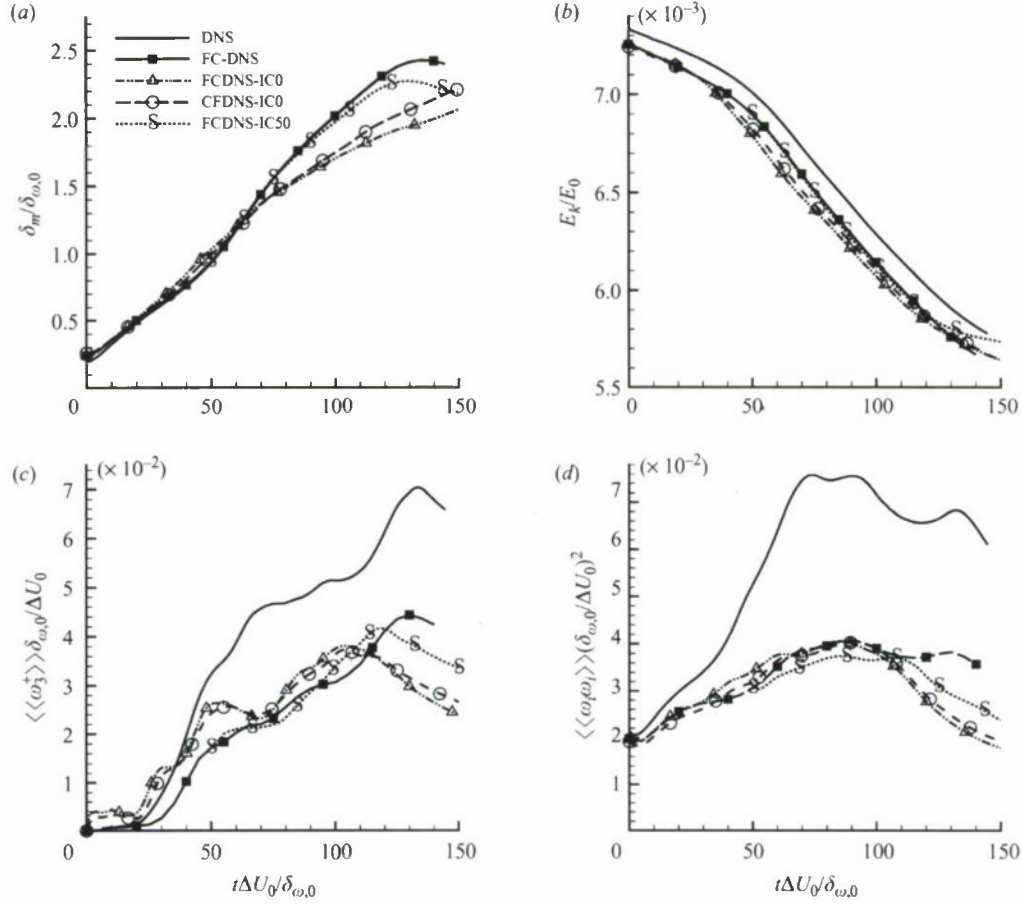
FIGURE 14. Time evolution of non-dimensional global quantities for HN600: (a) $\delta_m/\delta_{\omega,0}$, (b) E_K/E_0, (c) $\langle\langle\omega_3^+\rangle\rangle\delta_{\omega,0}/\Delta U_0$ and (d) $\langle\langle\omega_i\omega_i\rangle\rangle(\delta_{\omega,0}/\Delta U_0)^2$ for DNS, FC-DNS, LES initiated from FC-DNS at $t^* = 0$ (FCDNS-IC0 with GRCP), CF-DNS at $t^* = 0$ (CFDNS-IC0 with GRCP) and FC-DNS at $t^* = 50$ (FCDNS-IC50 with GRCP).

Companion flow visualizations of $|\nabla\rho|$, p/p_0 and Y_h, (not shown) for LES initiated from the FC-DNS conditions at $t^* = 0$, from the CF-DNS conditions at $t^* = 0$ and from the FC-DNS conditions at $t^* = 50$, along with the FC-DNS at $t^* = 135$, show that considering all three variables, FCDNS-IC50 produces the best match with the FC-DNS data. Also, p/p_0 and Y_h are slightly better predicted with CFDNS-IC0 than with FCDNS-IC0.

Thus, the results show that utilizing ICs at a time station past the largest pressure-gradient transients yields much more accurate LES results.

Appendix B. Influence of the grid size

The concept of grid convergence does not apply to LES because discretization errors, numerical errors and modelling errors are all intertwined as explained by Vreman, Geurts & Kuerten (1996a) and Meyer *et al.* (2003). For example, the discretization error depends not only on the numerical method but also on the choice of $\overline{\Delta}/\Delta x_{LES}$. What we wish to determine here is whether a finer LES grid

would be more beneficial in computing the HDGM regions, and if so, to what extent and at what cost. To investigate the grid choice, a finer-grid LES, with the grid having twice as many nodes in each direction, is performed, i.e. $\Delta x_{LES} = 2\Delta x_{DNS}$. Since $\overline{\Delta}/\Delta x_{LES}$ is kept at the same value, the filter size, $\overline{\Delta} = 4\Delta x_{DNS}$, is half of what it was for the coarse grid. This constant $\overline{\Delta}/\Delta x_{LES}$ strategy is preferred because the SGS p-correction model through the Taylor expansion is based on the assumption that $(\phi - \bar{\phi})$ is small. The GRCP model coefficient for the finer grid LES is the calibrated value at the DNS transitional time of 0.1346 (Selle *et al.* 2007). All calculations were started from the FC-DNS at $t^* = 0$.

The time evolution of global quantities (not shown) indicates that the fine grid solution has a better agreement with the filtered DNS in all four plots. For the fine-grid LES, both $\delta_m/\delta_{\omega,0}$ and E_K/E_0 decay are slightly overpredicted, and $\langle\langle\omega_3^+\rangle\rangle\delta_{\omega,0}/\Delta U_0$ and $\langle\langle\omega_i\omega_i\rangle\rangle(\delta_{\omega,0}/\Delta U_0)^2$ are slightly underpredicted. For comparison, the No Model LES solution with the finer grid yields reasonably good agreements with the DNS, indicating that there is no need for LES and SGS modelling at this resolution. Thus, at the fine resolution, the SGS model only represents an unnecessary computational overhead. No LES grid coarser than $\Delta x_{LES} = 4\Delta x_{DNS}$ (e.g. $\Delta x_{LES} = 8\Delta x_{DNS}$) has been attempted, since the accuracy of the initial profiles significantly deteriorates on coarser grids. The grid resolution is also dictated by the thickness of the HDGM regions

When analysing the $|\nabla\rho|$, p/p_0 and Y_h contour plots for the coarse grid and fine grid LES and for FC-DNS at the two $\overline{\Delta}$ widths corresponding to the coarse and fine grids (not shown), one observes that the FC-DNS at both fine and coarse filters displays $|\nabla\rho|$ and Y_h having very dense contour lines in narrow bands; this detail is not captured with the coarse-grid LES but is reproduced by the finer-grid LES.

Finally, the computational time requirement of the finer-resolution LES is 160 CPU hours computed as the aggregate over 64 parallel processors on an SGI Altix 3000 system. This is approximately 16 times more than that for the equivalent coarse-grid LES. Ultimately, the model user has the privilege of determining the grid size according to the objectives of the application.

Appendix C. Model evaluation using several realizations of the DNS database

Compared with HN600, the DNS realization HN500 displays HDGM regions which are thicker and more extensively spread over the domain, and the peak $|\nabla\rho|\delta_{\omega,0}/\Delta\rho_0$ (where $\Delta\rho_0 = \rho_1 - \rho_2$) at t_{tr}^* is smaller in magnitude. The DNS of HN800 exhibits a character different from HN500 or HN600 in that the peak $|\nabla\rho|\delta_{\omega,0}/\Delta\rho_0$ at t_{tr}^* is approximately twice that of HN500 and 60 % larger than that of HN600, and also because the HDGM regions are concentrated in a small region of the domain, and are smooth and relatively thin. However, $Re_{m,tr}$ for HN800 is similar to that of HN500 and only slightly smaller than that of HN600 (see table 3). Utilizing SSCP and MGRD in the LES to recover the FC-DNS for these two different realizations is a reasonable test of the LES model approach.

The LES conducted with each SSCP and MGRD required 13 CPU hours for HN500 and 12 CPU hours for HN800. In the SSCP model, the coefficient is taken to be the calibrated value obtained at the DNS transition time, $C_{SS} = 0.6260$ and $C_{SS} = 0.5870$ for HN500 and HN800, respectively; and $\hat{\Delta}/\bar{\Delta} = 2$, as for the HN600 LES. The global quantities $\delta_m/\delta_{\omega,0}$, E_K/E_0 $\langle\langle\omega_3^+\rangle\rangle\delta_{\omega,0}/\Delta U_0$ and $\langle\langle\omega_i\omega_i\rangle\rangle(\delta_{\omega,0}/\Delta U_0)^2$ presented in figure 15 show that the two LES models generally flank the corresponding FC-DNS, with SSCP generally overestimating and MGRD generally underestimating
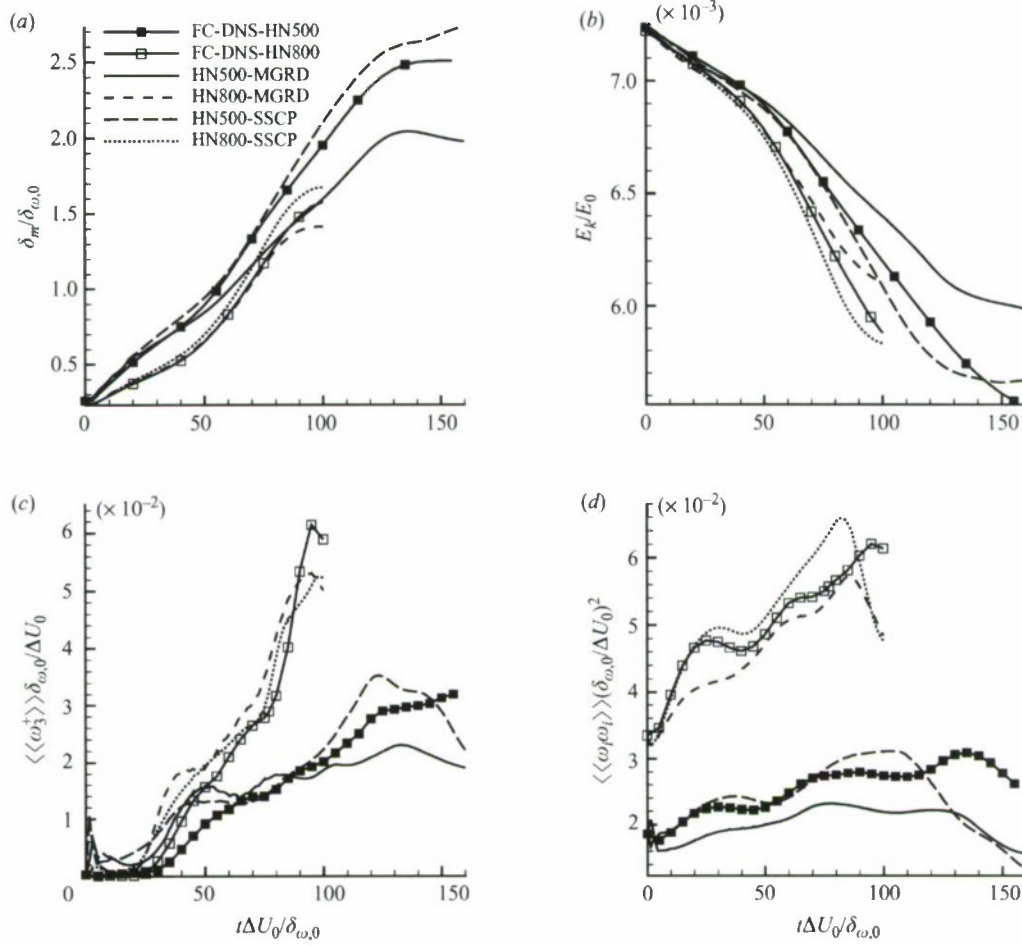
FIGURE 15. Time evolution of non-dimensional global quantities for HN500 and HN800: $(a)\delta_m/\delta_{\omega,0}$, (b) E_K/E_0, (c) $\langle\langle\omega_3^+\rangle\rangle\delta_{\omega,0}/\Delta U_0$ and (d) $\langle\langle\omega_i\omega_i\rangle\rangle(\delta_{\omega,0}/\Delta U_0)^2$ for FC-DNS and two LES models (MGRD and SSCP) both including the FOC model.

the target FC-DNS and with the SSCP consistently being a better approximation of the ideal objective. Of note is the tandem timewise path of SSCP and the FC-DNS for both $\langle\langle\omega_3^+\rangle\rangle\delta_{\omega,0}/\Delta U_0$ and $\langle\langle\omega_i\omega_i\rangle\rangle(\delta_{\omega,0}/\Delta U_0)^2$ until close to transition. The diverging MGRD LES from the FC-DNS is the result of the SM model contribution which, having dissipated energy excessively, makes the LES unable to sustain the small-scale necessary to promote further layer growth and the generation of vortical activity. Although the SSCP model agrees better with the FC-DNS template for all four quantities, it yields a larger positive vorticity peak for the HN500 case at the beginning of the simulation.

Complementary information in flow visualizations (not shown) of $|\nabla\rho|$, p/p_0 and Y_h comparing the LES with the FC-DNS indicates that for HN500 all $|\nabla\rho|$, p/p_0 and Y_h are better reproduced by MGRD than by SSCP. Particularly, for the SSCP model there are Y_h regions in the mixing layer in which fluid from the upper stream has been entrained and has not mixed with adjacent fluid, an occurrence which is not supported by the FC-DNS results. However, for HN800, the SSCP model is clearly

better duplicating than MGRD all $|\nabla\rho|$, p/p_0 and Y_h, including the entrained fluid from the upper stream which is being stirred into the mixing layer.

This necessarily limited application of the LES models to other realizations, spanning a range of Re values, brings some additional perspective and shows the models' robustness.

REFERENCES

BARDINA, J., FERZIGER, J. & REYNOLDS, W. 1980 Improved subgrid scale models for large eddy simulation. *Paper* 80-1357. AIAA.

BELLAN, J. 2006 Theory, modelling and analysis of turbulent supercritical mixing. *Combust. Sci. Technol.* **178**, 253–281.

BERSELLI, L. C., ILIESCU, T. & LAYTON, W. J. 2006 *Mathematics of Large Eddy Simulation of Turbulent Flows*. Springer.

CHEHROUDI, B., TALLEY, D. & COY, E. 1999 Initial growth rate and visual characteristics of a round jet into a sub- to supercritical environment of relevance to rocket, gas turbine and diesel engines. *Paper* 99-0206. AIAA.

CHOW, F. K. & MOIN, P. 2003 A further study of numerical errors in large-eddy simulations. *J. Comput. Phys.* **184**, 366–380.

CLARK, R., FERZIGER, J. & REYNOLDS, W. 1979 Evaluation of subgrid-scale models using an accurately simulated turbulent flow. *J. Fluid Mech.* **91** (1), 1–16.

GERMANO, M., PIOMELLI, U., MOIN, P. & CABOT, W. 1991 A dynamic subgrid-scale eddy viscosity model. *Phys. Fluids* A **3** (7), 1760–1765.

GEURTS, B. J. & FROHLICH, J. 2002 A framework for predicting accuracy limitations in large-eddy simulation. *Phys. Fluids* **14** (6), L41–L44.

GHOSAL, S. 1996 An analysis of numerical errors in large-eddy simulations of turbulence. *J. Comput. Phys.* **125**, 187–206.

HANNOUN, I. A., FERNANDO, H. J. S. & LIST, E. J. 1988 Turbulence structure near a sharp density interface. *J. Fluid Mech.* **189**, 189–209.

HARSTAD, K. & BELLAN, J. 1998 Isolated fluid oxygen drop behaviour in fluid hydrogen at rocket chamber pressures. *Intl J. Heat Mass Transfer* **41**, 3537–3550.

HARSTAD, K. & BELLAN, J. 2000 An all-pressure fluid-drop model applied to a binary mixture: heptane in nitrogen. *Intl J. Multiphase Flow* **26** (10), 1675–1706.

HARSTAD, K., MILLER, R. S. & BELLAN, J. 1997 Efficient high-pressure state equations. *AIChE J.* **43** (6), 1605–1610.

HIRSHFELDER, J., CURTIS, C. & BIRD, R. 1964 *Molecular Theory of Gases and Liquids*. John Wiley.

HONEIN, A. E. & MOIN, P. 2004 Higher entropy conservation and numerical stability of compressible turbulence simulations. *J. Comput. Phys.* **201**, 531–545.

KEIZER, J. 1987 *Statistical Thermodynamics of Nonequilibrium Processes*. Springer.

KENNEDY, C. & CARPENTER, M. 1994 Several new numerical methods for compressible shear layer simulations. *Appl. Numer. Math.* **14** 397–433.

LEBOISSETIER, A., OKONG'O, N. & BELLAN, J. 2005 Consistent large-eddy simulation of a temporal mixing layer laden with evaporating drops. Part 2. *A posteriori* modelling. *J. Fluid Mech.* **523**, 37–78.

LILLY, D. 1992 A proposed modification of the Germano subgrid-scale closure method. *Phys. Fluids* A **4** (3), 633–635.

LIU, S., MENEVEAU, C. & KATZ, J. 1994 On the properties of similarity subgrid-scale models as deduced from measurements in a turbulent jet. *J. Fluid Mech.* **275**, 83–119.

MAYER, W., SCHIK, A., SCHWEITZER, C. & SCHAFFLER, M. 1996 Injection and mixing processes in high pressure LOX/GH2 rocket combustors. *Paper* 96-2620. AIAA.

MAYER, W., IVANCIC, B., SCHIK, A. & HORNUNG, U. 1998 Propellant atomization in LOX/GH2 rocket combustors. *Paper* 98-3685. AIAA.

MEYER, J., GEURTS, B. J. & BAELMANS, M. 2003 Database analysis of errors in large-eddy simulation. *Phys. Fluids* **15** (9), 2740–2755.

MILLER, R., HARSTAD, K. & BELLAN, J. 2001 Direct numerical simulations of supercritical fluid mixing layers applied to heptane-nitrogen. *J. Fluid Mech.* **436**, 1–39.

MOIN, P., SQUIRES, K., CABOT, W. & LEE, S. 1991 A dynamic subgrid-scale model for compressible turbulence and scalar transport. *Phys. Fluids* **3** (11), 2746–2757.

MOSER, R. & ROGERS, M. 1991 Mixing transition and the cascade to small scales in a plane mixing layer. *Phys. Fluids* A **3** (5), 1128–1134.

MOSER, R. & ROGERS, M. 1993 The three-dimensional evolution of a plane mixing layer: pairing and transition to turbulence. *J. Fluid Mech.* **247**, 275–320.

MULLER, S. M. & SCHEERER, D. 1991 A method to parallelize tridiagonal solvers. *Par. Comput.* **17**, 181–188.

OEFELEIN, J. C. 2005 Thermophysical characteristics of shear-coaxial LOX-H_2 flames at supercritical pressure. *Proc. Combust. Inst.* **30**, 2929–2937.

OEFELEIN, J. C. & YANG, V. 1998 modelling high-pressure mixing and combustion processes in liquid rocket engines. *J. Propul. Power* **14**, 843–857.

OKONG'O, N. & BELLAN, J. 2000 Entropy production of emerging turbulent scales in a temporal supercritical n-heptane/nitrogen three-dimensional mixing layer. *Proc. Combust. Inst.* **28**, 497–504.

OKONG'O, N. & BELLAN, J. 2002a Consistent boundary conditions for multicomponent real gas mixtures based on characteristic waves. *J. Comput. Phys.* **176**, 330–344.

OKONG'O, N. & BELLAN, J. 2002b Direct numerical simulation of a transitional supercritical binary mixing layer: heptane and nitrogen. *J. Fluid Mech.* **464**, 1–34.

OKONG'O, N. & BELLAN, J. 2003 Real gas effects of mean flow and temporal stability of binary-species mixing layers. *AIAA J.* **41** (12), 2429–2443.

OKONG'O, N. & BELLAN, J. 2004a Consistent large eddy simulation of a temporal mixing layer laden with evaporating drops. Part 1. Direct numerical simulation, formulation and *a priori* analysis. *J. Fluid Mech.* **499**, 1–47.

OKONG'O, N. & BELLAN, J. 2004b Turbulence and fluid-front area production in binary-species, supercritical, transitional mixing layers. *Phys. Fluids* **16** (5), 1467–1492.

OKONG'O, N., HARSTAD, K. & BELLAN, J. 2002 Direct numerical simulations of O_2/H_2 temporal mixing layers under supercritical conditions. *AIAA J.* **40** (5), 914–926.

OSCHWALD, M. & SCHIK, A. 1999 Supercritical nitrogen free jet investigated by spontaneous Raman scattering. *Exp. Fluids* **27**, 497–506.

OSCHWALD, M., SCHIK, A., KLAR, M. & MAYER, W. 1999 Investigation of coaxial LN2/GH2-injection at supercritical pressure by spontaneous Raman scattering. *Paper* AIAA-99-2887. AIAA.

PAPAMOSCHOU, D. & ROSHKO, A. 1988 The compressible turbulent shear layer: an experimental study. *J. Fluid Mech.* **197**, 453–477.

POPE, S. B. 2004 Ten questions concerning the large-eddy simulation of turbulent flows. *New J. Phys.* **6**, 35–59.

PRAUSNITZ, J., LICHTENTHALER, R. & DE AZEVEDO, E. 1986 *Molecular Thermodynamics for Fluid-Phase Equilibrium*. Prentice-Hall.

PRUETT, C., SOCHACKI, J. & ADAMS, N. 2001 On Taylor-series expansions of residual stress. *Phys. Fluids* **13** (9), 2578–2589.

SARMAN, S. & EVANS, D. J. 1992 Heat flux and mass diffusion in binary Lennard-Jones mixtures *Phys. Rev.* A **45** (4), 2370–2379

SEGAL, C. & POLIKHOV, S. 2008 Subcritical to supercritical mixing. *Phys. Fluids* **20**, 052101-7.

SELLE, L. C., OKONG'O, N. A., BELLAN, J. & HARSTAD, K. G. 2007 modelling of subgrid scale phenomena in supercritical transitional mixing layers: an *a priori* study. *J. Fluid Mech.* **593**, 57–91.

SMAGORINKSY, J. 1963 General circulation experiments with the primitive equations. Part 1. basic experiments. *Mon. Weather Rev.* **91**, 99–164.

SMAGORINKSY, J. 1993 Some historical remarks on the use of nonlinear viscosities. In *Large Eddy Simulation of Complex Engineering and Geophysical Flows* (ed. B. Galperin & S. Orszag), chapter 1, pp. 3–36. Cambridge University Press.

SPEZIALE, C. G., ERLEBACHER, G., ZANG, T. A. & HUSSAINI, M. Y. 1988 The subgrid-scale modelling of compressible turbulence. *Phys. Fluids* A **31**, 940–942.

TENNEKES, H. & LUMLEY, J. L. 1989 *A First Course in Turbulence*. MIT Press.

VREMAN, B., GEURTS, B. & KUERTEN, H. 1996a Comparison of numerical schemes in large-eddy simulation of the temporal mixing layer. *Intl J. Num. Meth. Fluids* **22**, 297–311.

VREMAN, B., GEURTS, B. & KUERTEN, H. 1996b Large eddy simulation of the temporal mixing layer using the Clark model. *Theoret. Comput. Fluid Dyn.* **8**, 309–324.

VREMAN, B., GEURTS, B. & KUERTEN, H. 1997 Large-eddy simulation of the turbulent mixing layer. *J. Fluid Mech.* **339**, 357–390.

YOSHIZAWA, A. 1986 Statistical theory for compressible turbulent shear flows, with the application to subgrid modelling. *Phys. Fluids* **29** (7), 2152–2164.

ZANG, Y., STREET, R. L. & KOSEFF, J. R. 1993 A dynamic mixed subgrid-scale model and its application to turbulent recirculating flows. *Phys. Fluids* A **5**, 3186–3196.

ZONG, N., MENG, H., HSIEH, S.-Y. & YANG, V. 2004 A numerical study of cryogenic fluid injection and mixing under supercritical conditions. *Phys. Fluids* **16** (12), 4248–4261.

Appendix 2

Contents lists available at ScienceDirect

Computers & Fluids

Small-scale dissipation in binary-species, thermodynamically supercritical, transitional mixing layers

Nora Okong'o, Josette Bellan *

Jet Propulsion Laboratory, California Institute of Technology, 4800 Oak Grove Drive, M/S 125-109, Pasadena, CA 91109-8099, United States

ARTICLE INFO

ABSTRACT

The irreversible entropy production (i.e. the dissipation) has three distinct modes due to viscous, heat and species-mass fluxes. Computations of the dissipation and its modes are conducted using transitional states obtained from Direct Numerical Simulations (DNS) of O_2/H_2 and C_7H_{16}/N_2 temporal mixing layers at thermodynamically supercritical pressure. A non-dimensionalization of the mathematical expression for each dissipation mode is first performed and representative reference values computed using the DNS database are utilized to highlight the order of magnitude of each mode and their relative importance. For more quantitative results, the importance of each dissipative mode is assessed both at the DNS scale and at scales determined by filter sizes from four to sixteen times the DNS grid spacing. The subgrid-scale (SGS) dissipation is computed by subtracting the filtered-field dissipation from the DNS-field dissipation. For each species system, three layers are considered having different initial Reynolds number and perturbation wavelength. For all layers, it is found that the species-mass flux contribution dominates both the DNS and SGS dissipation due to high density-gradient-magnitude (HDGM) regions which are a distinctive physical aspect of these layers. Backscatter, indicated by regions of negative SGS dissipation, is found in a substantial portion (15–60%) of the domain, and decreases only slightly with increasing filter width. Regions of the most intense negative and positive SGS dissipation strongly correlate with the HDGM regions. On a domain-average basis, the proportional contribution of each dissipation mode to the total is similar at the DNS and SGS scales, indicating scale-similarity. The proportion of the species-mass dissipation mode to the total is remarkably similar in value across all simulations whether at the DNS or SGS scale. For each mode and the total, the SGS contribution to the DNS-field dissipation is only species-system and filter-size dependent but nearly independent of the initial Reynolds number and perturbation wavelength. The SGS contribution is smaller for O_2/H_2 layers than for C_7H_{16}/N_2 ones, but increases more rapidly with increasing filter width. The implications of these results for Larger Eddy Simulation modeling are discussed.

© 2010 Elsevier Ltd. All rights reserved.

1. Introduction

The dissipation is a crucial characteristic of a turbulent flow because it measures the conversion of all organized flow activity into heat.

In single-species atmospheric-pressure isothermal flows, the internal energy of the fluid is increased as a result of the kinetic energy dissipation into heat by the stress deformation work through the action of viscosity. In the conventional Kolmogorov concept this kinetic energy is cascaded from the largest scale to the small scales. This cascade is induced by the interaction of the vorticity field with the strain-rate: positive strain amplifies vorticity through stretching by the deformation work, while negative strain reduces it. Conceptually, a turbulent scale is associated with an

eddy [1]. The smaller eddies experience stretching by larger eddies, thereby increasing the energy of the smaller eddies at the expense of the larger eddies that must provide the work for the stretching. The Kolmogorov cascade process is not sequential because the energy from a specific scale is not only transmitted to the adjacent scale but also to all smaller scales, because all smaller eddies reside in the strain field of the larger eddy. Even this enlarged concept is an oversimplification of the real physics because locally in the flow, energy can also be transferred from the small to the large scales; this process is called backscatter. The backscatter energy is usually small compared to that of the cascade process, and thus the energy transfer in turbulent flows is dominated by the available energy in the large scales. This description of energy transfer among turbulent scales belongs to the classical literature in turbulence [1,2].

However, for more complex fluids and flows (i.e. multi-species, non-isothermal), the flow is governed by conservation equations more general than the Navier–Stokes equations; correspondingly,

* Corresponding author. Tel.: +1 818 354 6959; fax: +1 818 393 6682.
E-mail address: Josette.Bellan@jpl.nasa.gov (J. Bellan).

a more general description of dissipation is required that accounts for other transport properties than viscosity. Such a description is provided by considering the entropy transport equation rather than the kinetic energy transport equation. The advantage of the entropy equation is that its source term, called the irreversible entropy production, which is by definition is the dissipation [3], contains the full extent of the dissipative effects, particularly others than the classic viscous dissipation. Knowledge of the dissipation characteristics can be very valuable for understanding the behavior of the small-scale flow structure. Sreenivasan and Antonia [4] devoted an entire article to the intricacies of the small-scale structure in turbulence but due to the nature of the examined flows there were no considerations of flow thermodynamics.

The interest here is in turbulent flows in the thermodynamic supercritical regime defined as that in which either $p_r \equiv p/p_c > 1$ or $T_r \equiv T/T_c > 1$ where p is the pressure, T is the temperature and the subscript c denotes the critical point. This definition is semantically consistent with the classical definition for single species [3,7], with the utilization in the present study of a Peng–Robinson type real-gas Equation of State (EOS) and with recent experimental results [8] showing supercritical characteristics when either $p_r > 1$ or $T_r > 1$. Unlike in subcritical flows, in supercritical flows, thermodynamics plays a dominant role in the flow evolution and turbulence development [5,6]. The conceptual picture of turbulent flows described above has led to two simulation approaches, based on the conservation equations: (1) Direct Numerical Simulations (DNS) in which resolution of the smallest eddies, the size of which is of the order of the Kolmogorov scale, must be obtained and (2) Large Eddy Simulations (LES) in which only eddies larger than a specified filter width are resolved. Formally, the LES equations are derived by filtering the DNS equations and the effect of the thus removed subgrid scales (SGS) must be modeled. Understanding the small-scale dissipation can enlighten SGS modeling.

In this paper, we first non-dimensionalize the dissipation to examine the effects governing it. Then, we interrogate the DNS database of Okong'o and Bellan [5] and Okong'o et al. [6] to quantitatively assess the effects of species-dependent thermodynamics on the dissipation, which must be recovered in LES models. The effect of thermodynamics on the flow may be to change the distribution of small-scale activity to the extent that a new understanding may be necessary regarding the choice of the filter-to-LES grid ratio value to ensure that the SGS contributions are properly captured; the importance of this topic has already been realized and addressed for relatively simple flows [9,10]. There is no intent here to use the dissipation information to provide actual mathematical forms of the SGS fluxes, such as those already evaluated in Selle et al. [11], but rather to understand the important effects which must be modeled with increasing filter size. Indeed, the filter size is typically chosen as a multiple of the LES grid size [9,10], and practical applications require as coarse a grid size as possible to minimize computational costs.

This paper is organized as follows: in Section 2, we briefly recall the conservation equations, EOS and transport properties. Section 3 describes the DNS database. The entropy equation is presented in Section 4 and each of its modes is identified and analyzed through non-dimensionalization. Section 5 presents a quantitative study of the dissipation and devotes particular attention to the important topics of backscatter and filter size since larger filter sizes are associated with larger LES grid spacing. In Section 6, the consequences of the results are discussed.

2. Differential governing equations

A detailed description of the DNS methodology has been presented elsewhere for the C_7H_{16}/N_2 (HN) system [5,12] and for the O_2/H_2 (OH) system [6]; what follows is a succinct summary. The differential governing equations are the Navier–Stokes equations to which species and energy conservation equations have been coupled. For most generality, the ensemble of the differential governing equations have been derived using Keizer's [13] fluctuation-dissipation theory which is consistent with non-equilibrium thermodynamics, converges to kinetic theory in the low-pressure limit and relates fluxes and forces from first principles. Neglecting external forces, for a binary mixture, the conservation equations are

$$\frac{\partial \rho}{\partial t} + \frac{\partial(\rho u_i)}{\partial x_i} = 0, \tag{1}$$

$$\frac{\partial(\rho u_i)}{\partial t} + \frac{\partial(\rho u_i u_j + p\delta_{ij})}{\partial x_j} = \frac{\partial \sigma_{ij}}{\partial x_j}, \tag{2}$$

$$\frac{\partial(\rho Y_\alpha)}{\partial t} + \frac{\partial(\rho Y_\alpha u_i)}{\partial x_i} = -\frac{\partial j_{\alpha i}}{\partial x_i}, \quad \alpha = 1,2 \tag{3}$$

$$\frac{\partial(\rho e_t)}{\partial t} + \frac{\partial[(\rho e_t + p)u_i]}{\partial x_i} = -\frac{\partial q_{IKi}}{\partial x_i} + \frac{\partial \sigma_{ij}u_j}{\partial x_i}, \tag{4}$$

where t is time, $\mathbf{x}$ is the Cartesian coordinate system, ρ is the density, $\mathbf{u}$ is the velocity, Y_α is the mass fraction of species α with $Y_1 + Y_2 = 1$ for the binary species situation studied here, $\mathbf{j}_\alpha$ is the species α mass flux with $\mathbf{j}_1 + \mathbf{j}_2 = 0$, $e_t = e + u_i u_i/2$ is the total energy (i.e. internal energy, e, plus kinetic energy $e_k \equiv u_i u_i/2$), $\mathbf{q}_{IK}$ is the Irwing–Kirkwood (subscript IK) form of the heat flux vector (see Sarman and Evans [14]), and σ_{ij} is the Newtonian viscous stress tensor

$$\sigma_{ij} = 2\mu\left(S_{ij} - \frac{1}{3}S_{kk}\delta_{ij}\right) \tag{5}$$

where μ is the viscosity,

$$S_{ij} = \frac{1}{2}\left(\frac{\partial u_i}{\partial x_j} + \frac{\partial u_j}{\partial x_i}\right) \tag{6}$$

is the strain rate, and δ_{ij} is the Kronecker delta function. The species-mass flux and heat flux are given by

$$\mathbf{j}_2(\psi) = B_Y(\psi)\nabla Y_2 + B_T(\psi)\nabla T + B_P(\psi)\nabla p, \tag{7}$$

$$\mathbf{q}_{IK}(\psi) = C_Y(\psi)\nabla Y_2 + C_T(\psi)\nabla T + C_P(\psi)\nabla p \tag{8}$$

where ψ is the vector of primitive variables,

$$B_Y \equiv -\rho D\alpha_D, \quad C_Y \equiv -\rho D\alpha_D\alpha_{IK}R_u T\frac{m}{m_1 m_2}, \tag{9}$$

$$B_T \equiv -\alpha_{BK}Y_1 Y_2\frac{\rho D}{T}, \quad C_T \equiv -\lambda - \rho D\alpha_{IK}\alpha_{BK}R_u\frac{m}{m_1 m_2}Y_1 Y_2, \tag{10}$$

$$B_P \equiv -\rho D\frac{Y_1 Y_2}{R_u T}\frac{m_2 m_1}{m}\Lambda, \quad C_P \equiv -\rho D\alpha_{IK}\Lambda Y_1 Y_2, \tag{11}$$

D is the binary mass diffusion coefficient, m_α is the molar mass of species α, $m = m_1 X_1 + m_2 X_2$ is the mixture molar mass where the molar fraction is $X_\alpha = mY_\alpha/m_\alpha$, R_u is the universal gas constant and

$$\alpha_{BK} = \alpha_{IK} - \alpha_h, \quad \alpha_h = \frac{1}{R_u T}\frac{m_2 m_1}{m}\Theta, \tag{12}$$

$$\Lambda \equiv \left(\frac{1}{m_2}\frac{\partial v}{\partial X_2} - \frac{1}{m_1}\frac{\partial v}{\partial X_1}\right), \quad \Theta \equiv \left(\frac{1}{m_2}\frac{\partial(mh)}{\partial X_2} - \frac{1}{m_1}\frac{\partial(mh)}{\partial X_1}\right), \tag{13}$$

$$\alpha_D \equiv 1 + X_\alpha\frac{\partial \ln \gamma_\alpha}{\partial X_\beta} \tag{14}$$

where λ is the thermal conductivity with $\lim_{p\to 0}\lambda = \lambda_{KT}$ as discussed in Ref. [15] where subscript KT denotes the kinetic theory, $v = m/\rho$, h is the molar enthalpy and γ_α is the fugacity. Furthermore, α_{IK} is the IK form of the thermal diffusion factor, α_{BK} is the Bearman–Kirkwood (BK) form of the thermal diffusion factor and α_D is the mass diffusion factor. The thermal diffusion factor is

associated with Soret effects in the species conservation equations and Dufour effects in the energy equation.

3. Description of DNS database

The database consists of supercritical temporal mixing layer simulations of the two HN and OH binary mixtures. The pure species properties are listed in Table 1. The configuration, initial and boundary conditions, EOS, transport property relations and numerical method are summarized below. The initial conditions have been varied to encompass the two binary-species systems listed above, several Reynolds number values, different free-stream temperature values and several domain sizes. While the study on the initial conditions is not exhaustive due to the very large DNS CPU time and many meaningful initial conditions possibilities, it does highlight the important processes at play. We also discuss below the accuracy of the database and why this transitional database has relevance for fully turbulent flows.

3.1. Configuration, initial and boundary conditions

The configuration is illustrated in Fig. 1 for OH, as an example, showing the streamwise (x_1), cross-stream (x_2) and spanwise (x_3) coordinates. The temporal mixing layer is not symmetric in extent in the x_2 direction, to accommodate the larger layer growth in the lighter fluid side. For each layer, species 1 and 2 listed in Table 2 initially reside in the upper and lower stream, respectively. The free-stream density (ρ_1 or ρ_2) was calculated for each pure species at its free-stream temperature (T_1 or T_2) and at the initial uniform pressure (p_0) using the EOS. Initially, each layer hosts four spanwise vortices which are induced through a double pairing to merge into an ultimate vortex. The vorticity thickness was defined as $\delta_\omega(t) = \Delta U_0/(\partial\langle u_1\rangle/\partial x_2)_{max}$, where $\langle u_1\rangle$ is the (x_1,x_3) planar average of the streamwise velocity, and $\Delta U_0 = U_1 - U_2$ is the initial velocity difference across the layer. U_1 and U_2 were chosen with the intent of keeping the ultimate vortex stationary in the computational domain [12,16]; the specification of the convective Mach number, $M_{c,0}$, determines ΔU_0. Given the initial streamwise velocity profile u_1 based on U_1 and U_2, $(\partial\langle u_1\rangle/\partial x_2)_{max}$ and hence $\delta_{\omega,0} \equiv \delta_\omega(0)$ were calculated. The initial momentum ratio $|\rho_2 U_2|/|\rho_1 U_1| \sim 5$ for all HN and OH simulations and it is determined by the prescribed free-stream pressure, the chosen T_1 and T_2 (for HN cases it approximates conditions in gas turbine engines and for OH cases it is determined by the largest ρ_2/ρ_1 value that can be resolved in DNS [6]), the specified value of $M_{c,0}$ and the requirement that the ultimate vortex should be approximately steady in the computational domain. The momentum flux ratio $(\rho_2 U_2^2)/(\rho_1 U_1^2)$ is 1.0 for all OH layers and 2.2 for all HN layers. Therefore, from a certain viewpoint, the HN cases present a perspective on what can be expected for OH at larger momentum flux ratios which can reach values as large as 14 in liquid rocket engines [17]; the value of the momentum flux ratio plays a dominant role in jet disintegration [17]. The specified value of the initial flow Reynolds number, $Re_0 = (1/2)(\rho_1 + \rho_2)\Delta U_0\delta_{\omega,0}/\mu_R$, chosen so as to enable the resolution of all relevant length scales, was then used to calculate μ_R, which scales μ as shown in Table 3. The grid spacing was an
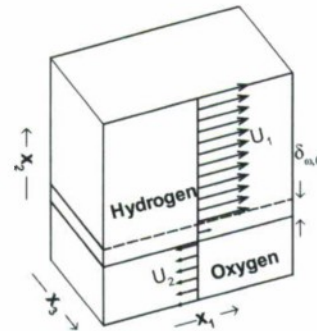

Fig. 1. Sketch of the O_2/H_2 mixing layer configuration.

approximately linear function of Re_0, suggested by the relationship $l/\eta_K \sim Re^{3/4}$ [1] where l is the integral scale and η_k is the Kolmogorov scale.

The simulations were started with error-function profiles for the mean streamwise velocity, mass fraction and temperature, upon which are imposed spanwise and streamwise vorticity perturbations [18,19] of strengths F_{2D} and F_{3D}, respectively, having streamwise (λ_1) and spanwise (λ_3) wavelengths $\lambda_1 = C\delta_{\omega,0}$ and $\lambda_3 = 0.6\lambda_1$, where $C = 7.29$ is the most unstable wavelength for incompressible flow. For the simulations reported here, the initial conditions are listed in Table 2 showing also other values of C used that were obtained from stability analyses [20]: $C = 4.57$ for the shortest (estimated) unstable wavelength for the HN layer, or C corresponding to the most unstable wavelength for OH layers. The grid was chosen for all simulations so as to accommodate four wavelengths in the streamwise and spanwise directions, and the evolution of the layer encompassed roll-up and two pairings of the four initial spanwise vortices into an ultimate vortex.

The boundary conditions were periodic in the streamwise and spanwise directions, and of outflow type for real gas in the cross-stream direction, as derived by Okong'o and Bellan [21]. The outflow type conditions were essential to maintain numerical stability since the initial perturbation induced large pressure waves that had to exit the domain with minimal reflection.

3.2. Equation of state

The pressure was calculated from the well-known Peng-Robinson (PR) EOS, given T and the PR molar volume (v_{PR}), as

$$p = \frac{R_u T}{(v_{PR} - b_m)} - \frac{a_m}{(v_{PR}^2 + 2b_m v_{PR} - b_m^2)}, \qquad (15)$$

where a_m and b_m are functions of T and X_α with a mathematical form given in detail in Refs. [12,6]. At high pressures, v_{PR} may differ significantly from the actual molar volume v [7]. Both v_{PR} and the volume shift ($v_S = v - v_{PR}$) can be calculated from the PR EOS given p, T and X_α [22], although for the HN system v_S is negligible. All thermodynamic quantities, including α_D, h, $C_p = (\partial h/\partial T)_{p,X}$ and the speed of sound $\langle a_s\rangle$, were calculated from the EOS using standard thermodynamic relations [12,5,6]. The implementation of the EOS to calculate p and T from ρ, e and Y_α utilized an iterative scheme [6] for OH, and an energy fit [5] for HN.

3.3. Transport coefficients

The viscosity, the Schmidt number ($Sc = \mu/(\rho\alpha_D D)$) and the Prandtl number ($Pr = \mu C_p/(m\lambda)$) were calculated from high-pressure single-species transport properties using mixing rules, as in Ref. [23]. The calculated values were correlated, as summarized in

Table 1
Pure species properties; v_c is the molar volume at the critical point.

Species	m (g/mol)	T_c (K)	p_c (MPa)	v_c(cm^3/mol)
H_2	2.016	33.0	1.284	64.3
N_2	28.013	126.3	3.399	89.8
O_2	31.999	154.6	5.043	73.4
C_7H_{16}	100.205	540.2	2.74	432.0

Table 2

Listing of the simulations and associated resolution for O_2/H_2 (OH) and C_7H_{16}/N_2 (HN) mixing layers. L_i is the size of the domain in the x_i direction, in meters. For all layers, $L_1 = 4\lambda_1$, $\delta_{\omega,0} = 6.859 \times 10^{-3}$ m and $F_{2D} = 0.1$. Temperatures are in degrees K. The subscript tr denotes the transitional time. The grid size is $352 \times 352 \times 208$ for all OH DNS, $240 \times 288 \times 144$ for HN500 and HN800 and $288 \times 336 \times 176$ for the HN600 DNS. The CPU time is based on an SGI Origin2000 300 MHz R12000 processor.

Run	Re_0	$T_2 : T_1$	ρ_2/ρ_1	$\lambda_1/\delta_{\omega,0}$	F_{3D}	$L_1 \times L_2 \times L_3$	$Re_{m,tr}$	t_{tr}^*	CPU (h)
OH500	500	235; 287	24.51	10.61	0.025	$0.291 \times 0.291 \times 0.1746$	1772	290	14,557
OH550	550	400; 600	24.40	10.35	0.025	$0.284 \times 0.284 \times 0.17$	1907	270	14,497
OH750	750	400; 600	24.40	7.29	0.05	$0.2 \times 0.2 \times 0.12$	1507	150	10,349
HN500	500	600; 1000	12.88	7.29	0.05	$0.2 \times 0.232 \times 0.12$	1250	155	1714
HN600	600	600; 1000	12.88	7.29	0.05	$0.2 \times 0.232 \times 0.12$	1452	135	5156
HN800	800	600; 1000	12.88	4.57	0.05	$0.125 \times 0.148 \times 0.075$	1258	100	1916

Table 3

Transport properties for binary mixtures. The reference temperature is $T_R = (T_1 + T_2)/2$, T in Kelvin; Y_O is the O_2 mass fraction, Y_h is the C_7H_{16} mass fraction.

System	C_7H_{16}/N_2	O_2/H_2
$\mu = \mu_R(T/T_R)^N$	$N = 0.7$	$N = 0.75$
$Sc \equiv \mu/(\rho\alpha_0 D)$	$1.5 - Y_h$	$(1.334 - 0.668Y_O - 0.186Y_O^2$ $-0.268Y_O^6)[1 + (88.6/T)^{1.5}]$
$Pr \equiv \mu C_p/(m\lambda)$	$0.5Sc/\exp(-1.5Y_h)$	$1.335/T^{0.1}$
α_{IK} or α_{BK}	$\alpha_{IK} = 0.1$ (Ref. [15])	$\alpha_{BK} = 0.2$ (Refs. [23,24])
T range	500–1100 K	200–800 K
p range	40–80 atm	~100 atm

Table 3, and these correlations were then used to compute the transport properties μ, D and λ. The relationship between α_{BK} and α_{IK} stated in Eq. (12) means that either one can be specified, and the other then calculated.

3.4. Numerical simulation characteristics

The conservation equations were numerically solved using a fourth-order explicit Runge–Kutta time integration and a sixth-order compact scheme with eighth-order filter for spatial derivatives [25]; the filtering (applied at interior points only) is required to maintain numerical stability for long-time integrations but since it acts only on the shortest waves that can be resolved on the grid, it does not act as a turbulence model allowing under-resolved computations. The computations were parallelized using three-dimensional domain decomposition and message passing, and an efficient parallel tridiagonal solver [26].

3.5. Relevance of the database to understanding fully turbulent flows

The database analyzed is summarized in Table 2, including the transitional time $t_{tr}^* = t_{tr}\Delta U_0/\delta_{\omega,0}$ and the value of the momentum-thickness based Reynolds number, $Re_m = Re_0\delta_m/\delta_{\omega,0}$ at transition. Time t_{tr} is that at which the one-dimensional velocity-fluctuation-based energy spectra become smooth, except for the forcing frequency, and δ_m is the momentum thickness which is mathematically defined in Ref. [5]. The resolution is such that the grid spacing was uniform in each direction with $\Delta x_1 \simeq \Delta x_2 \simeq \Delta x_3$; by definition $\Delta x = \max\{\Delta x_i\}$. The differing thermodynamics of the two species systems precluded matching of the initial density stratification (ρ_2/ρ_1) or of the transitional momentum thickness [6,20] within the regimes of practical interest, since there is no simple relationship between the initial conditions and the transitional state. As a result, the OH layers exhibited higher Re_m values at the transitional state, $Re_{m,tr}$, than the HN layers. Results from the database can be compared either for same species but at different $Re_{m,tr}$ (HN or OH layers), or same species and same $Re_{m,tr}$ (HN500, HN800), or different species and same $Re_{m,tr}$ (HN600, OH750).

Only the transitional states are here analyzed, as being the states displaying turbulent characteristics. As discussed in Miller et al. [12], Okong'o and Bellan [5], Okong'o et al. [6] and Selle et al. [11], the most specific feature of the transitional states are high density-gradient magnitude (HDGM) regions prominent throughout the mixing layer, shown in Fig. 2. Animations of the $|\nabla\rho|$ evolution from the initial state to transition showed the HDGM regions to form due to both species molecular mixing and the distortion of the initial $\nabla\rho$ boundary. While the HN layers had lower initial ρ_2/ρ_1, they had higher density-gradient magnitude $|\nabla\rho|\delta_{\omega,0}/\Delta\rho_0$ (where $\Delta\rho_0 = \rho_1 - \rho_2$) at the transitional state, depicted in Fig. 2, due to their higher mixture non-ideality [27] which impeded molecular mixing; in our terminology, stronger HDGM regions are those having higher $|\nabla\rho|\delta_{\omega,0}/\Delta\rho_0$ values. Quantitative evidence from three experiments with different species was presented in Selle et al. [11] indicating that the HDGM regions are not a peculiar aspect of transitional states, but exist with similar or even larger gradient magnitudes under fully turbulent conditions (the experimental data was for $Re = O(10^4) - O(10^5)$). Thus, examination of these transitional states should yield results entirely applicable to fully turbulent flows. This conclusion was additionally supported by the significant portion of domain turbulent kinetic energy that resides in the subgrid scales. An evaluation of the turbulent kinetic energy (TKE) based on filtered velocity fluctuations showed for a filter size $\Delta = 4\Delta x$ that up to 9.03% of the TKE resides in the small scales; the equivalent value for fluctuations based on the Favre averaged velocity was 10.63%. When the filter size increases by a factor of 2 to $\Delta/\Delta x = 8$, the corresponding fraction of the TKE in the small scales increases by more than a factor of 2.5 and at given $\Delta/\Delta x$, the TKE portion residing in the subgrid scales is smaller with increasing Re_0.

Our estimate (not shown) is that Δx is about three times η_k, and about twice the Batchelor scale, η_B. Despite not resolving η_k, the simulations in the database still qualify as DNS because the one-dimensional velocity-fluctuation-based energy spectra show no accumulation of energy at the smallest scales [5,6]. Indeed, Moin and Mahesh [28] point out that the requirement $\Delta x < \eta_k$ would be too constraining because physically it is sufficient to resolve the scales at which the overwhelming amount of dissipation occurs, which are only $O(\eta_k)$; additionally, the value of η_k is only defined through a dimensional argument, is subject to a choice in the averaging process entering its definition, and is thus not exact. Since $\Delta x \simeq 3\eta_k$, for $\Delta = 16\Delta x$ one obtains $\Delta/\eta_k = 48$, which according to Pope [29] means that even for the largest Δ value considered here, filtering is performed well within the dissipation range ($60\eta_k$ is the beginning of the inertial range [29]).

4. The entropy equation

Consider a single-phase flow that is a mixture of two chemical species which were initially at different temperatures. According to Okong'o and Bellan [30], the entropy equation for this flow is

$$\frac{\partial(\rho s)}{\partial t} + \frac{\partial(\rho s u_j)}{\partial x_j} = -\frac{\partial \Sigma_j}{\partial x_j} + g_{tot} \tag{16}$$
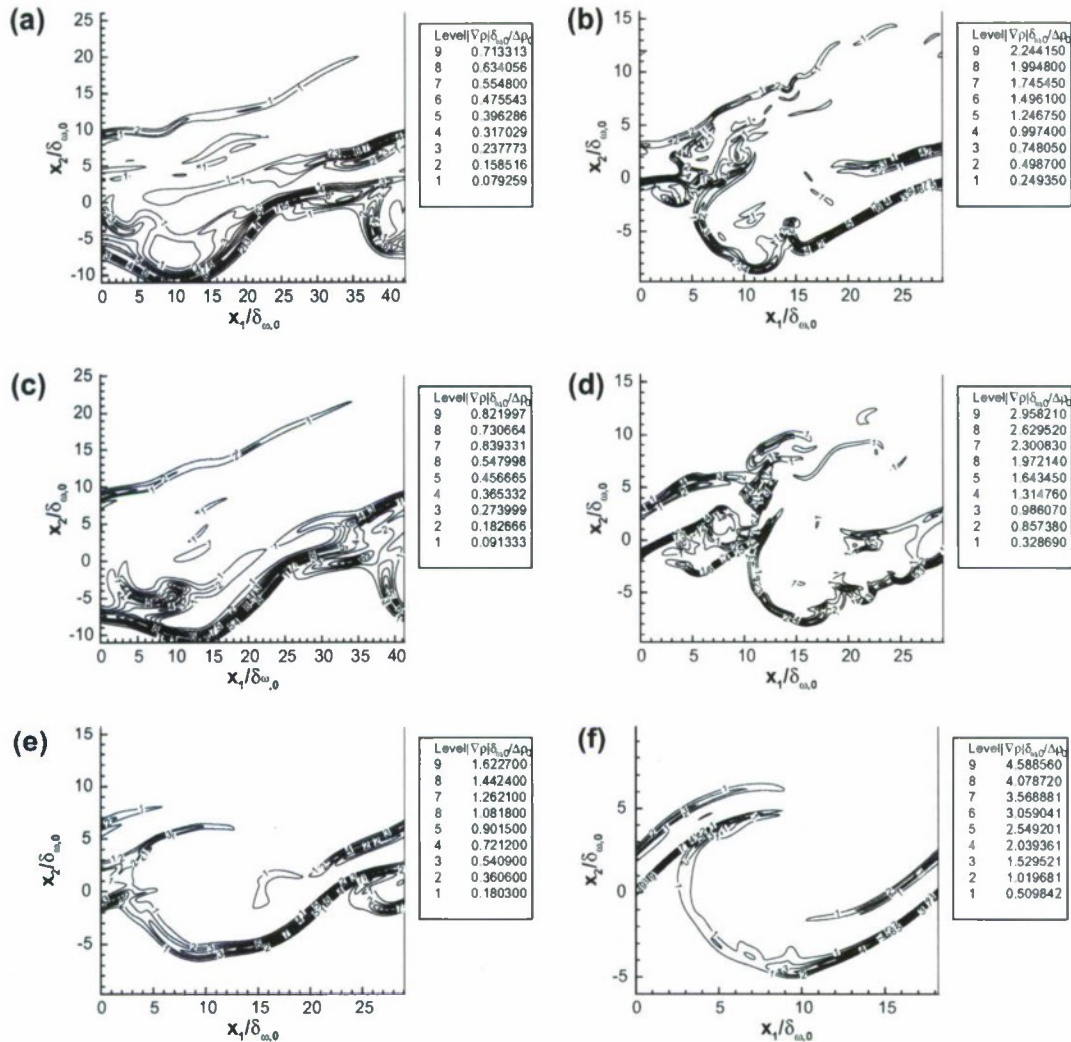
Fig. 2. Density gradient magnitude $|\nabla\rho|\delta_{\omega,0}/\Delta\rho_0$, where $\Delta\rho_0 = \rho_1 - \rho_2$, for (a) OH500, (b) HN500, (c) OH550, (d) HN600, (e) OH750 and (f) HN800: in the braid plane ($x_3 = L_3/16$).

which is derived from conservation of mass (Eq. (1)), momentum (Eq. (2)), species (Eq. (3)) and total energy (Eq. (4)), along with the thermodynamic relation

$$T\frac{Ds}{Dt} = \frac{De}{Dt} + p\frac{D(1/\rho)}{Dt} - \sum_{\alpha=1}^{N}\frac{\mu_\alpha}{m_\alpha}\frac{DY_\alpha}{Dt} \qquad (17)$$

where D/Dt is the substantial derivative and μ_α are the chemical potentials. In Eq. (16), s is the entropy per unit mass, Σ_j represents the reversible flux of entropy and g_{tot} is the rate of irreversible entropy production which is the dissipation. Also in Ref. [30], it was shown that the dissipation, g_{tot}, is the sum of three terms, each corresponding to a dissipation mode

$$g_{tot} = g_{visc} + g_{temp} + g_{mass}, \qquad (18)$$

with

$$g_{visc} = \frac{\mu}{T}2\left(S_{ij} - \frac{1}{3}S_{kk}\delta_{ij}\right)^2, \quad g_{temp} = \frac{\lambda}{T^2}\frac{\partial T}{\partial x_i}\frac{\partial T}{\partial x_i},$$

$$g_{mass} = \frac{1}{Y_1Y_2\rho D}\frac{R_u m}{m_1 m_2}j_{2i}j_{2i}, \qquad (19)$$

where g_{visc}, g_{temp} and g_{mass} represent contributions from the viscous, heat and mass fluxes, respectively. Different g_{tot} modes may be more prominent in various situations. For example, Okong'o and Bellan [31] have shown that in a compressible atmospheric-pressure transitional shear layer, g_{tot} is dominated by g_{visc}, with negligible g_{temp}. However, unlike for atmospheric-pressure turbulent flows, in situations where $p > p_c$ and under transitional-flow conditions, g_{tot} was shown to be dominated by g_{mass} with moderate contribution from g_{temp} and negligible portion from g_{visc}; this situation prevailed for each HN layers [5] and OH layers [6] both at the DNS scale and a filter size $\Delta = 4\Delta x$. By definition,

$$g_k^{SGS} = g_k(\phi) - g_k(\overline{\phi}) \qquad (20)$$

where $\overline{\phi}$ is the filtered vector of conservative variables, and k is tot, visc, temp or mass, having defined the spatial filtering operation for any function ψ as

$$\overline{\psi}(\vec{x}) = \int_V \psi(\vec{y})G(\vec{x} - \vec{y})\,d\vec{y} \qquad (21)$$

where G is the filter function and V is the filtering volume. Since the LES goal is to compute $\overline{\phi}$ at the points of the LES grid, an ideal LES solution is $\overline{\phi}$ computed from the DNS field ϕ.

Because considerations based on small-scale irreversible entropy production are not typical, it is enlightening to consider their relationship to the typical concept of energy dissipation. Given that unfiltered, filtered and density-weighted-filtered (Favre-filtered) quantities may be available, there are various manners in which SGS quantities may be defined. To clarify the connection between kinetic energy and entropy, the kinetic energy transport equation, derived from the conservation of mass (Eq. (1)) and momentum (Eq. (2)) is considered:

$$\frac{\partial(\rho e_k)}{\partial t} + \frac{\partial(\rho e_k u_j)}{\partial x_j} = -\frac{\partial}{\partial x_j}(pu_j - \sigma_{ij}u_j) + \left(p\frac{\partial u_j}{\partial x_j} - \sigma_{ij}\frac{\partial u_i}{\partial x_j}\right) \qquad (22)$$

where

$$\sigma_{ij}\frac{\partial u_i}{\partial x_j} = 2\mu\left(S_{ij} - \frac{1}{3}S_{kk}\delta_{ij}\right)^2 = Tg_{visc}. \qquad (23)$$

By tracing the origin of the entropy dissipation terms, it is clear that the kinetic-energy viscous-dissipation and the entropy viscous-dissipation are the same, save for the $(1/T)$ factor.

Analogous to Eq. (22) is the equation for the resolved kinetic energy $\epsilon_k = \tilde{u}_i\tilde{u}_i/2$:

$$\frac{\partial(\bar{\rho}\epsilon_k)}{\partial t} + \frac{\partial(\bar{\rho}\epsilon_k\tilde{u}_j)}{\partial x_j} = -\frac{\partial}{\partial x_j}(\bar{p}\tilde{u}_j - \bar{\sigma}_{ij}\tilde{u}_i + \bar{\rho}\tau_{ij}\tilde{u}_i)$$
$$+ \left(\bar{p}\frac{\partial\tilde{u}_j}{\partial x_j} - \bar{\sigma}_{ij}\frac{\partial\tilde{u}_i}{\partial x_j} + \bar{\rho}\tau_{ij}\frac{\partial\tilde{u}_i}{\partial x_j}\right) \qquad (24)$$

where $\tilde{u}_i = \overline{\rho u_i}/\bar{\rho}$ and $\tau_{ij} = \widetilde{u_iu_j} - \tilde{u}_i\tilde{u}_j$ is the SGS-flux for momentum. The SGS fluxes may be interpreted as augmenting or attenuating the effect of the viscous stresses. That is, their role is to transfer energy to the smaller scales, as is in the conceptual picture presented in Section 1. One may then draw an analogy between the kinetic-energy viscous-dissipation, entropy viscous-dissipation and SGS-flux viscous-dissipation.

Non-dimensionalization of Eq. (19) elucidates salient aspects of the g_k modes. By defining reference quantities (subscript R) based on characteristic values and non-dimensional quantities (superscript *):

$$x_j^* = x_j/L_R, t^* = t/t_R, t_R = L_R/U_R, \qquad (25)$$

$$\rho^* = \rho/\rho_R, u_j^* = u_j/U_R, T^* = T/T_R, \qquad (26)$$

$$j_{2j}^* = j_{2j}/(\rho_R U_R), D^* = D/(U_R L_R), \qquad (27)$$

$$g^* = g/g_R, \qquad (28)$$

with the reference Mach number, Ma_R and other non-dimensional quantities

$$Ma_R = U_R/a_{sR}, \qquad (29)$$

$$Re_R = (\rho_R U_R L_R)/\mu_R, \qquad (30)$$

$$Pr_R = (C_{pR}\mu_R)/(m_R\lambda_R), \qquad (31)$$

$$g_R = (\rho_R U_R^3)/(L_R T_R) \qquad (32)$$

one obtains

$$g_{tot}^* = g_{visc}^* + g_{temp}^* + g_{mass}^*, \qquad (33)$$

$$g_{visc}^* = \left(\frac{1}{Re_R}\right)\left[2\mu^*\frac{1}{T^*}\left(S_{ij}^* - \frac{1}{3}S_{kk}^*\right)^2\right], \qquad (34)$$

$$g_{temp}^* = \left(\frac{1}{Re_R Pr_R}\right)\frac{1}{Ma_R^2}\left(\frac{C_{pR}T_R}{m_R a_{sR}^2}\right)\left[\lambda^*\frac{1}{(T^*)^2}\frac{\partial T^*}{\partial x_j^*}\frac{\partial T^*}{\partial x_j^*}\right], \qquad (35)$$

$$g_{mass}^* = \frac{1}{Ma_R^2}\left(\frac{R_u T_R}{m_R a_{sR}^2}\right)\left[\frac{1}{\rho^* D^* Y_1 Y_2}\frac{m}{m_1}\frac{m}{m_2}\frac{m_R}{m}j_{2i}^* j_{2i}^*\right]. \qquad (36)$$

For a perfect gas, $(R_u T)/(ma_s^2) = 1/\gamma$ and $(C_p T)/(ma_s^2) = 1/(\gamma - 1)$, where $\gamma = C_p/C_v$. For a real gas, these quantities are calculated from the EOS. The values of the coefficients appearing in Eqs. (34)–(36)

are listed for the present DNS database in Table 4; for the present mixing layers, $M_{c,0}$ and the flow thermodynamics (i.e. ρ, a_s) determine the free-stream velocities (see [20]). The reference quantities (except U_R) are computed at the interface of the two streams i.e., at $x_2 = 0$. The goal of non-dimensionalization with characteristic values is to render the non-dimensional quantities O(1), which implies that the quantities in square brackets (involving starred quantities) of Eqs. (34)–(36) are of O(1). Then

$$\frac{g_{visc}^*}{g_{temp}^*} = O\left(Pr_R Ma_R^2\frac{m_R a_{sR}^2}{C_{pR}T_R}\right), \frac{g_{mass}^*}{g_{temp}^*} = O\left(Pr_R Re_R\frac{R_u}{C_{pR}}\right). \qquad (37)$$

Using Eqs. (32)–(37) and Table 4 we anticipate that: (i) For the DNS database, the Re_R effect will be minor, since Re_R^{-1} varies by at most a factor of 2. (ii) For fully turbulent flow Re_R values, the $O(Re_R^{-1})$ dependence of g_{visc}^* and g_{temp}^* makes their values much smaller than g_{mass}^* providing $Ma_R \sim O(1) - O(10)$ and $(R_u T_R/(m_R a_{sR}^2)) \sim O(1)$ (see Eqs. (34) and (36)), and $(Pr_R R_u/C_{pR})$ is not $\ll 1$ (see Eq. (37)). (iii) The $O(Ma_R^2)$ dependence of g_{temp}^* implies that for $Ma_R \sim O(1)$ one obtains $g_{temp}^* \sim g_{visc}^*$, however, if $Ma_R \ll 1$, then $g_{temp}^* > g_{visc}^*$ (see Eq. (37)). (iv) For the DNS database, OH layers will have larger dissipation due to their larger g_R values (see Eq. (32) and Table 4). (v) Considering the present DNS database, the g_{temp} contribution to g_{tot} will be relatively more important for HN layers compared to the g_{mass} contribution, due to their larger C_{pR}/R_u value (see Eq. (37) and Table 4).

While this non-dimensionalization brings insight into the relative importance of the g_k's to g_{tot}, it is clear that only an analysis of results derived from the database will reveal the relative importance of the three dissipation modes; this is particularly true for the small-scale dissipation and its dependence on the scale at which it is computed.

5. Results

General results are first presented leading to a deeper understanding of the species-specific origins of g_{tot} and its impact on the flow characteristics. The analysis then focusses exclusively on g_k^{SGS} particularly emphasizing backscatter and filter-size effects. Because the PR EOS cannot be written in a canonical form where it is only function of the reduced thermodynamic quantities $(v/v_c, T/T_c, p/p_c)$ [7], the EOS does not obey the corresponding states principle and is not the same for the HN and OH cases since a_m, b_m and v_{PR} in Eq. (15) are complex functions of T_c and v_c which are species-specific. The difference between the HN and OH EOS and the fact that the transport properties are also species-specific, induces the definition of classes according to the species system: one OH class and one HN class of simulations.

Table 4
Reference quantities for non-dimensionalization of entropy dissipation. For all layers: $Y_{2R} = 0.5$. $M_{c,0} = 0.4$, $L_R = \delta_{\omega,0} = 6.859 \times 10^{-3}$ m. $Re_R = Re_0$. (See Table 2 for Re_0 values.) $p_R = p_0 = 100$ atm (OH); 60 atm (HN); $m_R = m(Y_{2R}) = 3.793$ g/mol (OH); 43.785 g/mol (HN). $R_u = 8.3144$ J/mol K.

	OHS00	OHS50 OH750	HNS00 HN600 HN800
T_R (K)	261	500	800
$\rho_R = \rho(p_R, T_R, Y_{2R})$ (kg/m³)	16.665	8.896	39.328
$o_{sR} = a_s(p_R, T_R, Y_{2R})$ (m/s)	966.64	1285.4	419.42
$C_{pR} = C_p(p_R, T_R, Y_{2R})$ (J/mol K)	29.329	29.467	99.033
$U_R = \Delta U_0/2$ (m/s)	341.95	464.50	147.90
$g_R = (\rho_R U_R^3)/(L_R T_R)$ (Wm⁻³ K⁻¹)	3.722×10^8	2.600×10^8	2.319×10^7
$Pr_R = Pr(p_R, T_R, Y_{2R})$	0.7652	0.7171	1.0585
$Ma_R = U_R/o_{sR}$	0.354	0.361	0.353
$(C_{pR}T_R)/(m_R a_{sR}^2)$	2.16	2.35	10.29
$(R_u T_R)/(m_R o_{sR}^2)$	0.612	0.663	0.864

5.1. Dissipation at the DNS scale

To examine the dissipation, the databases from the previously performed DNS of Table 2 are interrogated using Eqs. (18) and (19). The domain averaged g_{visc}, g_{temp}, g_{mass} and g_{tot} are displayed in Table 5 for each of the simulations. The g_{tot} value is larger for the OH class than for the HN class, consistent with the reduced vortical features of the OH layers [27] and following the expectations of the analysis of Section 4. For each class, g_{tot} varies over a relatively small range (for OH layers the smallest value is 83% of the largest one, and for HN layers this ratio is 39%), and even the variation across classes is within percentages rather than orders of magnitude (the smallest g_{tot} value is 31% of the largest one). The global dissipation increases with Re_0 (HN500 versus HN600) and with an increased Re_0 combined with a reduction in $\lambda_1/\delta_{\omega,0}$ (OH500 or OH550 versus OH750; HN500 or HN600 versus HN800) due to stronger small-scale formation [32] as measured by the spanwise vorticity at the transitional state. Among the six simulations belonging to two different classes, the domain average for each of g_{visc}, g_{temp}, g_{mass} have values which differ by less than one order of magnitude (approximate deviations of 17%, 32% and 36% from maximum for g_{visc}, g_{temp}, g_{mass}, respectively), consistent with the non-dimensional arguments of Section 4.

Budgets of the dissipation listed in Table 6 show that, consistent with the non-dimensional analysis: (1) g_{temp}/g_{tot} is larger for the HN class than the OH class and (2) g_{mass} contains the largest proportion of g_{tot}. This proportion, spanning from 0.767 to 0.811, is remarkably invariant within each class and across classes, bodying well at this point for finding universal SGS models at these supercritical thermodynamic conditions. This possibility is not to be taken for granted given that the PR EOS is not the same for the HN and OH classes. For each class (and comparing classes), the layer with the highest g_{mass}/g_{tot} positively correlates with the smoothest well-defined HDGM features as seen in Fig. 2 illustrating $|\nabla\rho|\delta_{\omega,0}/\Delta\rho_0$. By definition, smoothness is the lack of small-scale activity and/or lack of structure, as subsumed in Chow and Moin [9]. The positive correlation for all layers between higher g_{mass}/g_{tot} values and increased HDGM smoothness is explained by the dissipation precisely having the effect of smoothing gradients. Whereas the layer features become smoother with increased g_{mass}/g_{tot} value, two different behaviors are observed regarding its variation with the maximum $|\nabla\rho|\delta_{\omega,0}/\Delta\rho_0$ magnitude in the layer (the maximum listed in the legend of Fig. 2 is representative): for HN layers g_{mass}/g_{tot} is an increasing function of the maximum $|\nabla\rho|\delta_{\omega,0}/\Delta\rho_0$ value in the layer while for OH layers it is a decreasing function of this value. Comparing classes, the opposite variation of g_{mass}/g_{tot} with the maximum $|\nabla\rho|\delta_{\omega,0}/\Delta\rho_0$ value in the layer stems from the fact that the domain average is the result of

both local values and the spatial extent of the HDGM regions created partially through the action of the Fick and Soret terms in **j**. For HN layers, the increasing-function variation implies very localized regions of large Fick and Soret terms activity, and for OH layers the decreasing-function variation implies a much larger extent of Fick and Soret terms activity; these aspects are confirmed by spatial distributions of $|\nabla\rho|\delta_{\omega,0}/\Delta\rho_0$ shown in Fig. 2. This difference between the two classes introduces the anticipation that, according to the class, the DNS database may respond in opposite ways to filtering. This topic is addressed next.

5.2. Subgrid-scale dissipation

Information regarding g_{tot}^{SGS} is helpful in many ways. This information is of interest to appropriately model the subgrid-scale mixture fraction [33] or scalar variance; the subgrid mixture fraction dissipation [33] or more generally the SGS scalar dissipation, χ^{SGS}, is part of the scalar-variance model, where $\chi \equiv g_{mass}Y_1Y_2m_1m_2/(R_u m)$. Studying g_{tot}^{SGS} can additionally bring a perspective on backscatter and enlighten considerations on viable SGS models, particularly since a universally applicable SGS model is still lacking for performing LES. The goal here is to systematically study g_{tot}^{SGS} in thermodynamically supercritical binary-species mixing layers and determine if and how its characteristics depend on the species system and initial conditions. Related to conducting LES, the interest is also in determining how these findings depend on filter size.

Filtering is performed with a cubic top-hat filter having a width $\Delta = N_F\Delta x$ where $N_F = 4, 8, 12, 16$; the top-hat filter is chosen as the only one in concert with a finite difference numerical discretization, which was the numerical scheme used to obtain the DNS database. The minimum value $N_F = 4$ is chosen based on the consideration that for computational efficiency compared to DNS, LES must have a grid at least $\Delta x_{LES} = 2\Delta x$, and that for a eighth-order Padé scheme Δ must at least be $\Delta = 2\Delta x_{LES} = 4\Delta x$ in order for the SGS contribution to be larger than the truncation error, without which the LES is not meaningful [9,10]. Although $g_k \geqslant 0$, there is no such requirement for g_k^{SGS}, which may display both positive and negative values; negative values indicate entropy backscatter.

5.2.1. Backscatter

As explained in Section 1, usually backscatter is considered small in turbulent flows and this assumption affects the SGS flux modeling strategy in LES. For example, the well-known Smagorinsky model [34] does not have the capability to portray backscatter, whereas the Clark et al. [35] and Bardina et al. [36] models do. To inquire whether in the supercritical turbulent flows under consideration backscatter is negligible, the percentage of the points in the domain with negative SGS irreversible entropy production was computed and is plotted in Fig. 3. For each of the databases, and whether in g_{tot}^{SGS} or in each mode, the extent of the domain affected by backscatter is very substantial. Typical is $N_F = 4$: for each simulation, more of the field is affected by backscatter from g_{mass}^{SGS} (from 46% to 59%) than g_{temp}^{SGS} (from 32% to 41%) and more from g_{temp}^{SGS} than g_{visc}^{SGS} (from 25% to 33%). For g_{tot}^{SGS}, the percentage of the $N_F = 4$ field with backscatter activity is from 35% to 41%.

For all dissipation modes as well as for the total dissipation, the extent of backscatter in the flow decreases with increasing filter size. This decrease is naturally induced by the averaging process which reduces gradient magnitude with increased filter size. Most of the decrease is in g_{visc}^{SGS} (up to 32%) followed by g_{temp}^{SGS} (up to 13%) and the least is in g_{mass}^{SGS} (up to 7.5%) for a fourfold increase in N_F, indicating that the HDGM regions harbor substantial species-induced backscatter regions even at large grid spacing. For HN800 the extent of species-induced backscatter first slightly increases with N_F and then slightly decreases with further increasing N_F. It is conjectured that this non-monotonic behavior is due to the

Table 5

Average irreversible entropy production (to three significant digits), in MW m^{-3} K^{-1}.

	OH500	OH550	OH750	HN500	HN600	HN800
g_{visc}	0.425	0.306	0.376	0.0712	0.0791	0.101
g_{temp}	0.113	0.225	0.296	0.143	0.218	0.349
g_{mass}	2.31	1.91	2.27	0.706	0.983	1.92
g_{tot}	2.85	2.44	2.94	0.920	1.28	2.37

Table 6

Average irreversible entropy production. Relative contribution of g_{visc}, g_{temp} and g_{mass} to g_{tot}.

	OH500	OH550	OH750	HN500	HN600	HN800
g_{visc}/g_{tot}	0.149	0.125	0.128	0.077	0.062	0.043
g_{temp}/g_{tot}	0.040	0.092	0.100	0.155	0.170	0.147
g_{mass}/g_{tot}	0.811	0.782	0.772	0.767	0.768	0.810

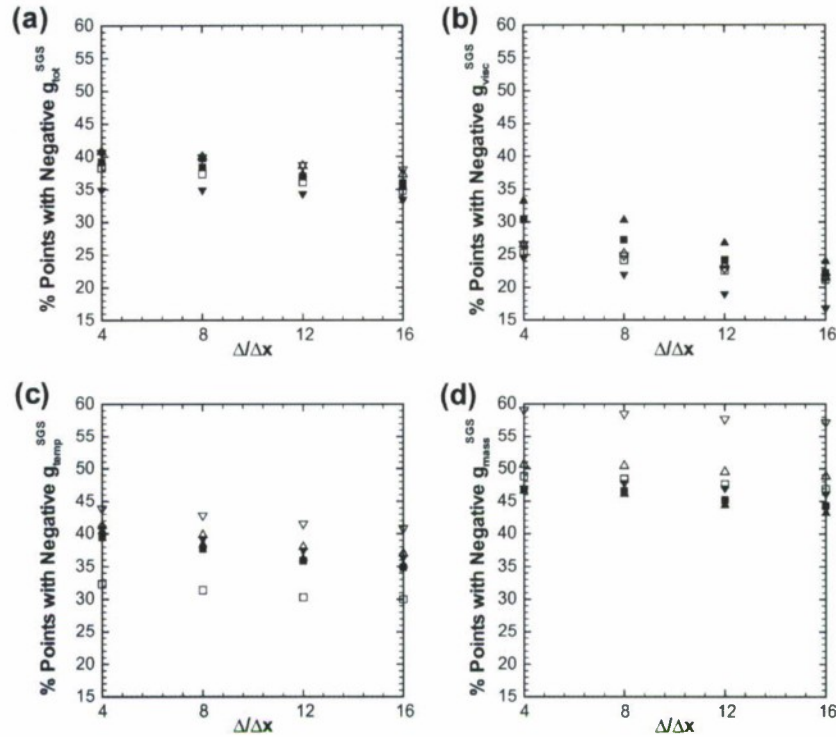**Fig. 3.** Percentage of points with negative SGS entropy production versus filter size for □ OH500, △ OH550, ▽ OH750, ■ HN500, ▲ HN600 and ▼ HN800. (a) g_{tot}^{SGS}, (b) g_{visc}^{SGS}, (c) g_{temp}^{SGS}, (d) g_{mass}^{SGS}.

much higher values of $|\nabla\rho|\delta_{\omega,0}/\Delta\rho_0$ for this simulation than for any other (Fig. 2), which brings the intriguing possibility that very strongly varying quantities multiplying the gradients in g_{mass} (Eq. (19)) may be responsible for this effect. For g_{tot}^{SGS}, there is a monotonic decrease in the spatial extent of backscatter with increasing N_F that ranges from 4% to 8% for N_F increasing by a factor of four, meaning that in this range of filter sizes, backscatter will still prevail in a substantial part of the computational domain.

The information in Fig. 3 only pertains to the extent of the computational field with backscatter activity, but does not instruct as to the magnitude of g_{tot}^{SGS} at the localities where $g_{tot}^{SGS} < 0$. To obtain information regarding relative magnitudes of $g_{tot}^{SGS} < 0$ and $g_{tot}^{SGS} \geq 0$ in the field, plotted in Fig. 4 appear braid-plane contours of g_{tot}^{SGS} for the six cases studied at $N_F = 4$. The plots show that the most prominent regions of $g_{tot}^{SGS} < 0$ flank those of $g_{tot}^{SGS} \geq 0$ all of which are embedded within the HDGM regions (compare visually with Fig. 2). Magnitude-wise, the highest level of $g_{tot}^{SGS} < 0$ in the field has a magnitude that is from 10% to 17% of the highest level of $g_{tot}^{SGS} \geq 0$ in the domain. The conclusion is that in all these simulations, backscatter cannot be neglected, implying that the Smagorinsky model is conceptually unsuited to capture the SGS fluxes in LES of supercritical flows. The argument that backscatter mainly appears here due to the transitional nature of the flow can be counteracted by the observation that the most preponderant $g_{tot}^{SGS} < 0$ locations are within the HDGM regions which are a feature of supercritical fully turbulent flow [11]; although the strength of the backscatter in terms of the maximum ratio of $g_{tot}^{SGS} < 0$ values by $g_{tot}^{SGS} \geq 0$ values will be flow dependent.

The information about backscatter eliminates the Smagorinsky SGS model as unsuited for SGS-flux modeling but does not give further information on the suitable characteristics that other eligible SGS-flux models should have. Such information can be obtained by studying the properties of the overall SGS dissipation activity embodied in the domain-average g_{tot}^{SGS}, which is investigated next.

5.2.2. Domain-average subgrid-scale dissipation

While, as discussed above, all layers display significant regions of backscatter at all filter widths, on a domain-average basis, $g_{tot} > 0$. The ratio of the domain-average g_{tot}^{SGS} to that of g_{tot} is an indicator of the rate of small-scale dissipation into heat compared to the rate of supply of organized activity. This ratio, g_{tot}^{SGS}/g_{tot}, is plotted in Fig. 5. Clearly, from Fig. 5, the SGS dissipation is an increasing quasi-linear function of N_F. These results unsurprizingly indicate that the larger is the filter size, the more important is the contribution of the SGS models. Notably, the g_{tot}^{SGS}/g_{tot} values shown in Fig. 5 are species-system specific and practically independent of the initial conditions. Whereas the SGS activity is considerably smaller for OH layers than for HN ones (a fact attributed to the smaller momentum flux ratio of OH layers), the increase with N_F is steeper for OH than HN cases. When increasing the filter by a factor of 4, g_{tot}^{SGS} increases by a factor of 4.8–5.6 for OH layers and 2.4–3.0 for HN layers. This distinctive class-specific behavior is conjectured to result for the much wider extent of the HDGM regions in OH layers compared to HN layers (Fig. 2); a wider extent means that when the filter is larger, more information is captured at the subgrid. On the other hand, for HN layers, the much higher structure (i.e. more convoluted aspect seen in Fig. 2) is conjectured to lead to the higher g_{tot}^{SGS}/g_{tot} compared to that of OH layers. Therefore, the indications are that SGS models will be relatively more important in reconstructing the physics in LES of HN layers relative to OH layers under the conditions of the present calculations, and that the HN layers may have more stringent resolution requirements.

The information obtained so far pertains to the total SGS dissipation, however, it is of interest to find out whether one of its modes governs the g_{tot}^{SGS} properties because if true, it is this mode that would deserve most attention in modeling. Thus, we next inquire into the contributions of the three dissipation modes and whether any species-specific behavior emerges from this inquiry.
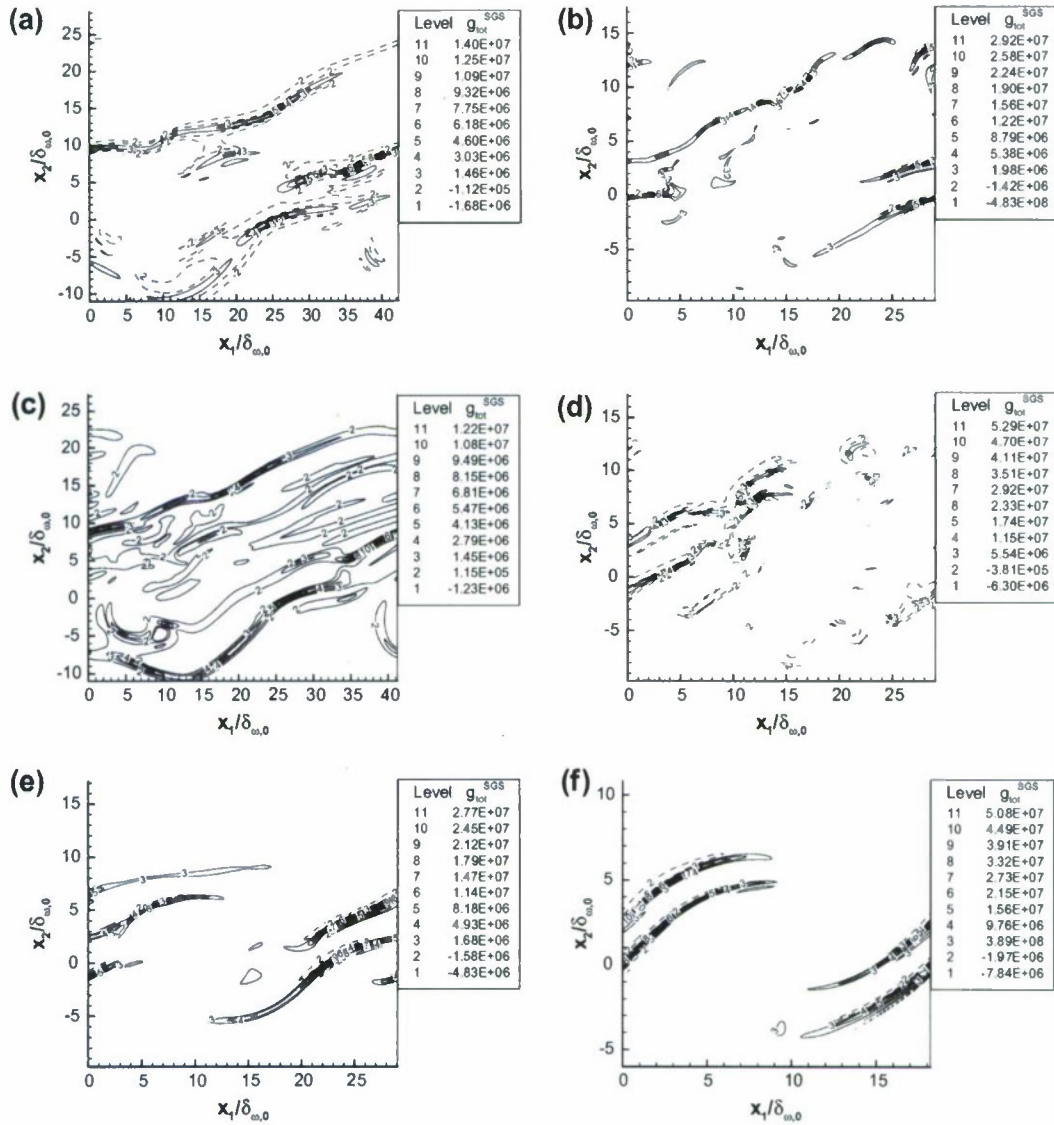
Fig. 4. SGS dissipation for (a) OH500, (b) HN500, (c) OH550, (d) HN600, (e) OH750 and (f) HN800: in the braid plane $(x_3 = L_3/16)$ for $\Delta = 4\Delta x$. Levels 1 and 11 are the minimum and maximum of the data in the plane, and do not appear on the plots. Negative levels appear in dashed lines.
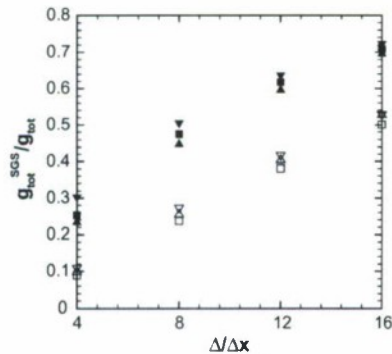

Fig. 5. Domain-averaged SGS entropy production versus filter size for □ OH500, △ OH550, ▽ OH750, ■ HN500, ▲ HN600 and ▼ HN800.

5.2.3. Modes of subgrid-scale dissipation

The relative contribution of each mode to the SGS dissipation is illustrated in Figs. 6 and 7, which show the ratio of the domain-average g_k^{SGS} to that of the domain-average g_{tot} and g_k (Fig. 6) or g_{tot}^{SGS} (Fig. 7). Expectably, the functional dependence of g_k^{SGS} on N_F is that of an increasing function. For each layer, g_k^{SGS}/g_{tot}^{SGS} varies weakly with N_F compared to the variation among layers. For example, for both $g_{visc}^{SGS}/g_{tot}^{SGS}$ and $g_{temp}^{SGS}/g_{tot}^{SGS}$ the variation for each layer is at most 25% whereas among layers there can be over a factor of three ratio at given N_F value; for $g_{mass}^{SGS}/g_{tot}^{SGS}$ the variation for each layer is at most 4% whereas among layers there is a maximum of 16% change at given N_F value.

For each layer, the ranges of values of g_k^{SGS}/g_k for the different modes are similar to one another and to g_{tot}^{SGS}/g_{tot} (compare Figs. 5 and 6) indicating a scale similarity type of behavior on the domain-average basis. Furthermore, the g_k^{SGS}/g_k values are species-specific and almost independent of the initial conditions. This suggests that scale-similarity SGS-flux models or dynamic-coeffi-
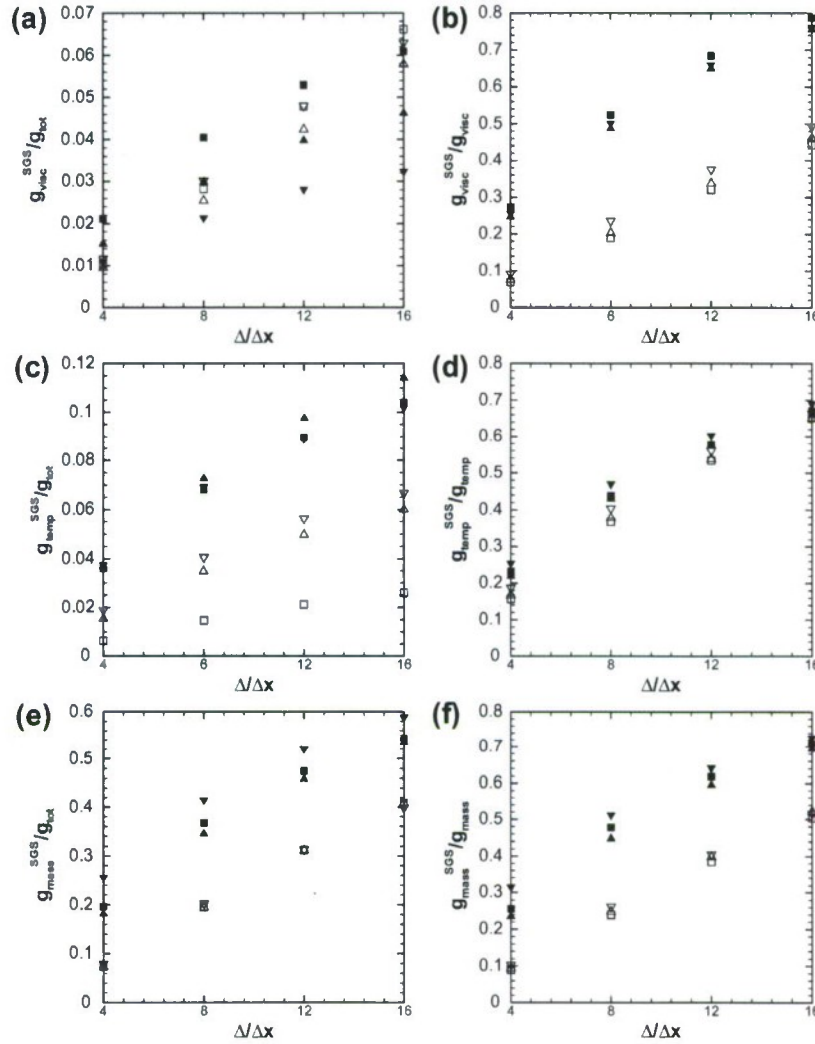
Fig. 6. Domain-averaged SGS entropy production versus filter size for □ OH500, △ OH550, ▽ OH750, ■ HN500, ▲ HN600 and ▼ HN800. (a and b) g_{visc}^{SGS}, (c and d) g_{temp}^{SGS}, (e and f) g_{mass}^{SGS}.

cient SGS flux models are particularly well suited for LES under these thermodynamic conditions, a fact confirmed by *a posteriori* studies [37].

The bulk of the SGS dissipation is due to species-mass-flux, with $g_{mass}^{SGS}/g_{tot}^{SGS}$ ranging from 72% to 84% for all N_F. Furthermore, g_{mass}^{SGS} is a significant contributor to the total (DNS) dissipation, with g_{mass}^{SGS}/g_{tot} values approaching 60% at the largest filter width; therefore, this mode should receive the most modeling attention. The significance of this result is that the largest contribution to the SGS dissipation will remain similar even for LES conducted with large grid spacing, indicating that the modeling approach should not be different with decreasing number of LES nodes. This finding is significant because according to Chow and Moin [9] and Ghosal [10], the filter size and LES grid size determine the magnitude of SGS effects that must be modeled relative to the truncation error. More discussions of the impact of LES grid and filter size appear in Pope [38].

Within the results for the OH class, noteworthy is the consistently larger g_{temp}^{SGS}/g_{temp} compared to the other two modes, independent of the OH simulation; this aspect is thus not attributable to a large initial T_2/T_1 since this temperature ratio is near unity for OH500. For HN layers, g_{temp}^{SGS}/g_{temp} tends to be the smallest of

the g_k^{SGS}/g_k. This contrasting behavior of OH layers and HN layers is conjectured to result from the greater extent of spatial distributions of large $|\nabla T|\delta_{\omega,0}/\Delta T_0(\Delta T_0 = T_1 - T_2)$ as shown in Fig. 8. Narrow regions of high $|\nabla T|\delta_{\omega,0}/\Delta T_0$ value produce a relatively small increase in the value of g_{temp}^{SGS} as shown for OH750 and HN800 (Fig. 8e and f). The implication is that SGS models in LES of OH layers should particularly concentrate on replicating the heat flux, a conclusion entirely consistent with and supported by the *a priori* results of Selle et al. [11] who showed that beyond the SGS fluxes, a SGS model to reconstruct $\nabla \cdot \overline{[q_{IK}(\phi) - q_{IK}(\bar{\phi})]}$ was necessary in the LES energy equation.

Considering the viscous SGS dissipation, while g_{visc}^{SGS}/g_{tot} does not show the same species-specific behavior as g_{mass}^{SGS}/g_{tot} and g_{temp}^{SGS}/g_{tot}, the values for the layers are in a very narrow range, at most 7%. The conjecture is that for these transitional states, the Reynolds number value is too low to result in a large contribution of g_{visc}^{SGS}, even with increased filter size. The obvious meaning of this information is that from the standpoint of viscous effects, once LES results are considered acceptable with a specific SGS model, it is foreseeable that the same SGS model will prevail for all LES in that class.
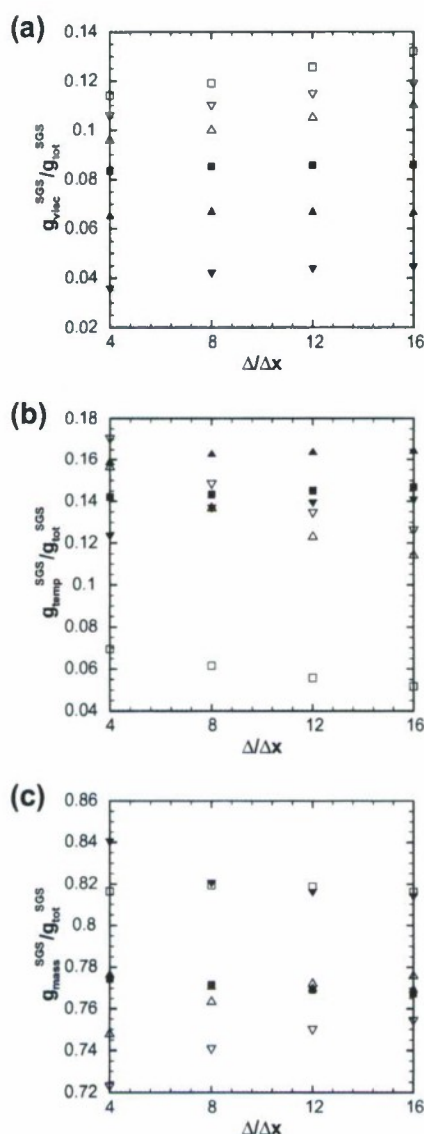
Fig. 7. Domain-averaged SGS entropy production versus filter size for □ OH500, △ OH550, ▽ OH750, ■ HN500, ▲ HN600 and ▼ HN800. (a) g_{visc}^{SGS}, (b) g_{temp}^{SGS}, (c) g_{mass}^{SGS}.

6. Summary and conclusions

Motivated by Large Eddy Simulation (LES) modeling of supercritical turbulent flows, transitional states of databases obtained from Direct Numerical Simulations (DNS) of binary-species supercritical temporal mixing layers were examined to understand the subgrid-scale irreversible entropy production, i.e. the dissipation, and its variation with filter size. The dissipation has contributions from three modes associated with viscous stresses, temperature-gradient and species-mass-gradient effects. Non-dimensionalization of the dissipation and its contributions revealed the essential mechanisms governing each of the modes and their relative contributions to the total dissipation. The viscous, temperature-gradient and species-mass-gradient dissipation contributions scale as $O(Re^{-1})$, $O(Re^{-1}Pr^{-1}Ma^{-2})$ and $O(Ma^{-2})$, respectively. As a result of this scaling, for Reynolds number values in the fully turbulent flow regime, the species-mass-gradient mode is predicted to dom-

inate the other modes. Even for the transitional Reynolds number values of the examined database, assessment of the DNS-scale domain-averaged dissipation confirmed previous findings that out of the three modes of dissipation, the species-mass dissipation is the main contributor to the total dissipation. The results revealed that, remarkably, the percentage of species-mass by total dissipation is nearly invariant across species systems and initial conditions. This dominance of the species-mass dissipation is due to high density-gradient magnitude (HDGM) regions populating the flow under the supercritical conditions of the simulations; such regions have also been observed in fully turbulent supercritical flows. The domain average being the result of both the local values and the extent of the HDGM regions, the expectations were that the response to filtering will vary with these flow characteristics. All filtering is here performed in the dissipation range of the Kolmogorov spectrum, at filter sizes from four to sixteen times the DNS grid spacing. The small-scale (subgrid-scale, SGS) dissipation was found by subtracting the filtered-field dissipation from the DNS-field dissipation.

In contrast to the DNS dissipation, the SGS dissipation is not necessarily positive; negative values indicate backscatter. Backscatter was shown to be spatially widespread in all modes of dissipation and in the total dissipation (25–60% of the domain). The maximum magnitude of the negative subgrid-scale dissipation was as much as 17% of the maximum positive subgrid-scale dissipation, indicating that not only is backscatter spatially wide spread in these flows, but it is considerable in magnitude and thus cannot be ignored for the purpose of LES modeling. The Smagorinsky model, for example, is unsuited for modeling SGS fluxes in LES because it cannot render backscatter. With increased filter size, there is only a modest decrease in the spatial extent of backscatter. The implication is that even at large LES grid spacings, the issue of backscatter and related SGS-flux modeling decisions are unavoidable.

As a fraction of the total dissipation, the small-scale dissipation is between 10% and 30% of the total dissipation for a filter size that is four times the DNS grid spacing, with all OH cases bunched at 10% and the HN cases spanning 24–30%. A scale similarity was found in that the domain-average proportion of each small-scale dissipation mode with respect to the total small-scale dissipation is very similar to equivalent results at the DNS scale. With increasing filter size, the proportion of the small-scale dissipation in the dissipation increases substantially, although not quite proportionally. When the filter size increases by fourfold, 52% for all OH runs and 70% for HN runs of the dissipation is contained in the subgrid-scale portion with virtually no dependence on the initial conditions of the DNS.

Whereas for HN simulations the proportion of the small-scale to DNS dissipation in all modes has similar values, for OH simulations, the temperature mode has the largest values. This behavior explained previous findings that particular attention must be devoted to modeling of the SGS heat flux for OH simulations [11]. With increased filter size, the small-scale dissipation in all modes increases similarly for the HN simulations irrespective of the initial conditions, whereas for OH simulations the viscous small-scale dissipation increased the most with filter size and the temperature small-scale dissipation increased the least.

Most current efforts at subgrid-scale modeling focusses on reproducing the viscous dissipation. We showed here that for supercritical mixing, the current focus is misplaced because the indications from the dissipation analysis are that modeling efforts in such LES should instead be focused primarily on mass-flux effects, with temperature and viscous effects being secondary although by no means negligible. Since LES feasibility for practical engineering calculations hinges on being able to use coarse grids, implying large filter sizes, our dissipation study as a function of
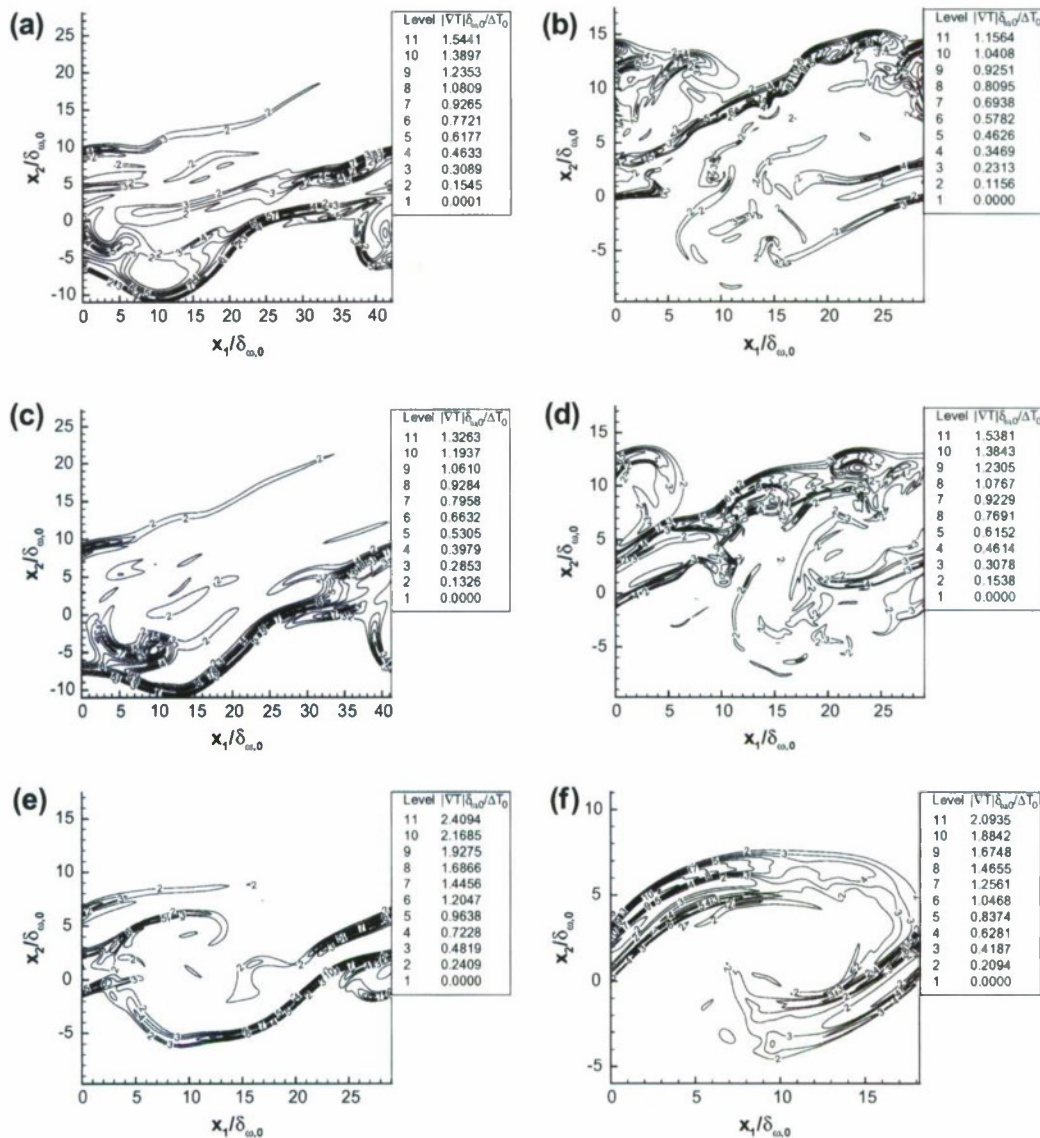
Fig. 8. Temperature gradient magnitude $|\nabla T|\delta_{\omega,0}/\Delta T_0$, where $\Delta T_0 = T_1 - T_2$, for (a) OH500, (b) HN500, (c) OH550, (d) HN600, (e) OH750 and (f) HN800: in the braid plane ($x_3 = L_3/16$). Levels 1 and 11 are the minimum and maximum of the data in the plane, and do not appear on the plots.

filter size is significant in that it shows what should the requirements of subgrid-scale models be as a function of filter size. The analysis also reveals a physical justification for scale-similarity type models and confirmation of their suitability was presented in *a posteriori* studies [37].

References

[1] Tennekes H, Lumley JL. A first course in turbulence. MIT Press; 1989.
[2] Holmes P, Lumley JL, Berkooz G. Turbulence, coherent structures, dynamical systems and symmetry. Cambridge University Press; 1996.
[3] Hirshfelder J, Curtis C, Bird R. Molecular theory of gases and liquids. John Wiley and Sons; 1964.
[4] Sreenivasan KR, Antonia RA. The phenomenology of small-scale turbulence. Annu Rev Fluid Mech 1997;29:435–72.
[5] Okong'o N, Bellan J. Direct numerical simulation of a transitional supercritical binary mixing layer: heptane and nitrogen. J Fluid Mech 2002;464:1–34.
[6] Okong'o N, Harstad K, Bellan J. Direct numerical simulations of O_2/H_2 temporal mixing layers under supercritical conditions. AIAA J 2002;40(5):914–26.
[7] Prausnitz J, Lichtenthaler R, de Azevedo E. Molecular thermodynamics for fluid-phase equilibrium. Prentice-Hall; 1986.
[8] Segal C, Polikhov S. Subcritical to supercritical mixing. Phys. Fluids 2008;20:052101–7.

[9] Chow FK, Moin P. A further study of numerical errors in large-eddy simulations. J Comput Phys 2003;184:366–80.

[10] Ghosal 5. An analysis of numerical errors in large-eddy simulations of turbulence. J Comput Phys 1996;125:187–206.

[11] 5elle LC, Okong'o NA, 8ellan J, Harstad KG. Modeling of subgrid scale phenomena in supercritical transitional mixing layers: an a priori study. J Fluid Mech 2007;593:57–91.

[12] Miller R, Harstad K, 8ellan J. Direct numerical simulations of supercritical fluid mixing layers applied to heptane–nitrogen. J Fluid Mech 2001;436:1–39.

[13] Keizer J. 5tatistical thermodynamics of nonequilibrium processes. New York: 5pringer-Verlag; 1987.

[14] 5arman 5, Evans D. Heat flux and mass diffusion in binary Lennard–Jones mixtures. Phys Rev A 1992;45(4):2370–9.

[15] Harstad K, Bellan J. An all-pressure fluid-drop model applied to a binary mixture: heptane in nitrogen. Int J Multiphase Flow 2000;26(10):1675–706.

[16] Papamoschou D, Roshko A. The compressible turbulent shear layer: an experimental study. J Fluid Mech 1988;197:453–77.

[17] Juniper M, Tripathi A, Scouflaire P, Rolon JC, Candel 5M. The structure of cryogenic flames at elevated pressure. Proc Combust Inst 2000;28:1103–9.

[18] Moser R, Rogers M. Mixing transition and the cascade to small scales in a plane mixing layer. Phys Fluids A 1991;3(5):1128–34.

[19] Moser R, Rogers M. The three-dimensional evolution of a plane mixing layer: pairing and transition to turbulence. J Fluid Mech 1993;247:275–320.

[20] Okong'o N, Bellan J. Real gas effects on mean flow and temporal, inviscid linear stability of binary-species mixing layers. AIAA J 2003;41(12):2429–43.

[21] Okong'o N, Bellan J. Consistent boundary conditions for multicomponent real gas mixtures based on characteristic waves. J Comput Phys 2002;176:330–44.

[22] Harstad K, Miller R, 8ellan J. Efficient high pressure state equations. AIChE J 1997;43(6):1605–10.

[23] Harstad K, Bellan J. Isolated fluid oxygen drop behavior in fluid hydrogen at rocket chamber pressures. Int J Heat Mass Transfer 1998;41:3537–50.

[24] Harstad K, Bellan J. The D^2 variation for isolated LOX drops and polydisperse clusters in hydrogen at high temperature and pressures. Combust Flame 2001;124:535–50.

[25] Kennedy C, Carpenter M. Several new numerical methods for compressible shear layer simulations. Appl Numer Math 1994;14:397–433.

[26] Muller 5M, 5cheerer D. A method to parallelize tridiagonal solvers. Parallel Comput 1991;17:181–8.

[27] Okong'o N, 8ellan J. Turbulence and fluid-front area production in binary-species, supercritical, transitional mixing layers. Phys Fluids 2004;16(5):1467–92.

[28] Moin P, Mahesh K. Direct numerical simulation: a tool in turbulence research. Annu Rev Fluid Mech 1998;30:539–78.

[29] Pope 5B. Turbulent flows. Cambridge University Press; 2000.

[30] Okong'o N, Bellan J. Entropy production of emerging turbulent scales in a temporal supercritical n-heptane/nitrogen three-dimensional mixing layer. Proc Combust Inst 2000;28:497–504.

[31] Okong'o N, Bellan J. Consistent large eddy simulation of a temporal mixing layer laden with evaporating drops. Part 1: direct numerical simulation, formulation and a priori analysis. J Fluid Mech 2004;499:1–47.

[32] Okong'o N, Bellan J. Perturbation and initial Reynolds number effects on transition attainment of supercritical mixing layers. Comput Fluids 2004; 33(8):1023–46.

[33] 8alarac G, Pitsch H, Raman V. Development of a dynamic model for the subfilter scale variance using the concept of optimal estimators. Phys Fluids 2008;20:035114-1. 9 p.

[34] Smagorinsky J. Some historical remarks on the use of nonlinear viscosities. In: Galperin B, Orszag 5, editors. Large eddy simulation of complex engineering and geophysical flows. Cambridge University Press; 1993. p. 3–36.

[35] Clark R, Ferziger J, Reynolds W. Evaluation of subgrid-scale models using an accurately simulated turbulent flow. J Fluid Mech 1979;91(1):1–16.

[36] 8ardina J, Ferziger J, Reynolds W. Improved subgrid scale models for large eddy simulation. AIAA Paper 80-1357.

[37] Taşkinoğlu E5, Bellan J. A posteriori study using a DN5 database describing fluid disintegration and binary-species mixing under supercritical pressure: heptane and nitrogen. J Fluid Mech 2010;645:211–54.

[38] Pope 58. Ten questions concerning the large-eddy simulation of turbulent flows. New J. Phys. 2004;6(35):1–24.

Appendix 3

Subgrid scale models and Large Eddy Simulation of oxygen disintegration and mixing with hydrogen or helium at supercritical pressure

By E Z G I S. T A S K I N O G L U[1]
and J O S E T T E B E L L A N[1,2]

[1]California Institute of Technology, Pasadena, CA 91125, USA

[2]Jet Propulsion Laboratory, California Institute of Technology, Pasadena, CA 91109, USA

For flows at supercritical pressure, p, the Large eddy Simulation (LES) equations consist of the differential conservation equations coupled with a real-gas equation of state, and the equations utilize transport properties depending on the thermodynamic variables. Compared to previous LES models, the differential equations contain not only the Subgrid Scale (SGS) fluxes but also new SGS terms, each denoted as a "correction". These additional terms, typically assumed null for atmospheric pressure flows, stem from filtering the differential governing equations and represent differences between a filtered term and the same term computed as a function of the filtered flow field. In particular, the energy equation contains a heat-flux correction (q-correction) which is the difference between the filtered divergence of the heat flux and the divergence of the heat flux computed as a function of the filtered flow field. We revisit here a previous *a priori* study (Selle *et al.* (2007)) where we only had partial success in modeling the q-correction term and show that success can be achieved using a different modeling approach. This *a priori* analysis,

based on a temporal mixing layer Direct Numerical simulation database, shows that the focus in modeling the **q**-correction should be on reconstructing the primitive variable gradients rather than their coefficients (Selle *et al.* (2007)), and proposes the approximate deconvolution model (ADM) as an effective means of flow field reconstruction for LES heat flux calculation. Further, an *a posteriori* study is conducted for temporal mixing layers initially containing oxygen (O) in the lower stream and hydrogen (H) or helium (He) in the upper stream to examine the benefit of the new model. Results show that for any LES including SGS-flux models (constant-coefficient Gradient or Scale-Similarity models; dynamic-coefficient Smagorinsky/Yoshizawa or mixed Smagorinsky/Yoshizawa/Gradient models), the inclusion of the **q**-correction in LES leads to the theoretical maximum reduction of the SGS heat-flux difference; the remaining error in modeling this new subgrid term is thus irreducible. The impact of the **q**-correction model first on the heat flux, and then on the mean, fluctuations, second-order correlations and spatial distribution of dependent variables is also presented. Discussions on the utilization of the models in general LES are presented.

1. Introduction

The simulation of high-pressure turbulent flows, where the pressure, p, is larger than the critical value, p_c, for the species under consideration, is relevant to a wide array of propulsion systems, e.g. gas turbine, diesel and liquid rocket engines. Most turbulence models have, however, been developed for atmospheric-p turbulent flows. The difference between atmospheric-p and supercritical-p turbulence is that whereas in the former situation the coupling between dynamics and thermodynamics is moderate to negligible, for the latter situation it is very significant and can dominate the flow characteristics

(Okong'o & Bellan (2002a), Okong'o *et al.* (2002)). The reason for this fact is in the mathematical form of the equation of state (EOS), which is the perfect-gas EOS in the former case and the real-gas EOS in the latter case. The perfect gas EOS is mildly non linear and, with the exception of the molar mass term, is the same for all chemical species; the molar mass term does not have substantial variation in the realm of species involved in combustion reactions relevant to propulsion systems. In contrast, the Peng-Robinson (PR) EOS (Prausnitz *et al.* (1986)), is strongly non-linear and does not obey the corresponding state principle, so it is species-dependent through coefficients which are strongly dependent on the critical properties and acentric factor of the species (e.g. Okong'o *et al.* (2002)) all of which exhibit considerable variation with the species. The PR EOS along with many other EOSs not obeying the corresponding state principle are of practical interest because they have been extensively tested and their range of validity is well known. These observations have important consequences for Large Eddy Simulations (LES) in which the conservation equations are filtered and, in order to solve the LES equations, models must be used for those filtered terms which are not directly computable from the LES solution. For atmospheric-p flows, it has been shown that the only significant filtered terms in the LES equations are the Subgrid Scale (SGS) fluxes (Vreman *et al.*(1995), Okong'o & Bellan (2004b)). However, for supercritical turbulent flows, additional terms were shown to be rivaling, and sometimes surpassing in r.m.s. magnitude the SGS flux terms (Selle *et al.* (2007)). Consistent with the strong EOS dependence on species, depending on the chemical species, different additional terms were found significant in the LES equations according to the species under consideration. For the heptane/nitrogen (HN) C_7H_{16}/N_2 mixing layer configuration, the new prominent term was in the momentum equation: the gradient of the difference between the filtered pressure, $\overline{p}$, and the gradient of p computed using the filtered flow field, $p(\overline{\phi})$.

Here $\phi = \{\rho, \rho u_i, \rho e_t, \rho Y_\alpha\}$ is the vector of conservative variables where ρ is the density, u_i is the velocity component in the x_i-direction spatial coordinate, e_t is the total energy and Y_α is the mass fraction of species α. For any component of the primitive variable vector $\psi(\phi) = \{u_i, p, X_\alpha, T\}$, where X_α is the mole fraction of species α, and T is the temperature, the filtering operation is defined as

$$\overline{\psi}(\vec{x}) = G * \psi = \int_V \psi(\vec{y}) G(\vec{x} - \vec{y}) d\vec{y} \tag{1.1}$$

where G is the filter function and V is the filtering volume. For the oxygen/hydrogen (OH) O_2/H_2 system, the additional prominent term was in the energy equation: the difference between the divergence of the filtered heat flux, $\overline{\mathbf{q}(\phi)}$ and the divergence of $\mathbf{q}(\overline{\phi})$. For the oxygen/helium (OHe) O_2/He system, each of these terms was less important than for the HN and OH systems, respectively, but was still non-negligible compared to the corresponding resolved term in the equation (i.e. $\nabla p(\overline{\phi})$ or $\nabla \cdot \mathbf{q}(\overline{\phi})$). The variation among species systems is traceable to the different EOS for these species systems (although all EOS had the PR form) and to the different transport properties. Physically, these additional terms were necessary to reproduce high density-gradient magnitude (HDGM) regions distributed throughout the flow (Taşkinoğlu & Bellan (2010)), as seen both in Direct Numerical Simulations (DNS) at transitional states (Okong'o & Bellan (2002a), Okong'o *et al.* (2002)) and in fully turbulent flow experiments (Mayer *et al.* (1996), Mayer *et al.* (1998), Chehroudi *et al.* (1999), Oschwald & Schik (1999), Oschwald *et al.* (1999), Segal & Polikhov (2008)). This filamentary morphology of the HDGM regions is a manifestation of fluid disintegration and it was found that in these filaments the fluid is a mixture of the heavy and light fluids (Okong'o & Bellan (2002a), Okong'o *et al.* (2002)); this situation is very different from that under atmospheric p where the equivalent of the HDGM regions exclusively contains the heavy fluid, as during atomization.

The additional terms in the LES equations stem from the usual 'LES assumptions' -

that the difference between a filtered quantity and the same quantity computed from the filtered flow field is negligible with respect to other terms in the equation - not being satisfied. The fact that the LES assumptions are not satisfied is the result of strong subgrid scale activity, which, if removed through filtering distorts the solution from its physical counterpart. Such finding is not restricted to supercritical flows, as has also been identified in atmospheric-p fully multicomponent species flows where non-uniformities are at a finer scale than in flows containing only a small number of species (Bellan & Selle (2009)). Basically, to enable LES computations, these new terms must be replaced in the LES equations with SGS models, similar in concept to the ubiquitous SGS-flux models.

For supercritical turbulent binary-species flows, the implication of the above-discussed findings is that, unlike in atmospheric-p binary-species turbulent flows, the type and mathematical form of SGS models may be species dependent. This species dependency may impose a large development burden in terms of obtaining appropriate SGS models, but given the importance of the applications it should not be dismissed. For example, the accurate prediction of the heat flux to the wall is a long standing problem in liquid rocket propulsion because of the implications it has for wall-material performance and rocket integrity. Several LES were compared to heat flux experimental data versus axial direction in Tucker *et al.* (2008) to predict single-element coaxial injector flow and combustion. The results showed that only the most computationally intensive LES, with 255×10^6 cells, requiring 2×10^6 CPU hours and the utilization of 2000 processors (on average) was closest to the experimental data, but this LES was based on classical SGS-flux models, without the additional terms we advocate. The expectation is that with the additional terms we propose, the LES grid could be made coarser because these terms would account for SGS activity that currently only a fine LES grid can resolve.

Having previously addressed the modeling of the momentum equation term in an a

posteriori study (Taşkınoğlu & Bellan (2010)), we here focus on the additional SGS term in the energy equation, with application to the OH and OHe systems. Following the presentation in §2 of the LES governing equations, the databases are summarized in §3, the LES initial and boundary conditions are presented in §4 and the LES numerical methodology is described in §5. In §6, we first revisit the *a priori* modeling of the additional SGS term for which a model was presented in §2.4.2, given that only partial success was achieved in a previous *a priori* analysis (Selle *et al.* (2007)). Results are presented in §6 by first assessing *a priori* the models presented in §2.4.2. Choosing the best model for the additional term, an *a posteriori* investigation is presented in §6.2 with the goal of reproducing in LES an approximation as close as possible to the filtered-and-coarsened (FC) DNS: filtered to remove the small scales that are not computed in LES, and coarsened to reduce the number of nodes from DNS to those of LES. Generally, the FC-DNS field can be considered as a sample of the DNS field and a typically ideal, unachievable, LES template. However, if the chosen LES grid is relatively coarse, as it must necessarily be for computational efficiency when the configuration has physically large dimensions (e.g., a rocket combustion chamber), enhancement to LES could be obtained through modeling of terms not satisfying the LES assumptions, and in the best case one may strive to achieve a LES having, from a view-point of specific interest, no more deficiency than FC-DNS with respect to the DNS. To assess the impact of the additional-term model, we first conduct LES without, and then with this additional term, and compare the results in §6.2. Conclusions and perspectives for using this methodology in LES are given in §7.

2. Large Eddy Simulation governing equations

The LES equations were derived by Selle *et al.* (2007) from the conservation equations by spatial filtering using the filter defined in equation (1.1). As typical for compressible

flows, Favre filtering is used, defined as $\tilde{\psi} = \overline{\rho\psi}/\bar{\rho}$. Furthermore, the variance of two quantities φ and θ is defined as $\vartheta(\overline{\varphi},\overline{\theta}) = \overline{\varphi\theta} - \overline{\varphi}\,\overline{\theta}$ or $\vartheta(\widetilde{\varphi},\widetilde{\theta}) = \widetilde{\varphi\theta} - \widetilde{\varphi}\widetilde{\theta}$, depending on the filtering. The governing equations are written for the conservative variable vector ϕ, and include the additional SGS term in the energy equation since it is the focus of our study.

2.1. *LES differential equations*

The LES differential equations, derived under the assumption that filtering and differentiation commute (the top-hat filter is used here for which the operations commute except near boundaries), are (Selle *et al.* (2007)):

$$\frac{\partial \bar{\rho}}{\partial t} + \frac{\partial \bar{\rho}\tilde{u}_j}{\partial x_j} = 0 \qquad (2.1)$$

$$\frac{\partial \bar{\rho}\tilde{u}_i}{\partial t} + \frac{\partial \bar{\rho}\tilde{u}_i\tilde{u}_j}{\partial x_j} = -\frac{\partial p\left(\overline{\phi}\right)}{\partial x_i} + \frac{\partial \sigma_{ij}\left(\overline{\phi}\right)}{\partial x_j} - \frac{\partial}{\partial x_j}\left(\bar{\rho}\tau_{ij}\right) \qquad (2.2)$$

$$\frac{\partial \bar{\rho}\tilde{e}_t}{\partial t} + \frac{\partial \bar{\rho}\tilde{e}_t\tilde{u}_j}{\partial x_j} = -\frac{\partial p\left(\overline{\phi}\right)\tilde{u}_j}{\partial x_j} - \frac{\partial q_{IKj}\left(\overline{\phi}\right)}{\partial x_j} + \frac{\partial \sigma_{ij}\left(\overline{\phi}\right)\tilde{u}_i}{\partial x_j}$$
$$-\frac{\partial}{\partial x_j}\left(\bar{\rho}\zeta_j\right) - \frac{\partial\left(\bar{\rho}\tau_{ij}\tilde{u}_i\right)}{\partial x_j} - \frac{\partial}{\partial x_j}\left[\overline{q_{IKj}(\phi)} - q_{IKj}\left(\overline{\phi}\right)\right] \qquad (2.3)$$

$$\frac{\partial \bar{\rho}\tilde{Y}_\alpha}{\partial t} + \frac{\partial \bar{\rho}\tilde{Y}_\alpha\tilde{u}_j}{\partial x_j} = -\frac{\partial j_{\alpha j}\left(\overline{\phi}\right)}{\partial x_j} - \frac{\partial}{\partial x_j}\left(\bar{\rho}\eta_{\alpha j}\right) \qquad (2.4)$$

where the SGS fluxes are

$$\tau_{ij} = \vartheta(\widetilde{u}_i, \widetilde{u}_j), \quad \zeta_j = \vartheta(\tilde{h}, \tilde{u}_j), \quad \eta_{\alpha j} = \vartheta(\widetilde{Y}_\alpha, \widetilde{u}_j) \text{ with } \sum_{\alpha=1}^{\mathcal{N}}\eta_{\alpha j} = 0, \qquad (2.5)$$

and the additional SGS term is $\left(\nabla \cdot \left[\overline{q_{IKj}(\phi)} - q_{IKj}\left(\overline{\phi}\right)\right]\right)$. In (2.1) - (2.4), t is the time, σ is the viscous stress tensor, $\mathbf{q}_{IK}$ is the Irwing-Kirkwood (subscript IK) heat flux (Sarman and Evans (1992)), $e = e_t - e_K$ is the internal energy, $e_K = u_i u_i/2$ is the kinetic energy, $\mathcal{N}$ is the number of species and $\mathbf{j}_\alpha$ is the species-mass flux of species α. Conservation principles impose

$$\sum_{\alpha=1}^{\mathcal{N}} Y_\alpha = 1, \quad \sum_{\alpha=1}^{\mathcal{N}} j_{\alpha j} = 0. \qquad (2.6)$$

The Einstein summation is used for roman indices (i, j, k), but not for Greek indices (α, β). The thermodynamic variables are functions of the LES flow field $\overline{\phi}$:

$$e = e\left(\overline{\phi}\right), \quad p = p\left(\overline{\phi}\right), \quad Y = Y\left(\overline{\phi}\right), \quad T = T\left(\overline{\phi}\right), \quad h = h\left(\overline{\phi}\right) \qquad (2.7)$$

where p, T and the enthalpy $h = e + p/\rho$ are computed from the EOS; likewise, the fluxes are functions of $\overline{\phi}$:

$$\sigma_{ij} = \sigma_{ij}\left(\overline{\phi}\right), \quad j_{\alpha j} = j_{\alpha j}\left(\overline{\phi}\right), \quad q_{IKj} = q_{IKj}\left(\overline{\phi}\right). \qquad (2.8)$$

For a Newtonian fluid,

$$\sigma_{ij} = \mu\left(\frac{\partial u_i}{\partial x_j} + \frac{\partial u_j}{\partial x_i} - \frac{2}{3}\frac{\partial u_k}{\partial x_k}\delta_{ij}\right), \quad S_{ij} = \frac{1}{2}\left(\frac{\partial u_i}{\partial x_j} + \frac{\partial u_j}{\partial x_i}\right), \qquad (2.9)$$

where μ is the viscosity and S_{ij} is the rate-of-strain tensor.

The species-mass and heat fluxes originate in the fluctuation-dissipation theory (see Keizer (1987)) which is consistent with non-equilibrium thermodynamics, converges to kinetic theory in the low-p limit, and relates fluxes and forces from first principles. For a binary-species system (light species 1, heavy species 2), the species-mass and heat fluxes, including Soret and Dufour effects (Harstad & Bellan (2000)), are:

$$\mathbf{j}_2(\overline{\psi}) = B_Y(\overline{\psi})\nabla Y_2\left(\overline{\phi}\right) + B_T(\overline{\psi})\nabla T\left(\overline{\phi}\right) + B_P(\overline{\psi})\nabla p\left(\overline{\phi}\right), \qquad (2.10)$$

$$\mathbf{q}_{IK}(\overline{\psi}) = C_Y(\overline{\psi})\nabla Y_2\left(\overline{\phi}\right) + C_T(\overline{\psi})\nabla T\left(\overline{\phi}\right) + C_P(\overline{\psi})\nabla p\left(\overline{\phi}\right), \qquad (2.11)$$

where $\overline{\psi} \equiv \psi(\overline{\phi})$ and functionally

$$B_Y \equiv -\rho D\alpha_D, \qquad\qquad C_Y \equiv -\rho D\alpha_D\alpha_{IK}R_uT\frac{m}{m_1 m_2}, \qquad (2.12)$$

$$B_T \equiv -\alpha_{BK}Y_1Y_2\frac{\rho D}{T}, \qquad C_T \equiv -\lambda - \rho D\alpha_{IK}\alpha_{BK}R_u\frac{m}{m_1 m_2}Y_1Y_2, \qquad (2.13)$$

$$B_P \equiv -\rho D\frac{Y_1Y_2}{R_uT}\frac{m_2 m_1}{m}\Lambda, \qquad C_P \equiv -\rho D\alpha_{IK}\Lambda Y_1Y_2. \qquad (2.14)$$

In (2.12)-(2.14)

$$\alpha_{BK} = \alpha_{IK} - \alpha_h, \quad \alpha_h = \frac{1}{R_uT}\frac{m_2 m_1}{m}\Theta, \qquad (2.15)$$

$$\Lambda \equiv \left(\frac{1}{m_2} \frac{\partial v}{\partial X_2} - \frac{1}{m_1} \frac{\partial v}{\partial X_1} \right), \quad \Theta \equiv \left(\frac{1}{m_2} \frac{\partial (mh)}{\partial X_2} - \frac{1}{m_1} \frac{\partial (mh)}{\partial X_1} \right), \quad (2.16)$$

$$\alpha_D \equiv 1 + X_\alpha \frac{\partial \ln \gamma_\alpha}{\partial X_\beta}, \quad (2.17)$$

where λ is the thermal conductivity with $\lim_{p \to 0} \lambda = \lambda_{KT}$ as discussed in Harstad & Bellan (2000) and the subscript KT denotes the kinetic theory, R_u is the universal gas constant, m is the mixture molar mass, and v is the molar volume with $v = m/\rho$. For species α, m_α is the species-α molar mass, $X_\alpha = mY_\alpha/m_\alpha$, and γ_α is the fugacity. Furthermore, α_{IK} is the IK form of the thermal diffusion factor, α_{BK} is the Bearman-Kirkwood (BK) form of the thermal diffusion factor, D is the binary diffusion coefficient and α_D is the mass diffusion factor.

The models for the unclosed terms in (2.1) - (2.4), namely, $\tau_{ij}, \zeta_j, \eta_{\alpha j}$ and $\left(\nabla \cdot \overline{[q_{IKj}(\phi)]} - q_{IKj}\left(\overline{\phi} \right) \right)$ are described in §2.4.1 and 2.4.2, respectively.

2.2. Equation of state

The pressure is calculated from the well-known Peng-Robinson (PR) EOS, given T and the PR molar volume (v_{PR}), as

$$p = \frac{R_u T}{(v_{PR} - b_m)} - \frac{a_m}{(v_{PR}^2 + 2b_m v_{PR} - b_m^2)}, \quad (2.18)$$

where a_m and b_m are functions of T and X_α, the mathematical forms of which is given in detail in Miller *et al.* (2001) and Okong'o *et al.* (2002). At high p, the v_{PR} value may differ significantly from that of v (Prausnitz *et al.* (1986)) and this difference has been taken into account by using a volume shift (Harstad *et al.* (1997), Okong'o *et al.* (2002)) $v_s = v - v_{PR}$ which is calculated from the EOS using the Gibbs energy. All thermodynamic quantities, including α_D, h, $C_p = (\partial h/\partial T)_{p,X}$ and the speed of sound (a_s), are calculated from the EOS using standard thermodynamic relations (Miller *et al.* (2001), Okong'o & Bellan (2002a), Okong'o *et al.* (2002)). The implementation of the EOS to calculate p and T from ρ, e and Y_α uses an iterative fit for the OH and OHe

mixtures (Okong'o *et al.* (2002), Selle *et al.* (2007)). The pure species properties are listed in table 1.

2.3. *Transport coefficients*

The viscosity, the Schmidt number ($Sc = \mu/(\rho\alpha_D D)$) and the Prandtl number (Pr $= \mu C_p/(m\lambda)$) were calculated from high-pressure single-species transport properties using mixing rules, as in Harstad & Bellan (1998). The calculated values were correlated, as summarized in table 2, and these correlations were then used to compute the transport properties μ, D and λ. The relationship between α_{BK} and α_{IK} stated in equation (2.15) means that either one can be specified, and the other then calculated.

2.4. *Subgrid-scale models*

2.4.1. *SGS-flux models*

Two categories of models are here used for SGS fluxes (τ_{ij}, $\eta_{\alpha j}$, ζ_j), namely, constant-coefficient models and dynamic-coefficient models (Germano *et al.* (1991)). The constant-coefficient SGS models are the Gradient (GRC) (Clark *et al.* (1979)) and the Scale-Similarity models (SSC) (Bardina *et al.* (1980)); the dynamic-coefficient models are the dynamic Smagorinsky (Smagorinksy (1963), Smagorinksy (1993)) model (SMD) and a dynamic 'mixed' model (Clark *et al.* (1979), Vreman *et al.* (1996)) combining the Smagorinsky and Gradient model (MGRD). The consideration of dynamic modeling stems from the transient, strongly non-uniform aspect of the present flows.

The GRC model, derived from a Taylor series expansion (Okong'o & Bellan (2004b)), is

$$\vartheta_{GR}(\widetilde{\psi}_m, \widetilde{\psi}_n) = C_{GR}\bar{\Delta}^2\frac{\partial\tilde{\psi}_m}{\partial x_k}\frac{\partial\tilde{\psi}_n}{\partial x_k}. \tag{2.19}$$

(Note: $\vartheta\left(\tilde{u}_1, \tilde{u}_1\right) = \tau_{11}$, $\vartheta\left(\tilde{u}_2, \tilde{u}_2\right) = \tau_{22}$, $\vartheta\left(\tilde{u}_3, \tilde{u}_3\right) = \tau_{33}$.) Theoretically, C_{GR} is pro-

portional to the moments of inertia of the filtering volume; for a cubic top-hat filter $C_{GR} = 1/12$ (Okong'o & Bellan (2004b)).

The SSC model, which postulates similarity between the SGS and the small resolved scale, is (Bardina *et al.* (1980))

$$\vartheta_{SS}(\widetilde{\psi}_m, \widetilde{\psi}_n) = C_{SS} \left(\widehat{\widetilde{\psi}_m \widetilde{\psi}_n} - \widehat{\widetilde{\psi}}_m \widehat{\widetilde{\psi}}_n \right), \tag{2.20}$$

where the overhat ($\widehat{}$) denotes (unweighted) filtering at the test-filter level $\hat{\Delta}$. The specified test filter width is $\hat{\Delta}/\bar{\Delta} = 2$, being that generally recommended. While scale similarity would imply that $C_{SS} = 1$, it has been shown that the actual value is filter-width dependent (Liu *et al.* (1994), Clark *et al.* (1979), Pruett *et al.* (2001), Okong'o & Bellan (2004b)).

Dynamic modeling (Germano *et al.* (1991)) is based on the assumption that the SGS behavior is akin to that of the small resolved scales. Then, a test filter is introduced, $\hat{\Delta}$, $\hat{\Delta} > \bar{\Delta}$, and by double filtering, $\widehat{\bar{\Delta}}$, a field with scales larger than those of the resolved field is produced. The effective filter width $\widehat{\bar{\Delta}}$, not actually used for filtering, corresponds to filtering at $\bar{\Delta}$ followed by filtering at $\hat{\Delta}$, and its value depends on the filter type. Considering the top-hat filter used here for both the grid and test filter, $\widehat{\bar{\Delta}}$ is optimally approximated by $\widehat{\bar{\Delta}}^2 = \bar{\Delta}^2 + \hat{\Delta}^2$ (Vreman *et al.* (1997)). The essence of dynamic modeling is to relate the grid-level SGS flux and the test-level SGS flux to the test-level resolved flux. For any quantity φ, such as $\tilde{h}$, $\tilde{Y}_\alpha$ or $\tilde{u}_i$, the grid-level and the test-level SGS fluxes associated with the velocity $\tilde{u}_j$ are denoted as $\vartheta_j(\varphi)$ and $\mathcal{T}_j(\varphi)$, respectively, and defined as

$$\vartheta_j(\varphi) = \widetilde{\varphi u_j} - \tilde{\varphi} \tilde{u}_j, \tag{2.21}$$

$$\mathcal{T}_j(\varphi) = \vartheta_j(\widehat{\varphi}) = \widehat{\widetilde{\varphi u_j}} - \hat{\tilde{\varphi}} \hat{\tilde{u}}_j, \tag{2.22}$$

where $\vartheta_j(u_i) = \tau_{ij}$, $\vartheta_j(Y_V) = \eta_j$, and $\vartheta_j(h) = \zeta_j$. The test-level resolved flux, L_j, is

computed through the Germano identity (Germano *et al.* (1991)). For compressible flows, L_j takes the form (Moin *et al.* (1991))

$$L_j\left(\varphi\right) \equiv \hat{\bar{\rho}}\mathcal{T}_j - \widehat{\overline{\rho\vartheta}}_j = \widehat{\overline{\rho\tilde{\varphi}\tilde{u}}}_j - \frac{\widehat{\overline{\rho\tilde{\varphi}}}\,\widehat{\overline{\rho\tilde{u}}}_j}{\hat{\bar{\rho}}}, \tag{2.23}$$

where $\hat{\tilde{\psi}} = \widehat{\overline{\rho\psi}}/\hat{\bar{\rho}}$. In the above equation, $\vartheta_j(\varphi)$ can be modeled using the generic model coefficient, $C(\varphi)$, as

$$\vartheta_j\left(\varphi\right) = C(\varphi)\mu_j\left(\varphi, \bar{\Delta}\right), \tag{2.24}$$

where $\mu_j\left(\varphi, \bar{\Delta}\right)$ is associated with the filter width, $\bar{\Delta}$, and the velocity, $\tilde{u}_j$. Similarly, $\mathcal{T}_j$ can be modeled as $\mu_j(\hat{\varphi}, \hat{\bar{\Delta}})$, associated with $\hat{\bar{\Delta}}$ and the velocity $\hat{\tilde{u}}_j$. If $C(\varphi)$ is assumed constant within the test filter, then, the left hand side of (2.23) can be calculated in terms of $C(\varphi)$ as

$$L_j(\varphi) = C(\varphi)M_j\left(\varphi\right) = C(\varphi)(\hat{\bar{\rho}}\mu_j(\hat{\varphi}) - \widehat{\bar{\rho}\mu_j\left(\varphi\right)}). \tag{2.25}$$

The SMD model relies on the gradient-diffusion (eddy-viscosity) concept, and therefore it does not lend itself to computing variances in general. The SGS fluxes in (2.5) are

$$\vartheta_{SM}(\widetilde{\psi}_m, \tilde{u}_j) = -C_{SM}\bar{\Delta}^2 S\left(\bar{\phi}\right)\frac{1}{2}\frac{\partial\widetilde{\psi}_m}{\partial x_j}, \quad \psi_m \neq u_j, \tag{2.26}$$

with τ_{ij} modeled in trace-free form as

$$\tau_{ij} - \frac{1}{3}\tau_{kk}\delta_{ij} = -C_{SM}\bar{\Delta}^2 S\left(\bar{\phi}\right)\left[S_{ij}\left(\bar{\phi}\right) - \frac{1}{3}S_{kk}\left(\bar{\phi}\right)\delta_{ij}\right], \tag{2.27}$$

where $S^2\left(\phi\right) = S_{ij}\left(\phi\right)S_{ij}\left(\phi\right)$. The YO model (Yoshizawa (1986)) for τ_{kk} is

$$\tau_{kk} = C_{YO}\bar{\Delta}^2 S^2\left(\bar{\phi}\right). \tag{2.28}$$

Thus, for the SMD model, μ_j has the mathematical form provided in (2.26) excluding the model coefficient; the coefficients are computed according to (2.25).

The MGRD model, chosen here for its focus on gradient computation through the Gradient model (reasons explained in §6.2), follows the approach of Vreman *et al.* (1997): the

coefficient of the Smagorinsky model is dynamically calculated and that of the Gradient model is kept constant at its theoretical value. For the MGRD model, (2.25) becomes

$$L_j(\varphi) = H_j(\varphi) + C(\varphi)M_j(\varphi), \tag{2.29}$$

with $H_j(\varphi) = (\hat{\bar{\rho}}\vartheta_j(\widehat{\varphi}) - \widehat{\bar{\rho}\vartheta_j(\varphi)})$, and ϑ_j is computed using the theoretical value $C_{GR} = 1/12$. Following Lilly (1992), we use a least-squares method to minimize the error in computing the coefficient from an overdetermined equation set, which yields the coefficients

$$C_H(\varphi) = \frac{\langle(L_j(\varphi) - H_j(\varphi))M_j(\varphi)\rangle}{\langle M_j(\varphi) M_j(\varphi)\rangle}, \tag{2.30}$$

where, for the present mixing layer configuration $\langle\rangle$ denotes averaging over homogeneous (x_1, x_3) planes. For the Smagorinsky model, the summation over repeated indices in (2.30) is over three quantities for the SGS stress diagonal terms and over three quantities for the SGS stress off-diagonal terms. Unlike for the Smagorinsky model, the summation for the Gradient model is over six quantities for the SGS stress terms. For dynamic models, both ζ_j and η_j are found by summation over the three components. (The use of dimensional variables in the present formulation necessitates the separate computation of the coefficient for each type of SGS flux.) The simulations are performed with a single-coefficient formulation for all SGS fluxes.

The dynamic coefficient values are computed as follows:

(a) For the dynamic SMD model, μ_j is computed from (2.26) (2.28), and $H_j = 0$;

(b) For the MGRD model, μ_j is computed from (2.26)–(2.28), and ϑ_j in H_j is computed from (2.19) using $C_{GR} = 1/12$.

Ezgi S. Taskinoglu and Josette Bellan

2.4.2. *Revisiting of the heat-flux term correction model*

To model $(\nabla \cdot [\overline{q_{IKj}(\phi)} - q_{IKj}(\overline{\phi})])$, Selle *et al.* (2007) have used several approximations, none of which was entirely successful. The most tractable approximation was

$$\overline{\mathbf{q}_{IK}(\psi)} \simeq \overline{C_T(\psi)}\nabla T(\overline{\phi}) + \overline{C_P(\psi)}\nabla p(\overline{\phi}) + \overline{C_Y(\psi)}\nabla Y_2(\overline{\phi}) \qquad (2.31)$$

where each function $\overline{C_T(\psi)}, \overline{C_P(\psi)}$ and $\overline{C_Y(\psi)}$ was modeled following a Taylor series expansion in conjunction with the assumption that the filter is a projection which leads to only retaining the second order term. For example,

$$\overline{C_T(\phi)} - C_T(\overline{\phi}) \equiv \frac{1}{2}\left.\frac{\partial^2 C_T}{\partial \phi_m \partial \phi_n}\right|_{\psi=\overline{\psi}}\left(\overline{\phi_m \phi_n} - \overline{\phi_m}\;\overline{\phi_n}\right) = \frac{1}{2}\left.\frac{\partial^2 C_T}{\partial \phi_m \partial \phi_n}\right|_{\psi=\overline{\psi}}\vartheta(\overline{\phi_m},\;\overline{\phi_n}).$$
$$(2.32)$$

Due to lack of knowledge regarding the transport coefficients dependency on ψ, the analytical functions $C_T(\phi), C_P(\phi)$ and $C_Y(\phi)$ are typically not available, and thus a numerical multivariate differentiation technique was used to obtain the results. When the DNS-computed $(\overline{C_T(\phi)} - C_T(\overline{\phi})), (\overline{C_P(\phi)} - C_P(\overline{\phi}))$ and $(\overline{C_Y(\phi)} - C_Y(\overline{\phi}))$ were compared in (x_1, x_2) planes to the corresponding model, the results were very encouraging, however, when these results were used in conjunction with a Taylor expansion of the entire heat flux according to (2.31), the DNS-extracted difference $\nabla \cdot (\overline{q_{IKi}(\phi)} - q_{IKi}(\overline{\phi}))$ did not compare well the model predictions, indicating that this approach may not be appropriate. We show in §6.1 that the large gradients in the HDGM regions, which were approximated in Selle *et al.* (2007) using the filtered flow field, e.g. $\overline{\nabla T(\phi)} \simeq \nabla T(\overline{\phi})$, were responsible for the lack of success.

The interest is here in developing a model for each of $\overline{\nabla T(\phi)}, \overline{\nabla Y_2(\phi)}$ and $\overline{\nabla p(\phi)}$, as functions of $\nabla T(\overline{\phi}), \nabla Y_2(\overline{\phi})$ and $\nabla p(\overline{\phi})$, respectively. To this end, we consider deconvolution methods (e.g. Geurts (1997) who constructed higher order polynomial inversions) the goal of which is to recover the unresolved part of the LES solution from the LES

solution. Among deconvolution methods, the focus is here on the Approximate Deconvolution Model (ADM) described in Stolz & Adams (1999), Stolz *et al.* (2001). The ADM procedure is based on the fact that if spatial filtering is defined through (1.1), then an approximate deconvolution ϕ^* can be obtained by applying an operator Q_N

$$\phi^* = Q_N * \overline{\phi}. \tag{2.33}$$

We choose to apply ADM to ϕ rather than ψ because it is ϕ which is computed in DNS, and thus its reconstruction has better accuracy potential than ψ which is calculated from ϕ using for T the strongly non-linear EOS, as discussed in §2.2. The ADM procedure is based on the assumption that G has an inverse G^{-1}, and in that case the inverse operator is expendable in a series of filter operators. Some filters may not be invertible, but a regularized inverse operator Q_N is obtainable by truncating the series at integer N (Stolz *et al.* (2001)), obtaining a regularized approximation of G^{-1}

$$Q_N = \sum_{l=0}^{N} (I - G)^l \approx G^{-1} \tag{2.34}$$

where regularization is defined as the process through which subgrid-scale dissipation is provided, I is the identity operator and N is the order of the reconstruction. Thus,

$$\begin{aligned}
\phi^* &= \left[\sum_{l=0}^{N} (I - G)^l \right] * \overline{\phi} \\
&= \overline{\phi} + (\overline{\phi} - \overline{\overline{\phi}}) + (\overline{\phi} - 2\overline{\overline{\phi}} + \overline{\overline{\overline{\phi}}}) + ... \\
&= 3\overline{\phi} - 3\overline{\overline{\phi}} + \overline{\overline{\overline{\phi}}} + ...
\end{aligned} \tag{2.35}$$

Generally, it has been found (Stolz *et al.* (2001)) that $N = 3$ is sufficient to bring an improvement in that $(\phi^* - \overline{\phi})$ is not null, and for $N \geqslant 5$ the value of $(\phi^* - \overline{\phi})$ did not change appreciably form that obtained with $N < 5$. However, it is possible that in other situations than those studied by Stolz *et al.* (2001) there could be another asymptotic best value of N, which will be investigated in §6.1. Noteworthy, the ADM only takes into

account the solution obtained at the LES scale and does not involve accurate information at the subgrid scale since that accurate information is unavailable in LES and instead replaced by the SGS - in particular SGS-flux - models. Thus, the result of the ADM is SGS-model dependent.

When considering the heat flux symbolically written as

$$\overline{\mathbf{q}_{IK}(\phi)} = \sum_{j=1}^{j=3} \overline{C_{A_j}(\phi)\nabla A_j(\phi)}, \tag{2.36}$$

several models for $\overline{\mathbf{q}_{IK}(\phi)}$ are possible, as follows

$$\overline{\mathbf{q}_{IK}(\phi)} = \sum_{j=1}^{j=3} C_{A_j}(\overline{\phi})\nabla A_j(\overline{\phi}) \quad \text{No HF} \tag{2.37}$$

$$\overline{\mathbf{q}_{IK}(\phi)} = \sum_{j=1}^{j=3} \overline{C_{A_j}(\phi^\star)\,\nabla A_j(\phi^\star)} \quad \text{M1} \tag{2.38}$$

$$\overline{\mathbf{q}_{IK}(\phi)} = \sum_{j=1}^{j=3} \overline{C_{A_j}(\phi^\star)} \ \overline{\nabla A_j(\phi^\star)} \quad \text{M2} \tag{2.39}$$

$$\overline{\mathbf{q}_{IK}(\phi)} = \sum_{j=1}^{j=3} \overline{C_{A_j}(\phi^\star)} \ \nabla A_j(\overline{\phi}) \quad \text{M3} \tag{2.40}$$

$$\overline{\mathbf{q}_{IK}(\phi)} = \sum_{j=1}^{j=3} C_{A_j}(\overline{\phi}) \ \overline{\nabla A_j(\phi^\star)} \quad \text{M4} \tag{2.41}$$

$$\overline{\mathbf{q}_{IK}(\phi)} = \sum_{j=1}^{j=3} \overline{C_{A_j}(\overline{\phi}) \ \nabla A_j(\overline{\phi})} \quad \text{M5} \tag{2.42}$$

where "HF" is the acronym for the Heat Flux correction model. The most sophisticated model is M1 where all coefficients and gradients are computed using a reconstructed vector ϕ, $\phi^\star$, after which the product of each coefficient and associated gradient is filtered and the three contributions according to (2.11) are added. The least sophisticated model is the No HF model case which uses the FC-DNS solution, and the second least sophisticated is M5 which also entirely relies on the filtered flow field. Between M1 and M5 are various approximations where either $\phi^\star$ is used but the filtering is individually performed on coefficients and gradients, or in which either the coefficient of the gradient

is computed from $\overline{\phi}$ rather than ϕ^*. Each of these models is investigated in §6.1. Without q-correction, in (2.3)

$$\left(\nabla \cdot \mathbf{q}(\phi_{LES}) + \left(\overline{\nabla \cdot \mathbf{q}(\phi)} - \nabla \cdot \mathbf{q}(\phi_{LES})\right)\right) \text{ is computed as } \nabla \cdot \mathbf{q}(\phi_{LES}). \quad (2.43)$$

With q-correction, in (2.3)

$$\left(\nabla \cdot \mathbf{q}(\phi_{LES}) + \left(\overline{\nabla \cdot \mathbf{q}(\phi)} - \nabla \cdot \mathbf{q}(\phi_{LES})\right)\right) \text{ is computed as } \overline{\nabla \cdot \mathbf{q}(\phi^*)}. \quad (2.44)$$

3. Description of the DNS database

The DNS database consists of supercritical temporal mixing layer simulations ($\mathcal{N} = 2$) of OH or OHe (subscripts o, h and he for oxygen, hydrogen and helium, respectively) mixtures. The DNS methodology has been previously described (Miller *et al.* (2001), Okong'o & Bellan (2002a), Okong'o *et al.* (2002)). The database represents solutions of the differential conservation equations (Miller *et al.* (2001), Okong'o & Bellan (2002a), Okong'o *et al.* (2002)) and the EOS (see §2.2), utilizing transport coefficient models (see §2.3). These equations were numerically solved using a fourth-order explicit Runge-Kutta time integration in conjunction with a sixth-order compact scheme with eighth-order filter for spatial derivatives (Kennedy & Carpenter (1994)); the filtering (applied at interior points only) is required to maintain numerical stability for long-time integrations but since it acts only on the shortest waves that can be resolved on the grid, it does not act as a turbulence model allowing under-resolved computations. A parallelization using three-dimensional domain decomposition and message passing, and an efficient parallel tridiagonal solver (Muller & Scheerer (1991)) were used.

The configuration is illustrated in figure 1 for the OH case, which shows the mixing layer composed of the two streams (species 1 and 2 initially reside in the upper and lower stream, respectively), and the streamwise (x_1), cross-stream (x_2) and spanwise (x_3)

coordinates. The layer is not symmetric in extent in the x_2 direction, to accommodate the larger layer growth in the lighter fluid side. The free-stream density (ρ_1 or ρ_2) is calculated for each pure species at its free-stream temperature (T_1 or T_2) and at the initial uniform pressure (p_0). The vorticity thickness is defined as $\delta_\omega\left(t\right) = \Delta U_0/\left(\partial \langle u_1 \rangle /\partial x_2\right)_{max}$, where $\Delta U_0 = \left(U_1 - U_2\right)$ is the velocity difference across the layer. U_1 and U_2 were chosen so as to keep the ultimate vortex stationary in the computational domain (Miller *et al.* (2001), Papamoschou & Roshko (1988)); the specification of the convective Mach number (see table 3), $M_{c,0}$, determines ΔU_0. Given the initial streamwise velocity profile u_1 based on U_1 and U_2, $\left(\partial \langle u_1 \rangle /\partial x_2\right)_{max}$ and hence $\delta_{\omega,0} \equiv \delta_\omega\left(0\right)$ are calculated. The initial momentum ratio $|\rho_2 U_2|/|\rho_1 U_1| \sim 5$ for the OH layer and 3.5 for the OHe layer, as the choice of T_2 and T_1 for OHe determines ρ_2 and ρ_1 which together with information from the EOS yields U_1 and U_2. Although the momentum ratio has different values for the two layers, the momentum flux ratio, $\left(\rho_2 U_2^2/\rho_1 U_1^2\right)$, is unity for both layers. The specified value of the initial flow Reynolds number, $\mathrm{Re}_0 = \left(1/2\right)\left(\rho_1 + \rho_2\right)\Delta U_0 \delta_{\omega,0}/\mu_R$, chosen so as to enable the resolution of all relevant length scales, is then used to calculate μ_R, which scales μ. The grid spacing is approximately inversely proportional to Re_0, suggested by the relationship $l/\eta_K \sim \mathrm{Re}^{3/4}$ (Tennekes & Lumley (1989)) where l is the integral scale and η_K is the Kolmogorov scale.

The simulations are started with error-function profiles for the mean streamwise velocity, mass fraction and temperature, upon which are imposed spanwise and streamwise vorticity perturbations (Moser & Rogers (1991), Moser & Rogers (1993)) of strengths F_{2D} and F_{3D} respectively, whose streamwise (λ_1) and spanwise (λ_3) wavelengths are $\lambda_1 = C\delta_{\omega,0}$ and $\lambda_3 = 0.6\lambda_1$, where $C=7.29$ is the most unstable wavelength for incompressible flow. For the OHe DNS listed in table 3, the value of C was obtained from a stability analysis (similar to Okong'o & Bellan (2003)). The grid is the same for both simulations,

being chosen to accommodate four wavelengths in the streamwise and spanwise directions, and the layer evolution encompasses roll-up and two pairings of the four initial spanwise vortices into an ultimate vortex.

The boundary conditions are periodic in the x_1 and x_3 directions, and of outflow type for real gas in the x_2 direction, as derived by Okong'o & Bellan (2002b). The outflow conditions based on real-gas analysis are indispensable to maintain numerical stability since the initial perturbation causes large-amplitude p waves that must be allowed to exit the domain with minimal reflection.

The DNS database is summarized in table 3, including the transitional time $t_{tr}^* = t_{tr} \Delta U_0 / \delta_{\omega,0}$ and the value of the momentum-thickness based Reynolds number, $\text{Re}_m = \text{Re}_0 \, \delta_m / \delta_{\omega,0}$, at transition, with

$$\delta_m = \frac{\int_{x_2,\text{min}}^{x_2,\text{max}} \left[\langle \rho u_1 \rangle_{x_2,\text{max}} - \langle \rho u_1 \rangle \right] \left[\langle \rho u_1 \rangle - \langle \rho u_1 \rangle_{x_2,\text{min}} \right] dx_2}{\left(\langle \rho u_1 \rangle_{x_2,\text{max}} - \langle \rho u_1 \rangle_{x_2,\text{min}} \right)^2}, \tag{3.1}$$

where $x_{2,\text{max}} = L_2/2$, $x_{2,\text{min}} = -L_2/2$ (Okong'o & Bellan (2002a)), and t_{tr} is the time at which the one-dimensional velocity-fluctuation-based energy spectra become smooth, except for the forcing frequency. The goal of the LES is to reproduce the dependent variables, e.g. mean values, fluctuations and as much as possible their spatial distribution exhibited by the HDGM regions. The HDGM regions, discussed by Miller *et al.* (2001) and Bellan (2006) redistribute turbulent energy from the normal direction to the tangential direction, as found in the experiments of Hannoun *et al.* (1988) at sharp density boundaries. Unless one can capture this local aspect of the flow, it is very unlikely that phenomena crucial to mixing and combustion could be accurately predicted in propulsion systems; particularly, the p distribution has a strong impact on the prediction of the velocity field and the T, Y and p gradients influence the heat flux computation (see (2.11)).

4. LES initial and boundary conditions

Consistent with the LES equations, which are obtained from the original conservation equations through filtering, the LES initial conditions are also obtained by filtering followed by grid coarsening (e.g. Leboissetier *et al.* (2005), Vreman *et al.* (1997), Geurts and Frohlich (2002)) to retain only those nodes that will be used in LES.

The boundary conditions are periodic in the x_1 and x_3 homogeneous directions and non-reflective in the x_2 direction, similar to that of DNS. The non-reflective boundary conditions, which were developed on the equivalent Euler equations (Okong'o & Bellan (2002b)), do not explicitly involve the **q**-correction term. In these boundary conditions, the dependent variables are those computed in LES, which, according to the SGS model, may or may not contain an additional correction term.

5. LES numerical methodology

The numerical method in LES is essentially the same as in DNS (see §3), so as to attribute differences between LES and DNS to the SGS models rather than the numerical method. For LES to be meaningful, the computational grid must be specified to be fine enough to represent the mean initial profiles and to resolve the large eddies, and coarse enough to require SGS modeling.

The chosen grid for LES is here $\Delta x_{LES} = 4\Delta x_{DNS}$. This grid resolution is justified by the energy spectra and also by LES comparisons both with FC-DNS and with a LES devoid of SGS-flux model, called the "No SGS" model case; see §6.2. Although the mathematical form of the equations for the combined No SGS model with the No HF model is identical to the unfiltered equations, the meaning of the dependent variables is different since in the first case the computed solution is that of the filtered equations; the meaning of the variables is important when one wishes to compare simulation results

with experimental data. Thus, even for the No SGS model with No HF model case, the scientific target is to reproduce the FC-DNS. Because of the identical form of the equations, one may consider the No SGS model with No HF model case to be an under-resolved DNS, depending on the viewpoint of interest, and then it should be compared to the coarsened DNS.

The grid and test filters have a cubic top-hat mathematical form (for which the filtered value is simply the integrated value over the filter width), being the only one consistent with easy interpretation of results when using a finite difference scheme. The spatial discretization is the same sixth-order accurate compact scheme used in the DNS, and time integration is also performed using a fourth-order explicit Runge-Kutta scheme, as in DNS. The $\bar{\Delta}$ width is a compromise between retaining the maximum amount of information in the resolved scales and minimizing the discretization-error influences. In order to limit numerical errors, $\bar{\Delta}/\Delta x_{LES}$ must be chosen according to the accuracy of the space discretization scheme, irrespective of the grid resolution. For a sixth-order Padé scheme, this ratio must be $\bar{\Delta} \geqslant 2\Delta x_{LES}$ (Chow and Moin (2003), Ghosal (1996)), and the present choice is $\bar{\Delta} = 2\Delta x_{LES}$, meaning that the smallest resolved eddy is represented by at least two grid points.

Time stability is ensured by applying an explicit high-order filter to the conservative variables in each spatial direction. Since the role of this filter is to prevent aliasing from contaminating the lower wave-number scales of the solution (Kennedy & Carpenter (1994)), it is sometimes advisable to filter at every time step. Although for the well-resolved DNS grid the frequency of the high-order filtering is not expected to alter the solution, for LES devoid of a SGS model, since the LES grid resolution is only sufficient to resolve the large scales, the selected filtering frequency is expected to affect the solution. After some experimentation, we filtered the solution every five time steps for all LES,

including those devoid of SGS models (i.e. either No HF or No SGS models). Additionally, unlike in DNS, filtering is performed over the entire domain including the points at and near the non-periodic boundaries, and the order of the filter is increased to twelve in the interior with sixth-order boundary closures. Finally, the CFL number was unity, as in the DNS.

6. Results

The solution of the LES (2.1)-(2.4) and (2.18), ϕ_{LES}, and the equivalent $\psi_{LES} \equiv \psi(\phi_{LES})$, are each here compared to the solution represented by $\overline{\phi}$ computed from the FC-DNS and the corresponding vector $\overline{\psi} = \psi(\overline{\phi})$. As stated in §1, ϕ_{LES} will be here compared to $\overline{\phi}$ at the LES grid nodes and the hope when using the q-correction model is to obtain a ϕ_{LES} that is closer to $\overline{\phi}$ than when using a SGS-flux model alone, so as to enhance the prediction accuracy when utilizing coarse grids. We first re-visit our previous *a priori* study (Selle *et al.* (2007)) in §6.1 by examining the performance of the heat-flux correction models proposed in §2.4.2. Then, we select the best q-correction term model and in §6.2 we assess, *a posteriori*, LES results obtained either without or with the q-correction in conjunction with a variety of SGS-flux models for OH750; for OHe600 LES we only use a selection of the SGS-flux models utilized for OH750. The stringent goal here is to reproduce in LES both the spatial and temporal equivalence of the FC-DNS. If only statistical equivalence is desired (Pope (2004)), the flexibility in the choice of a model is considerably larger.

6.1. *Revisiting the a priori study on the heat-flux correction*

Unlike in Selle *et al.* (2007), we rank here the magnitude of terms in the LES energy equation based on x_2-r.m.s. activity using the FC-DNS, and as in Selle *et al.* (2007) we use this information to assess the need for additional SGS models to those for the

SGS heat flux. Having established that such additional SGS models are needed, models No HF and M1-M5 are then evaluated to understand their capabilities in reproducing the desired term; as stated in §2.4.2, the goal is to obtain a model which minimizes $\left(\nabla \cdot \overline{[q_{IKj}(\phi) - \overline{q_{IKj}(\phi)}_M]} \right)$, where the subscript M denotes a model. We next examine the influence of the N value and finally we inspect the impact of the filter discrete representation on the accuracy of the model.

6.1.1. x_2-r.m.s. activity

The r.m.s. activity of each term in the energy equation is computed by integrating its x_2 variation of the homogeneous plane average. The integration is performed at selected times corresponding to landmark stages in the layer's development and is tabulated in table 4 for OH and table 5 for OHe. For OH, the table lists the terms ranked from that having the most significant contribution at $t_{tr}^* = 150$ to that with the least contribution at that time station, and for OHe the ranking follows that at $t_{tr}^* = 220$. At all listed times, the leading order terms are the advection, pressure work, SGS-flux term, heat flux and **q**-correction. Compared to the pressure work which ranks second in order of magnitude, the **q**-correction term varies from 10% to 27% of the pressure work magnitude for OH and from 4% to 8% for OHe, and thus the impact of the **q**-correction on the total energy prediction is expected to be small. However, at the listed times, the **q**-correction term represents from a minimum of 32% at $t^* = 150$ to a maximum of 56% at $t^* = 50$ of the heat flux for the OH case, and the equivalent values for OHe are 35% at $t^* = 220$ and 64% at $t^* = 50$. The indication is that the **q**-correction may play an important role in the accurate **q** prediction.

To complement the tabulated data, the x_2-r.m.s. of the leading order terms in the LES energy equation are compared using the FC-DNS database and the results are plotted in figure 2 at $t^* = 50$ and $t^* = 150$ for the OH750 layer, and figure 3 at $t^* = 100$ and $t^* = 220$

for the OHe600 layer. For the OHe600 layer, the influence of the $\bar{\Delta}/\Delta x_{DNS}$ ratio is also

illustrated. For the OH750 case displayed in figure 2, the advection term has the largest

contribution, being followed by the pressure work and the subgrid term, which compete

at the early times of the simulation with the pressure work and becomes dominant at

$t^* = 100$ (not shown) and $t^* = 150$. The heat flux contribution is approximately half of

that of the SGS-flux subgrid term, and that from $\left(\nabla \cdot \overline{[\mathbf{q}(\phi)} - \mathbf{q}(\bar{\phi})]\right)$ is half of the heat

flux term value. All other terms in the energy equation are small in comparison, and

thus not shown. Based on this analysis we conclude that the $\mathbf{q}$-correction is necessary

particularly at the early stages of the layer development and that its contribution is larger

than the viscous work term but smaller than the SGS-flux term. The OHe results shown

in figure 3 support the conclusions from the OH750 analysis and additionally show that,

as expected, when $\bar{\Delta}/\Delta x_{DNS}$ increases, the value of $\left(\nabla \cdot \overline{[\mathbf{q}(\phi)} - \mathbf{q}(\bar{\phi})]\right)$ increases as

well: for $\bar{\Delta}/\Delta x_{DNS} = 4$, the contribution of $\left(\nabla \cdot \overline{[\mathbf{q}(\phi)} - \mathbf{q}(\bar{\phi})]\right)$ is up to 30% of $\nabla \cdot \mathbf{q}(\bar{\phi})$

at $t^* = 100$ and up to 25% $t^* = 220$, whereas for $\bar{\Delta}/\Delta x_{DNS} = 8$, the corresponding

values are approximately 50% and 40% respectively. Thus, if the LES prediction of the

effective heat flux is of concern, as it is in liquid rocket engines (Tucker *et al.* (2008)), it

is apparent that a $\mathbf{q}$-correction term will be necessary in the energy equation.

To gain a better understanding of the primary effect governing the heat flux in the

present DNS, the three terms of (2.11) are further examined for the OH750 layer. The

x_2-r.m.s. difference between the filtered heat flux divergence and the heat flux divergence

calculated using $\bar{\phi}$ for each of the three terms is compared in figure 4 at $t^* = 50$ and

150. At both t^* values, the maximum contribution is from the species mass-fraction

gradient term, being comparable to the heat flux value. The temperature gradient and

pressure gradient terms are comparable, being less than one fifth the value of the species

mass gradient term. When the difference between the free-stream temperatures is larger

than the 200K of the OH750 case, the ratios of the respective contributions may change; indeed, for rocket propulsion applications, this difference will be one order of magnitude larger.

Furthermore, to assess whether $C_{A_j}(\phi)$ or $\nabla A_j(\phi)$ dominate each contribution, the corresponding coefficients and gradients are separately examined using the FC-DNS for the OH750 layer. The species mass-fraction gradient is the smallest but its associated coefficient is the largest among all three coefficients (not shown). The largest difference between the filtered contribution and the contribution computed using the filtered flow field is obtained from the pressure gradient term but since its coefficient is very small, the overall contribution to the heat flux difference due to the pressure gradient is small compared to that of the species mass-fraction gradient term. Based on the high coefficient values of the species mass-fraction gradient contribution (the main contributor of the heat flux; see figure 4), it is natural to hypothesize that the modeling effort should focus on the coefficients; this strategy was the approach of Selle *et al.* (2007). Although Selle *et al.* (2007) were successful in modeling the coefficients, the heat flux representation was deemed unsatisfactory. To investigate this paradox, we examine here both the mean and the r.m.s. of the difference between the filtered term and the term computed using the filtered flow field due to the species mass gradient; the examination is both from the standpoint of coefficients and total contribution to the q-correction. Figure 5(a) illustrates the x_2-r.m.s. of the differences in coefficients, gradients and heat flux at $t^* = 150$. The results show that although the difference between coefficient values is high compared to that between the gradients, there is no correlation between the x_2-distribution of the coefficients' difference and the heat flux difference, whereas, the difference in gradients closely follows that of the corresponding term in the heat flux. This indicates that the heat flux difference is governed by the gradients rather than the coefficients. Unrigorously

assuming that

$$\overline{C_A(\phi)\nabla A(\phi)} = \overline{C_A(\phi)}\ \overline{\nabla A(\phi)}, \tag{6.1}$$

then the heat flux difference, proportional to the difference in gradients, becomes

$$\overline{C_A}\ \overline{\nabla A} - C_A(\bar{\phi})\ \nabla A(\bar{\phi}) \simeq \alpha(\overline{\nabla A} - \nabla A(\bar{\phi})). \tag{6.2}$$

This implies that

$$\overline{C_A} \simeq C_A(\bar{\phi}) \simeq \alpha \tag{6.3}$$

where α is approximately constant. Although, having an approximately constant coefficient value seems inconsistent with the aforementioned large difference in species mass coefficients (see figure 5), this seemingly inconsistent result is understood if the coefficient value is examined. Indeed, $(\overline{C_A} - C_A(\bar{\phi}))$ is only 2% of either of the coefficient's values, hence it can be considered negligible. This finding highlights why the models proposed in the previous *a priori* study Selle *et al.* (2007), focussing on the coefficient correction rather than the gradient terms, had limited success.

6.1.2. *Effect of the mathematical model*

To measure the effectiveness of **q**-correction (2.37)-(2.42) models, the x_2-r.m.s. activity study of §6.1.1 is now performed for No HF and M1-M5 and the results are listed in table 6 for $N = 2$. As clearly seen from table 6, the minimum difference, $\frac{\partial}{\partial x_j}\left(\overline{q_j(\phi)} - \overline{q_j(\phi^*)}\right)$, is obtained when using M1, followed by M2 and M4, as expected. These three models are approximately 30% better than the No HF case. Model M3 is the least satisfactory, yielding results no better than the No HF model, which confirms the importance of the gradient reconstruction rather than that of the coefficients. The main deficiency of the No HF model is the calculation of gradients from $\bar{\phi}$, as in M3. This can be partially avoided if the gradients are calculated from the approximated values instead, ϕ^*, as in M1, M2, M4. The fact that models M2 and M4, which only differ in calculation of the

coefficients, give similar results shows that different coefficient calculations have small effect on the final outcome, confirming the conclusions of §6.1.1, as also supported by the M3 and No HF model results.

The evaluation of the models' performance is also conducted through a visual inspection of the x_2-r.m.s. activity for models M1 to M5 using $N = 5$. Figure 6 displays the difference between the filtered heat flux divergence and the heat flux divergence calculated from the filtered field at $t^* = 50$ and 150. The results are consistent with the domain-r.m.s. activity study; the best model is M1, followed by M2; M3 yields comparable results with the No Model case; M4 produces similar results with M2. The explicit-filtering model (M5) has a better performance than the No HF model at $t^* = 50$, but not at $t^* = 150$.

6.1.3. *Influence of the ADM reconstruction order*

Stolz *et al.* (2001) report that generally $N = 3$ gives acceptable approximations and $N > 5$ does not lead to substantial improvement in the reconstruction. To investigate the effect of the N value for the present purposes, the M1 approximation is obtained using $N \in [0,5]$. For $N = 0$ one recovers M5. The results are displayed in figure 7. As expected, as N increases the discrepancy between the filtered heat flux and that computed from the filtered solution decreases. However, consistent with the results of Stolz *et al.* (2001), the improvement after $N = 3$ is minimal. Based on this analysis, we use $N = 3$ as the reconstruction order.

6.1.4. *Impact of the discrete representation of the filter*

Stolz *et al.* (2001) performed ADM using a discrete implicit Padé filter which is different from the top-hat filter (in conjunction with the trapezoidal rule) used in our study. It is thus legitimate to inquire if there is an effect of the discrete representation for the top-hat

filter on the reconstruction achieved through ADM. We thus investigate the explicit filter

of Stolz *et al.* (2001) along with three other filter formulations:

- **Filter A.** $G(\omega) = (1 + cos(\omega))/2$, top hat using trapezoidal rule.

- **Filter B.** $G(\omega) = (2 + cos(\omega))/3$, top hat using Simpson's rule

- **Filter C.** $G(\omega) = (10 + 8cos(\omega) - 2cos(2\omega))/16$, explicit Padé filter.

- **Filter D.** $G(\omega) = (16 - 2cos(3\omega) + 18cos(\omega))/32$, explicit filter.

for which the transfer functions are shown in figure 8 and the filter-to-grid ratio is 2,

except for the explicit Padé filter for which it is 1.5.

Figure 9 displays the r.m.s. of the difference between the divergence of the filtered

heat flux and that obtained from the model, i.e., $\left(\nabla \cdot \left(\overline{\mathbf{q}(\phi)} - \overline{\mathbf{q}(\phi)_M} \right) \right)$, where $\mathbf{q}(\phi)$ is

calculated on the coarse grid $4\Delta x_{DNS}$. For the No HF model case, $\overline{\mathbf{q}(\phi)}_M = \mathbf{q}(\bar{\phi})$, which

is computed using the FC-DNS. The comparison is between the No HF model at $t^* = 50$

or 150 and the equivalent quantity obtained from M1 using $N = 5$. In figure 9(a), the

largest and smallest deficits are obtained with Filters D and B, respectively. Considering

that Filter B is not as dissipative as the others (see figure 8), obtaining the smallest error

when using this filter is not surprising. When M1 is employed, more than half of the

discrepancy in heat flux divergence is avoided for all filters. A similar trend is observed

at $t^* = 150$, however, the need for **q**-correction is reduced at $t^* = 150$ compared to

$t^* = 50$ (see figure 9(b)).

Filter A was adopted in the *a posteriori* study, in concert with our previous LES of

supercritical pressure flows (Taşkinoğlu & Bellan (2010)).

6.2. *A posteriori analysis*

The *a priori* study indicates the need for a **q**-correction term in the energy equation, but

the ultimate test for the correction necessity is whether it does improve the LES solution

so that it compares more favorably with the FC-DNS. That is, as stated in §1, the desire

is to rely on the **q**-correction to reintroduce some of the filtered physics back into LES. Here, we assess whether the **q**-correction can indeed introduce filtered information into LES additional to that introduced by the SGS-flux models. The assessment is for the two DNS which were performed for different species mixtures, free stream temperatures and initial layer perturbations, but that, however, have the same initial momentum flux ratio value of unity. Examination of the **q**-correction model for different species mixtures introduces generality to the concept since both the EOSs and transport properties are species-mixture dependent.

We first examine the effect of the **q**-correction model directly on the heat flux taking as an example the OH750 simulation, and then we continue with an analysis of the dependent variables from the standpoint of x_2-r.m.s. mean values, fluctuations and second-order correlations for the OH750 simulation and spatial visualizations for the OHe600 simulation.

6.2.1. *Effect of* **q**-*correction on heat flux computation*

The SGS-flux models used are GRC, SSC, SMD, and the mixed model MGRD. The GRC and SSC models are used with their calibrated coefficient values for $\bar{\Delta}/\Delta x_{DNS} = 8$ obtained from the corresponding DNS at $t_{tr}^* = 150$, as follows:

$$C_{GR} = 0.0910 \qquad\qquad \text{GRC,} \qquad\qquad (6.4)$$

$$C_{SS} = 0.4009 \text{ for } \widehat{\Delta} = 2\bar{\Delta} \qquad\qquad \text{SSC.} \qquad\qquad (6.5)$$

As stated in §2.4.1, among all possible dynamic mixed SGS-flux models, MGRD is here selected based on the formulation of the GR model emphasizing the reconstruction of a variable through its gradients (Okong'o & Bellan (2004b)), which as highlighted in §6.1, play a crucial role in the heat flux reconstruction. LES is conducted either with no SGS-flux model, denoted as "No SGS" model as already stated, or with SGS-flux

models. The flow field ϕ^* obtained from the FC-DNS using M1 is labeled RFC-DNS, where "R" stands for "Reconstructed". When the **q**-correction is included in a LES, the corresponding label for that LES has HF attached to the model, e.g. SMD HF. To investigate the effect of the **q**-correction, LES without **q**-correction are first performed. Then, LES using the same SGS-flux models are conducted, now with the **q**-correction model M1 using $N = 3$ and Filter A. The results are compared with the DNS, and with the FC-DNS or the RFC-DNS.

The comparisons in figure 10(a) are for the OH750 case and involve evaluating the x_2-r.m.s. activity of the divergence of the heat flux computed from the filtered flow field of either LES or FC-DNS when no **q**-correction model is used, as in (2.43). The comparison is with respect to the DNS quantity it means to reproduce, i.e., $\overline{\nabla \cdot \mathbf{q}(\phi)}$. The results show that the target LES solution, FC-DNS, overpredicts the filtered heat flux divergence (the maximum overprediction is 20% at $x_2/\delta_{\omega,0} = 6$); this is understandable since on the coarse FC-DNS grid the computed gradients will be larger, and it was determined in §6.1.1 that the gradients govern the heat flux. All LES using SGS-flux models also overpredict the DNS, with the maximum overprediction being approximately 40% except for the SMD model for which it is 70% at $x_2/\delta_{\omega,0} = 2$. The heat flux divergence of the No SGS model solution is twice as large as the divergence obtained from the FC-DNS, yielding worse results than any LES using a SGS-flux model, thus indicating the significance of the SGS-flux modelling. Illustrated in 10(b) is the filtered divergence of the heat flux computed from the reconstructed flow field of either LES or FC-DNS when the LES uses the **q**-correction as in (2.44); this quantity is also compared to the DNS-extracted quantity it means to reproduce, i.e., $\overline{\nabla \cdot \mathbf{q}(\phi)}$. Figures 10(a) and 10(b) are plotted at the same scale to facilitate the comparison between models without and with **q**-correction. When implementing the **q**-correction one computes the divergence of the

heat flux from the reconstructed flow field, ϕ^*, instead of the LES or FC-DNS flow field. This leads to a better heat flux divergence approximation as the **q**-correction model shifts the FC-DNS curve to the RFC-DNS which practically coincides with the DNS, with less than 1% discrepancy (10(b)). Additionally, when the **q**-correction is employed, a clear improvement is exhibited in the x_2-r.m.s. values of the filtered heat flux divergence for all LES, including the No SGS model case, as all LES better predict the filtered DNS heat flux divergence than the LES of figure 10(a). The remarkable improvement of the predictions even in the absence of SGS-flux model indicates that the **q**-correction model has the ability to insert considerable SGS activity into the LES equations. In fact, with the exception of the SMD model overprediction, within the layer all SGS-flux model predict values that almost coincide with $\overline{\nabla \cdot \mathbf{q}(\phi)}$, with the best prediction within the layer being obtained with the MGRD model.

Complementing the information in figure 10, displayed in figure 11(a) is the x_2-r.m.s. of $\left(\overline{\nabla \cdot \mathbf{q}(\phi)} - \nabla \cdot \mathbf{q}(\overline{\phi}) \right)$ where $\overline{\phi}$ is either the LES or the FC-DNS flow field for LES devoid of the **q**-correction. Correspondingly exhibited in figure 11(b) is the x_2-r.m.s. of $\left(\overline{\nabla \cdot \mathbf{q}(\phi)} - \overline{\nabla \cdot \mathbf{q}(\phi^*)} \right)$ where ϕ^* is the reconstructed flow field of either LES or FC-DNS for LES conducted with **q**-correction. Each of these quantities represents the difference between the value that should have entered (2.3) according to the ideal LES based on the DNS and the value that has actually been used. The goal of SGS modeling is to minimize $\left(\overline{\nabla \cdot \mathbf{q}(\phi)} - \nabla \cdot \mathbf{q}(\overline{\phi}) \right)$ by using SGS-flux models and $\left(\overline{\nabla \cdot \mathbf{q}(\phi)} - \overline{\nabla \cdot \mathbf{q}(\phi^*)} \right)$ by using the combination of SGS-flux and **q**-correction models. The effectiveness of the **q**-correction model is measured by the reduction in magnitude from $\left(\overline{\nabla \cdot \mathbf{q}(\phi)} - \nabla \cdot \mathbf{q}(\overline{\phi}) \right)$ to $\left(\overline{\nabla \cdot \mathbf{q}(\phi)} - \overline{\nabla \cdot \mathbf{q}(\phi^*)} \right)$. For figure 11(a), since the LES is conducted without **q**-correction, the evaluated difference represents the neglected SGS heat flux contribution in (2.3) according to either the FC-DNS or the LES solution;

for figure 11(b), since the LES is conducted with **q**-correction, the computed quantity

measures the deficit, despite **q**-correction modeling, between the ideal LES heat flux ac-

cording to the DNS and that included according to either the RFC-DNS or the LES

solution. Moreover, on both figures 11(a) and 11(b) we present, for comparison, the x_2-

r.m.s. of $\overline{\nabla \cdot \mathbf{q}(\phi)}$ computed from the DNS and note that it does not correspond to the

quantity stated on the ordinate axis. The ordinate non-dimensionalization is such that

the x_2-r.m.s. of $\overline{\nabla \cdot \mathbf{q}(\phi)}$ reaches a maximum of unity. Clearly, without **q**-correction, the

smallest neglected SGS contribution is that of the FC-DNS, which is still substantial at a

maximum of 35% of the ideal $\overline{\nabla \cdot \mathbf{q}(\phi)}$. At the other extreme of deviation from the ideal

$\overline{\nabla \cdot \mathbf{q}(\phi)}$ is the No SGS model for which the neglected SGS contribution is as large as

a factor of 1.85 of the filtered DNS heat flux; an overestimate is indeed expected since

without the dissipative effect of the SGS-flux models, gradients are larger, and as shown

above, the gradients govern the heat flux. With a SGS-flux model, this factor is reduced

to a maximum of 1.5 of the filtered DNS heat flux. The SGS-flux model for which the

neglected quantity is smallest is the GRC model, presumably because its essence is to

focus on reconstruction through gradient computation, but even the GRC-model LES

is only slightly closer to the FC-DNS than those with other SGS-flux models. Thus,

without **q**-correction, the neglected value is as much as 1.5-1.85 larger than the filtered

DNS heat flux. With the **q**-correction, the divergence discrepancy computed using the

RFC-DNS is almost null which fulfills the best expectation one may have, and that of

the No SGS model is reduced from the maximum of 1.85 to as much as a factor of 1.3.

When a SGS-flux model is used, the overestimate is reduced to a maximum factor of 1.2

for the MGRD model, which is the model having the smallest discrepancy. This means

that although the model $\overline{\nabla \cdot \mathbf{q}(\phi^*)}$ for $\overline{\nabla \cdot \mathbf{q}(\phi)}$ is very accurate, as shown in figure 10(b),

in LES with any SGS-flux model and even including the **q**-correction, the activity of the

SGS heat flux discrepancy exceeds that of the ideal filtered heat flux, $\overline{\nabla \cdot \mathbf{q}(\phi)}$.

According to statement (2.44), $\left(\overline{\nabla \cdot \mathbf{q}(\phi^*)} - \nabla \cdot \mathbf{q}(\overline{\phi}) \right)$ plotted in figure 11(c) repre-

sents the correction term added to (2.3) using the **q**-correction model. Examination of

the results illustrated in figure 11(c) indicates that with the implementation of the **q**-

correction in LES and the utilization of the reconstructed LES flow field for heat flux

computation, this SGS heat-flux divergence difference is similar to that of the RFC-DNS

for all SGS-flux models (with the exception of the No SGS model case for which it is

larger). This is the best that could be hoped and indicates that this remaining error is

irreducible for the SGS heat-flux divergence difference, as also implied by the results of

figure 10(b).

It is thus clear that $\overline{\nabla \cdot \mathbf{q}(\phi^*)}$, where ϕ^* is the reconstructed flow field from LES

including a SGS-flux model and the **q**-correction, is a much better approximation of the

filtered DNS heat flux divergence, $\overline{\nabla \cdot \mathbf{q}(\phi)}$, than is $\nabla \cdot \mathbf{q}(\phi_{LES})$ computed from a LES

which does not include the **q**-correction model (compare figures 10(a) and 10(b)).

6.2.2. *Effect of the* **q**-*correction on flow-variable means, fluctuations and second-order*

correlations

So far, the focus has been on the heat flux prediction and it was shown that irrespective

of the employed SGS model, the proposed **q**-correction method improves the LES heat

flux prediction. It is though also of interest to examine whether the effect of **q**-correction

additionally improves the prediction of flow variables. For this purpose, the SGS model

most sensitive to the **q**-correction according to the above OH750 analysis — MGRD —

is selected and LES for the OH750 case, with or without **q**-correction (MGRDHF or

MGRD No HF, respectively) are compared. Comparisons are first conducted for the

timewise variation and then for the spatial variation at the transitional time ($t_{tr}^* = 150$).

Ezgi S. Taskinoglu and Josette Bellan

The time variations are obtained by integrating the homogeneous-plane means for each flow variable in the non-homogenous x_2-direction. For any variable A, fluctuations are computed either as $A' = A - <A>$, or for Favre-averaged quantities $\{A\} = <\rho A> / <\rho>$ as $A'' = A - \{A\}$.

Figure 12 illustrates the time variation of non-dimensionalized quantities representing the evolution of $\{T\}, <p>, \{T''\}, <p'>, <\rho'>$ and $\{Y_2''\}$. Except for $<p>$ and $<p'>$ which exhibit improvement over most of or over the entire history, respectively, with the addition of the **q**-correction (figures 12(b) and (d)), the other variables' variation does not benefit from the **q**-correction by comparison with the FC-DNS template other than towards the end of the calculation when the corresponding curve is redressed with respect to the computation devoid of **q**-correction reaching towards the FC-DNS. This is particularly pronounced for $\{T\}$ and $\{T''\}$ (figures 12(a) and (c)) which show that the addition of the **q**-correction causes $\{T\}$ to increase and $\{T''\}$ to decrease. It is conjectured that the less favorable agreement of MGRDHF with the FC-DNS than MGRD No HF except towards the end of the simulation is due to the lack of strong HDGM regions before that time, invalidating the need for **q**-correction. However, the positive impact of the **q**-correction over the $<p>$ and $<p'>$ timewise prediction foretells of corresponding improvements in the velocity field that are explored below.

To check whether the **q**-correction indeed beneficially affects the solution at the transitional state, the variables examined in figure 12 are now spatially assessed versus the non-homogeneous direction at $t_{tr}^* = 150$ in figure 13. Although the positive effect of **q**-correction is subtle for $\{T\}, <p>$ and $\{T''\}$ (figures 13(a), (b) and (c), respectively), it is definitely discernible for $<p'>, <\rho'>$ and $\{Y_2''\}$ (figures 13(d), (e) and (f), respectively), particularly for $<p'>$ and $\{Y_2''\}$ for which substantial improvement is observed.

Since the fluctuation part of the velocity field imparts to a turbulent flow its character, in figure 14 both timewise (figures 14(a), (c) and (e)) and spatial variations (figures 14(b), (d) and (f)) are displayed for each u_1, u_2, and u_3 fluctuations. Clearly, with the **q**-correction an amelioration of temporal quantity prediction is obtained especially at the later times of the layer evolution, consistent with the development of strong HDGM regions at those times. Noteworthy, for this LES the velocity field benefits more than the thermodynamic variables (figure 12) from the **q**-correction. The inclusion of the **q**-correction also enables LES to capture the spatial variation of velocity fluctuations at $t_{tr}^* = 150$ with a dramatic recovery of the FC-DNS template particularly in the cross-stream and spanwise directions. Without **q**-correction, the fluctuating u_2 velocity is underestimated whereas the fluctuating u_3 velocity is overestimated, which could partially conceal in turbulent kinetic energy calculations the effect of **q**-correction.

Finally, the spatial variation of second-order correlations is scrutinized including the Reynolds stresses, $< \rho u_1'' u_2'' >, < \rho u_2'' u_3'' >$, and correlations between dynamic and thermodynamic variables $< \rho u_1'' Y_2'' >, < \rho u_2'' Y_2'' >, < \rho u_1'' T'' >, < \rho u_2'' T'' >$; the results are displayed in figure 15. All second-order correlations substantially benefit from the **q**-correction, but most considerably those involving u_2 (figures 15(b), (d) and (f)). Since recovery of the second-order correlations is at the heart of turbulence modeling, it is clear that the **q**-correction considerably improves the accuracy of supercritical LES computations.

6.2.3. *Effect of the* **q***-correction on flow variable visualizations*

To illustrate the effect of the **q**-correction model on flow visualizations, the OHe600 case is selected because at the same momentum flux ratio, $(\rho_2 U_2^2 / \rho_1 U_1^2) \sim 1$, it achieves a 25% higher value of $\text{Re}_{m,tr}$ (see table 3) than the OH750 case and thus the results are slightly more relevant to fully turbulent flows.

To assess the influence of the **q**-correction model for the OHe600, selected LES were performed without and with the M1 **q**-correction model, and they were compared to the FC-DNS. Results are displayed in figure 16 and on figure 17 for the SMD and MGRD SGS-flux models, respectively. The comparisons are made for $|\nabla\rho|$ because the structure of the HDGM regions crucially affects turbulence distribution in the flow field (Hannoun *et al.* (1988)), p/p_0 because of the strong coupling among thermodynamic quantities through the EOS and because the accurate p prediction governs that of the velocity field, Y_o because it is a manifestation of mixing, and T because it is intertwined with **q**.

Considering figure 16 and comparing the results of the LES using the SMD model devoid of **q**-correction model with the FC-DNS template, it appears that the former is unable to accurately reproduce the HDGM regions of the FC-DNS, even though these regions do not exhibit much small-scale structure. In this LES, the p field is overpredicted in that regions of either small or large p are enlarged, and the detailed structure of both Y_o and T inside the vortex is missed although the size of the vortex is reasonably well captured. The LES including the **q**-correction model is no more successful than that devoid of this **q**-correction model in recovering the structure of the FC-DNS, indicating that the overdissipative deficiency of the SMD model cannot be palliated by the **q**-correction model since the ADM reconstruction is SGS-flux model dependent, as stated in §2.4.2.

As shown in figure 17, when using the MGRD model alone, without the **q**-correction, the LES mispredicts all spatial distributions of $|\nabla\rho|$, p/p_0, Y_o and T. The spatial extent of the HDGM regions is overpredicted, the relative placement of the low and high p regions is incorrect, the size of the vortex is reduced with respect to that of the FC-DNS and as a result the Y_o and T fields are incorrect. Including the **q**-correction model in LES enlarges the vortex size, although it is still somewhat reduced with respect to that

of the FC-DNS, leads to a much better representation of the HDGM regions, redresses the incorrect relative placement of the low and high p regions although all details of the FC-DNS are still not captured, and improves the Y_o and T distributions, although the entire structure of the template is still not well reproduced.

Given the lack of predictive capability of the LES using the SMD model whether devoid of or in conjunction with the **q**-correction model, and the serious deficiencies of the LES utilizing the MGRD model without **q**-correction, by elimination, the LES utilizing the MGRD model and including the **q**-correction seems the most promising.

7. Summary and conclusions

A priori and *a posteriori* studies were both here conducted to identify the necessary subgrid-scale (SGS) models in Large Eddy Simulation (LES) for predicting counterflow fluid motion, disintegration and mixing of either oxygen/hydrogen or oxygen/helium at an initial pressure higher than the critical pressure of these fluids. The LES governing equations consist of the filtered original equations for conservation of mass, momentum, species and total energy coupled with a real-gas equation of state (EOS); these equations were previously solved using Direct Numerical Simulation (DNS) with transport properties which were functions of the thermodynamic variables. Identified in a previous *a priori* investigation (Selle *et al.* (2007)), for these fluids, the SGS terms in the filtered differential equations consist of two types: (i) the typical SGS-flux terms, and (ii) a heat flux correction in the energy equation accounting for the difference between the filtered divergence of the heat flux computed using the DNS flow field and the divergence of the heat flux computed from the filtered flow field. The second type of SGS term is the direct result of the strong coupling between the flow dynamics represented by the differential governing equations and the fluid thermodynamics represented by the highly

non-linear EOS. This coupling manifests through the appearance of high density-gradient magnitude (HDGM) regions having either a filamentary or blob-like aspect.

The configuration was that of a three-dimensional mixing layer with initially oxygen in the lower stream and either hydrogen or helium in the upper stream, and the DNS followed, for each realization, the evolution of the layer from an initial laminar state to a transitional state. The LES were carried out with the same numerical discretization and time advancement numerical scheme as the DNS. Both LES were conducted up to the same non-dimensional simulation time as the respective DNS using the filtered DNS initial conditions. In both cases, the LES grid volume was 64 times larger than the DNS grid volume.

In the *a priori* study, we identified the primitive variable gradients, rather than their associated coefficients, as controlling both the heat flux value and its spatial variation. This indicated that the focus should be on reconstructing these gradients from the filtered flow field rather than the coefficients as previously done by Selle *et al.* (2007). Among the three contributions to the heat flux due to temperature, species mass fraction and pressure gradients, the gradients due to species non-uniformities were by far the most important contribution to the heat flux; it was conjectured that the relative importance of these contributions may change in situations in which the initial temperature difference between free streams is larger than that constrained in the present DNS by the necessity to resolve the initial density gradient in the vorticity thickness layer. Several models were proposed for the gradient reconstruction and the success in this endeavor was checked by comparing the results to the filtered-and-coarsened DNS (FC-DNS), which is considered the LES template. Additionally, analyses for the selection of the reconstruction filter mathematical form and reconstruction order were conducted, leading to the choice of the Approximate Deconvolution Model (ADM) (Stolz & Adams (1999)) using a reconstruc-

tion order of 3 for the *a posteriori* study. With this model, the *a priori* analysis showed that the SGS heat-flux difference can be improved by as much as 60%. It was also shown that as the filter-to-grid ratio increases, the importance of the heat flux correction term with respect to the resolved heat flux increases.

The *a posteriori* LES tests were performed without or with the heat-flux correction model. Because the heat-flux correction model is computed from a LES with a specified SGS-flux model (which also encompasses a null SGS-flux model), the result of the heat-flux correction was intertwined with that of the SGS-flux model. The LES were conducted for the oxygen/hydrogen case with two constant-coefficient (Scale-Similarity and Gradient), two dynamic-coefficient (Smagorinsky/Yoshizawa and mixed Smagorinsky/Yoshizawa/Gradient) SGS-flux models, and with a null SGS-flux model. For the oxygen/helium case, LES were conducted with two dynamic-coefficient (Smagorinsky/Yoshizawa and mixed Smagorinsky/Yoshizawa/Gradient) SGS-flux models either devoid of or including the heat-flux correction model. The results showed that the heat flux representation is indeed improved through the heat-flux correction. For all SGS-flux models, with the exception of the null SGS-flux model, the use of the heat-flux correction through the ADM reconstruction effectively reduced the SGS heat-flux difference to that obtained from a reconstructed FC-DNS, called RFC-DNS, and thus further reduction is theoretically impossible. Examination of timewise and spatial cross-stream r.m.s. variations of variable means, fluctuations and second-order correlations highlighted the beneficial effect of the heat-flux correction. Flow visualizations showed that by elimination, the dynamic-coefficient mixed Smagorinsky/Yoshizawa/Gradient SGS-flux model including the heat-flux correction model was the most promising.

Lastly, the methodology of introducing in LES other SGS models than those addressing the SGS-fluxes may prove crucial for performing LES for turbulent flow in large

geometries for which coarse grids are the only option. For these coarse LES grids, neglected small-scale effects other than SGS fluxes could be considerable and the only way to reintroduce these effects into the LES computation may be through modeling differences between the unknown filtered quantity and the quantity computed in LES (using e.g. ADM). Such models may be necessary not only for the heat flux, but also for the pressure gradient in the momentum equation (see Taşkinoğlu & Bellan (2010)), for the stresses in the momentum equation, and/or for the work due to pressure or stresses in the energy equation. This strategy may enable LES in situations in which they are currently unpractical because the required grid for acceptable accuracy is too fine for computational efficiency.

Appendix A. Transport properties for O_2/He mixtures

For O_2/He mixtures, the Prandtl number is approximated as

$$\text{Pr} = 0.68 + 0.0283\xi - 0.5017\xi^2 - 0.5390\xi^3 + \Delta\,\text{Pr} \qquad (A\,1)$$

where

$$\xi = \min\left(0.5, Y_2 - 0.81\theta^{0.35}\right), \quad \theta = (T - 100)/800, \;\; 0 \leqslant \theta \leqslant 1, \; (T \text{ in Kelvin})$$

For $0.02 \leqslant \theta \leqslant 0.368$, $\Delta\,\text{Pr} = 2.42 Y_2^{14.6} \max\left(0.0, -0.23\left(1 + \ln\theta\right)\right)$, otherwise $\Delta\,\text{Pr} = 0$.

For O_2/He mixtures, the Schmidt number is approximated as

$$Sc = \Sigma\left(Y_2\right)\left[1 + (114/T)^{1.5}\right]/\left(1 + \Delta_s\right) \qquad (A\,2)$$

$$T < 200\text{K: } \Sigma = \left(1.292 - 0.757 Y_2 + 0.444 Y_2^2 - 0.757 Y_2^3\right)$$

$$T > 200\text{K: } \Sigma = \left(1.318 - 0.772 Y_2 + 0.453 Y_2^2 - 0.772 Y_2^3\right)$$

For $p < 30$ MPa, $\Delta_s = \min\left(0.08, 0.1264 + 0.226 Y_R\right) + 0.1\exp\left(-2400\theta^{4.5}\right)$ where $Y_R = Y_2 - \min\left(1, 0.5 + 0.78\theta^{0.6}\right)$, otherwise $\Delta_s = 0$.

Acknowledgements

REFERENCES

BARDINA, J., FERZIGER, J. & REYNOLDS, W. 1980 Improved subgrid scale models for large eddy simulation. AIAA 80-1357.

BELLAN, J., 2006 Theory, modeling and analysis of turbulent supercritical mixing, *Combust. Sci. Techn.* **178**, 253-281.

BELLAN, J. & SELLE, L. C. 2009 Large Eddy Simulation composition equations for single-phase and two-phase fully multicomponent flows. *Proc. Combust. Inst.*, **32**, doi:10.1016/j.proci.2008.06.005.

CHEHROUDI, B., TALLEY, D. & COY, E. 1999 Initial growth rate and visual characteristics of a round jet into a sub- to supercritical environment of relevance to rocket, gas turbine and diesel engines. AIAA 99-0206.

CHOW, F. K. & P. MOIN, P. 2003 A further study of numerical errors in large-eddy simulations. *J. Comp. Phys.* **184**, 366-380.

CLARK, R., FERZIGER, J., & REYNOLDS, W. 1979 Evaluation of subgrid-scale models using an accurately simulated turbulent flow. *J. Fluid Mech.* **91**(1), 1–16.

GERMANO, M., PIOMELLI, U., MOIN, P. & CABOT, W. 1991 A dynamic subgrid-scale eddy viscosity model. *Phys. Fluids A* **3** (7), 1760–1765.

GEURTS, B. J. 1997 Inverse modeling for large-eddy simulation, *Phys. Fluids* **9(12)**, 3585-3587.

Ezgi S. Taskinoglu and Josette Bellan

GEURTS, B. J. AND FROHLICH, J. 2002 A framework for predicting accuracy limitations in large-eddy simulation *Phys. Fluids* **14**(6), L41-L44.

GHOSAL, S. 1996 An analysis of numerical errors in large-eddy simulations of turbulence. *J. Comp. Phys.* **125**, 187-206.

HANNOUN, I. A., FERNANDO, H. J. S. & LIST, E. J.1988 Turbulence structure near a sharp density interface. *J. Fluid Mech.* **189**, 189-209.

HARSTAD, K. & BELLAN, J. 1998 Isolated fluid oxygen drop behavior in fluid hydrogen at rocket chamber pressures. *Int. J. Heat Mass Transfer* **41**, 3537–3550.

HARSTAD, K. & BELLAN, J. 2000 An all-pressure fluid-drop model applied to a binary mixture: heptane in nitrogen. *Int. J. Multiphase Flow* **26**(10), 1675–1706.

HARSTAD, K., MILLER, R. S. & BELLAN, J. 1997 Efficient high-pressure state equations. *A.I.Ch.E. J.* **43**(6), 1605-1610.

KEIZER, J., 1987 *Statistical Thermodynamics of Nonequilibrium Processes* Springler-Verlag, New York.

KENNEDY, C. & CARPENTER, M. 1994 Several new numerical methods for compressible shear layer simulations. *Appl. Num. Math.* **14** 397–433.

LEBOISSETIER, A., OKONG'O, N. & BELLAN J., 2005 Consistent large-eddy simulation of a temporal mixing layer laden with evaporating drops. Part 2: *A posteriori* modeling. *J. Fluid Mech.* 523, 37-78.

LILLY, D. 1992 A proposed modification of the Germano subgrid-scale closure method. *Physics of Fluids A* **4** (3), 633–635.

LIU, S., MENEVEAU, C. & KATZ, J. 1994 On the properties of similarity subgrid-scale models as deduced from measurements in a turbulent jet. *J. Fluid Mech.* **275**, 83–119.

MAYER, W., SCHIK, A., SCHWEITZER, C. & SCHAFFLER, M. 1996 Injection and mixing processes in high pressure LOX/GH2 rocket combustors. AIAA 96-2620.

MAYER, W., IVANCIC, B., SCHIK, A. & HORNUNG, U. 1998 Propellant atomization in LOX/GH2 rocket combustors. AIAA 98-3685.

MILLER, R., HARSTAD, K. & BELLAN, J. 2001 Direct numerical simulations of supercritical fluid mixing layers applied to heptane-nitrogen. *J. Fluid Mech.* 436, 1–39.

MOIN, P., SQUIRES, K., CABOT, W. & LEE, S. 1991 A dynamic subgrid-scale model for compressible turbulence and scalar transport. *Phys. Fluids* **3**(11), 2746-2757.

MOSER, R. & ROGERS, M. 1991 Mixing transition and the cascade to small scales in a plane mixing layer. *Phys. Fluids A* **3**(5), 1128–1134.

MOSER, R. & ROGERS, M. 1993 The three-dimensional evolution of a plane mixing layer: pairing and transition to turbulence. *J. Fluid Mech.* **247**, 275–320.

MULLER, S. M. & SCHEERER, D. 1991 A method to parallelize tridiagonal solvers. *Parallel Computing* **17**, 181–188.

OKONG'O, N. & BELLAN, J. 2002a Direct numerical simulation of a transitional supercritical binary mixing layer: heptane and nitrogen. *J. Fluid Mech.* **464**, 1–34.

OKONG'O, N. & BELLAN, J. 2002b Consistent boundary conditions for multicomponent real gas mixtures based on characteristic waves. *J. Comp. Phys.* **176**, 330–344.

OKONG'O, N. & BELLAN, J. 2003 Real gas effects of mean flow and temporal stability of binary-species mixing layers. *AIAA J.* **41**(12), 2429–2443.

OKONG'O, N. & BELLAN, J. 2004a Turbulence and fluid-front area production in binary-species, supercritical, transitional mixing layers. *Phys. Fluids* 16(5), 1467–1492.

OKONG'O, N. & BELLAN, J. 2004b Consistent large eddy simulation of a temporal mixing layer laden with evaporating drops. Part 1: Direct numerical simulation, formulation and *a priori* analysis. *J. Fluid Mech.* **499**, 1–47.

OKONG'O, N., HARSTAD, K., & BELLAN, J. 2002 Direct numerical simulations of O_2/H_2 temporal mixing layers under supercritical conditions. *AIAA J.* **40**(5), 914–926.

OSCHWALD, M. & SCHIK, A. 1999 Supercritical nitrogen free jet investigated by spontaneous Raman scattering. *Exp. Fluids* **27**, 497–506.

OSCHWALD, M., SCHIK, A. KLAR, M. & MAYER, W. 1999 Investigation of coaxial LN2/GH2-injection at supercritical pressure by spontaneous Raman scattering. AIAA-99-2887.

PAPAMOSCHOU, D. & ROSHKO, A. 1988 The compressible turbulent shear layer: an experimental study, *J. Fluid Mech.* **197**, 453–477.

POPE, S. B. 2004 Ten questions concerning the large-eddy simulation of turbulent flows, *New Journal of Physics* **6**, 35-59.

PRAUSNITZ, J., LICHTENTHALER, R. & DE AZEVEDO, E. 1986 *Molecular Thermodynamics for Fluid-Phase Equilibrium* Prentice-Hall.

PRUETT, C., SOCHACKI, J. & ADAMS, N. 2001 On Taylor-series expansions of residual stress. *Phys. Fluids* **13**(9), 2578–2589.

SARMAN, S. & EVANS, D. J. 1992 Heat flux and mass diffusion in binary Lennard-Jones mixtures *Phys. Rev.* **A45**(4), 2370-2379

SEGAL, C. & POLIKHOV, S. 2008 Subcritical to supercritical mixing. *Phys. Fluids* **20**, 052101-7.

SELLE, L. C., OKONG'O, N. A., BELLAN, J. & HARSTAD, K. G. 2007 Modeling of subgrid scale phenomena in supercritical transitional mixing layers: an *a priori* study. *J. Fluid Mech.* **593**, 57-91.

SMAGORINKSY, J. 1963 General circulation experiments with the primitive equations: part 1, basic experiments. *Mon. Weather Rev.* **91**, 99–164.

SMAGORINKSY, J. 1993 Some historical remarks on the use of nonlinear viscosities. *Large Eddy Simulation of Complex Engineering and Geophysical Flows*, edited by B. Galperin and S. Orszag, chap. 1, Cambridge University Press, 3–36.

STOLZ, S. & ADAMS, N. A. 1999 An approximate deconvolution procedure for large-eddy simulation, *Phys. Fluids* **11(7)**, 1699-1701.

STOLZ, S., ADAMS, N. A. & KLEISER, L. 2001 An approximate deconvolution model for large-eddy simulation with application to incompressible wall-bounded flows, *Phys. Fluids* **13(4)**, 997-1015.

TAŞKINOĞLU, E. S. & J. BELLAN, J. 2010 A posteriori study using a DNS database describing fluid disintegration and binary-species mixing under supercritical pressure: Heptane and Nitrogen. *J. Fluid Mech.* **645**, 211-254.

TENNEKES H. & LUMLEY, J. L. 1989 *A First Course in Turbulence* MIT Press.

TUCKER, P. K., MENON, S., MERKLE, C. L., OEFELEIN, J. C. & YANG, V. 2008 Validation of high-fidelity CFD simulations for rocket injector design. AIAA 2008-5226, presented at the 44th Joint Propulsion Conference, Hartford, CT.

VREMAN, B., GEURTS, B. & KUERTEN, H. 1995 A priori tests of large eddy simulation of the compressible plane mixing layer. *Journal of Engineering Mathematics* **29**, 299–327.

VREMAN, B., GEURTS, B. & KUERTEN, H. 1996 Large eddy simulation of the temporal mixing layer using the Clark model. *Theor. Comput. Fluid Dyn.* 8, 309–324.

VREMAN, B., GEURTS, B. & KUERTEN, H. 1997 Large-eddy simulation of the turbulent mixing layer. *J. Fluid Mech.* **339**, 357–390.

YOSHIZAWA, A. 1986 Statistical theory for compressible turbulent shear flows, with the application to subgrid modeling. *Phys. Fluids* **29**(7), 2152–2164.

Ezgi S. Taskinoglu and Josette Bellan

Species	m (g/mol)	T_c (K)	p_c(MPa)
H_2	2.016	33.0	1.284
He	4.003	5.19	0.227
O_2	31.999	154.6	5.043

TABLE 1. Pure species properties.

System	O_2/H_2	O_2/He
$\mu = \mu_R \left(T/T_R \right)^n$	$n = 0.75$	$n = 0.59$
$Sc \equiv \mu / \left(\rho \alpha_D D \right)$	$\left[\begin{array}{c} \left(1.334 - 0.668 Y_2 - 0.186 Y_2^2 - 0.268 Y_2^6 \right) \\ \times \left[1 + \left(88.6/T \right)^{1.5} \right] \end{array} \right]$	Eq. (A 2)
$\Pr \equiv \mu C_p / \left(m \lambda \right)$	$1.335/T^{0.1}$	Eq. (A 1)
α_{IK} or α_{BK}	$\alpha_{BK} = 0.2$	$\alpha_{BK} = 0.25$
T Range	200K–800K	100K–900K
p Range	$\sim$100atm	$\sim$100atm

TABLE 2. Transport properties for binary mixtures. $T_R = (T_1 + T_2)/2$, T in Kelvin. α_{BK} from Harstad & Bellan (1998) and Harstad & Bellan (2001).

Run	Re_0	$T_2; T_1$	ρ_2/ρ_1	$\lambda_1/\delta_{\omega,0}$	F_{2D}	F_{3D}	$L_1 \times L_2 \times L_3$	Δx	$Re_{m,tr}$	t_{tr}^*
							m^3	10^{-4} m		
OH750	750	400;600	24.40	7.29	0.1	0.05	$0.200\times0.200\times0.120$	5.77	1507	150
OHe600	600	235;287	12.17	9.31	0.05	0.0125	$0.255\times0.255\times0.153$	7.36	2004	220

TABLE 3. Listing of the Direct Numerical Simulation realizations and associated resolution. Both simulations were performed at $p_0 = 100$ atm and $M_{c,0} = 0.4$. L_i is the size of the domain in the x_i direction, in meters. For both layers, $L_1 = 4\lambda_1$, $\delta_{\omega,0} = 6.859\times10^{-3}$ m. For both simulations the grid has $352\times352\times208$ nodes. The subscript tr denotes the transitional time.

Energy	$t^* = 25$	$t^* = 50$	$t^* = 100$	$t^* = 150$
$\frac{\partial}{\partial x_j}\left(\bar{\rho}\tilde{e}_t\tilde{u}_j\right)$	52.39	123.67	191.59	199.63
$\frac{\partial}{\partial x_j}\left[p\left(\bar{\phi}\right)\tilde{u}_j\right]$	21.09	50.08	78.11	81.56
$\frac{\partial}{\partial x_j}\left(\bar{\rho}\zeta_j\right)$	17.17	40.80	40.10	32.22
$\frac{\partial}{\partial x_j}\left[q_{IKj}\left(\bar{\phi}\right)\right]$	11.51	21.07	28.40	25.27
$\frac{\partial}{\partial x_j}\left[\Delta\left(\bar{q}_{IKj}\right)\right]$	5.70	11.77	11.92	8.15
$\frac{\partial}{\partial x_j}\left(\bar{\rho}\tau_{ij}\tilde{u}_i\right)$	0.36	0.82	0.82	0.65
$\frac{\partial}{\partial x_j}\left[\sigma_{ij}\left(\bar{\phi}\right)\tilde{u}_i\right]$	0.49	0.65	0.78	0.52
$\frac{\partial}{\partial x_j}\left[\Delta\left(\overline{\sigma_{ij}u_i}\right)\right]$	0.23	0.33	0.31	0.18
$\frac{\partial}{\partial x_j}\left\{\Delta\left(\bar{p}\right)\tilde{u}_j\right\}$	0.11	0.23	0.21	0.16
$\frac{\partial}{\partial x_j}\left(\bar{\rho}\kappa_j - \bar{\rho}\tau_{ij}\tilde{u}_i\right)$	0.15	0.31	0.21	0.14

$$\Delta\left(\bar{f}\right) \equiv \overline{f\left(\phi\right)} - f\left(\bar{\phi}\right)$$

TABLE 4. Magnitude (x_2 r.m.s.) of terms in LES equations at $t^* = 25$, 50, 100 and 150. The computation is performed using the O$_2$/H$_2$ DNS database for $\bar{\Delta} = 8\Delta x$. Units are 10^9Jm^{-3}s^{-1}.

Energy	$t^* = 50$	$t^* = 100$	$t^* = 150$	$t^* = 220$
$\frac{\partial}{\partial x_j}\left(\bar{\rho}\tilde{e}_t\tilde{u}_j\right)$	36.51	85.03	97.31	136.62
$\frac{\partial}{\partial x_j}\left[p\left(\bar{\phi}\right)\tilde{u}_j\right]$	21.44	51.29	56.48	77.40
$\frac{\partial}{\partial x_j}\left(\bar{\rho}\zeta_j\right)$	13.39	29.25	23.62	24.41
$\frac{\partial}{\partial x_j}\left[q_{I\kappa_j}\left(\bar{\phi}\right)\right]$	2.64	7.02	7.27	8.17
$\frac{\partial}{\partial x_j}\left[\Delta\left(\bar{q}_{I\kappa_j}\right)\right]$	1.69	3.78	3.43	2.84
$\frac{\partial}{\partial x_j}\left(\bar{\rho}\tau_{ij}\tilde{u}_i\right)$	0.52	1.16	1.02	1.43
$\frac{\partial}{\partial x_j}\left\{\Delta\left(\bar{p}\right)\tilde{u}_j\right\}$	0.25	0.58	0.56	0.68
$\frac{\partial}{\partial x_j}\left(\bar{\rho}\kappa_j - \bar{\rho}\tau_{ij}\tilde{u}_i\right)$	0.18	0.41	0.29	0.45
$\frac{\partial}{\partial x_j}\left[\sigma_{ij}\left(\bar{\phi}\right)\tilde{u}_i\right]$	0.15	0.35	0.36	0.36
$\frac{\partial}{\partial x_j}\left[\Delta\left(\overline{\sigma_{ij}u_i}\right)\right]$	0.10	0.19	0.16	0.14

$$\Delta\left(\bar{f}\right) \equiv \overline{f\left(\phi\right)} - f\left(\bar{\phi}\right)$$

TABLE 5. Magnitude (x_2 r.m.s.) of terms in LES equations at $t^* = 50$ 100, 150 and 220. The computation is performed using the O_2/He DNS database for $\bar{\Delta} = 8\Delta x$. Units are $10^9 \mathrm{Jm}^{-3}\mathrm{s}^{-1}$.

			$t^* = 25$	$t^* = 50$	$t^* = 100$	$t^* = 150$
No HF	$\frac{\partial}{\partial x_j}\left(\overline{q_j\left(\phi\right)} - q_j\left(\bar{\phi}\right)\right)$		5.70	11.77	11.92	8.15
M 1	$\frac{\partial}{\partial x_j}\left(\overline{q_j\left(\phi\right)} - \overline{q_j\left(\phi^\bullet\right)}\right)$		1.60	4.01	3.22	1.46
[h] M 2	$\frac{\partial}{\partial x_j}\left(\overline{q_j\left(\phi\right)} - \overline{q_j\left(\phi^\bullet\right)}\right)$		2.67	5.89	4.78	2.09
M 3	$\frac{\partial}{\partial x_j}\left(\overline{q_j\left(\phi\right)} - \overline{q_j\left(\phi^\bullet\right)}\right)$		5.38	11.17	11.39	7.81
M 4	$\frac{\partial}{\partial x_j}\left(\overline{q_j\left(\phi\right)} - \overline{q_j\left(\phi^\bullet\right)}\right)$		3.19	6.83	5.55	2.38
M5	$\frac{\partial}{\partial x_j}\left(\overline{q_j\left(\phi\right)} - \overline{q_j\left(\bar{\phi}\right)}\right)$		3.93	8.80	10.48	8.74

TABLE 6. Comparison through the x_2-r.m.s. of the modeled filtered heat flux term obtained with the model approximations in (2.38)-(2.42) at $t^* = 25, 50, 100$ and 150 using equation (2.35). The computation is performed using the O_2/H_2 DNS with $\bar{\Delta} = 8\Delta x_{DNS}$. Units are $10^9 \mathrm{Jm}^{-3}\mathrm{s}^{-1}$.

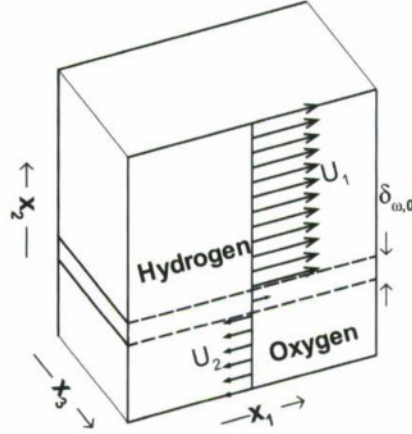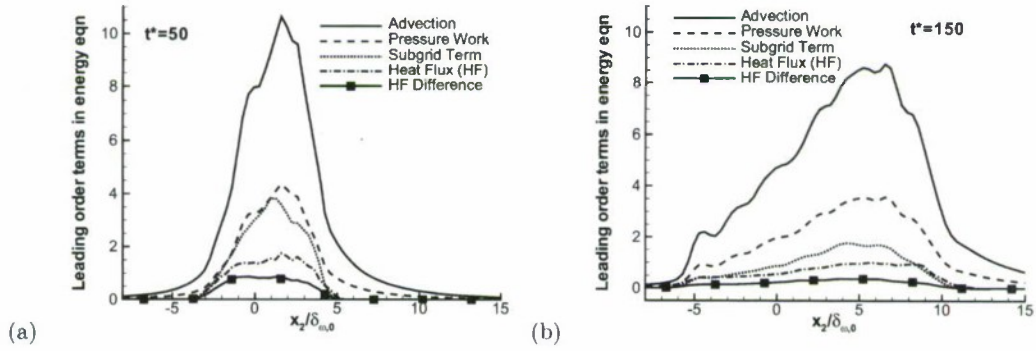FIGURE 1. O_2/H_2 mixing layer configuration.

(a)   (b)

FIGURE 2. The x_2 r.m.s. of the leading order terms in the energy equation at (a) $t^* = 50$ and (b) $t^* = 150$. The computation is performed using the O_2/H_2 DNS with $\bar{\Delta} = 8\Delta x_{DNS}$. HF denotes the heat flux. The values shown are non-dimensionalized by 7×10^{10} $Jm^{-3}s^{-1}$.
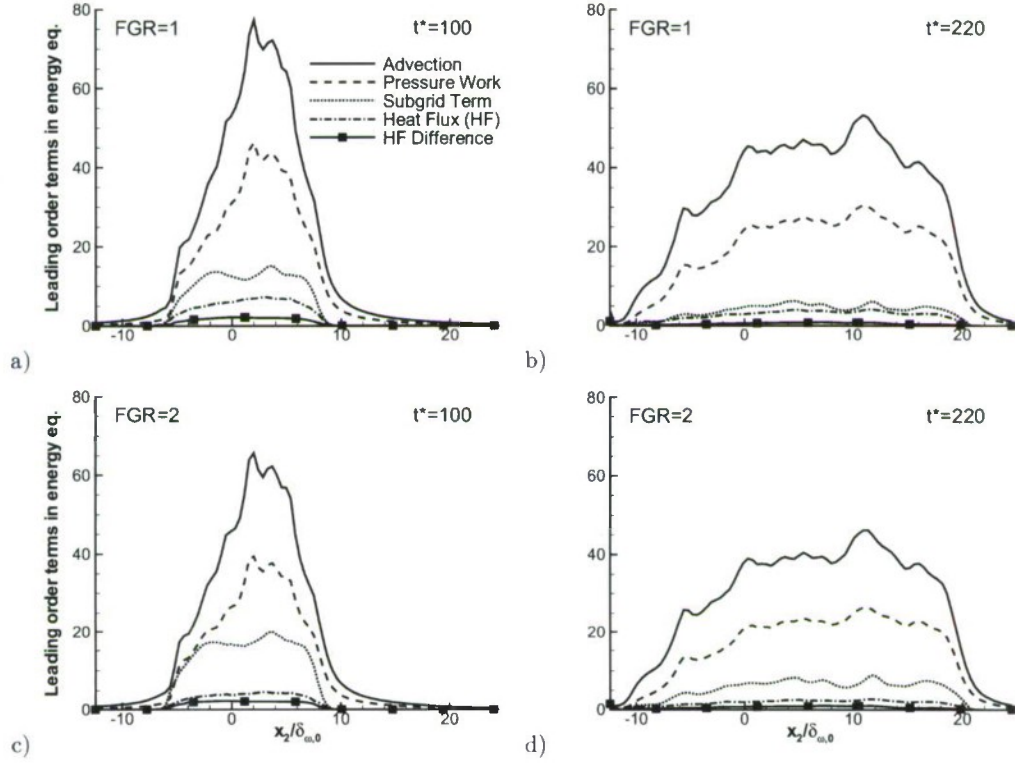
Ezgi S. Taskinoglu and Josette Bellan

FIGURE 3. The x_2 r.m.s. activity of the leading order terms in the energy equation for the O_2/He DNS database at (a, b) $\overline{\Delta}/\Delta x_{LES} = 1$ and (c, d) $\overline{\Delta}/\Delta x_{LES} = 2$ for (a, c) $t^* = 100$ and (c, d) $t^* = 220$ where the prospective LES grid size is $\Delta x_{LES} = 4\Delta x_{DNS}$. The values shown are non-dimensionalized by 0.5×10^{10} $Jm^{-3}s^{-1}$.
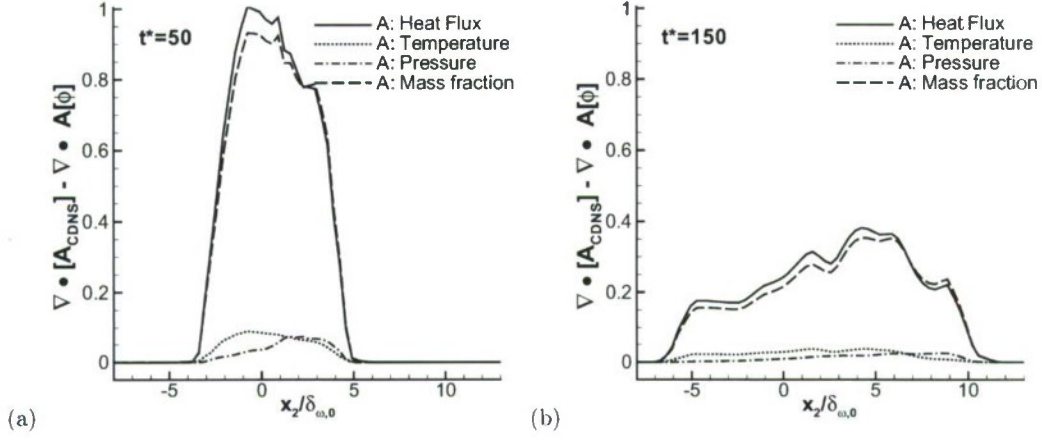
FIGURE 4. The x_2 r.m.s. of the difference of the heat flux and each of its contributions at (a) $t^* = 50$ and (b) $t^* = 150$. The computation is performed using the O_2/H_2 DNS with $\bar{\Delta} = 8\Delta x_{DNS}$. The filtering operation is denoted by square brackets. The values shown are non-dimensionalized by 1.15×10^8 $Jm^{-3}s^{-1}$.
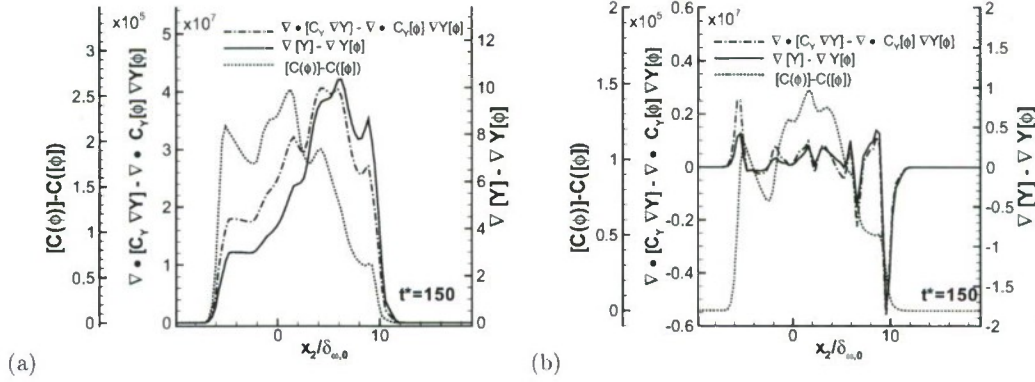
FIGURE 5. Comparison of the difference in coefficients, gradients, and the heat fluxes, (a) r.m.s, (b) mean at $t^*_{tr} = 150$. The computation is performed using the O_2/H_2 DNS with $\bar{\Delta} = 8\Delta x_{DNS}$. The filtering operation is denoted by square brackets. Units are consistent with the heat flux in $Jm^{-2}s^{-1}$.
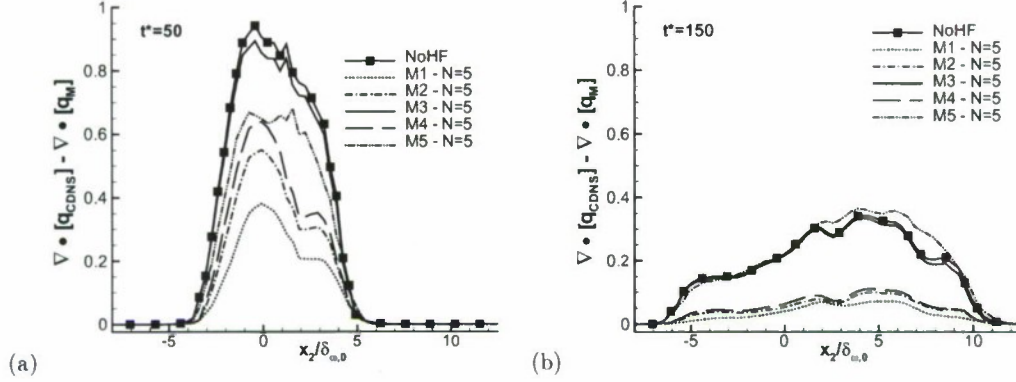
FIGURE 6. The x_2 r.m.s. of the difference between the divergence of the filtered heat flux computed using the O_2/H_2 DNS with $\bar{\Delta} = 8\Delta x_{DNS}$, and the divergence of the heat flux divergence obtained with the No HF model and M1-M5 reconstruction models (equations (2.38)-(2.42)). Results are shown at (a) $t^* = 50$ and (b) $t^* = 150$. The values shown are non-dimensionalized by 6.5×10^{10} Jm^{-3}s^{-1}. The filtering operation is denoted by square brackets.
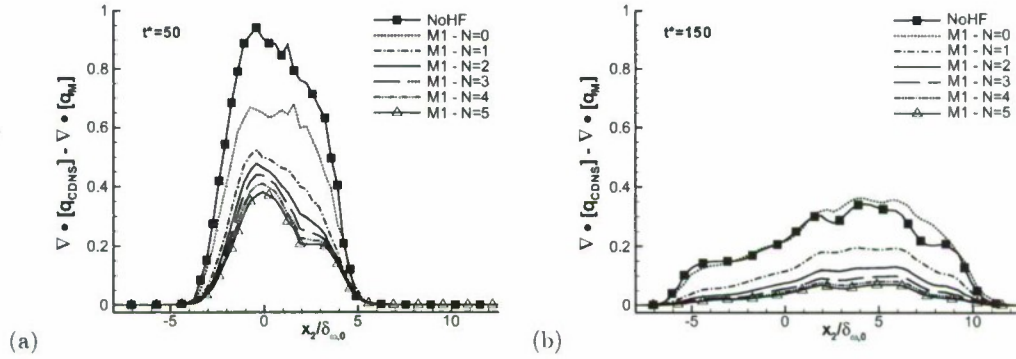

FIGURE 7. Effect of order of reconstruction (r.m.s. activity), N, on the heat flux correction at (a) $t^* = 50$ and (b) $t^* = 150$. The computations were performed using the O_2/H_2 DNS with $\bar{\Delta} = 8\Delta x_{DNS}$. The values shown are non-dimensionalized by 6.5×10^{10} Jm^{-3}s^{-1}. The filtering operation is denoted by square brackets.
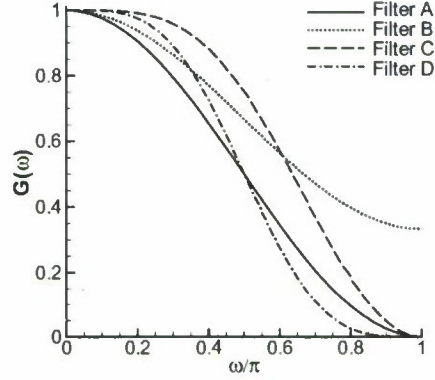
FIGURE 8. Transfer functions of the filters tested for which definitions are given in §6.1.4.
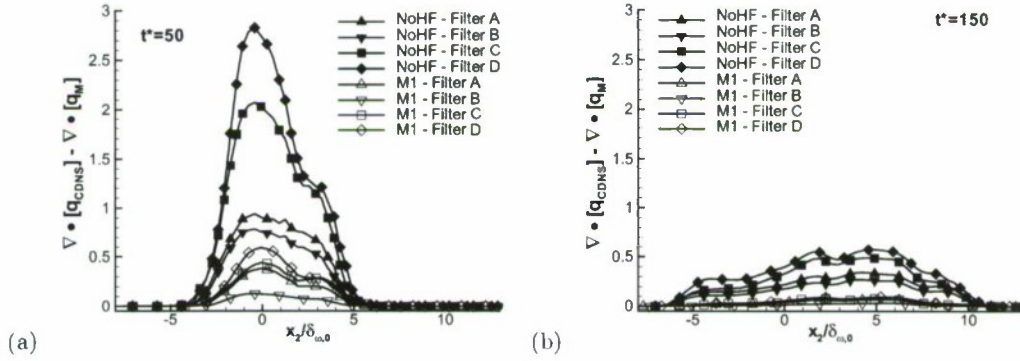
FIGURE 9. The x_2 r.m.s. of the difference of heat flux divergence at (a) $t^* = 50$ and (b) $t^* = 150$. The computations were performed using the O_2/H_2 DNS with $\bar{\Delta} = 8\Delta x_{DNS}$. The values shown are non-dimensionalized by 6.5×10^{10} $\text{Jm}^{-3}\text{s}^{-1}$. The filtering operation is denoted by square brackets.
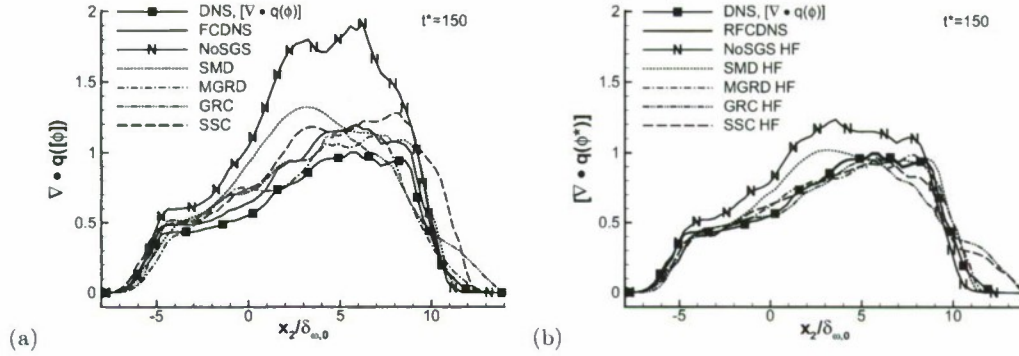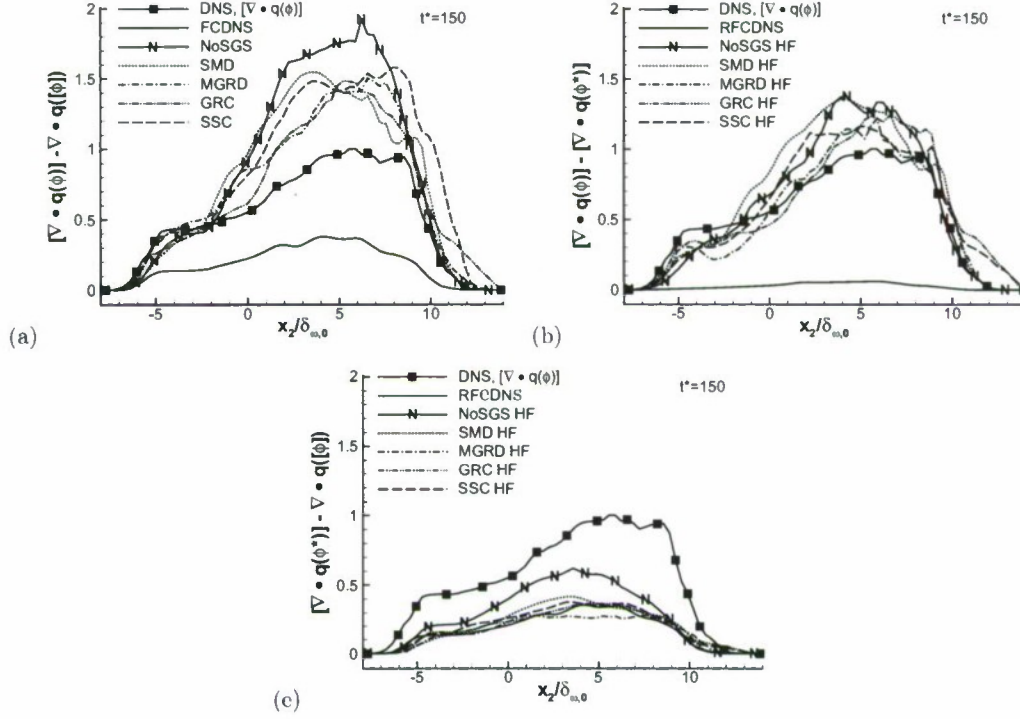
FIGURE 10. The x_2-r.m.s. of several quantities: (a) The divergence of the heat flux computed from the filtered flow field of either LES or FC-FNS; the LES is without heat flux correction. (b) The filtered divergence of the heat flux computed from the reconstructed flow field of either LES or FC-DNS; the LES is with heat flux correction. The LES with heat flux correction is denoted by HF and is obtained using model M1. The LES use various SGS-flux models, all defined in §2.4.1. All results are displayed at $t_{tr}^* = 150$. The computations were performed using the O_2/H_2 DNS with $\bar{\Delta} = 8\Delta x_{DNS}$. The values shown are non-dimensionalized by 6.5×10^{10} $Jm^{-3}s^{-1}$. The filtering operation is denoted by square brackets.

FIGURE 11. The x_2-r.m.s. of several quantities: (a) The difference between the filtered divergence of the (coarsened) DNS heat flux and the divergence of the heat flux computed from the filtered flow field of LES or FC-DNS; the LES is without heat flux correction. (b) The difference between the filtered divergence of the heat flux computed from the (coarsened) DNS heat flux and the filtered divergence of the reconstructed heat flux using the filtered flow field of either LES or the FC-DNS; the LES is with heat flux correction. (c) The difference between the filtered divergence of the reconstructed heat flux and the heat flux computed from the filtered flow field of either LES or FC-DNS; the LES is with heat flux correction. The LES with heat flux correction is denoted by HF and is obtained using model M1. The LES use various SGS-flux models, all defined in §2.4.1. All results are displayed at $t_{tr}^* = 150$. The computations were performed using the O_2/H_2 DNS with $\bar{\Delta} = 8\Delta x_{DNS}$. The values shown are non-dimensionalized by 6.5×10^{10} $Jm^{-3}s^{-1}$. The filtering operation is denoted by square brackets.
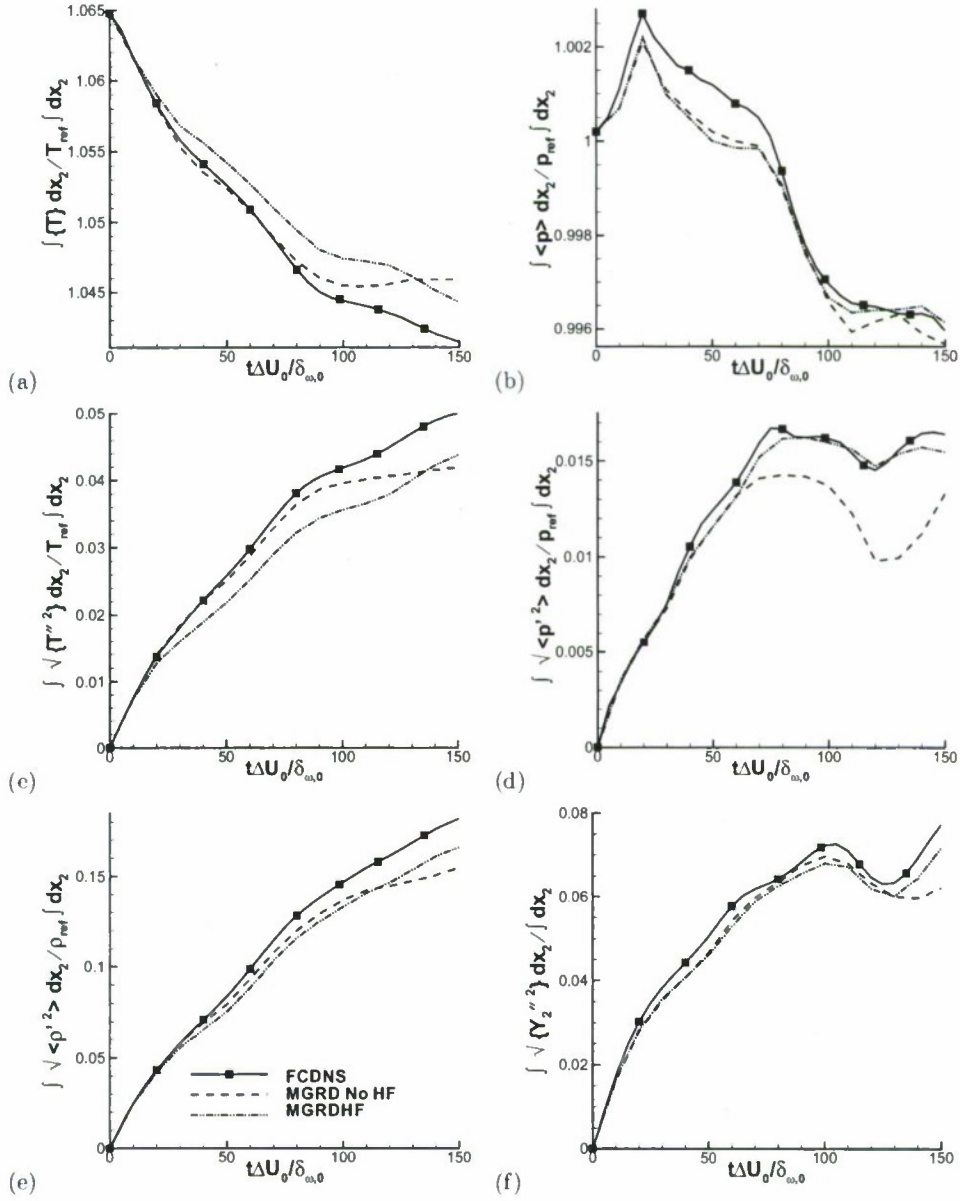
FIGURE 12. Timewise evolution of non-dimensionalized x_2-r.m.s. quantities. (a) mean temperature, (b) mean pressure, (c) temperature fluctuations, (d) pressure fluctuations, (e) density fluctuations, and (f) mass fraction fluctuations. Comparisons are performed among FC-DNS, MGRD without **q**-correction (MGRD No HF) and MGRD with **q**-correction (MGRDHF). $\Delta x_{LES} = 4\Delta x_{DNS}.\rho_{ref} = (\rho_1 + \rho_2)/2$, $T_{ref} = (T_1 + T_2)/2$ and $p_{ref} = p_0$.
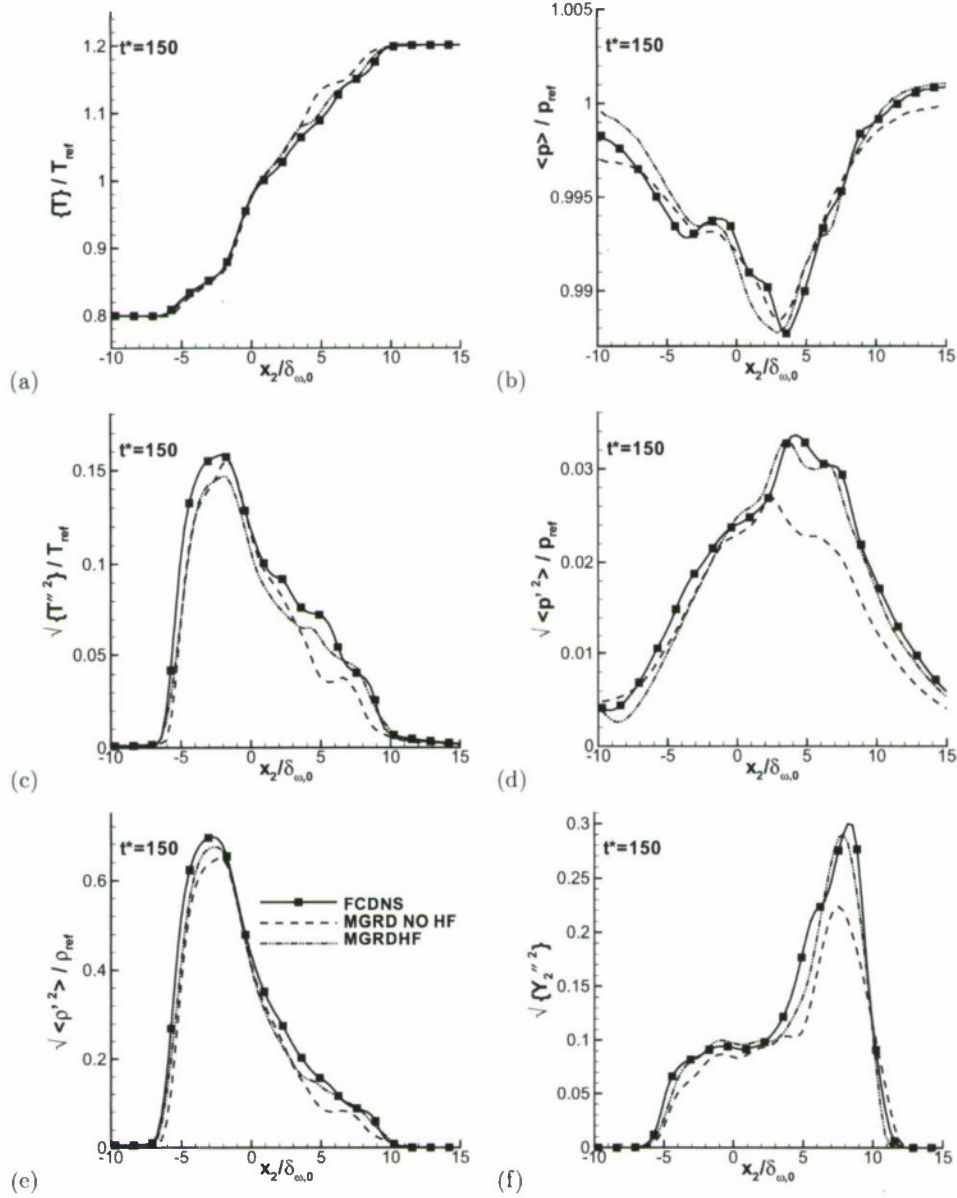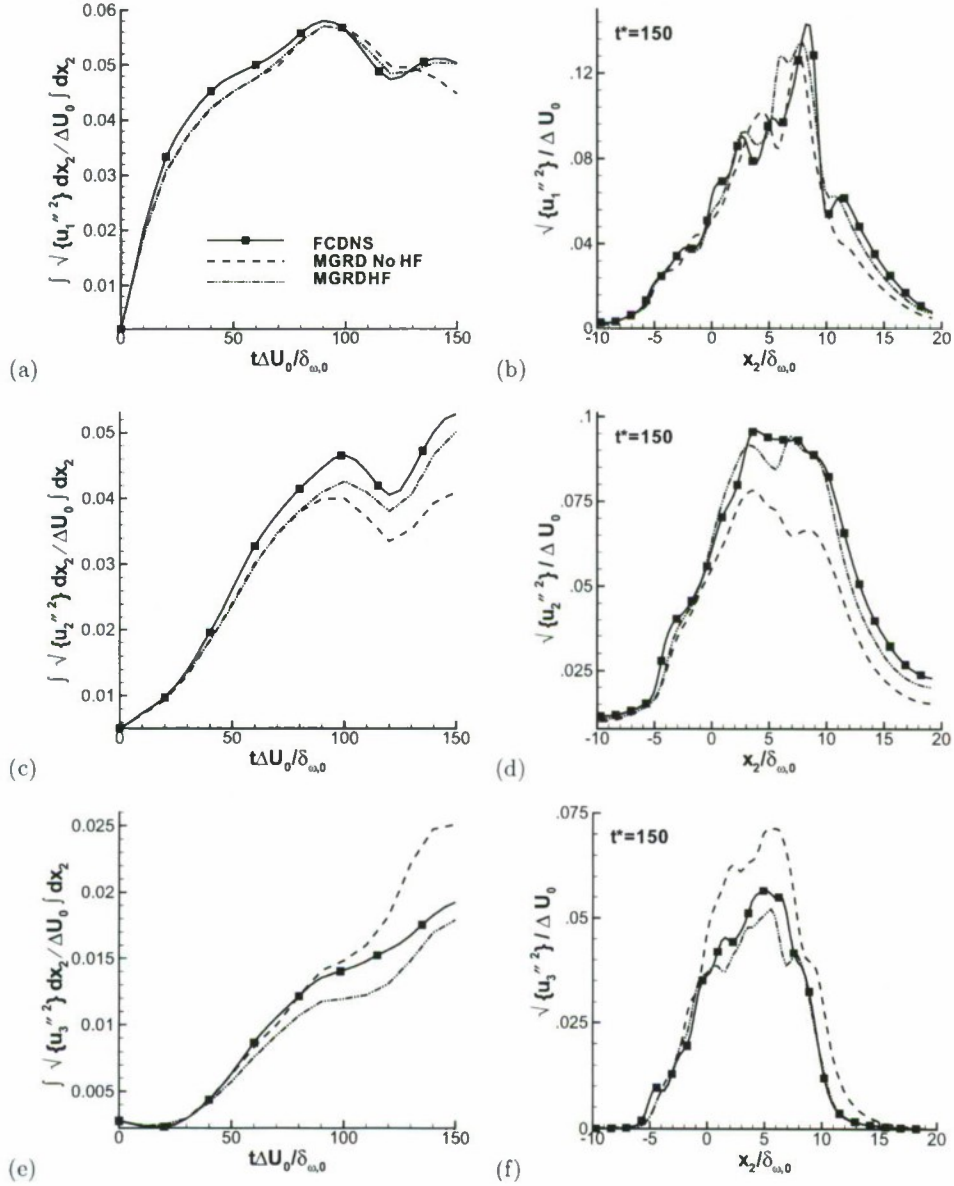
FIGURE 13. Cross-stream variation of non-dimensionalized x_2-r.m.s. quantities at $t^*_{tr} = 150$. (a) mean temperature, (b) mean pressure, (c) temperature fluctuations, (d) pressure fluctuations, (e) density fluctuations, and (f) mass fraction fluctuations. Comparisons are performed among FC-DNS, MGRD without q-correction (MGRD No HF) and MGRD with q-correction (MGRDHF). $\Delta x_{LES} = 4\Delta x_{DNS}.\rho_{ref} = (\rho_1 + \rho_2)/2$, $T_{ref} = (T_1 + T_2)/2$ and $p_{ref} = p_0$.

FIGURE 14. Timewise evolution of non-dimensionalized x_2-r.m.s. quantities: (a) u_1 velocity fluctuations, (c) u_2 velocity fluctuations, (e) u_3 velocity fluctuations. Cross-stream variation of x_2-r.m.s velocity fluctuations at $t_{tr}^* = 150$ for (b) u_1,(d) u_2, and (f) u_3. Comparisons are performed among FC-DNS, MGRD without **q**-correction (MGRD No HF) and MGRD with **q**-correction (MGRDHF). $\Delta x_{LES} = 4\Delta x_{DNS}$.

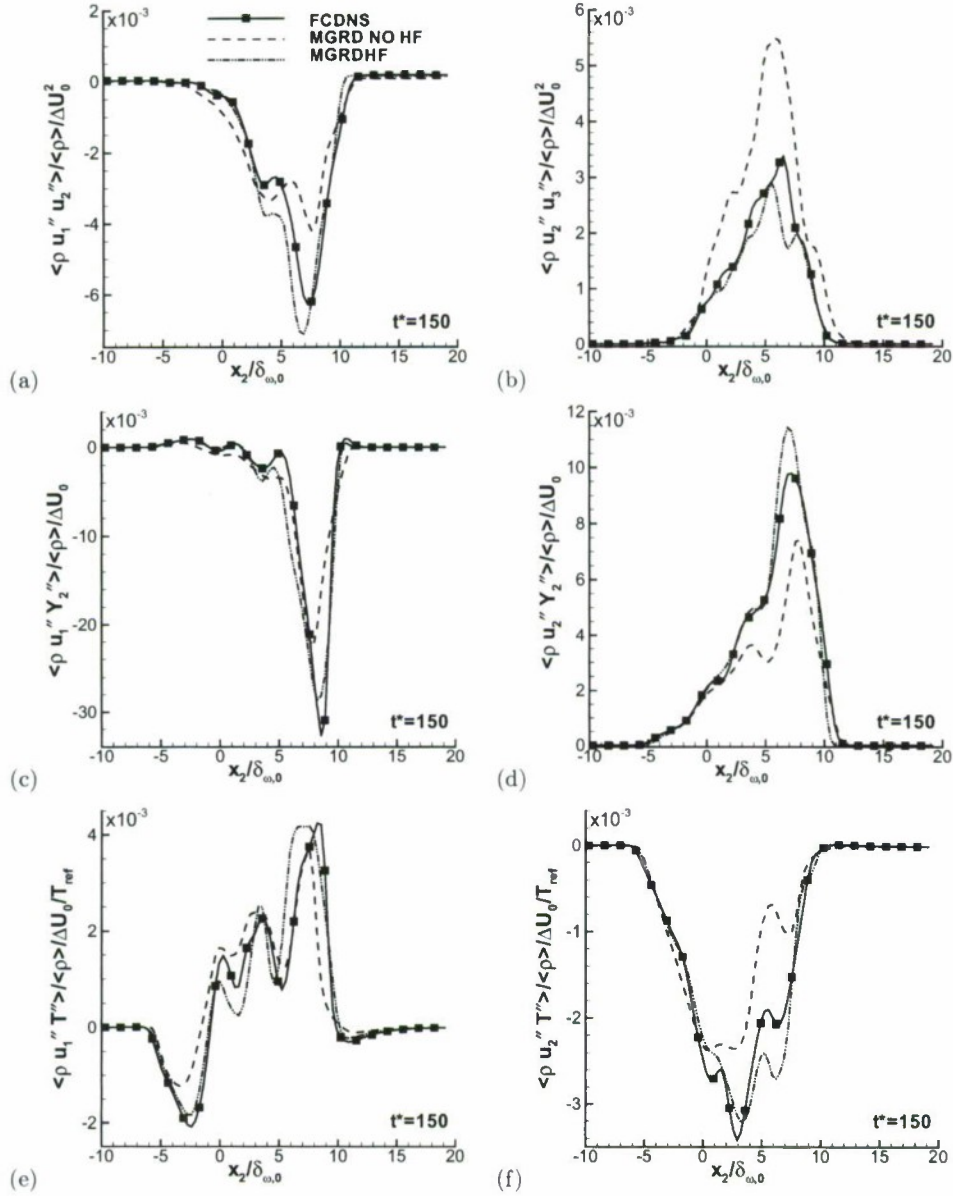FIGURE 15. Cross-stream variation of non-dimensional second-order correlations at $t^*_{tr} = 150$ (a) $< \rho u''_1 u''_2 >$, (b) $< \rho u''_2 u''_3 >$, (c) $< \rho u''_1 Y''_2 >$, (d) $< \rho u''_2 Y''_2 >$, (e) $< \rho u''_1 T'' >$, and (f) $< \rho u''_2 T'' >$. Comparisons are performed among FC-DNS, MGRD without **q**-correction (MGRD No HF) and MGRD with **q**-correction (MGRDHF). $\Delta x_{LES} = 4 \Delta x_{DNS}$. $T_{ref} = (T_1 + T_2)/2$.
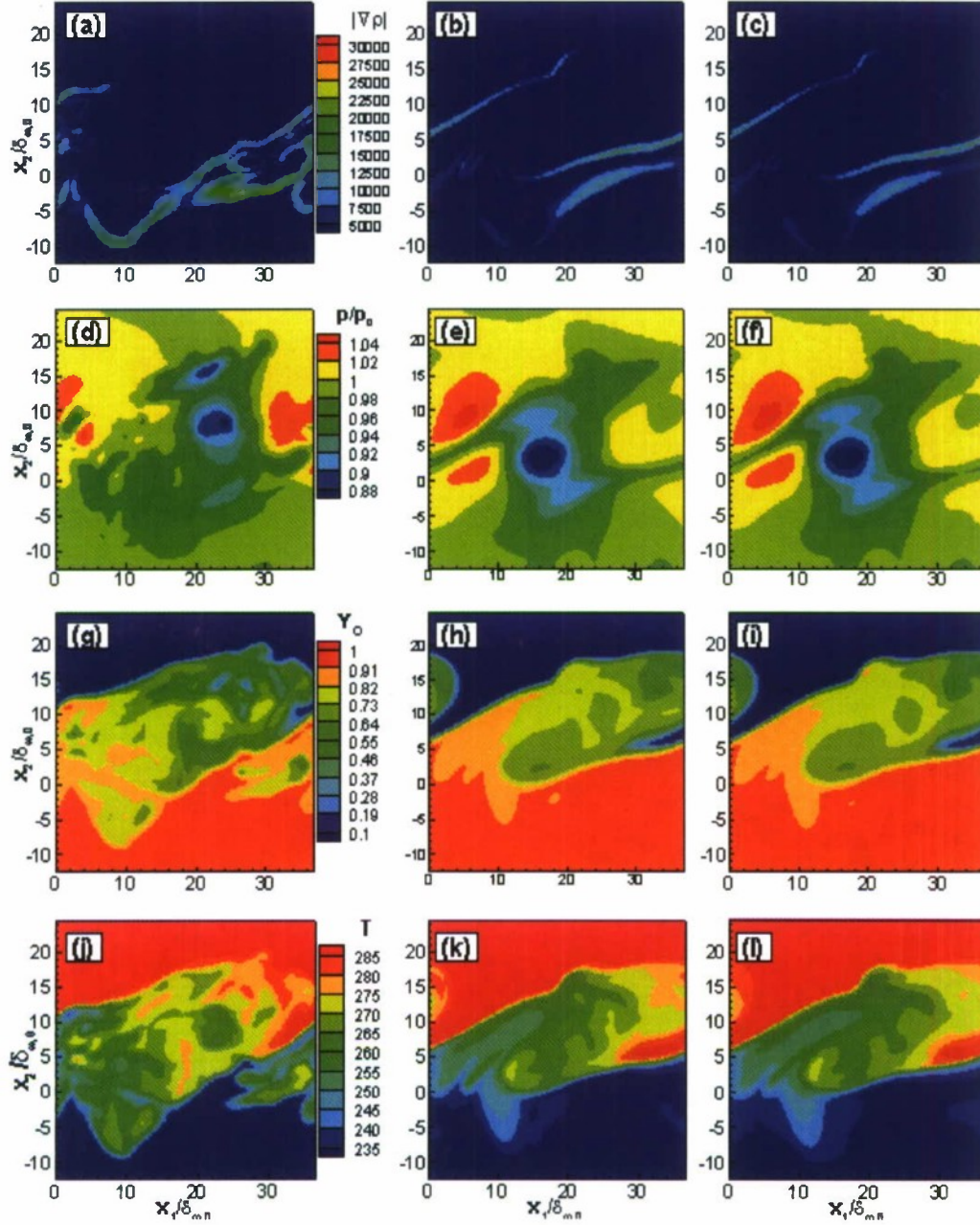
FIGURE 16. Comparison of $|\nabla\rho|$ in kg/m^4 (first row), p/p_0 (second row) and Y_o (third row) and T in K (fourth row) for the O$_2$/He layer at the t_{tr}^* of the DNS ($t^* = 220$) in the between-the-braid plane ($x_3/L_3 = 0.06$) for: FC-DNS (first column); SMD without **q**-correction (second column); and SMD with **q**-correction (third column). $\Delta x_{LES} = 4\Delta x_{DNS}$.
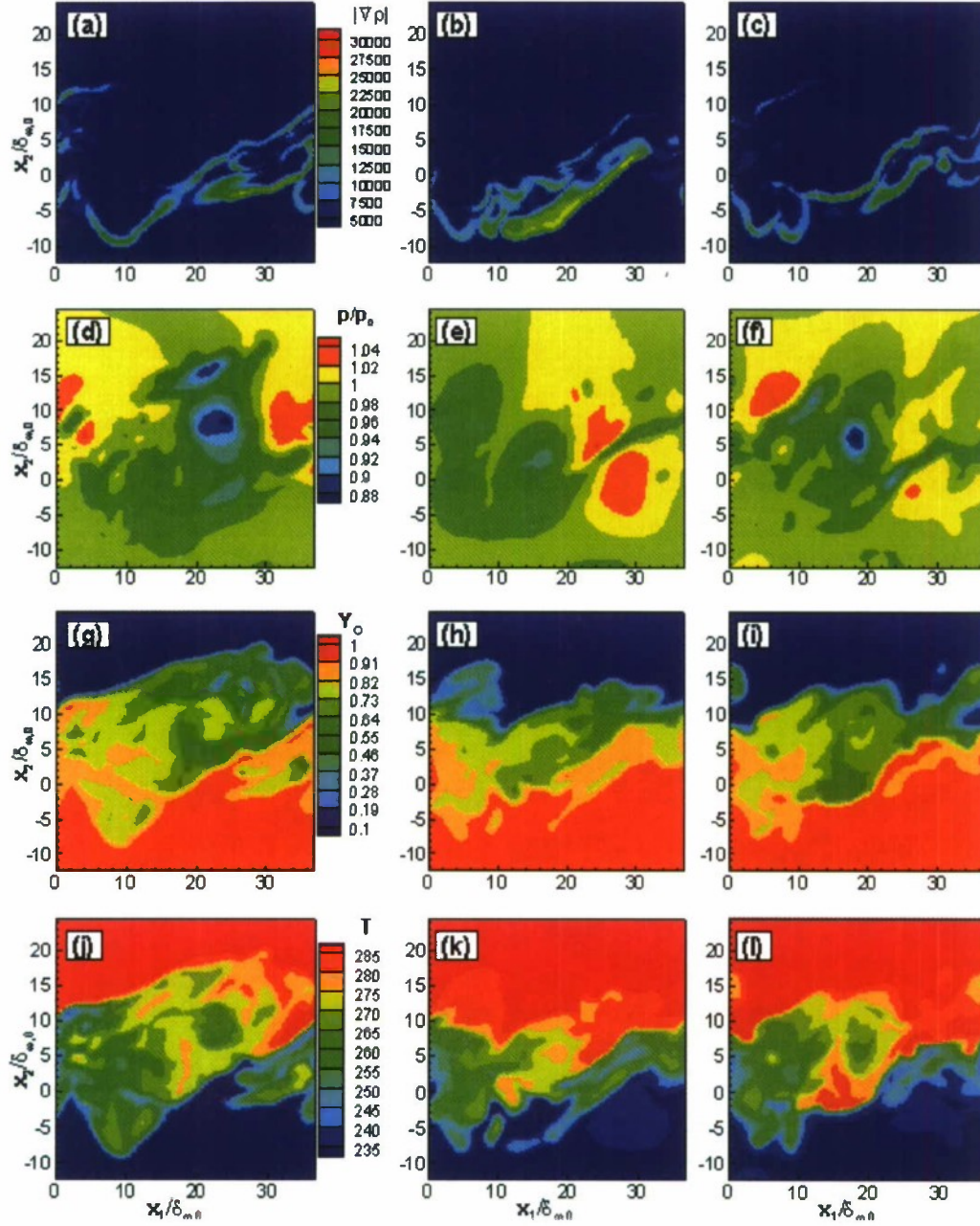
FIGURE 17. Comparison of $|\nabla\rho|$ in kg/m^4 (first row), p/p_0 (second row) and Y_o (third row) and T in K (fourth row) for O$_2$/He at the t_{tr}^* of the DNS ($t^* = 220$) in the between-the-braid plane ($x_3/L_3 = 0.06$) for: FC-DNS (first column); MGRD without **q**-correction (second column); and MGRD with **q**-correction (third column). $\Delta x_{LES} = 4\Delta x_{DNS}$.

Appendix 4

Large Eddy Simulation composition equations for single-phase and two-phase fully multicomponent flows

J. Bellan [a,b,*], L.C. Selle [b]

[a] Jet Propulsion Laboratory, California Institute of Technology, 4800 Oak Grove Drive, M/S
125-109, Pasadena, CA 91109-8099, USA
[b] California Institute of Technology, Mechanical Engineering Department, CA 91125, USA

Abstract

The Large Eddy Simulation (LES) equations for multicomponent (MC) fuel single-phase (SP) flow and two-phase (TP) flow with phase change are derived from the Direct Numerical Simulation (DNS) equations by filtering the DNS equations using a top-hat filter. Additional to the equations solved for single-component (SC) fuels, composition equations enter the formulation. The species composition is represented through a Probability Distribution Function (PDF), and DNS equations for the PDF moments are solved to find the composition. The TP filtered equations contain three categories of subgrid-scale (SGS) terms: (1) SGS–flux terms, (2) filtered source terms (FSTs) and (3) terms representing the 'LES assumptions'. For SP flows no FSTs exist. The SGS terms in the LES equations must be either shown negligible or modeled. It is shown that for the composition equations, two equivalent forms of the DNS equations lead to two non-equivalent forms of the LES equations. Criteria are proposed to select the form best suited for LES. These criteria are used in conjunction with evaluations based on a DNS database portraying mixing and phase change, and lead to choosing one of the LES forms which satisfies all criteria. It is shown that the LES assumptions lead to additional SGS terms which require modeling. Further considerations are made for reactive flows.
© 2009 Published by Elsevier Inc. on behalf of The Combustion Institute.

Keyword: Multicomponent LES equations

1. Introduction

The modeling of MC-fuel mixing and combustion has been a long standing goal as all practical fuels used in energy production contain a myriad

---
* Corresponding author. Address: Jet Propulsion Laboratory, California Institute of Technology, 4800 Oak Grove Drive, M/S 125-109, Pasadena, CA 91109-8099, USA. Fax: +1 818 393 6682.
  E-mail address: Josette.Bellan@jpl.nasa.gov (J. Bellan).

of species. When attempting to reduce the complexity of large elementary-reaction mechanisms, lumping of species has been proposed based on 'similar' species (like isomers) [1] and when modeling flames, bundling for modeling diffusivities has also been recommended [2]. In the same framework, a formulation has been proposed [3–7] for modeling SP and TP MC flows using statistical concepts that lump species according to their molar mass, m, a quantity strongly related to the diffusivity. DNS performed with this formulation has unraveled many fundamental aspects of MC flows. However, for practical applications, LES

is more promising for the computationally efficient simulation of turbulent flows. The LES equations are obtained through filtering of the DNS equations which represent the exact model equations at all flow scales of interest in turbulence. The filtering operation removes the exact effect of the small scales and produces terms that contain their effect, albeit in an unknown way since these terms are not directly calculable from the LES solution, and instead must be modeled. Two categories of subgrid-scale (SGS) terms appear in the LES equations: filtered-term SGS contributions (SGS-flux and FSTs) that must be modeled to reintroduce the lost information at a scale smaller than that of the LES, and 'LES assumptions' that must either be verified or modeled as additional SGS terms. For volumetrically dilute sprays modeled in an Eulerian frame for the gas and a Lagrangian frame for the drops (e.g. [8,9]), the SGS terms contain two types of contributions: terms resulting from the filtering of the convective terms and terms resulting from the filtering of the source terms representing the impact of the drop/flow interaction in the Eulerian equations. Modeling of the two types of contributions has been performed both by analyzing the small scale behavior in what is called *a priori* studies (e.g. [9]) and by using these SGS models in LES and evaluating their performance in what is called *a posteriori* studies (e.g. [10]). This body of cited work has been devoted to SC flows. For SC TP flow with phase change, the only quantity indicating the result of drop evaporation is the vapor mass fraction temporal and spatial distribution. No such studies exist for MC flows where the interest is also in the vapor composition equivalent distribution.

This study focuses on the composition equations and aims at establishing the corresponding MC LES equations. It is shown in particular that filtering of the DNS equations leads to two non-equivalent LES forms. A methodology is developed for selecting which of the two forms should be adopted for LES. This methodology is general and could be applied to other situations where ambiguity of choice exists for the LES equations and a DNS database is available to guide the choice.

2. DNS and LES governing equations

The DNS governing equations for mixing and evaporation have been presented in [5,6] and transitional states have been created and analyzed in depth in [7]. Summarizing, the DNS equations consist of two sets of coupled governing equations, one for gas, the other for the drops. For the gas, the perfect-gas equation of state is coupled to three-dimensional (3D) Eulerian governing equations for mass, momentum, energy, species partial density and vapor composition,

each equation including transient, convection and diffusion terms. For the drops, Lagrangian governing equations follow each physical drop in its trajectory as it changes mass, momentum, energy, species and liquid composition, due to its dynamic and thermodynamic interaction with the gas, here taken to be air. Because the drops are much smaller than the Kolmogorov scale, they can be treated as sources of mass, species, momentum and energy for the gas [11] (e.g. [8]). Correspondingly, the interaction of the drops with the gas manifests as mass, species, composition, momentum and energy source terms in the gas governing equations, coupling thus the drops and gas. Although a model is used to describe the drops' behavior and thus these simulations are not strictly DNS, this terminology [12] has been adopted in the literature [8,9] and is also used here for consistency.

The vapor composition is modeled following the mathematical description for practical liquid fuels containing many species [3]. The concepts of Continuous Thermodynamic (CT) [13,14] are adopted. In the CT theory the chemical potential for a mixture containing numerous components is appropriately represented, and the Gibbs function is derived through molecular thermodynamic methods in terms of the PDF describing the mixture composition. The concepts are fundamental and independent of the physicochemical model chosen for the chemical potential. Having specified an initial composition PDF, the evolution of the mixture is governed by thermodynamic relationships and/or conservation equations. Although the most general PDF will depend on many variables, it has been shown, with validation, that the single-Gamma PDF depending on m can represent a homologous species class [14,15]. Single-Gamma PDF models applied to drop evaporation [3] have been shown [4] to be restricted to negligible fuel vapor in the drop-surrounding gas. A combination of two Gamma PDFs (DGPDF) as a function of m is necessary to capture the evaporation of drops in a gas containing substantial fuel vapor [4], as in sprays. Because the DGPDF representation requires the knowledge of five parameters, only five moments of the PDF must be computed. Furthermore, it has been shown [4] that one moment can be empirically determined, which reduces the calculation to that of only four moments, $n \in [1, 4]$. Thus, four conservation equations are solved for the vapor composition.

For reactive flows, the equation formulation of [5,7] can be enlarged by adding source terms: the molar reaction rate of vapor (gaseous fuel), $\dot{\omega}_{X_v}$, where subscript X_v denotes the mole vapor (subscript v) fraction, and sources of compositional change issued from reactive mechanisms, $\dot{\omega}_{\xi_{vn}}$, where ξ_{vn} is the nth moment of the composition PDF for the vapor. The interest here is in the

ξ_{vn} equations, as all other equations emulate the LES equations of the SC study of [9] (not shown). Mathematical manipulations of the moment, continuity and vapor partial molar-density equations lead to the DNS equation

$$\frac{\partial(\rho\xi_{vn})}{\partial t} + \frac{\partial[\rho\xi_{vn}u_j]}{\partial x_j} = \frac{\partial}{\partial x_j}\left[\rho\mathscr{D}\frac{\partial\xi_{vn}}{\partial x_j}\right]$$
$$+ 2\rho\mathscr{D}\frac{\partial}{\partial x_j}\left[\ln\left(\frac{X_v}{m}\right)\right]\frac{\partial\xi_{vn}}{\partial x_j} + \frac{\theta_v}{Y_v}(S_{\xi_{vn}} - \xi_{vn}S_{mole})$$
$$+ \xi_{vn}S_{mass} + \frac{\theta_v}{Y_v}(\dot\omega_{\xi_{vn}} - \xi_{vn}\dot\omega_{X_v}) \tag{1}$$

where u is the velocity, t is time, x is the spatial coordinate indexed by subscript j, ρ is the mass density, $\mathscr{D}$ is an effective diffusivity defined as the proportionality coefficient between the vapor mass flux and $cm\nabla(X_v/m)$ where c is the molar density, $\theta_v(\equiv\xi_{v1})$ is the mean vapor molar mass, $Y_v = \theta_v X_v/m$ is the vapor mass fraction with m being the molar mass of the gas (vapor and air), and $S_{\xi_{vn}}$, S_{mole} and S_{mass} are evaporative sources of ξ_{vn}, moles and mass, respectively, for which mathematical expressions have been given elsewhere [5–7]. The diffusion and diffusion-like term of Eq. (1) can be combined forming two equivalent expressions

$$-\frac{\theta_v}{Y_v}\left(\frac{\partial K_{vn,j}}{\partial x_j} - \xi_{vn}\frac{\partial L_{v,j}}{\partial x_j}\right)$$
$$= -\frac{\partial M_{vn,j}}{\partial x_j} + 2M_{vn,j}\frac{\partial}{\partial x_j}\left[\ln\left(\frac{Y_v}{\theta_v}\right)\right] \tag{2}$$

where
$K_{vn} = -\rho\mathscr{D}\nabla(Y_v\xi_{vn}/\theta_v)$, $L_v = -\rho\mathscr{D}\nabla(Y_v/\theta_v)$ and $M_{vn} = -\rho\mathscr{D}\nabla(\xi_{vn})$.

Because the LES equations are derived from the DNS set by spatial filtering, the two equivalent DNS forms, lead, expectably, to two non-equivalent LES forms. With the usual notation of ( ) and (̃) denoting regular and Favre averaging, the generic LES moment equation is

$$\frac{\partial(\bar\rho\tilde\xi_{vn})}{\partial t} + \frac{\partial(\bar\rho\tilde\xi_{vn}\tilde u_j)}{\partial x_j} = -\frac{\partial(\bar\rho\pi_{nj})}{\partial x_j} + \mathscr{F}_k$$
$$+ \left[\frac{\tilde\theta_v}{\tilde Y_v}\bar S_{\xi_{vn}} - \frac{\tilde\theta_v\tilde\xi_{vn}}{\tilde Y_v}\bar S_{mole} + \tilde\xi_{vn}\bar S_{mass}\right]$$
$$+ \frac{\tilde\theta_v}{\tilde Y_v}(\bar\omega_{\xi_{vn}} - \tilde\xi_{vn}\bar\omega_{X_v}) + \text{LESassu} \tag{3}$$

where $\pi_{nj} = \vartheta(\tilde\xi_{vn}, \tilde u_j)$, $\vartheta(\tilde\varphi, \tilde\chi) = \widetilde{\varphi\chi} - \tilde\varphi\tilde\chi$ being the variance of two quantities φ and χ, and $k = 1, 2$ indicating Form 1 or Form 2 of the LES equation

$$\mathscr{F}_1 = -\frac{\tilde\theta_v}{\tilde Y_v}\left(\frac{\partial K_{vn,j}}{\partial x_j} - \tilde\xi_{vn}\frac{\partial L_{v,j}}{\partial x_j}\right) \tag{4}$$

$$\mathscr{F}_2 = -\frac{\partial M_{vn,j}}{\partial x_j} + 2M_{vn,j}\frac{\partial}{\partial x_j}\left[\ln\left(\frac{\tilde Y_v}{\tilde\theta_v}\right)\right] \tag{5}$$

where K_{vn}, L_v and M_{vn} are computed from the filtered flow field $\bar\phi$, and LESassu comprises all differences between filtered DNS terms and the same DNS term computed as a function of the filtered flow field, e.g. $[\overline{\xi_{vn}S_{mass}} - \tilde\xi_{vn}\bar S_{mass}]$. There currently is no experience with choosing between non-equivalent LES-equation forms. The focus of this study is in establishing general criteria for making such a choice and then examining the modeling requirements for these specific equations. The guide in making this choice is a DNS database.

3. Description of the databases

The DNS equations for the non-reactive case have been solved in a 3D temporal mixing layer of dimensions $(L_1 \times L_2 \times L_3)$ with (x_1, x_2, x_3) being the streamwise, cross-stream and spanwise directions, respectively (see Fig. 1 in [6]) for 15 various conditions listed in Table 1 of [7]. Perturbations were used to excite the layer in order to induce roll-up and pairing [9,16]. For TP flows, initially, all the drops are in the lower stream and have the same temperature, $T_{d,0}$ (subscripts d and 0 denote a drop and initial condition, respectively), which is lower than the initial gas temperature T_0 and the liquid boiling point temperature so as to promote evaporation; the initial velocity of each drop is the same as that of the gas phase at its location. The drop size distribution is specified through the Stokes number $St = \tau_d\Delta U_0/\delta_{\omega,0}$, as given in Table 1; $\Delta U_0 = 2U_0$ is the initial velocity difference across the layer with $U_0 = M_{c,0}\sqrt{R_a T_0 C_{p,a}/C_{v,a}}$ where $M_{c,0}$ is the convective Mach number, $R_a = R_u/m_a$, R_u is the universal gas constant, subscript a denotes the carrier gas (here air), and C_p and C_v are constant-pressure and constant-volume heat capacities; $\tau_d = \rho_l D^2/(18\mu)$ is a characteristic drop time constant where ρ_l is the liquid density, D is the drop diameter and μ is the gas viscosity; and $\delta_{\omega,0}$ is the initial vorticity thickness calculated as in [9]. The specified value of $Re_0 = \rho_0\Delta U_0\delta_{\omega,0}/\mu$ is used to calculate μ. The thermal conductivity and diffusivity are computed using this value of μ and specified values of Prandtl, Pr, and Schmidt, Sc, numbers ($Pr = Sc$, 0.696 at $T_0 = 375$ K and 0.694 at $T_0 = 400$ K [17]). For TP flows, the initial number of drops, N_0, is determined by the initial mass loading ML_0 (initial ratio of liquid mass to mass of carrier gas in drop-laden part of domain). The vapor molar fractions in the lower stream, $X_{v,0}^l$, and upper stream, $X_{v,0}^u$, are here specified $X_{v,0}^l = X_{v,0}^u = 10^{-4}$ (an arbitrarily small non-null value is necessary to avoid instabilities). For each fuel, the free-stream vapor composition is found from a single-drop simulation in air at the specified T_0, being chosen to be the first-time-step surface-vapor composition.

Table 1
Initial conditions

Simulation	Case #	Fuel	T_0	ML_0	ρ_l	$\{\{D_0\}\} \times 10^5$	$N_0 \times 10^{-3}$	t_{tr}^*	$Re_{m,tr}$
die375ML2R5	1*	Diesel	375	0.2	828	7.601	2586	100	1386
die375ML5R5	2	Diesel	375	0.5	828	7.601	6451	100	1336
die400ML2R5	3	Diesel	400	0.2	828	7.359	2670	100	1396
jetA375ML2R5	4	Jet A	375	0.2	800	7.732	2543	100	1365

T_0 in K, ρ_l in kg/m^3, D_0 in m. In all simulations, $M_{c,0} = 0.35, \delta_{\omega,0} = 6.859 \times 10^{-3}$ m, $\{\{St_0\}\} = 3$ and $\{\{(St_0 - \{\{St_0\}\})^2\}\}^{1/2} = 0.5$, the double curly brackets denoting drop-ensemble averaging. $T_{d,0} = 345$ K, and $X_{v,0}^u = 10^{-4}$. In all cases $Re_0 = 500$ and the grid is $360 \times 400 \times 216$. The baseline case is indicated by a superscript asterisk. The jetA375ML2R5 simulation was performed on a SGI Origin 2000 platform (on 64, R12000, 300 MHz processors); all other simulations were conducted on a SGI Altix 3000 machine (on 32, Intel Itanium2, 900 MHz processors). t_{tr}^* denotes the non-dimensional transition time. $Re_{m,tr} = Re_0(\delta_{m,tr}/\delta_{\omega,0})$ is the momentum-thickness-based Reynolds number and $\delta_{m,tr}$ is the momentum thickness, both at t_{tr}^*.

The boundary conditions in the (x_1, x_3) homogeneous directions were periodic, and adiabatic slip-wall conditions derived for multicomponent mixtures [6] were utilized in the x_2 direction. Drops reaching the slip walls were assumed to stick to them.

The numerics consisted of an eighth-order central finite-difference discretization in space and a fourth-order Runge–Kutta for temporal advancement. A geometric weighting factor distributes each drop-source contributions to the nearest eight grid points proportionally to its distance from the drop location. The ratio of the drop volume by the discretization volume is initially $O(10^{-3})$ and decreases with time as the drops evaporate. A fourth-order Lagrange interpolation was used to obtain gas-phase variable values at drop locations. Drops the mass of which decreased below 3% of the initial mass were removed from the calculation; for all computations, mass was conserved in the system to a maximum relative error of $O(10^{-5})$. The time step was controlled by the CFL number. The grid size $(\Delta x_1, \Delta x_2, \Delta x_3)$ was chosen such that resolution was excellent as manifested by velocity-fluctuation-based one-dimensional energy spectra which showed no accumulation of energy at the small scales [7]. The thirteen simulations listed in Table 2 of [7] reached a transitional state, evidenced by a smooth energy spectrum except for a small peak at the perturbation frequency. The momentum-thickness-based Reynolds number is defined in Table 1 and its value at transitional (subscript tr) times $t_{tr}^* = t_{tr}\Delta U_0/\delta_{\omega,0}$ is listed in the table. The full set of transitional states constitutes the present database; for brevity, only the representative results of Table 1 simulations are here discussed.

Fuel compositions [18] were provided by Edwards [19] and were fitted elsewhere [6] as a single-Gamma PDF. Thermodynamic and transport properties for these liquid fuels are available [6,7]. For specified initial conditions, the MC liquid was the same for all drops; as the simulation evolved in physical time, each drop developed its own liquid composition according to its dynamic/thermodynamic history due to preferential evaporation or condensation of some species with respect to others. Thus, information about the vapor partial density is complemented by the composition details both for the liquid and the evolving vapor. The molar (mass) vapor composition is expected to have non-uniformities at a finer scale than the vapor mole (mass) fraction in the gas; this is the simple consequence of the fact that the vapor mole (mass) fraction is the sum of the species mole (mass) fractions and thus for a given number of species there is an infinite number of species mole(mass)-fraction-value arrangements that can result in the same vapor mole (mass) fraction value. Examples of the DNS composition spatial distribution at t_{tr}^* are presented in Fig. 1 for some cases of Table 1. For diesel, with increasing ML_0, the θ_v and vapor PDF standard deviation σ_v upper range decreases (Fig. 1a vs b and d vs e) because drop heating is impeded by the large number of drops and the lower drop temperature prevents the evaporation of the higher molar mass species which have a higher boiling point. Also, vapor originating from diesel evaporation has a higher and wider θ_v and σ_v range than vapor originating from Jet A (Fig. 1a vs c and d vs f), emulating the liquid PDF (Fig. 2 in [7]) which is much wider for diesel and spreads to much higher molar mass species. The very strong non-uniformity of both θ_v and σ_v is noteworthy, and the goal is to recover it at the LES scale from the LES equations.

4. Results

The databases are examined at t_{tr}^*. The data is appropriate for analysis in the context of fully turbulent flows because the range of scales at t_{tr}^* is even larger than that for equivalent SC liquid DNS [7] for which databases were found relevant to *a priori* studies [9], and for example, the SGS momentum fluxes have already an activity (on an r.m.s. base) exceeding that of the resolved stresses in the LES equations (not shown).
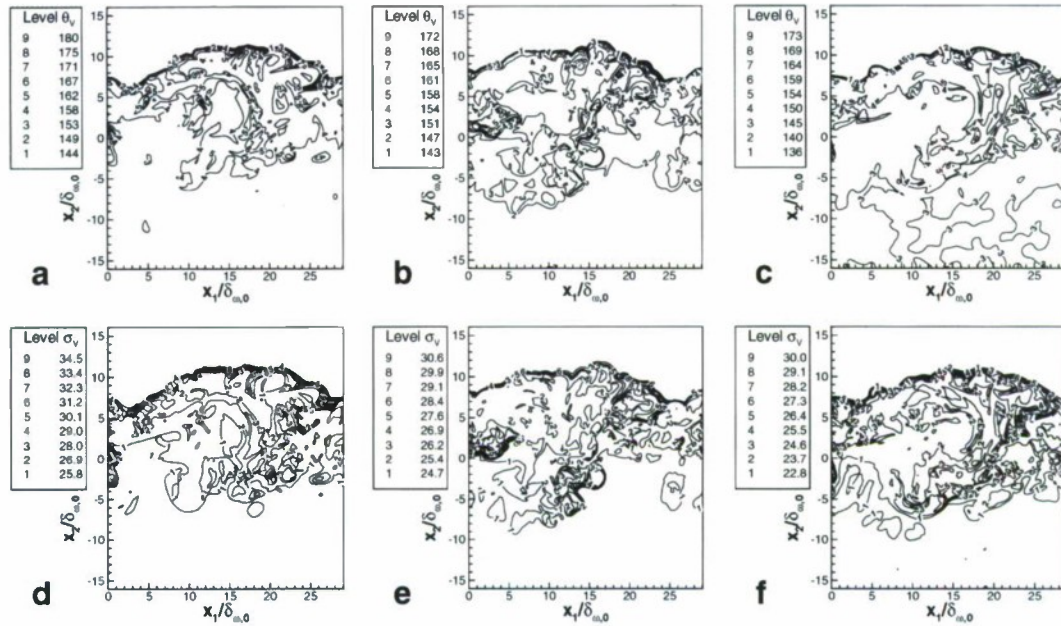
Fig. 1. Contour plots of θ_v (a–c) and σ_v (d–f) in the between-the-braid plane $x_3/L_3 = 0.5$ at t_{tr}^* for Case 1 (a and d), Case 2 (b and e) and Case 4 (c and f). Units for θ_v and σ_v are in kg/kmol.

We propose several criteria for choosing between Forms 1 and 2 of the composition equations. The desirable LES form will have the following attributes: (1) Correlations and least-square-fit slopes between $\mathscr{F}_k$ terms and the database should be as close to unity as possible. The rationale is that modeling any term in a LES equation involves assigning it a functional form multiplied by a calibrating coefficient. Thus, the primary focus is on obtaining LES equations in which terms have a high correlation with the database because they would be a more accurate functional representation of the DNS; the slope's departure from the perfect unity is a secondary concern, as it could be corrected by attempting higher accuracy of the calibrating coefficient. Also, given variations with n, it is desirable that the best correlations and slopes be obtained for the smaller n rather than vice versa. (2) For each n, the terms in $\mathscr{F}_k$ should be as small as possible according to a given norm, in anticipation of possibly neglecting them with respect to other terms common to both forms; this would address the desire for computational efficiency. (3) The LES equations should have the smallest number of terms calculable as function of $\bar{\phi}$, for computational efficiency. (4) The form should have the largest number of LES assumptions satisfied so as to minimize the modeling and computational effort. The criteria stated are entirely universal and do not depend on the geometric configuration or filter functional form.

Whether Form 1 or Form 2 satisfies all four attributes, and if not which are the most important of these attributes, remains to be determined.

The investigation is here performed using a top-hat filter because other filters are not in concert with the finite-difference discretization used in the DNS that produced the database. This finite-difference discretization is the choice for practical applications because aliasing errors are significantly smaller than for other discretization schemes [20]; dealiasing can be both computationally expensive and very difficult in complex geometries, and also counter to the LES spirit of reduced computational costs.

4.1. Correlations and slopes

Examination of the correlation between the exact and filtered terms (not shown), is made at two filter sizes, $\overline{\Delta} = 4\Delta x$ and $8\Delta x$. Although outside of the $\mathscr{F}_k$ term inquiry, term $(\tilde{\xi}_{vn}\overline{S}_{mass})$ has in all simulations and for both filter sizes a perfect correlation of unity with the exact term; term $[(\tilde{Y}_v/\tilde{\theta}_v) \times \overline{S}_{\xi_{vn}}]$ has a correlation of 0.961–0.971 at $\overline{\Delta} = 4\Delta x$, and of 0.894–0.909 at $\overline{\Delta} = 8\Delta x$ with the exact value; and $[(\tilde{Y}_v\tilde{\xi}_{vn}/\tilde{\theta}_v)\overline{S}_{mole}]$ has a correlation of 0.965–0.980 at $\overline{\Delta} = 4\Delta x$, and of 0.906–0.934 at $\overline{\Delta} = 8\Delta x$ with the exact term. For a given DNS case, the correlation slightly increases with increasing n or decreasing $\overline{\Delta}$. The correlation slightly decreases with increasing ML_0 or T_0 and with increasing liquid volatility, as the subgrid magnitude of the source terms increases. Across all moments and the entire database, the slopes are a minimum of 0.906 for $\overline{\Delta} = 4\Delta x$ and 0.791 for $\overline{\Delta} = 8\Delta x$.

Addressing the $\mathscr{F}_k$ terms, the special focus is on correlations for the $\mathscr{K}_n$, $\mathscr{L}_n$, $\mathscr{M}_n$ and $\mathscr{N}_n$ terms (defined in Table 2). Distinguishing between Form 1 and Form 2, at both filter sizes, the correlations for Form 1 terms $\mathscr{K}_n$ and $\mathscr{L}_n$ monotonically increases with n, with the slopes being randomly distributed in value over the n values (not shown); while for Form 2 both correlation and slope decrease with increasing n (not shown). This aspect suggests that Form 2 is to be preferred over Form 1 if the correlation value is similar for the two forms since the lower moments in a PDF are more important, with the higher moments providing only 'corrections'. Scrutiny of the database (not shown) reveals that the $\mathscr{M}_n$ constituents $(\partial M_{vn,j}/\partial x_j)$ for each $j = 1, 2, 3$ have a perfect correlation with the DNS solution and unity slope. $\mathscr{N}_n$ has, over $n = 1$–4, correlations between 0.930 and 0.949 and slope values between 0.888 and 0.957 for $\overline{\Delta} = 4\Delta x$; correlations are between 0.844 and 0.885, and slopes are between 0.613 and 0.665 for $\overline{\Delta} = 8\Delta x$. Similarly, $\mathscr{K}_n$ has, over $n = 1$–4, correlations between 0.878 and 0.914 and slope values between 0.737 and 0.789 for $\overline{\Delta} = 4\Delta x$; correlations are between 0.689 and 0.763, and slopes are between 0.466 and 0.523 for $\overline{\Delta} = 8\Delta x$. Finally, $\mathscr{L}_n$ has, over $n = 1$–4, correlations between 0.873 and 0.907 and slope values between 0.689 and 0.774 for $\overline{\Delta} = 4\Delta x$; correlations are between 0.681 and 0.732, and slopes are between 0.415 and 0.512 for $\overline{\Delta} = 8\Delta x$. Clearly, on account of both the correlation and slope values, as well as their value distribution across moments n, Form 2 has a better potential for LES than Form 1.

4.2. Activity of terms in $\mathscr{F}_k$

A comparison appears in Table 2 for the $\mathscr{F}_k$ terms. Vreman et al. [21] utilized the L2 norm to perform such a comparison. The selected norm is here the domain r.m.s. (square root of the L2 norm) because it quantifies each term's activity. Listed in the table are domain r.m.s. of the $\mathscr{K}_n$, $\mathscr{L}_n$, $\mathscr{M}_n$ and $\mathscr{N}_n$ terms and associated LES assumptions for all four ξ_{vn} conservation equations at the two filter sizes above. The computation is made for Case 1 and is representative of the entire Table 1 database. Examination of the entries under Form 1 and Form 2 shows that the r.m.s. values of Form 2 are smaller than those for Form 1, and thus are more likely to have negligible contributions in the LES equations since they must be compared to terms that are identical in both formulations, according to Eq. (3). Moreover, for Form 1 both LES assumptions are of same magnitude as the flux terms, and therefore cannot be neglected. This observation holds for all ξ_{vn} at both $\overline{\Delta}$ values. In contrast, for Form 2, the term $\Delta(\overline{\mathscr{M}_n})$ is generally one order of magnitude smaller than the two flux terms and can therefore be neglected. Whether $\Delta(\overline{\mathscr{N}_n})$ can also be eventually neglected depends on comparison of its value with the other terms in the LES equations. To inquire about this possibility, we next examine the magnitude of terms in LES ξ_{vn} equations, having now eliminated Form 1 and chosen Form 2 as the most likely to lead to a computationally efficient and functionally accurate LES.

4.3. Activity of terms in LES ξ_{vn} equations

In Table 3 we show the activity, according to the domain r.m.s., of terms in the ξ_{v1} equation which is representative of all four ξ_{vn} (not shown). The comparison reveals that $\Delta(\overline{\mathscr{M}_n})$ is indeed negligible under all conditions, being at least one order of magnitude and as much as three orders of magnitude smaller than the leading, convective term. Other negligible terms are $(\check{\xi}_{vn}\overline{S}_{mass})$ and $\Delta(\check{\xi}_{vn}\overline{S}_{mass})$, being under all conditions typically two and four orders of magnitude smaller than the leading terms, respectively. Regarding $\Delta(\overline{\mathscr{N}_n})$, it is generally three orders of magnitude smaller than the leading terms and smaller by two orders of magnitude than other resolved terms for $\overline{\Delta} = 4\Delta x$. However, for $\overline{\Delta} = 8\Delta x$, $\Delta(\overline{\mathscr{N}_n})$ becomes of same order of mag-

Table 2
Magnitude of terms (r.m.s.) at t_{tr}^* for the two LES formulations

Moments	R	Form 1				Form 2			
		$\mathscr{K}_n$	$\mathscr{L}_n$	$\Delta(\overline{\mathscr{K}_n})$	$\Delta(\overline{\mathscr{L}_n})$	$\mathscr{M}_n$	$\mathscr{N}_n$	$\Delta(\overline{\mathscr{M}_n})$	$\Delta(\overline{\mathscr{N}_n})$
ξ_{v1} units: $10^4 \times$ kg^2/(m^{3}s kmol)	4	15	14.5	7.53	7.49	0.563	0.944	0.00841	0.307
	8	9.58	9.19	9.34	9.22	0.300	0.547	0.0692	0.366
ξ_{v2} units: $10^7 \times$ kg^3/(m^{3}s kmol^2)	4	2.52	2.35	1.24	1.23	0.184	0.292	0.00277	0.0976
	8	1.58	1.46	1.55	1.51	0.0977	0.168	0.0229	0.115
ξ_{v3} units: $10^9 \times$ kg^4/(m^{3}s kmol^3)	4	4.36	3.97	2.11	2.10	0.465	0.699	0.00706	0.242
	8	2.09	2.42	2.65	2.59	0.247	0.401	0.0579	0.282
ξ_{v4} units: $10^{11} \times$ kg^5/(m^{3}s kmol^4)	4	7.78	6.98	3.72	3.72	1.08	1.54	0.0164	0.551
	8	4.76	4.19	4.68	4.60	0.570	0.877	0.133	0.640

Listed are the flux terms and associated LES assumptions for Case 1 of Table 1. All functions are calculated from the filtered field.
$\mathscr{K}_n = \frac{\theta_x}{Y_v}\frac{\partial K_{vn,j}}{\partial x_j}$, $\mathscr{L}_n = \frac{\theta_x}{Y_v}\xi_{vn}\frac{\partial L_{v,j}}{\partial x_j}$, $\mathscr{M}_n = \frac{\partial M_{vn,j}}{\partial x_j}$, $\mathscr{N}_n = 2M_{vn,j}\frac{\partial}{\partial x_j}\left[\ln\left(\frac{Y_v}{\theta_x}\right)\right]$, $R \equiv \overline{\Delta}/\Delta x$, $\Delta(\bar{f}) \equiv \overline{f(\phi)} - f(\bar{\phi})$.

Table 3
Magnitude (r.m.s.) of terms in LES equations at t_{tr}^* using the formulation of Form 2

Vapor composition first PDF moment	$\bar{\Delta} = 4\Delta x$				$\bar{\Delta} = 8\Delta x$			
	1	2	3	4	1	2	3	4
$\frac{\partial}{\partial x_j}(\bar{\rho}\tilde{\xi}_{v1}\tilde{u}_j)$	76.5	72.4	93.3	74.2	63.6	62.9	75.6	62.4
$\frac{\partial}{\partial x_j}(\bar{\rho}\pi_j)$	4.77	4.67	5.99	4.20	6.51	6.23	8.31	5.87
$\mathcal{M}_1(\bar{\phi})$	5.63	4.75	6.98	5.13	3.00	2.53	3.64	2.70
$\mathcal{N}_1(\bar{\phi})$	9.44	7.57	12.6	10.1	3.66	4.42	7.17	5.79
$\Delta(\overline{\mathcal{M}_1})$	0.0841	0.0779	0.101	0.0745	0.692	0.523	0.680	0.555
$\Delta(\overline{\mathcal{N}_1})$	3.07	2.45	4.37	3.44	3.66	2.87	4.93	3.80
$(\tilde{Y}_v/\tilde{\theta}_v) \times \overline{S}_{\xi v1}$	133	192	118	113	110	160	95.0	93.7
$(\tilde{Y}_v\tilde{\xi}_{v1}/\tilde{\theta}_v)\overline{S}_{mole}$	122	183	106	105	98.7	150	83.3	84.5
$\tilde{\xi}_{v1}\overline{S}_{mass}$	1.71	2.84	2.17	2.20	1.45	2.42	1.83	1.86
$\Delta[(\tilde{Y}_v/\tilde{\theta}_v) \times \overline{S}_{\xi v1}]$	31.3	54.4	30.5	30.9	45.9	75.6	41.8	42.2
$\Delta[(\tilde{Y}_v\tilde{\xi}_{v1}/\tilde{\theta}_v)\overline{S}_{mole}]$	27.5	50.7	26.4	27.4	40.2	69.9	35.8	37.0
$\Delta(\tilde{\xi}_{v1}\overline{S}_{mass})$	0.0126	0.0173	0.0183	0.0149	0.0224	0.0289	0.0317	0.0278

Units are 10^3 kg^2 s^{-1} m^{-3} kmol^{-1}.
$\mathcal{M}_1 = \frac{\partial M_{v1,j}}{\partial x_j}$, $\mathcal{N}_1 = 2M_{vl,j}\frac{\partial}{\partial x_j}\left[\ln\left(\frac{Y_v}{\theta_v}\right)\right]$, $\Delta(\bar{f}) \equiv \overline{f(\phi)} - f(\bar{\phi})$.

nitude as $\mathcal{N}_n$ and sometimes exceeds the $\mathcal{M}_n$ magnitude; the conservative attitude is to retain this term. Other terms that must be retained are $\Delta[(\tilde{Y}_v/\tilde{\theta}_v) \times \overline{S}_{\xi v_n}]$ and $\Delta[(\tilde{Y}_v\tilde{\xi}_{vn}/\tilde{\theta}_v)\overline{S}_{mole}]$ because under all conditions they are either comparable to the leading terms for $n = 1$ or exceed $\mathcal{M}_n$ for $n > 1$ (not shown). The physical interpretation for the source terms is that addition of mass through $(\tilde{\xi}_{vn}\overline{S}_{mass})$ has a negligible impact on vapor composition, and moreover because it is almost equally well computed as a function of $\bar{\phi}$ or ϕ according to the results of Table 3, this term has only minor variation at the LES subgrid scale. In contrast, for each ξ_{vn}, the vapor composition is substantially affected either by sources of that moment, $[(\tilde{Y}_v/\tilde{\theta}_v) \times \overline{S}_{\xi v_n}]$, or by sources of moles to the vapor through $[(\tilde{Y}_v\tilde{\xi}_{vn}/\tilde{\theta}_v)\overline{S}_{mole}]$. Moreover, at the level of the LES subgrid, the variation of these terms is substantial enough to lead to misestimates if computed as a function of $\bar{\phi}$ rather than ϕ. Because the correlation of these important filtered source terms to the exact corresponding values is high, as discussed above, the expectation is that with appropriate modeling, to be performed in forthcoming *a priori* studies, the LES composition moment equations could be modeled.

4.4. Reactive-flow considerations

Brevity dictates that we focus here succinctly on only two items: consistency of the formulation with known physics and modeling requirements for future LES. To check consistency we preliminarily rely on a limiting case. The vapor PDF before ignition is only known through ξ_{vn} $n \in [1, 4]$ and is not necessarily a DGPDF as discussed in [7]. To find the vapor composition from a finite number of moments, one can use the techniques described in [22]. Although not as accurate

as discrete species calculations, the PDF method is consonant with species lumping techniques. Because, as above, the term $\xi_{vn}S_{mass}$ is expected to have a minor contribution, whether ξ_{vn} increases or decreases due to source terms is determined according to Eq. (1) by the sign of $[S_{\xi vn} + \dot{\omega}_{\xi vn} - \xi_{vn}(S_{mole} + \dot{\omega}_{X_v})]$. For a perfectly stirred reactor, Eq. (1) can be approximated by

$$\xi_{vn} = (S_{\xi vn} + \dot{\omega}_{\xi vn})/(S_{mole} + \dot{\omega}_{X_v}). \qquad (6)$$

Because $\xi_{vn} \geqslant 0$, this means that for the vapor-composition problem to be well posed, $(S_{\xi vn} + \dot{\omega}_{\xi vn})$ and $(S_{mole} + \dot{\omega}_{X_v})$ must have same sign. Under typical evaporative conditions $S_{mole} > 0$, and under typical reactive conditions $\dot{\omega}_{X_v} < 0$ as vapor is transformed into reaction products, making the sign of $(S_{mole} + \dot{\omega}_{X_v})$ subject to temporal variation during concomitant evaporation and reaction; no conclusions may be obtained for this situation in absence of a simulation. If phase transition is completed (i.e. $S_{mole} = S_{\xi vn} = 0$) before reaction, Eq. (6) implies $\xi_{vn} = \dot{\omega}_{\xi vn}/\dot{\omega}_{X_v}$ which means that $\dot{\omega}_{\xi vn} < 0$, physically implying that $\forall n$, $\xi_{vn} \to 0$ with increasing t. This conclusion is consistent with known physics in that the vapor will disappear during reaction.

Because chemistry rates are higher than evaporation rates in reacting sprays, similar requirements to those for LES of non-reacting-flow source-term modeling will be necessary for reaction source terms. This statement is also valid for simulations where pre-vaporization is desired before combustion. That is, modeling will be necessary in Eq. (3) for both filtered reaction source terms and reaction-originated LES assumptions due to high subgrid rates that do not allow the replacement of a filtered DNS quantity by the quantity calculated from the filtered solution.

5. Conclusions

The LES equations have been derived for reactive fully multicomponent single-phase flows and two-phase flows with evaporation. The derivation is consistent with species lumping for reaction scheme reduction and species bundling for the diffusivity matrix in flames. The LES equations were derived by filtering the DNS equations. It was shown that from two equivalent DNS formulations, two non-equivalent LES formulations emerge for the vapor-composition conservation equations. Four criteria were proposed for choosing the more promising LES formulation. Based on an assessment using a DNS database, the more promising formulation has been identified for non-reactive flows that satisfies all criteria. For this formulation, an examination of the activity of all terms in the equations revealed terms other than the SGS flux that will require modeling in future *a priori* studies; these other terms include LES assumptions for evaporation-originated source terms. Based on the fact that reaction rates are higher than evaporation rates, with correspondingly higher local subgrid activity, it is foreseen that similar requirements will be necessary for reaction-originated source terms in the composition equations.

Acknowledgments

References

[1] E. Ranzi, M. Dente, A. Goldaniga, G. Bozzano, T. Faravelli, *Prog. Energy Combust. Sci.* 27 (2001) 99–139.
[2] T. Lu, C.K. Law, *Combust. Flame* 148 (2007) 117–126.
[3] W.L.H. Hallett, *Combust. Flame* 121 (2000) 334–344.
[4] K.G. Harstad, P.C. Le Clercq, J. Bellan, *AIAA J.* 41 (10) (2003) 1858–1874.
[5] P.C. Le Clercq, J. Bellan, *Proc. Combust. Inst.* 30 (2005) 2007–2015.
[6] P.C. Le Clercq, J. Bellan, *J. Fluid Mech.* 533 (2005) 57–94.
[7] L.C. Selle, J. Bellan, *Phys. Fluids* 19 (6) (2007), 063301-1-33.
[8] F. Mashayek, *J. Fluid Mech.* 367 (1998) 163–203.
[9] N.A. Okong'o, J. Bellan, *J. Fluid Mech.* 499 (2004) 1–47.
[10] A. Leboissetier, N.A. Okong'o, J. Bellan, *J. Fluid Mech.* 523 (2005) 37–78.
[11] M. Boivin, O. Simonin, K.D. Squires, *J. Fluid Mech.* 375 (1998) 235–263.
[12] K.D. Squires, J.K. Eaton, *Phys. Fluids A* 3 (1991) 1169–1178.
[13] B. Gal-Or, H.T. Cullinan Jr., R. Galli, *Chem. Eng. Sci.* 30 (1975) 1085–1092.
[14] R.L. Cotterman, R. Bender, J.M. Prausnitz, *Ind. Eng. Chem. Process Des. Dev.* 24 (1985) 194–203.
[15] G.F. Chou, J.M. Prausnitz, *Fluid Phase Equilibr.* 30 (1986) 75–82.
[16] R.D. Moser, M.M. Rogers, *Phys. Fluids A* 3 (1991) 1128–1134.
[17] R.S. Miller, K. Harstad, J. Bellan, *Int. J. Multiphase Flow* 24 (1998) 1025–1055.
[18] T. Edwards, L.Q. Maurice, *J. Propul. Power* 17 (2) (2001) 461–466.
[19] T. Edwards, private communication, 2002.
[20] A.G. Kravchenko, P. Moin, *J. Comput. Phys.* 131 (1997) 310–322.
[21] B. Vreman, B. Geurts, H. Kuerten, *J. Eng. Math.* 29 (1995) 299–327.
[22] V. John, I. Angelov, A.A. Öncül, D. Thévenin, *Chem. Eng. Sci.* 62 (2007) 2890–2904.